FORMING OF MULTILAYERED FABRIC REINFORCED THERMOPLASTIC COMPOSITES

Kristof VANCLOOSTER

Promotoren:
Prof. I. Verpoest
Prof. S.V. Lomov

Leden van de examencommissie:
Prof. C. Vandecasteele (voorzitter)
Prof. D. Vandepitte
Prof. B. Verlinden
Prof. A. Van Bael
Prof. P. Harrison

Proefschrift voorgedragen
tot het behalen van de
graad van Doctor in de
ingenieurswetenschappen

ISBN 978-94-6018-223-5
D/2010/7515/62

Voorwoord

"The ideal engineer is a composite ... He is not a scientist, he is not a mathematician, he is not a sociologist or a writer; but he may use the knowledge and techniques of any or all of these disciplines in solving engineering problems."

N. W. Dougherty, 1955

In dit voorwoord wil ik enkele mensen bedanken die rechtstreeks of onrechtstreeks mee hebben geholpen aan het tot stand komen van dit doctoraat. De weg die je volgt tijdens een doctoraat is niet altijd de makkelijkste en gaat meestal gepaard met vallen en opstaan. Gelukkig kon ik op de steun rekenen van een heleboel mensen.

In de eerste plaats wil ik mijn beide promotoren, Ignaas Verpoest en Stepan Lomov, oprecht bedanken om me deze kans te geven. Dit doctoraat is vooral tot stand gekomen door op jullie ervaring te bouwen. Ook bedank ik graag Dirk Vandepitte, Bert Verlinden en Bert Van Bael voor het doornemen van deze tekst. Thank you, Philip Harrison, for reading my text, your comments and remarks helped to improve my dissertation. Tevens dank ik Carlo Vandecasteele als voorzitter van de doctoraatsjury.

De medewerkers van MTM en PMA verdienen zeker een woord van dank. Zonder het technisch vernuft en het praktische doorzicht van Bart, Kris, Jo en Manuel van MTM en Dirk Bastiaensen op PMA zou dit doctoraat een hachelijke onderneming zijn geweest. Ook de "ALMA"niakken, Frans, Huberte en Regine, bedankt voor de ontspannende babbels tijdens de middagpauze.

Ook wens ik de vele bureau- en postbuscollega's die ik heb gekend tijdens deze 4,5 jaar hartelijk te danken. Bedankt, An, onze discussies waren zeer leerrijk en vooral motiverend voor me. Ook de vele ESAFORM conferenties die we samen hebben bezocht en vooral de trip naar Alcalá de Henares zal ik niet snel vergeten. Ook Joris, Jan, Katleen en Greet mag ik niet vergeten, jullie zijn meer dan collega's geworden voor me. Daarnaast wens ik de andere leden van de composietgroep te bedanken voor de fijne herinneringen.

Als laatste bedank ik de mensen die op tijd en stond daar waren om me te ondersteunen als ik eens een dipje had. Mélissa, je bent in m'n leven gekomen ruwweg 2 jaar geleden, door jou ben ik te weten gekomen dat het leven meer inhoudt dan enkel werken. Je bent mijn zonnetje en ik hoop dat je me nog lang zal toeschijnen…

Mams en paps, er zijn geen woorden genoeg om jullie te bedanken voor jullie zorg en liefde. Zonder jullie zou ik nooit de kansen hebben gekregen om dit doctoraat te volbrengen. Bedankt!

Abstract

Woven reinforced thermoplastic polymers are used widely in a number of composite applications. During production of multilayered composites, the woven reinforcement undergoes large deformations and slip needs to occur between the layers. This affects the final product quality and may lead to forming related defects (e.g. wrinkling).

The nonlinear finite element method supports the process optimization by predicting the local fibre orientations and the occurrence of defects during forming. To support the optimization of forming multilayered composites, a suitable contact model is needed that incorporates the complex contact behaviour that occurs between the individual plies of a composite laminate.

The major aim of this study is first of all to obtain an understanding of the formability of multilayered woven thermoplastic composites. This has led to the development of a Forming Limit Diagram. Moreover, an experimental design is developed and executed to screen the influence of the process parameters on the formability of a two-layered woven composite. From the results, a suggestion to increase the formability of multilayered woven composite is made.

A second aim is related to the development of a model that can describe the complex contact behaviour that occurs between the individual plies of a composite and between the tooling (e.g. punch and blankholder) and the composite surface. Previously developed models are investigated and a new model is proposed. This model is combined with an elastic macro-scale material model that incorporates the drape behaviour of a single layer of woven composite.

Finally, forming of a two-layered composite is simulated and compared to some of the experimental forming cases. The thickness of the interlayer is found to be the most influential parameter to eliminate the occurrence of wrinkling.

List of abbreviations

AEM	Affine Elastic Model
AFA	Advancing Front Approach
CCD	Charge-Coupled Device
DC	Drape Coefficient
DIC	Digital Image Correlation
DOF	Degree of freedom
DSC	Differential Scanning Calometry
FE(M)	Finite Element (Method)
FLD	Forming Limit Diagram
GSA	Grid Strain Analysis
IR	InfraRed
IRSGA	InfraRed Square Grid Analysis
KES	Kawabata Evaluation System
OT	Orthotropic stacking
PMD	Principal material directions
PP	Polypropylene
PP_{int}	Polypropylene used for sheet material
PP_{tw}	Polypropylene used in Twintex material
QI	Quasi-Isotropic stacking
TCC	Thermal Contact Conductivity
TCR	Thermal Contact Resistance
TGA	ThermoGravimetric Analysis
TP	Tepex material Dynalite 104
TW_1	Twintex material TPEET44
TW_2	Twintex material TPEET22
SB	Amount of springback

List of symbols

A_0, A_1	Fitting parameters of the traction model
A_c	Total contact area
A_p	Area on which piston pressure acts
$Ar(T)$	Fitted parameter for Arrhenius model
Ar_0, Ar_1	Fitting parameters for Arrhenius model
$\mathbf{b}$	Body force vector
$\mathbf{B}$	Strain-displacement matrix
B_0, $B_{1,}$ B'_1	Fitting parameters of the traction model
$\mathbf{C}$	Damping matrix
$C(T)$	Fitting parameter for Ellis model
c_1,c_0	Fitting parameters for Stribeck model
c_d	Current effective dilatational wave speed
C_p	Drag coefficient
c_p	Specific heat capacity
c_p	Specific heat capacity
$\mathbf{D}$	Elasticity matrix
d_{avg}	Average distance between formed composite and fitted oblate spheroid
d_{cr}	Critical slip displacement
$D_{f,i}$	Displacement of node after draping
$Dslip_n$	Slip increment
dU	Change in internal heat energy
E_{11}, E_{22}	Tensile elastic moduli in warp and weft direction
E_i	Internal energy
E_k	Kinetic energy
E_{max}	Maximum principal strain
E_{min}	Minimum principal strain
f	Frequency
F_{cr}	Critical frictional force
F_D	Drag force
F_f	Frictional force
F_N	Normal force
F_{Ncr}	Critical normal force
F_p	Piston force

G	In-plane shear modulus
G^*	Complex modulus
h	Interlayer thickness
He	Hersey number
h_t	Heat transfer coefficient
h_t	Heat transfer coefficient
$\mathbf{K}$	Stiffness matrix
k_t	Thermal conductivity
k_t	Thermal conductivity
l	Height of formed composite
$L(t)$	Momentary contact length of specimen
L1, L2, L3	Cross-section lines
L_e	Characteristic element dimension
L_h	Line along the top of the semi-hemisphere
l_{max}	Maximum measure height of formed composite
$\mathbf{M}$	Mass matrix
$\mathbf{N}$	Shape function matrix
n	Power law coefficient
n_0	Fitting parameter of the traction model
P	Pressure
P1, P2, P3	Impact point used in kinematic draping
P_{cr}	Critical pressure
p_h	Normalized distance between formed composite and fitted oblate spheroid
$\mathbf{p_n}$	Total load vector
P_p	Piston pressure
$\mathbf{q^e}$	External force vector applied on element e
R	Radius
S^e	Element surface
S_{max}	Maximum principal stress
S_{min}	Minimum principal stress
s_T	Total slip
T	Temperature
T_∞	Temperature of the environment
T_d	Degradation temperature
T_g	Glass transition temperature
T_m	Melting temperature

v	Velocity
V^e	Volume of element e
VP1, VP2	Viewpoint 1 and Viewpoint 2
w	Width of specimen
W_1	Paper weight of full specimen
W_2	Paper weight of drape shadow
α	Enclosed angle between warp and weft yarns
β	Slip factor
β_i, β_{ij}, I	Fitting parameters for screening design
γ	Shear angle
$\dot{\gamma}$	Shear rate
$\Delta D_{f,i}$	Difference in local displacement between adjacent plies after
δQ	Energy received by the system
Δt	Time increment
δW	Work done by the system
ε_{max}	Major strain
ε_{min}	Minor strain
η, $\eta(\dot{\gamma})$	Shear viscosity
$\eta^*(\omega)$	Complex dynamic viscosity
$\eta_0(T)$	Zero shear viscosity
θ	Ply orientation / latitude
μ	Friction coefficient
μ_{cr}	Critical friction coefficient
ν	Poisson ratio
ρ	Density
τ	Traction
τ^*	Steady-state traction
τ_0	Fitting parameter of the traction model
τ_{cr}	Critical peak traction
τ_p	Peak traction
τ_{yield}	Yield traction
φ	Sliding angle
ω	Angular frequency
$\bar{\mathbf{t}}$	Surface force vector
$\mathbf{u_n}$	Nodal displacement vector
$\dot{\mathbf{u}}_{\mathbf{n}}$	Nodal velocity vector
$\ddot{\mathbf{u}}_{\mathbf{n}}$	Nodal acceleration vector

$\bar{n}_0$	Average power-law index for the traction model

Table of contents

Chapter 1

Literature review

1.1. Introduction

A composite is a material composed of two or more individual materials. In most cases one of the constituents acts as reinforcement, having a high strength and stiffness, but lacking structural integrity. This reinforcing material is then embedded in matrix material, which often has a low density, but lacks strength and stiffness. Combining these materials results in a composed material that has both a high stiffness and strength, but also a low density, making it a suitable replacement for heavy structures.

In fibre reinforced thermoplastic composites, a fibrous reinforcement is embedded in a thermoplastic polymer matrix. The fibres can be arranged in many different reinforcing structures. A common reinforcement type is a textile, whereby the fibres are often first assembled in yarns, which are then interlaced to form a flexible material.

In this chapter a state-of-the-art in forming of textile reinforced thermoplastic composites is provided. First, an overview is given of the most common types of textile reinforcements. Then, thermoplastic polymers will be introduced and the processing and deformation mechanisms of textile composites are discussed. Afterwards, a more detailed review on the frictional behaviour of the composite during forming is presented. At the end of this chapter several forming simulation approaches and forming limit diagrams, which are used to indentify whether defects in the final part occur, are treated.

1.2. Textile thermoplastic composites

Textile thermoplastic composites combine a textile reinforcement and a thermoplastic polymer matrix material. Textiles offer superior handleability and formability over traditional unidirectional reinforcements, often at the cost of a somewhat lower stiffness. This makes textile composites very popular in a broad range of high volume applications, going from automotive to leisure.

Figure 1-1 illustrates different commercial products made from woven reinforced thermoplastic polymers. Figure 1-1(a) shows a suitcase made from woven self-reinforced polypropylene, which allows for a high degree of recyclability. Woven glass fibre reinforced polypropylene can be formed into floor guards for sport cars, Figure 1-1(b), or into a canoe for recreative use, Figure 1-1(c)).

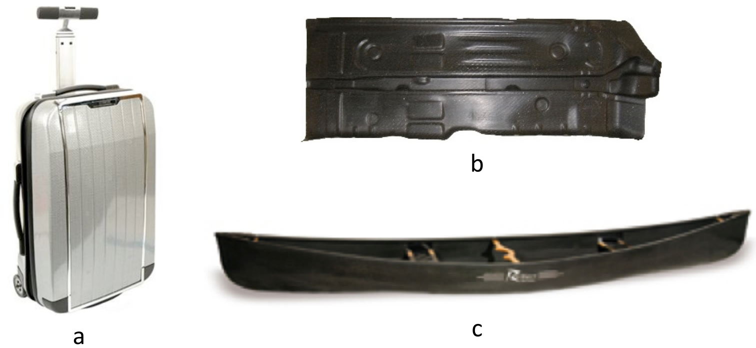

Figure 1-1. Typical commercial products made from woven reinforced thermoplastic composites: (a) X'lite suitcase from Samsonite, (b) floor guard for a race car and (c) a canoe

1.2.1. Textile reinforcements

Textile or fabric reinforcements are by definition made by fibres, which are assembled in yarns or tows. By weaving, braiding or knitting, these yarns are then interlaced into fabrics. Textiles can be subdivided into 2D and 3D reinforcements. 3D reinforcements also contain through the thickness yarns. This type of textile will not be treated in this study. Figure 1-2 shows typical examples for common 2D textile structures. A woven and braided fabric have two principal yarn directions, while in a knitted fabric the interlaced yarns form loops.

Figure 1-2. Typical textile structures with (a) a weave, (b) a braiding and (c) a knit (adapted from [1])

The difference in fabric structure, determines both the mechanical response and the drapeability of the textile. In Figure 1-3 the stiffness of woven and knitted fabrics is visualized in polar diagrams. In such diagrams, the stiffness is plotted as a function of the loading direction and indicates the in-plane variation (anisotropy) of the stiffness of the fabrics. The vertical axis refers to the machine direction of fabric production (warp), while the horizontal axis indicates the cross direction (weft). The woven fabric behaves highly anisotropic with a high stiffness in warp and weft direction, but a much lower stiffness in bias (45°) direction. Figure 1-2(a) indicates that the principal yarn directions agree with the warp and weft orientation, explaining the high stiffness. Knitted fabrics behave more isotropic and generally have a lower stiffness than weaves, since no principal yarn orientation exists.

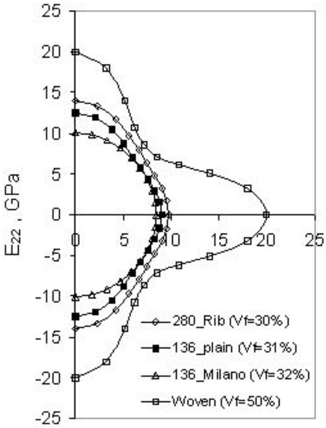

Figure 1-3. Polar diagram representing the stiffness of several woven (indicated as Woven) and knitted fabrics (indicated as 280_Rib, 136_plain and 136_Milano) [2]

As can be seen in Figure 1-1, complex shapes can be formed with textile reinforcements. The ease with which textile materials conform to a certain shape has been the subject for research for many decades and finds it origin within the draping of garments. Chu et al. [3] developed the earliest quantification method for fabric drape. They quantified the drapeability of a fabric into a dimensionless value termed the drape coefficient (DC), which is defined as the percentage of the circular area of flat fabric covered by the vertical projection of the same fabric after draping. They introduced a drape coefficient (DC):

$$DC = \frac{W_2}{W_1} \quad \text{Eq. 1-1}$$

Where W_1 is the paper weight of the full specimen and W_2 the paper weight of the shadow of the draped fabric, which is clarified in Figure 1-4(a). From this definition it follows that, the higher the drape coefficient, the less the fabric deforms under its own weight and thus the more effort it will take to drape it.

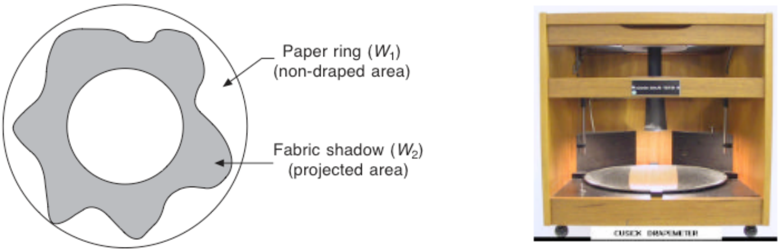

a b

Figure 1-4. Measuring the DC of a fabric with (a) typical drape profile of a fabric and (b) the drape meter developed by Cusick (modified from [4])

Cusick [5] further developed the experimental apparatus, shown in Figure 1-4(b), using a parallel light source that reflects the drape shadow of a circular fabric specimen, which freely hangs under its own weight, onto a paper ring. He showed that stiff fabrics have a high DC, while a limp fabric possesses a low DC. Further studies [6] showed that three-dimensional drape in terms of DC are closely associated with two-dimensional drape studies in terms of bending rigidity. Moreover, the DC is also influenced by shear and tensile properties as well as by fabric weight and fabric thickness [7, 8]. Kawabata [9] has developed an evaluation system, referred to as KES (Kawabata Evaluation System), which determines the mechanical properties that correspond to the deformation of fabrics. KES includes the measurement of fabric bending, shearing, tensile and compressive stiffness as well as the frictional properties of the fabric surface. The information provided by this system can increase production efficiency and product performance since the mechanical properties of fabrics not only govern the performance of fabric products but also influence fabric production.

In the composite forming industry, however, the drape coefficient is of no use since the fabric reinforcement does not freely hang, but instead is forced to conform to the product shape. Also the use of KES is fairly limited since it only provides information of the fabric behaviour at relatively low levels of deformation, coupled with the limited availability of the expensive testing equipment [1]. Instead, the drapeability of textile reinforcements is usually expressed in terms of the “locking” angle. This angle is related to the in-plane shear properties of the fabric and denotes the amount of deformation a fabric can undergo before wrinkling is initiated (see section 1.4.1). However, it has been shown by Rozant [10] that a higher locking angle does not necessarily mean that the fabric possesses a higher drapeability. In-plane shear is just one of the possible deformation modes. During draping of textile composites a number of draping mechanisms, which are further elaborated in section 1.4, occur simultaneously and moreover they heavily interact with one another, making it difficult to assess the drapeability of a textile composite. In section 1.7 experimental forming studies of textile thermoplastic composites are further discussed and it will be shown in Chapter 5 that the locking angle does not give any indication of the drapeability of multilayered composites.

1.2.2. Polymer matrix materials

In composite materials the reinforcement is embedded in a matrix. The main purpose of this matrix is to hold the reinforcing constituents in place relative to each other, restricting their mutual displacement and providing structural integrity. Most commercially produced composites use a polymer as matrix material. Polymers are made up of small molecular blocks (called monomers) and can be divided into two main classes with respect to their thermal behaviour, namely thermosets and thermoplastics. The difference in the thermal behaviour of the stiffness of these two groups is indicated in Figure 1-5. Thermosets include those polymers that are irreversibly cured[1] and remain solid until a temperature, T_d, is reached where the polymer chains are oxidised, i.e. degrade[2]. Thermoplastics, however, are polymers that turn to a liquid state, at temperatures above T_m, when heated and behave as a solid when cooled below their glass transition temperature T_g. The focus in this dissertation lies on reinforced thermoplastics and therefore thermoplastics will be further introduced.

1.2.3. Thermoplastics

Thermoplastic polymers consist out of polymer chains with a high molecular weight, which interact with each other via physical bonds, namely entanglements and van der Waals forces. These physical bonds can be overcome by addition of thermal energy. Figure 1-5 shows the influence of the temperature on the elastic modulus of a thermoplastic polymer.

Increasing the temperature increases the rotation frequency of the polymer segments between the entanglements. The weak van der Waals forces are easily broken and thus the density of the van der Waals interactions decreases. This phenomenon explains the drop in stiffness that occurs at the glass transition temperature T_g. Increasing the temperature even more increases the vibration of the molecules, which leads to increasing disentanglement of the polymer chains and in case of semi-crystalline polymers, like polypropylene, the crystalline structure will be broken at the melt temperature T_m. This event allows the polymer chains to freely move relative to each other, making the polymer a liquid. The physical bonds and the semi-crystalline structure are remade during cooling, which makes a thermoplastic polymer recyclable.

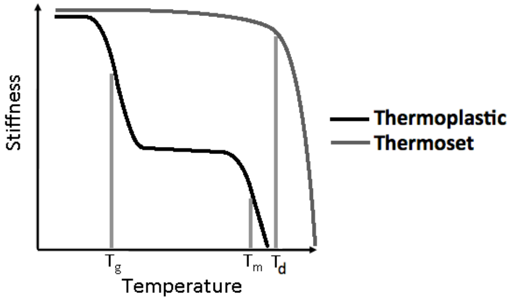

Figure 1-5. Typical stiffness behaviour of thermoplastic and thermosetting polymers

During forming of thermoplastic materials, the temperature should be high enough to assure that the material can cope with large deformations without rupture. Therefore, before forming thermoplastic composites, they are heated

---

[1] Forming of a 3D-polymer network by primary bonds between polymer chains

[2] Decompose into atoms or smaller molecules

until the matrix behaves as a liquid. In its liquid state the viscosity η, which is a measure for the resistance against flow, characterises the molten polymer.

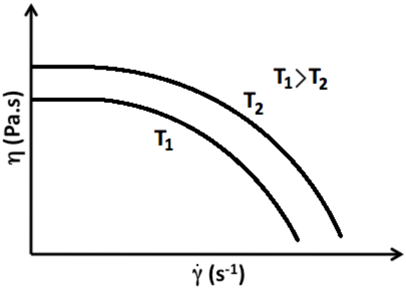

Figure 1-6. Typical flow curve for thermoplastic polymer at different temperatures

The viscosity of the matrix material is an essential parameter that determines both the impregnation[3] and consolidation[4] of the final product [11, 12], but moreover also has a great impact on the draping mechanisms of the composite with thermoplastic matrix (see sections 1.4 and 1.5). A consequence of the high molecular weight is a high viscosity for a thermoplastic polymer. The viscosity of thermoplastic materials ranges from 100 to 10000 Pa•s, which is several factors higher than the 1 Pa•s for thermosets before curing. These high viscosity values lead to difficult impregnation of the reinforcement, since the matrix materials needs to fully wet the individual fibres within the yarns. Therefore, the reinforcing material is usually pre-impregnated with the polymer, limiting the flow length during processing.

Figure 1-6 presents a typical flow curve of a molten thermoplastic polymer, the viscosity, η, is depicted as a function of the shear rate, $\dot{\gamma}$. The decrease of the viscosity when the shear rate increases is denoted as shear thinning behaviour. The polymer molecules align with each other at high shear rates, which decreases the internal friction and thus also the viscosity. At higher temperatures the van der Waals forces between the polymer chains are more easily broken, which makes the viscosity decrease. The influence of the pressure on the viscosity is negligible due to the incompressibility of the polymer liquid.

1.3. Textile thermoplastic composite processing

This section focuses on the different forming processes for textile reinforced thermoplastic polymers. The discussion is based on three reviews on composite processing [1, 13, 14]. The processing of textile reinforced thermoplastic composites is influenced by the continuous nature of the reinforcement. Traditional thermoplastic composite processing techniques,

---

[3] Surrounding the reinforcing fibres with matrix material

[4] Act of compaction whereby the volume of the composite decreases

suited for short fibre composites, like injection moulding or sheet extrusion are not suitable to process textile reinforcements due to the continuous nature of the yarns in the textile. Instead textile composites adapt to complex shapes by specific draping mechanisms, which are discussed in section 1.4.

A typical thermal and pressure cycle for thermoplastic composite processing is shown in Figure 1-7. First, the reinforced polymer sheet is heated until the desired temperature is reached. This temperature lies above the glass transition temperature T_g or the melt temperature T_m of the matrix. Afterwards, the flat heated sheet is formed in a mould through vacuum, compressed air, a fluid or a punch. Then, the hot deformed composite is cooled down under pressure, until it is dimensionally stable and the part can be demoulded.

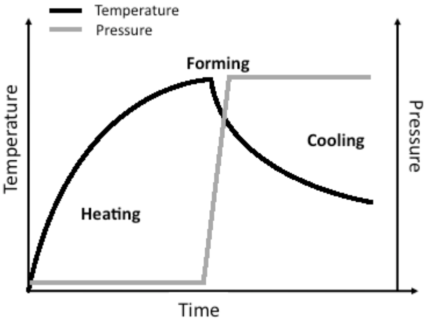

Figure 1-7. Typical temperature and pressure cycle during processing of thermoplastic composites

During forming of thermoplastic composites two key features, i.e. draping and impregnation/consolidation, are essential to develop a high quality product. When the flat sheet is draped, it needs to conform to the mould geometry. Here it is essential that no defects arise and that the fibres are oriented in the desired directions. Increasing the pressure is needed to assure that all fibres are surrounded by matrix material, i.e. good impregnation, and no voids are present in the end product, i.e. good consolidation. In this text the focus will be on the draping aspect of forming.

The last decades, thermoforming of polymers and metal sheet forming were adapted to be suitable to process continuous fibre reinforced thermoplastic composites. This resulted in a number of variations to the thermoforming technique, namely hydro-, rubber, stretch, roll, diaphragm and press forming. Especially diaphragm and press forming are very popular because of their versatility and the possibility to manufacture complex components.

1.3.1. Press forming

Press forming is the most commonly used processing technique for long fibre or continuous reinforced composites. It was deduced from deepdrawing of sheet metal, where it has been successfully used for making automotive body panels, fuel tanks, kitchen sinks, two-piece aluminium cans, etc. During deepdrawing a sheet of material is drawn into a forming die by the mechanical action of a punch. At the end of the forming step no pressure is applied on the material, which makes deepdrawing not suitable to produce composite parts with a high impregnation and consolidation quality. However, in Chapter 6 deepdrawing will be used to investigate the defects that arise during forming of multilayered woven composites.

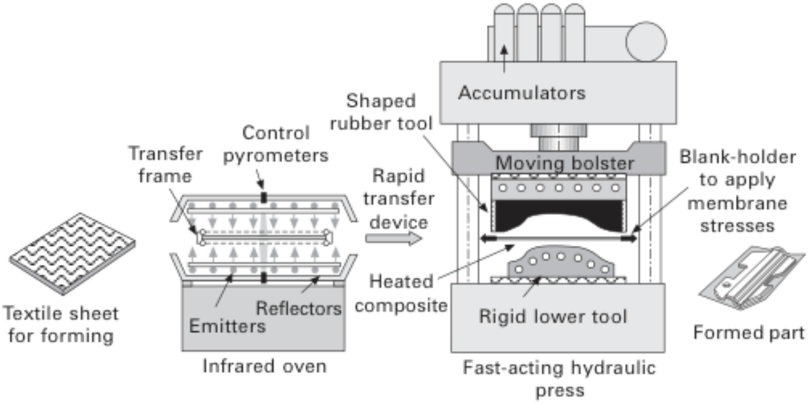

Figure 1-8. Non-isothermal rubber die forming [1]

During press forming a hot blank is pressed between two tools (punch and die) as indicated Figure 1-8. When these tools are complementary and made out of metal or a hard composite, press forming is referred too as matched die forming. If instead one or more tools are made from a high-temperature rubber, press forming is also known as rubber die moulding. The rubber tool generates a more homogeneous pressure distribution, which benefits a uniform consolidation in the finished part. Drawbacks of the rubber die moulding are associated with the low heat transfer coefficient, increasing the cooling time, and the low hardness, making it vulnerable for abrasions, of the rubber material.

1.3.2. Blankholder

The blankholder is a device that holds the sheet, i.e. the blank, while it is formed. The main purpose is to introduce tensile forces in the sheet to counteract the in-plane compressive forces that trigger out-of-plane buckling or wrinkling. The friction between the blankholder and the sheet and the normal force/pressure exerted by the blankholder determine the amount of tensile stresses that are invoked. If the blankholder force is too low, wrinkling will occur more easily. A too high blankholder force, however, often results in tearing of the material.

Different types of blankholders are developed, going from continuous to discrete. Planar continuous blankholders with a homogeneous pressure distribution were the first ones to be developed for metal sheet forming and are also often used for composite sheet forming. Breuer et al. [15] developed an alternative clamping system that consists of a discrete number of rollers. The sheet material is drawn into the mould between two rollers. The normal pressure on these rollers can be changed depending on their position and the draw depth. This allows for a better control of the membrane forces in the sheet during forming, giving rise to a better quality product.

1.3.3. Diaphragm forming

In diaphragm forming one or two deformable membranes, called diaphragms, deform the flat composite sheet [16]. Figure 1-9 shows that by a combination of pressure and vacuum the sheet is deformed and adapts to the rigid mould. Two variations of the diaphragm forming process exist, namely the single and double diaphragm forming process. In the single diaphragm process the deformed sheet comes in direct contact with the mould.

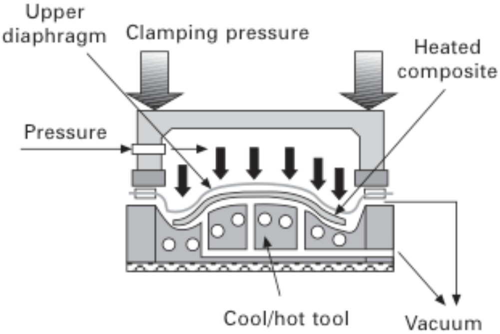

Figure 1-9. Isothermal single diaphragm forming [1]

The main advantage of this forming process is that the deformable sheets stretch during forming and keep the composite under tension, reducing its tendency to wrinkle. The main disadvantages of diaphragm forming are a slow cycle time (about 1 hour) and the high cost, since each new part requires one or two new diaphragms.

1.3.4. Vacuum forming

Figure 1-10 illustrates the basic isothermal process. The thermoplastic composite is laid up on a single-sided mould and covered with a release film and breather cloth. A vacuum bag is used to seal of the material and the air is pumped out of the bag. The whole arrangement is then placed in a circulating air oven and the temperature is raised to above the matrix melting point, which allows forming, impregnation and consolidation to take place. This process is often subject to significant heating times making it a low volume process.

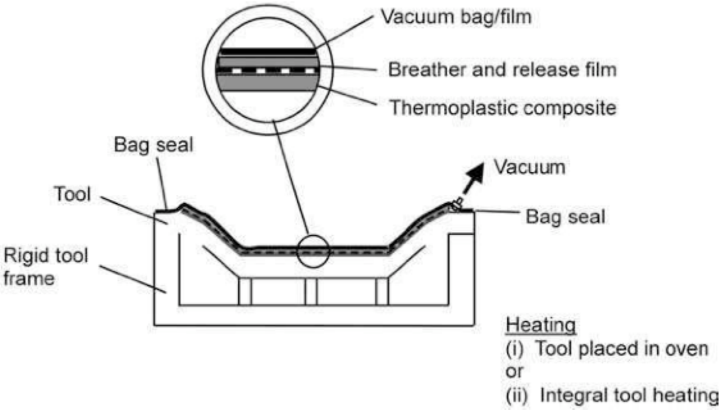

Figure 1-10. Schematic diagram of the isothermal vacuum forming process [17]

Alternatively non-isothermal vacuum forming enables faster cycle times to be achieved. Here the thermoplastic sheet is heated in an oven, transferred and rapidly laid up on a cold mould whereby vacuum is applied to shape the hot sheet. This is clearly a rapid process with a low investment cost, since the tooling is only subject to a pressure of 1 bar, but it is restricted to the size of the part. Above about $1m^2$ preheated charge transfer becomes problematic. Moreover, since the consolidation pressure is limited, the impregnation and consolidation quality of the final product are generally lower than in press or diaphragm forming [18].

Table 1-1. Overview of different forming processes

Process	Characteristic	Advantage	Disadvantage
Press forming	▪ Moulds usually made of aluminium or rubber deform the flat composite	▪ Low cycle times ▪ High consolidation pressures can be reached ▪ High surface finish quality	▪ Cost ▪ Limited in complexity of the parts
Diaphragm forming	▪ The flat composite is pressed between membranes	▪ High surface finish quality ▪ Complex parts can be formed	▪ Expensive membranes need to be replaced (for some materials every cycle)
Vacuum forming	▪ The composite material is pressed by applying a vacuum	▪ Simple technique ▪ Low cost ▪ Versatile technique	▪ Long cycle times ▪ Limited in size of parts ▪ Low quality of surface finish

Table 1-1 provides an overview of different forming processes for thermoplastic composites, indicating their characteristics, advantages and disadvantages.

In the experimental part of this research, matched die forming and deepdrawing are used in combination with a continuous planar blankholder to investigate the forming behaviour of single and multilayered textile thermoplastic composites. The forming methodology is further explained in Chapter 3.

1.4. Deformation/draping mechanisms of textile composites

This section introduces the deformation mechanisms of textile thermoplastic composites.

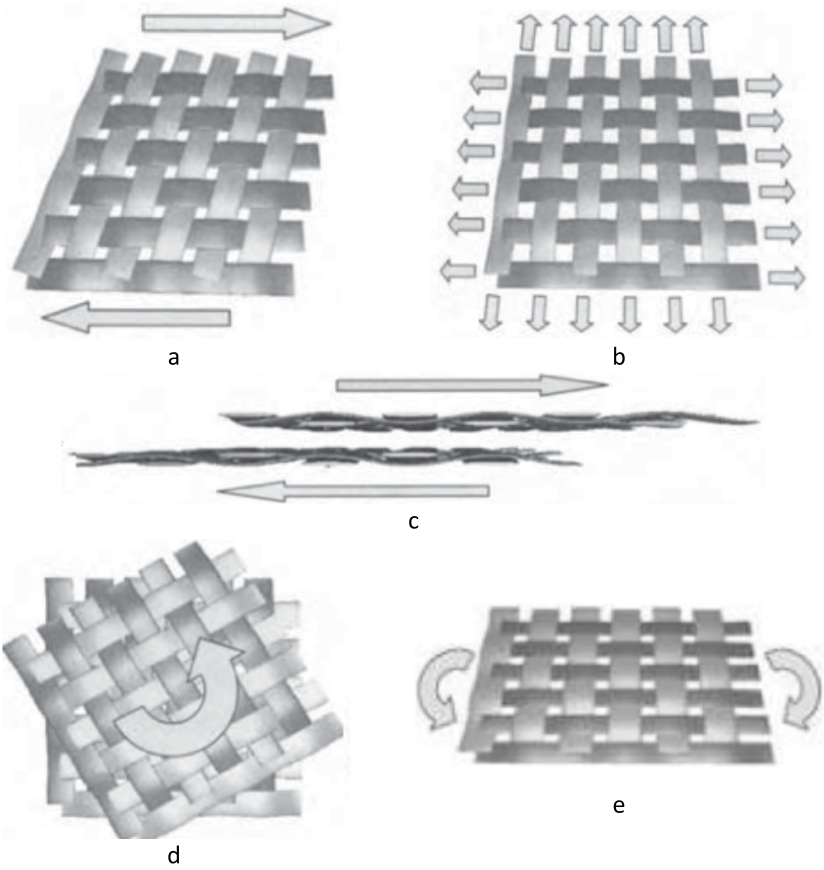

Figure 1-11. Draping mechanisms for textile reinforcements: (a) intra-ply shear, (b) intra-ply extension, (c) inter-ply slip, (d) inter-ply rotation and (e) ply bending (adapted from [1, 17])

During draping, textile composites need to undergo large deformations to adapt to complex shapes. Figure 1-11 depicts the different macroscopic draping mechanisms that occur during forming of a woven textile reinforced composite. Due to the limited stretch the textile preforms, with the exception of knits, can undergo in the yarn direction, intra-ply shear or trellising is needed to allow a textile preform to conform to a compound curvature. However, in woven fabrics a small degree of stretch in the yarn directions may occur due to uncrimping of the yarns [19]. When multilayered materials are formed, slip between the adjacent layers must also be considered. Inter-ply shear slip and rotation are needed to release the compressive stresses that would else invoke out of plane buckling. For thermoplastic composites these draping mechanisms can only occur at temperatures where the matrix is liquid.

1.4.1. Intra-ply shear

As mentioned above intra-ply shear is considered to be the primary deformation mechanism during forming of textile reinforcements to 3D shapes. This type of deformation is characterized by a change of fibre orientation, due to rotation of the yarns at their crossovers. The amount of in-plane shear is indicated by a shear angle γ, which is defined as the complement of the enclosed angle, α, between the warp and the weft yarn (see Figure 1-12(a)). The two methods used to determine the inter-ply shear behaviour are the picture frame test [20-22], see section 7.2.2, and the bias extension test [23]. Recently Harrison et al. [24, 25] developed a third technique to characterise the shear behaviour by using a biaxial test set-up. A typical shear compliance curve, recorded by these test methods, is seen in Figure 1-12(b).

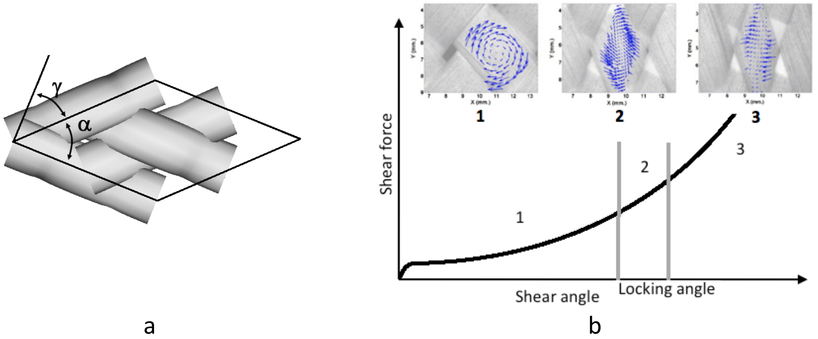

Figure 1-12. In-plane shear of a plain woven fabric with (a) an indication of the shear angle γ and (b) typical picture frame result for a fabric composite (adapted from [26])

The small jump at the beginning of the curve is due to the static friction between the interlaced yarns of the fabric. Though, generally speaking, the shear compliance curve is divided into three regions, which has been analytically modelled in [27]. At low shear angles, the resistance to in-plane shear is low. Skelton [28] suggested that the resistance was a result of friction between the warp and the weft yarns at their crossovers. In this phase, the yarns are submitted to a rigid body rotation. The displacements at the crossover point are visualized in inlets in Figure 1-12(b), the blue vectors indicated the orientation and magnitude of the local displacement. There is no shearing inside the yarns. The global fabric shear is due to relative parallel displacement of yarns [26]. With increasing shear angle, the yarns are coming in close contact and are compressed in region 2. When the yarns are fully compressed a rapid increase in shear force and consequently in shear stiffness occurs [29]. The point at which full yarn compression takes place is often denoted as the shear locking point, with a corresponding locking angle. When this angle is reached, out-of-plane wrinkling tends to occur. Recently, a benchmarking effort has taken place between different research groups [22] in order to investigate and characterize the in-plane shear behaviour of textile composites. Each group performed tests according to their experience of best practice, such that experience can be shared and recommendations for test methods deduced. This benchmarking effort showed the importance of the sample configuration and tensile preload on the shear resistance variability. The higher the tensile preload, the higher the shear resistance. Moreover, the inter-lab variability was found to be significant, which shows the difficulty to objectively characterize the in-plane shear properties of a fabric.

1.4.2. Inter-ply and tool-ply slip

Due to the inextensibility of the reinforcing fibres, adjacent plies of a laminate need to slip across one another during the forming of single and doubly curved multilayered preforms. Figure 1-13 shows that if this slippage is prohibited, compressive strains occur in the innermost plies, which invoke out-of-plane buckling of these plies. A more complex form of the inter-ply slip deformation is inter-ply rotation. This deformation mechanism occurs when doubly curved components are formed and the angle between the fibre directions in adjacent plies must change to adapt to the tool geometry. Inter-ply slip is also referred to as ply-ply friction [1].

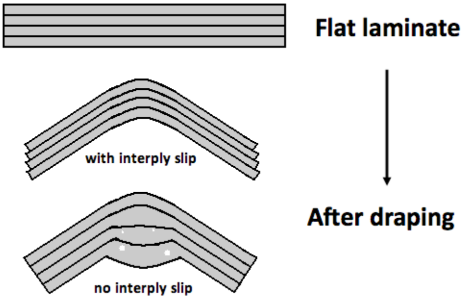

Figure 1-13. Inter-ply slip during draping of multilayered materials

During forming, contact between the tools (punch, die and blankholder) and the composite can have an important effect on the final product. High friction coefficients can invoke tearing of the material, while a low friction coefficient would reduce the tensile membrane forces initiated by the blankholder and facilitate wrinkling. Tool-ply slip and inter-ply slip are very closely related to each other. A resin-rich interface layer between the plies and at the tool-ply surface dominates both mechanisms.

A more extensive overview of inter-ply and tool-ply slip is provided in sections 1.5 and 1.6 and in Chapter 7 both deformation mechanisms will be subject of research.

1.4.3. Ply bending/buckling

During draping, a fabric is heavily bent and when intra-ply or inter-ply deformation is restricted, it usually deform further by out-of-plane buckling. Buckling is unwanted since it leads to wrinkles that deteriorate the mechanical and aesthetical properties of the final product. Buckling occurs due to the presence of in-plane compressive stresses [30]. Clapp et al. [31] performed buckling experiments using the setup depicted in Figure 1-14(a), on a dry plain weave fabric by loading the sample in in-plane compression. The force is measured per unit width of the sample as a function of displacement. Figure 1-14(b) shows a typical compression force-deflection curve. The fabric buckling process is initiated at the point where the load reaches its highest amplitude. After that point, the load rapidly decreases and then starts to increase gently at large deflections.

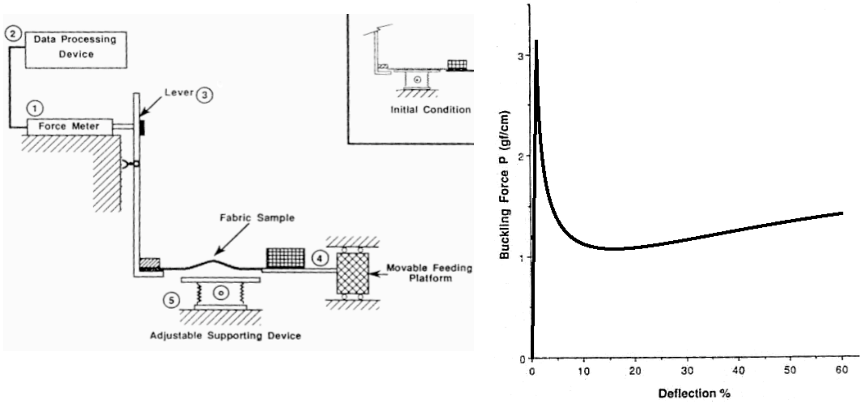

a b

Figure 1-14. Buckling of a fabric with (a) schematic setup of the buckling test and (b) a typical compression force vs. displacement for a woven fabric (adapted from [31])

Wrinkling, which is a post-buckling phenomenon, is thus triggered from the moment a critical compressive force or strain is reached. For buckling of fabric-reinforced polymers it was shown by Wang et al. [32] that this critical load is influenced by the compression rate and fibre architecture.

1.5. Experimental characterization of friction during forming

The measurement of the inter-ply slip and the tool-ply behaviour is related to the frictional properties between adjacent surfaces. A well-known and simple method to determine the friction coefficient between two surfaces is the inclined plane method [33, 34] The test specimen of one material is placed on a flat horizontal surface of the second material. The horizontal surface is then gradually inclined until the test specimen begins to slide. By knowing the sliding angle φ, the friction coefficient μ can be calculated according to:

$$\mu = \tan(\varphi) \qquad \textbf{Eq. 1-2}$$

Several researchers [35-38] have developed alternatives to the inclined plane method in order to simulate the process conditions that occur during forming. In general, however, these alternative methods do not differ severely from each other and can be used to determine both the tool-ply and the ply-ply frictional properties. First, a layer of the thermoplastic material is pressed between two plies, which are made either from the same thermoplastic material in case of ply-ply measurements or from tooling material in case of tool-ply measurements. This central ply is then pulled from between the two stationary plies. The force needed to invoke this slippage is recorded as function of the displacement. Figure 1-15 shows the experimental set-up used by Murtagh et al. [35] and Lebrun et al. [36].

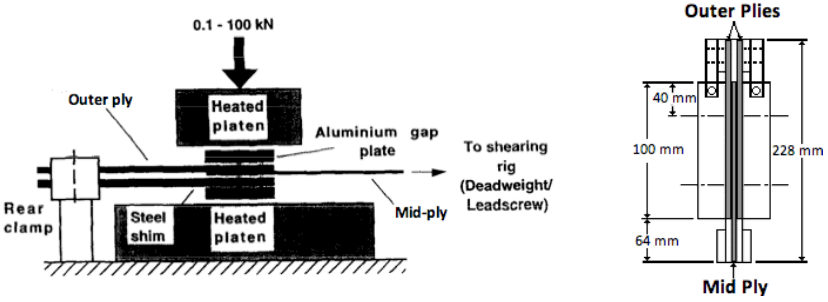

a b

Figure 1-15. Experimental set-up used by (a) Murtagh et al. [35] and (b) Lebrun et al. [36] to investigate inter-ply slip in thermoplastic composites

The subsequent paragraphs discuss the experimental characterization of the frictional behaviour of thermoplastic composites under forming conditions. The last paragraph will deal with the constitutive behaviour of both inter-ply and tool-ply friction.

1.5.1. Inter-ply and tool-ply slip characterization

Initially, inter-ply and tool-ply slip characterization was focussed on unidirectional composites [39, 40]. Temperature, slip velocity, pressure and lay-up configuration were found to be the major influences on the slipping behaviour. Scherer and Friedrich [39] showed that a yield shear stress had to be overcome to initiate slipping. A resin rich layer is observed between different plies and it was shown that the viscous nature of this interlayer influences the slip behaviour at elevated temperatures. The shear stress was found to increase with increasing velocity, though at higher velocities it levels off, similar to shear thinning behaviour of the matrix. Increasing the temperature decreased the resistance to slip due to a decrease of the matrix viscosity. The shear stress was also found to be proportional to the pressure and depended on the relative fibre orientation between adjacent plies, where a maximum shear stress is found for plies with the same fibre orientation. The thickness of this interlayer is not known, but is thought to be about 5% of the thickness of the ply [14].

A first effort to characterize the inter-ply slip behaviour for woven reinforced polymers was performed by Murtagh et al. [35]. A custom-built shearing apparatus was developed together with a consolidation unit. A 500 N load cell recorded the shearing load. Figure 1-15(a) gives a schematic representation of the apparatus. A layer of the thermoplastic composite material is pressed between two composite plies. During the test this central ply is pulled from between the two stationary plies. They observed yarn straightening of the woven reinforcement to occur prior to inter-ply slip.

Lebrun et al [36] performed a more recent study on the slip behaviour of thermoplastic woven reinforced composites. They used an experimental setup consisting of 4 calibrated springs to apply pressure on the laminate. Typical force vs. displacement curves and the corresponding shear stress vs. normal pressure curves are depicted in Figure 1-16.

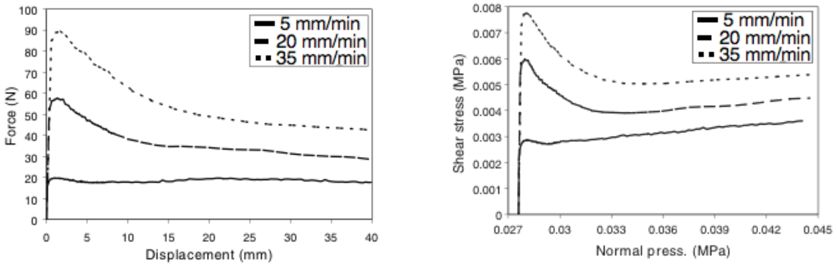

a b

Figure 1-16. Typical (a) force vs. displacement curve and (b) shear stress vs. normal pressure measured using the pull-out method [36]

It can be observed from Figure 1-16(a) that an initial peak shear stress, similar to a yield point, needs to be overcome, however no explanation for this phenomenon is given. In Chapter 6 it will be suggested that this yield is due to the start-up effect during shear flow of a polymer. In contrast with the findings of Murtagh no yarn straightening effect is reported. A plateau, corresponding to a steady-state shear stress, followed this shear stress peak.
Both Murtagh and Lebrun observed a decrease in shear stress with increasing temperature and decreasing pullout velocity. The influence of the pressure on the shear stress was found to be minimal, a slight increase in shear stress occurred at higher pressures. This behaviour was attributed to the intra-laminar deformation of the pulled ply, which becomes more important at higher pressures.

The effects of the processing conditions on tool-ply friction are similar to that of inter-ply friction due to the presence of a resin-rich layer between the tool and the preform. Proof to support this assumption was found by Gorczyca et al. [37, 41]. They made use of the Stribeck theory of lubrication to show that hydrodynamic effects, originating from the viscous nature of the polymer, dominate tool-ply friction.

In Chapter 5, inter-ply slip will be investigated with a custom-build apparatus similar to that of Murtagh, though with the possibility to incorporate cooling effects.

1.6. Constitutive equations for inter-ply and tool-ply slip

Due to the complex nature, i.e. heavily depending on the process conditions, of the inter-ply slip behaviour no predictive models exist, instead phenomenological models were developed. All of these models are based on the fact that the viscous interlayer plays a determining role in the inter-ply shear slip behaviour. Since for tool-ply slip the dependence of the contact behaviour on the process conditions is similar to that of inter-ply slip, the presented models can also be used to describe tool-ply contact. However, for tool-ply contact a predictive model is recently introduced by Akkerman et al. [42].

Following their experimental investigation, Murtagh et al. [14] modelled the inter-ply slip behaviour of a thermoplastic reinforced fabric using a modified form of a Herschel-Buckley power law model:

$$\tau = \tau_{yield} + k \cdot (v)^n \qquad \textbf{Eq. 1-3}$$

Where τ is the shear stress that acts between the neighbouring plies and v is the relative velocity between the plies. The yield shear stress, τ_{yield}, in this

formula is defined as the shear stress at zero velocity. The values of the parameters *k* and *n* are dependent on the process conditions and are determined using a curve-fitting technique. Second-degree polynomial functions were used to describe the dependence of k and n on the temperature and pressure. In order to combine the influence of the different process conditions a master equation was developed. Using this master equation the shear stress for any set of processing conditions could then be calculated.
Wilks [43] suggested to separate the shear stress into two parts:

$$\tau = \mu \cdot F_N + \eta \cdot \dot{\gamma} \qquad \textbf{Eq. 1-4}$$

Where the first term represents the Coulomb friction caused by contacting fibres of adjacent plies, μ is the friction coefficient and F_N is the normal force. The second term is related to the shearing of a polymer film, η the viscosity of the polymer interlayer and $\dot{\gamma}$ is the shear rate of this film, which requires the thickness of the interlayer.
Lamers [44] proposed to define a viscous slip law that is able to describe the sliding of the individual plies. This law is expressed by the velocity difference, *v*, between adjacent plies. He assumed a friction law that depends linearly on the velocity difference between the plies, the interface traction τ is defined as:

$$\tau = \frac{1}{\beta} \cdot v \qquad \textbf{Eq. 1-5}$$

Where β is defined as the slip factor, which is calculated as:

$$\beta = \frac{h}{\eta} \qquad \textbf{Eq. 1-6}$$

Here *h* is the averaged thickness of the interface layer and η the viscosity of the interface layer. This formulation is deduced from Newton's law of viscosity. The main drawback of this formula is, like with Eq. 1-4, the need to identify the interlayer thickness for different process conditions and assuming that this interlayer thickness is constant throughout the whole specimen. However, the factor β can be calculated directly from inter-ply slip experiments:

$$\tau(t) = \frac{F(t)}{2 \cdot w \cdot L(t)} \qquad \textbf{Eq. 1-7}$$

$$\beta = \frac{2w \cdot L(t) \cdot v}{F(t)} \qquad \textbf{Eq. 1-8}$$

The traction at a given moment is defined as the load, *F(t)*, measured at time t and defined by the contact area at time t. The contact area can be calculated by multiplying the width, *w*, of the specimen and the momentary contact length, *L(t)*, see Figure 1-17. The factor 2 arises from the fact that both surfaces of the pull-out ply are in contact with the neighbouring plies. Combining Eq. 1-7 and 1-5 results in an expression that allows calculating β directly from the obtained data points (Eq. 1-8).

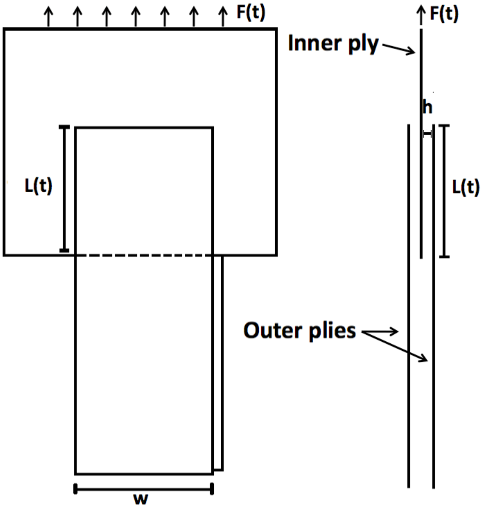

Figure 1-17. Inter-ply slip test experiment

Gorczyca et al. [45] investigated the influence of the processing conditions on the tool-ply frictional behaviour. They used the Stribeck curve, which plots the friction coefficient vs. the Hersey number, *He*. In the original work of Stribeck [46], the Hersey number is calculated using the normal pressure, which results in a dimensionless number. However, Gorczyca used the normal pressure to calculate the Hersey number:

$$He = \frac{\eta \cdot v}{F_N} \qquad \textbf{Eq. 1-9}$$

Where η is the viscosity of the matrix, *v* is the velocity and F_N the normal load. Gorczyca showed that for the woven material they investigated the friction coefficient increases at increasing Hersey number. Therefore, it was concluded that hydrodynamic lubrication exists between the textile preform and the tool at processing conditions. They proposed a linear relationship between the Hersey number and the friction coefficient:

$$\mu = c_1 \cdot He + c_0 \qquad \textbf{Eq. 1-10}$$

Where c_1 and c_0 are fitting parameters. To derive the Hersey number a constant interlayer thickness of 0.07 mm was assumed. This value was determined from a series of optical micrographs from untested samples. In [45] this model was implemented in finite element forming simulation software and it was found that if the punch velocity was doubled from 165 mm/s to 330 mm/s, the force on the punch increased from 1 kN to 13 kN. In Chapter 7 the Stribeck approach will be further discussed.

An alternative to the pull-out method is developed by Lin et al. [47]. They used a conventional rheometer to investigate the tool-ply friction. They measured the normal force and angular velocity for a range of applied shear stresses, between 500 and 5000 Pa, and temperatures, between 160 and 220°C. Afterwards the experimental results are shifted to obtain a master curve by using normalized variables. The shear stress is then expressed as:

$$\tau_s = \tau_{s,ref} \cdot \sqrt[m]{\frac{v^n \cdot F_N}{c_{ref} \cdot a_T}} \qquad \textbf{Eq. 1-11}$$

$$\log(a_T) = A_T \cdot \left(\frac{1}{T} - \frac{1}{T_{ref}} \right) \qquad \textbf{Eq. 1-12}$$

Where τ_s is the shear stress, $\tau_{s,ref}$ is the reference shear stress, v the velocity, n the power-law coefficient, F_N the normal pressure, m, c_{ref} and A_T are fitting parameters, T is the temperature and T_{ref} is the reference temperature. A good agreement between this method and the conventional tool-ply slip characterization was found.

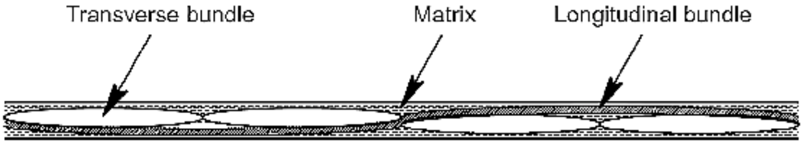

Figure 1-18. Cross-section of a woven reinforced composite [42]

A first effort to predict the friction coefficient was performed by Akkerman et al. [42]. They used a 1D mesoscale model, shown in Figure 1-18, in combination with the Reynolds' equation for hydrodynamic lubrication to derive the film thickness between the tool and the ply. The shape of the transverse and longitudinal yarns were determined by optical micrographs and were approximated by a parabolic curve and the pressure distribution over each yarn was assumed to follow the boundary conditions depicted in Figure 1-19.

These boundary conditions are also known as Reynolds boundary conditions [48] in the lubrication theory for bearing systems. Knowing the film thickness allows calculating the shear force needed to slide the preform across the tool surface:

$$F_f = \int_{-L}^{x_0} \left[\frac{h}{2} \cdot \frac{\partial P}{\partial x} + \eta \cdot \frac{v}{h} \cdot dx \right] \qquad \textbf{Eq. 1-13}$$

Here F_f is the frictional force needed to slide the preform, *h* is the interlayer thickness, *P(x)* is the pressure distribution acting on a yarn, η is the shear viscosity and *v* the velocity at which the preform slides relatively to the tool surface. A good agreement between the model and the measured steady-state shear force was found, though it was shown in later work [38] that the friction coefficient is sensitive to any pressure inhomogeneities that arise during testing. These pressure inhomogeneities are a consequence of the rigid tooling that is used, any misalignment leads to an unevenly distributed pressure of the specimen. Expanding this mesoscopic description to inter-ply friction will be cumbersome, since the interlayer thickness is not constant and locally changes during slip.

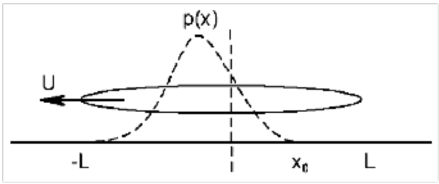

Figure 1-19. Assumed pressure distribution underneath a yarn [42]

In Chapter 6, an alternative descriptive model will be developed for inter-ply and tool-ply slip and both will be implemented in a commercial finite element code in Chapter 7.

1.7. Experimental investigation of fabric-reinforced thermoplastic forming

Initially, experiments were especially concerned with the impregnation and consolidation of the final product [49, 50]. A high amount of voids decreases the mechanical properties and thus should certainly be avoided.

Research on the formability or drapeability of fabric reinforced thermoplastics started in the 90's. Breuer et al. [15] investigated the wrinkling formation during matched die forming of a fabric preform consisting of 4 plies. They replaced the traditional blankholder by a flexible roller-tracking device to invoke tensile membrane stresses during forming. A decrease in fabric wrinkling was observed by applying in-plane tension in the sheet during forming. This approach to reduce wrinkling was also used by Nowacki et al. [51].

Rozant et al. [10] compared different types of dry fabrics and introduced a formability parameter based on maximum depth a fabric could undergo before wrinkles appear. They noticed that every woven fabric they investigated at some point starts to wrinkle. The formability of a fabric could also not directly be linked to the locking angle of the fabric. A higher locking angle did not necessarily imply a better formability. They attributed this effect to the complex deformation a textile preform undergoes during draping. This complex deformation field is not simulated during in-plane shear characterization of the fabric.

Promodou et al. [52] performed vacuum assisted double diaphragm forming on a preform consisting of 7 layers of non-impregnated fabric. They used a number of different ply orientations. When all layers were oriented in the same direction no wrinkling is observed. For all other lay-ups wrinkling was observed to take place at shear angle values that were significantly lower (i.e. wrinkling occurs sooner) than the locking angle measurements for the single layer experiments.

More recent, Lamers [44] investigated the influence of the fabric lay-up on the formability of the laminate during rubber die moulding. Four different lay-up configurations were formed. They ranged from a cross-ply to a quasi-isotropic configuration. Severe wrinkling of the quasi-isotropic perform was observed, while the cross-ply adapted to the mould without defects. By increasing the angle between the adjacent plies with steps of 15°, it was found that the number of wrinkles and their size increases when the difference in the lay-up angle increases.

In Chapter 4, the experiment of Lamers and Promodou will be repeated, the cause of early wrinkling will be identified and a thorough screening of the process parameters that may influence the wrinkling formation will be made. Moreover, a suggestion to reduce wrinkling in a complex lay-up during draping will be presented.

1.8. Textile draping simulation

This section describes the different simulation approaches for draping of textile composite sheets into complex products. The aim of these simulations is to evaluate, on the one hand, whether a shape can be formed without defects. On the other hand, if the forming goes well, the local deformations that happen during forming should be known since they determine the mechanical response of the formed product. Both, the fibre orientation and the local fibre volume fraction define the mechanical properties of a composite and hence also the performance of the formed part. The final goal is to create a tool that allows optimization in the virtual world and thus to reduce or even to eliminate the time consuming and costly “trial and error” approach.

To predict the forming of fabric reinforcements two modelling approaches are commonly used [53]. The earliest and easiest techniques are based on mapping schemes, a.k.a. kinematic models. In contrast to the mapping approach, the constitutive material behaviour is required for a mechanical approach. These two approaches will be further elaborated in the subsequent paragraphs.

1.8.1. Kinematic mapping approach

The kinematic mapping model is based on the assumption that deformation is restricted to in-plane shear. It is also called ‘pin-jointed net’ (PJN), because the yarns are considered inextensible and pin-jointed at crossover points with no relative slippage. The fabric behaves as a ‘fishnet’ and is mapped accordingly onto the surface of the forming tool. Hereby only geometric information about the draping process is provided. Stresses or applied forces are not considered. Furthermore, it is also assumed that the material can shear by any amount that is required to conform to the tool.

Geometrical predictions of woven fabrics were already carried out in the mid ‘50s, when Mack and Taylor [54] showed how a surface can be covered with cloth. Since then a lot of research has been done using different mapping approaches [55-57] . The difference in the used approaches is technical and lies in the description of the surface of the mould and the calculation method of the crossover points. Heisley [55] calculates the distance between crossover points by using a geodesic description along a continuously differentiable surface. Van West [57] calculates the distance between the crossover points as a straight line for shapes assembled of bicubic polynomial surfaces. The difference in mathematics does not affect the principle of the fishnet method. More recently Long et al. [58, 59] developed an iterative procedure, which is an intermediate model between a kinematical and a mechanical approach. It uses a fishnet model that minimizes the total shear strain energy using an optimization technique. The advantage of using the energy approach instead of the normal kinematical model is that the effect of asymmetrical shear behaviour can be incorporated. Moreover, the influence of applying a blankholder force can be assessed using this approach.

Hankcock and Potter [60] use the kinematic approach to create manufacturing instructions, which take the form of an animation illustrating how the ply is fitted to the tool to achieve the required lay-up. Also, input for laser guidance equipment is generated automatically from the lay-up design.

The major benefit of the kinematical modelling approach is the simplicity of applying this method, which results in small CPU-times, typically less than a minute, needed for a simulation. Due to their fast and easy approach, kinematic models have been of great value in defining the potential for covering a surface with a woven reinforcement using manual manipulation of the cloth.

Limitations of the kinematic drape simulation are associated with the method of specifying constraints, e.g. start point of draping, fibre orientations, and the fact that the physics of the forming process is not represented. Constraints need to be defined in order to obtain a unique draping solution, see section 4.3.1. Two methods of defining constraints are often used. In the first method an initiation point and the initial fibre directions in this point need to be defined. This method will be further elaborated in Chapter 4. In the second method, developed by Hancock and Potter [61], two yarn paths across the surface are chosen and the resulting shape is evaluated whether to be practically useful. This is an inverse drape modelling technique, starting from a unique drape pattern, which corresponds to a unique geometry. An illustration of this approach is shown in Figure 1-20.

Consider in Figure 1-20(a), the two semi-circular curves, Curve 1 and Curve 2, generated in orthogonal planes with radii equal to R_1 and R_2, respectively. Curve 1 can be labelled the weft yarn trajectory and Curve 2, the warp yarn trajectory. The weft tow trajectories are then generated when Curve 1 moves in increments along a path defined by Curve 2, indicated in Figure 1-20(b), the length of each increment being equal to the required step length of the net. Similarly the warp tows are generated when Curve 2 glides along the path defined by Curve 1. The geometry generated, Figure 1-20(c), is called curve glide geometry and possesses information about the local yarn orientations. Although the kinematic method may find a theoretically possible draped solution, whether or not that solution is practically achievable, is not obvious [60]. The kinematic approach is confined for draping single layered fabrics, it cannot take into account the inter-ply slip that occurs when multiple layered materials are formed.

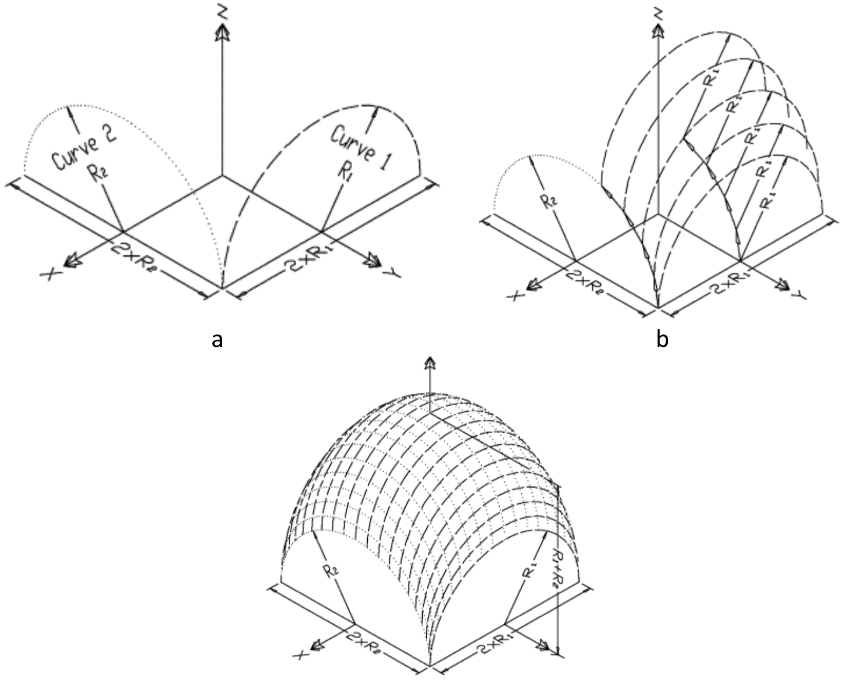

a

b

c

Figure 1-20. Inverse drape modelling with (a) definition of two yarn paths, (b) geometry generation, (c) resulting curve glide geometry.

Despite these drawbacks, the mapping approach is often used in the design phase due to the simplicity of use [60]. However, in Chapter 4 it will be shown that it is dangerous to rely on the mapping approach for automated forming of woven reinforced composites alone.

1.8.2. Mechanical approach

The alternative to the mapping approach is a mechanical model. It offers the benefit to represent the resistance against deformation using a non-linear material model and to include realistic boundary conditions at the price of being computationally more expensive.

Traditional mechanical forming simulations are performed using the finite element (FE) method. In the FE method, the solution region is discretised in small subregions called finite elements. These finite elements are connected via nodes on which the appropriate boundary conditions and/or loads are applied. The governing non-linear equations can be solved using an implicit or explicit solution scheme [62]. The high degree in complexity of forming simulations has led to the application of explicit based solution methods for this type of simulations. This method is computationally cheaper for the complicated contact conditions that arise in forming simulations compared to implicit calculations [63].

FE forming simulations require a constitutive material model that can describe the non-linear anisotropic behaviour of fabric-reinforced composites. In addition it should also be able to track the local yarn directions during forming. An extensive overview of the different approaches and constitutive models developed for fabric draping are provided in [17, 64-66]. Three mechanical approaches can be found in the literature, namely a discrete, a continuous and a semi-discrete approach. All these approaches study the phenomena at the macro-scale of the fabric composite. These macro-scale models require the input of correct material behaviour of the fabric, which is performed via textile testing (picture frame, bias extension, pull-out, etc…) or by using meso-scale models that study the interactions at the unit cell level [67].

In a discrete approach beams or trusses represent the yarns and the interactions between the yarns are modelled using springs. The major benefit of this approach is that the yarn directions are tracked “naturally” since they coincide with the orientation of the beams or trusses. The major pitfall, however, is the relatively high computational cost needed to perform a simulation.

A second possibility is to consider the fabric as an anisotropic homogeneous medium. Hereby the fibrous reinforcement and the matrix are considered as a continuum. The benefit of these models is the possibility to be integrated in standard shell or membrane elements. Though, due to the complexity of the draping mechanisms, the continuum needs to convey the specific mechanical behaviour of the fabric, which implies the yarn directions need to be tracked during forming. In order to do so, several elegant solutions have been developed. Willems [64] has studied four hypo-elastic frameworks that incorporate in-plane drape behaviour in a membrane element. From this study, the affine elastic model (AEM) will be used in Chapter 7.

A third possibility uses a combination of both the continuum and discrete approach and has been presented by Hamila et al. [68]. This semi-discrete model considers the components at the mesoscale level, but they are part of finite elements and their strains are given by the nodal displacements of the corresponding element.

1.8.3. Multilayered textile draping simulations

Multilayered draping simulations are usually be performed using a mechanical approach, since the complex interaction between the plies needs to be incorporated. Scherer et al. [14, 63] used the modified form of a Herschel-Buckley power law model, proposed by Murtagh, and implemented it in finite-element software. For a laminate consisting of unidirectional plies, they noticed a reduction of the amount of slip and buckling of the bottom layer of the laminate occurred when the yield shear stress was increased.

De Luca et al. [69] performed textile draping simulations using a continuum approach. Here the interaction between the layers was incorporated based on the experimental results of Murtagh et al. [35]. The friction coefficient was only made dependent on the velocity and the pressure and temperature dependence were neglected. They found that during forming of a quasi-isotropic woven laminate, the chance of wrinkling is severe, which agrees with the experimental findings of Lamers [44] and Promodou [52].

Lamers [44] developed a special finite element, where multiple layers are incorporated in one element. This model involves an energy minimization approach of the composite laminate for each element in the implicit updated Lagrangian FE scheme. Contributions are formulated for each of the fabric layers and the interface layers within the laminate. A minimization technique is used to find the individual incremental ply deformations, based on the average incremental deformation of an element. Lamers also introduced complex interaction behaviour between the plies, though it is not clear whether cooling of the laminate during forming is incorporated.

In Chapter 7 the complex frictional behaviour is implemented in a commercial finite element code.

1.8.4. Prediction of forming defects – Forming limit diagrams

One of the main reasons for developing such extensive models is the ability to predict the occurrence of defects in formed parts. A convenient tool to evaluate the formability has been developed for sheet metal forming, i.e. forming limit diagrams. Figure 1-21(a) depicts a typical forming limit diagram. It shows the critical combinations of major strain and minor strain in the sheet surface at the onset of necking or wrinkling failure. By evaluating the local strains during the predicted shaping step and comparing these strains to the forming limit, the critical regions can be determined and the type of failure can be identified. If the combination of the local major and minor strain lie within the light grey area of Figure 1-21(a) no defects are presented. Optimization of the forming can be performed by pursuing a processing path such that none of the material points of the sheet will experience strains beyond the forming limit.

Dessenberger et al. [70] adopted the technique of a forming limit for a random fibre mat. They used a biaxial tensile testing machine to apply a complex multi-state loading condition in the fibre mat and defined the onset of failure to correspond to a maximum in load. A typical forming limit diagram is shown in Figure 1-21(b). Here the forming limit is determined by a combination of the principal stretch ratios, whereby a stretch ratio of one means no deformation has occurred. The strain space is divided in regions where failure (wrinkling and tearing) is likely to occur and a region where the deformation is acceptable.

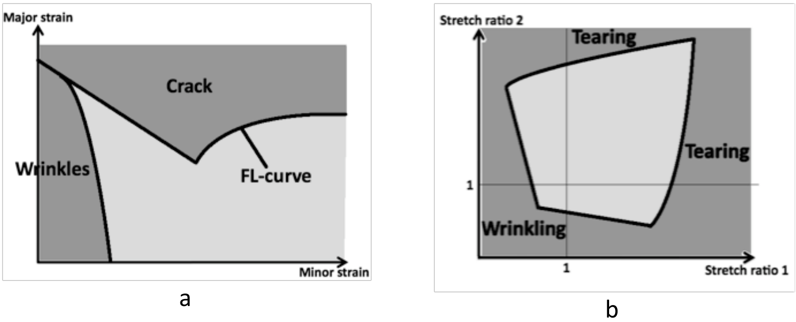

Figure 1-21. Forming limit diagram for (a) a sheet metal and (b) a random mat reinforcement (Adapted from [17, 70])

For fabric-reinforced composites the dominant types of forming defects involve buckling or wrinkling (Figure 1-22):

a. Yarn buckling: in-plane compressive stresses in the fibre direction of a yarn, may cause in- or out-of-plane yarn buckling.
b. Shear wrinkling: when in-plane shear is prevented, compressive forces will give rise to wrinkling of the preform. The region where this type of buckling occurs is usually characterized by a large amount of in-plane shear.

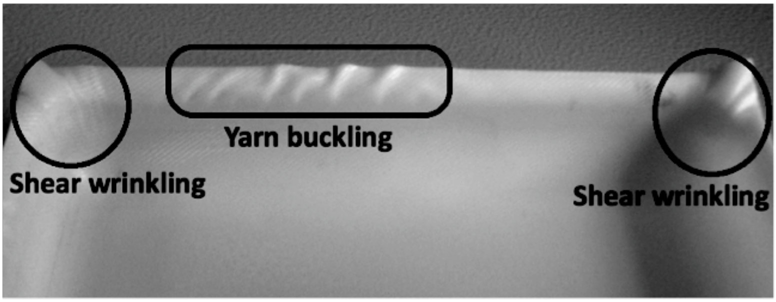

Figure 1-22. Out-of plane yarn buckling and shear wrinkling in a vacuum-formed woven reinforced thermoplastic composite part

Unfortunately forming limit diagrams for fabric-reinforced composites do not exist yet. Instead, for the draping simulations obtained via a mapping approach, the locking angle, which is measured experimentally using a picture frame or using the bias extension test, is taken as the limit of formability. The locking angle is defined as the shear angle achieved just before the onset of buckling. However, this is a very subjective way to determine whether or not wrinkling occurs, since the locking angle strongly depends on the processing and boundary conditions [15, 71].

Using a mechanical approach to simulate the draping of textile composites allows visualization of wrinkling [72, 73]. Though, the occurrence of wrinkling depends on the element type, aspect ratio and bending resistance [74, 75]. Therefore, the formability is often assessed by evaluating the compressive stresses or strains during forming. When a negative stress is detected, the membrane will wrinkle. Recently, a lot of research is devoted to develop wrinkling criteria for membrane elements [76]. The main purpose of these criteria is to account for wrinkling by not allowing any negative stress to appear. However, such a criterion does not yet exist for textile-reinforced composites.

In Chapter 5, a forming limit diagram for multilayered textile composites will be proposed and in Chapter 7 the occurrence of compressive stresses in a forming simulation will be linked to the presence of wrinkles.

1.8.5. Experimental forming evaluation methods

This section deals with different methods that are used to check the accuracy of the forming simulations against experimentally formed products. Two forming indicators, namely the local shear angle and the local draw-in at the edge of the formed sheet, are often used to compare experiments versus predictions. A popular method for analysing sheet formed materials is the ‘Grid Strain Analysis’ (GSA). Its origin lies in vision based strain measurements of sheet metal parts [77]. Here, a reference pattern is edged on a flat sheet. After deforming the sheet, the grid was analysed using digital images. This allows local measurement of the amount of strain.

At the end of the '90s it was adapted by Long et al. [78] to track and calculate fibre orientations in woven reinforced composites. A square grid, which corresponds with the yarn directions in the fabric, is marked on the flat sheet. After draping the fabric sheet, photographs are taken of the final product. By combining two images with known angular difference, the 3D coordinates of the gridlines can be computed. The amount of intra-ply shear can be obtained by calculating the angle at the intersection points of the grid. Nino and Bersee [79] developed an extension of the GSA towards multilayered materials. They carried out forming experiments on multilayered materials that were interwoven with metallic wires. Using an electrical device these wires are thermally activated, which allows them to be detected by an infrared camera. This technique, called Infra Red Square Grid Analysis or IRSGA, allows investigating the deformation of layers that are not on the outside of the final product.

In Chapter 3 an optical system consisting of two digital cameras is used to measure shear angles in the formed fabric reinforced composites and compare them with the results obtained by predictive software.

1.9. Conclusions

This chapter gives an overview of the state-of-the-art in textile thermoplastic composite forming. Textile composites need to undergo large deformations in order to adapt to the desired shape. The amount of deformation a textile can undergo depends on the material and the process conditions. For single layered textile plies large deformations can lead to unwanted defects like wrinkling or tearing. The formability of multilayered textile structures is very dependent on the lay-up configuration of the composite sheet and limited due to the ply-ply interaction during draping.

Inter-ply and tool-ply pull-out experiments are performed to characterize the contact behaviour of a textile laminate during forming. Although, some authors have reported the dependence on the process conditions of this contact behaviour, no full-scale screening has been yet performed.
Predictive software has been developed to support process optimization. The mechanical approach seems the most suitable to simulate the draping of textile reinforcement. These models do not yet consider the complex contact behaviour of the formed textile composite with the tooling equipment and the ply-ply interaction within the laminate itself.

Chapter 2

Problem statement

From the literature review, it can be deduced that thermoplastic textile composites offer great potential for rapid forming. Textiles adapt to complex shapes by very specific draping mechanisms of which the key mechanisms are inter-ply shear and intra-ply slip. These materials can be shaped by fast and high-volume processes, moreover they provide potential for recyclability.

The formability of textile composites is limited due to the occurrence of defects, of which the most common is wrinkling. When during forming of a single ply, a critical deformation limit is reached and compressive forces arise, which induce local out-of-plane buckling of the material. However, it has been shown that for a multilayered stacking of woven reinforced composites, in some case, wrinkling occurs before the wrinkling threshold, i.e. the locking angle, for a single woven reinforcement is reached. It would therefore be very helpful if *the formability of multilayered woven reinforced composite materials could be quantified*, so that critical combinations that lead to wrinkling can be identified. There is also little known about the influence of the process conditions on the forming capacity of a multilayered composite laminate. Which *process conditions are favourable to create wrinkle-free product*s consisting of multiple plies of woven reinforced thermoplastic polymers?

Draping affects the local fibre orientation, fibre volume fraction and thickness of the shaped part. These local properties in their turn, affect the mechanical response and the quality of the final product. In order to perform process optimization, drape simulation tools have been developed to identify the effect of the process conditions on these local properties and thus eliminate costly “trial-and-error” experiments. These simulations should, on the one hand, be able to suggest process conditions so that defect-free products can be formed and on the other hand predict the structural behaviour of the final product.
Two simulation approaches, the kinematical and mechanical, are often referred to.

The kinematic and mechanical approaches have been benchmarked for shapes where either the distribution in shear angles is quite uniform (hemisphere) or where the shape is complex (double dome) and it is difficult to measure the shear angle precisely. The orientation of the reinforcement in scientific studies is often chosen so that the distribution in shear is symmetric, in such cases the kinematic approach performs well since the initial conditions are unambiguously recognized.

In industrial applications, product shapes are often unsymmetrical, and generally multilayered stackings are draped. A relevant question is therefore *which simulation approach is most suited to describe the draping of fabric reinforced composites onto an arbitrary shape?*

For the drape simulation of multilayered woven textile materials, it is clear that the mechanical approach is best suited, since it provides the possibility to incorporate the complex contact conditions that arise between the layers. The mechanical approach requires dedicated constitutive models that incorporate both the drape and the contact behaviour of the fabric laminate. Therefore, an experimental study of the *frictional properties of the inter-ply and tool-ply contact* is needed to gain understanding.

Moreover, this contact behaviour needs to be *implemented into the mechanical approach*. This implies that a model is needed that is able to adequately describe the contact properties during forming.

The major aim of this study is to present a *"thorough investigation of the formability of multilayered woven reinforced thermoplastic composites both on an experimental and a simulation level"*, and to eventually develop an understanding on how the formability can be increased.

The general goal is split up in a series of research questions, which each focus on a specific topic important for the forming of fabric-reinforced thermoplastic composites:

1. Can the kinematic draping approach be used to predict the local deformations that occur in forming of woven reinforced materials? If not, does the finite element model provide a good alternative?

2. What are the major factors that determine the formability of multilayered woven thermoplastic composites? What triggers the early local out-of-plane buckling during draping?

3. How can the formability of such materials be improved, i.e. what is the influence of the process parameters on the defects, e.g. wrinkling, that occur during forming?

4. What is the importance of inter-ply shear slip and what is the influence of the process conditions on both the inter-ply and tool-ply contact behaviour? Moreover, how can this contact behaviour be implemented in FE models?

5. Does the current state of the art allow using a FE model to help optimize the draping of multilayered thermoplastic composites, i.e. can the occurrence of wrinkling be predicted?

The doctoral research has extended the state of the art by:

1. A thorough experimental investigation of the forming of multilayered woven thermoplastic composites. Severe wrinkling occurs for certain lay-up configuration. Adding extra matrix material between the neighbouring plies is found to heavily influence the formability of the composite.
2. A specific test apparatus has been developed that allows assessing the sensitivity of the contact behaviour to the process conditions that arise during forming.
3. A dedicated contact law for tool-ply and ply-ply contact for textile prepregs has been developed and incorporated into a commercial finite element program. This contact law takes into account the process conditions, i.e. velocity, temperature and pressure, which were experimentally identified to significantly affect the friction behaviour.

The different research questions stated above will be addressed in the following chapters. First, in Chapter 3 the materials and experimental methods used in this research are introduced. For a single layered woven reinforcement, forming predictions can be obtained by the kinematic approach, which is popular due to its low computational cost or by the mechanical approach that often requires long computational times. Because, so far no distinctive proof has been provided that the kinematic method results in incorrect predictions, it will be compared in Chapter 4 to the mechanical approach for single layered draping. The results of these predictions will be validated with experimental results obtained by rigid die forming.

Forming of multilayered textile thermoplastic composites is often confined to laminates of which the yarns of the individual plies have the same orientation. In Chapter 5 it will be shown that the formability highly depends on the lay-up configuration. A forming limit diagram is identified, which visualizes the limitations associated with forming woven laminates, and the influence of the most important process parameters on the formability will be screened. An alternative method, whereby the matrix is concentrated between the different layers before forming, is suggested, in an attempt to increase the formability of these materials.

Chapter 6 aims at developing an appropriate descriptive constitutive model of the contact behaviour. Therefore, a custom made apparatus is developed that is used to identify the frictional resistance for both tool-ply and ply-ply contact. From the results different constitutive models will be derived and compared to each other. One of the descriptive models will be implemented in a commercial finite element program, ABAQUS, in Chapter 7. A wrinkling criterion, based on the maximum compressive stress, is used to compare the experimental results from Chapter 5 with the forming simulations.

The last chapter, Chapter 8, presents the main conclusions of the experimental and simulation work. Moreover, it also indicates an outlook on the further research needed in this field in the future.

Appendix A provides the reader with the basic terminology of woven fabric parameters.

Chapter 3

Materials and methods

3.1. Introduction

This chapter introduces the different materials and main experimental methods that are used in this dissertation. In the first part of this chapter the fabric reinforced thermoplastic composites and the interlayer material are characterized. Afterwards, a method for determining the local fibre directions on shaped composites is introduced. The last paragraph describes the thermoforming equipment and forming methodology.

3.2. Composite materials - reinforcement

Three glass woven reinforced materials are under investigation. Figure 3-1 depicts the different preconsolidated materials[5], these images are obtained by using the μCT imaging technique. This technique also allows for measuring the amount of crimp in the fabric, which is, together with other textile characteristics, summarized in Table 3-1. The numbers between brackets are measured in [80] on dry not preconsolidated material.

Table 3-1. Textile characteristics of the composites used in this thesis

Manufacturer	Owens Corning	Owens Corning	Bond Laminates
Manufacturer's ID	TPEET44	TPEET22	Dynalite 104
Dissertation's ID	TW_1	TW_2	TP
Fibres	Glass	Glass	Glass
Matrix	Polypropylene	Polypropylene	Polypropylene
Fibre volume fraction [%]	35	35	45
Weave pattern	Twill 2/2	Plain	Twill 2/2
Warp linear density [tex]	1870 (2050)	1870 (2110)	204
Weft linear density [tex]	2x1870 (2x2050)	1870 (2110)	204
Ends count [yarn/cm]	3.99 (4.08)	1.90 (1.91)	7.10
Picks count [yarn/cm]	1.86 (1.88)	1.90 (1.90)	7.10
Areal density [g/m^2]	1485 (1550)	743 (815)	290
Crimp warp [%]	5.20 (10.3)	3.23 (1.20)	2.64
Crimp weft [%]	5.43 (0.1)	4.10 (1.32)	3.61
Thickness [mm]	1.02	0.58	0.25

---

[5] Material that is already in a consolidated state prior to processing

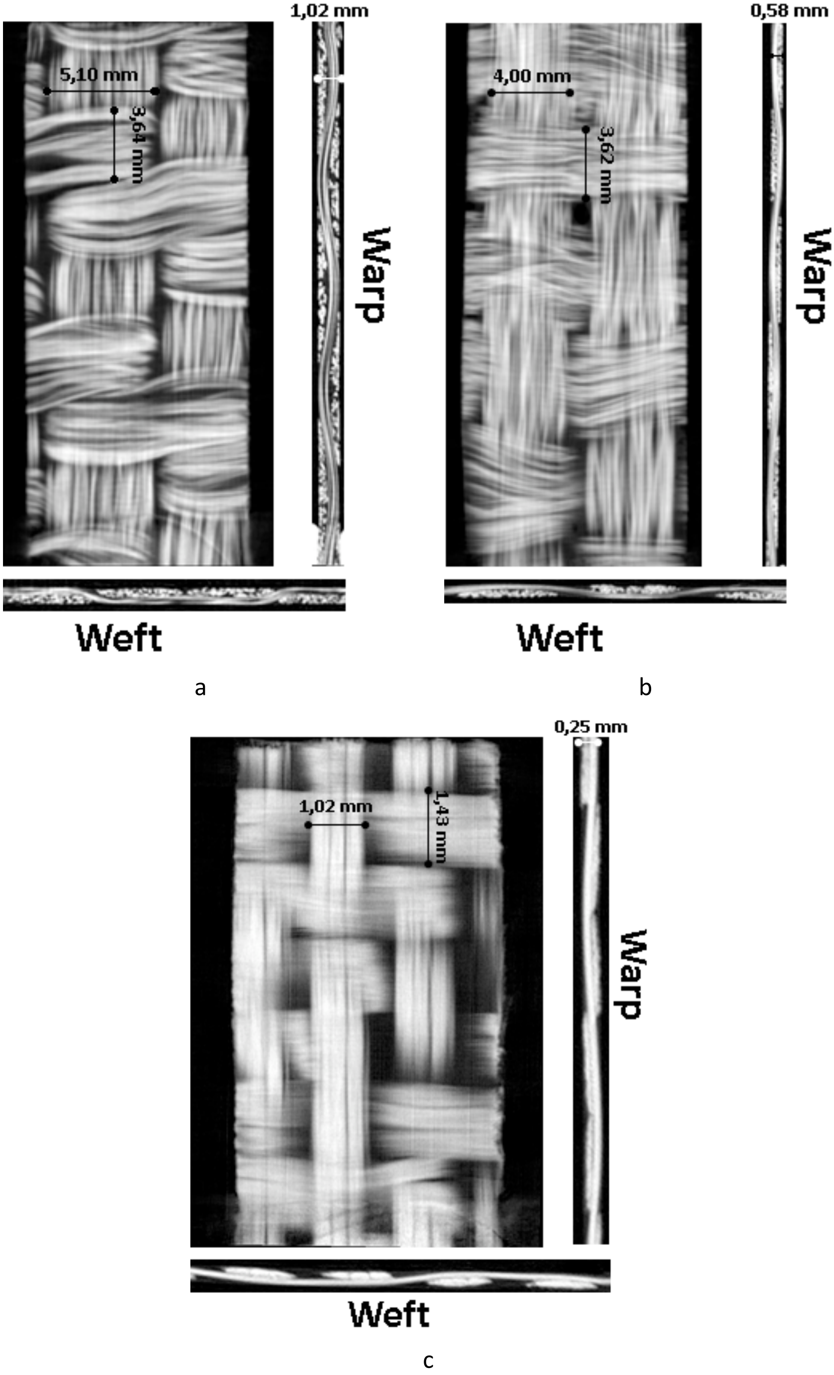

Figure 3-1. Overview of the different textile composites: (a) Twintex TPEET 44 – TW_1, (b) Twintex TPEET 22 – TW_2 and (c) TEPEX dynalite F104 - TP

For all the fabrics the number of fibres in warp and weft direction is the same. Fabric TW_1, however, at first glance looks unbalanced, but in weft direction yarns with half the linear density are compensated by a higher picks count, making the number of fibres in warp and weft equal. Both TW_1 and TW_2 are very coarse fabrics, with a low number of heavy yarns in warp and weft direction, but with a high areal density. They have been the subject of a benchmark study on the characterization of mechanical behaviour of woven fabrics [22]. TP, on the contrary, is a relatively fine fabric with a high number of lighter yarns in warp and weft.

These composite materials are preconsolidated prior to delivery. Despite the 20% higher material cost, it makes the materials more handleable at room temperature and thus allows for easier processing of the material. Dry weaves possess both a low bending resistance and a low resistance to inter-ply shear. If preconsolidation is not performed, the dry fabric tends to sag severely during the preheating stage (see section 3.5). This means the fabric starts to hang under its own weight. Although this effect is also noticed for preconsolidated sheets, it is more pronounced for dry fabrics. Severe sagging can lead to an inhomogeneous temperature profile over the fabric, since the middle region of the fabric will be close to the bottom in the heating zone. If sagging is not compensated for the material will collide with the female die during transport from the heating to the forming unit. Moreover, during sagging the dry fabric tends deform via intra-ply shear making the yarns already non-orthogonal prior to forming.

3.3. Composite materials - matrix

The woven reinforcements are all combined with a polypropylene matrix. Polypropylene is a thermoplastic polymer and a polyolefin made from the monomer propylene. The chemical structure of polypropylene is shown in Figure 3-2(a), it consist of a hydrocarbon backbone grafted with methyl groups.

Figure 3-2. Indicating (a) the chemical structure of polypropylene and (b) fibrous sample material of the extruded polypropylene used in the TW_2.

Some sample material of the polypropylene used in the TW_1 and TW_2 materials (PP_{tw}) has been provided by the manufacturer and is thoroughly investigated on its thermal and viscous behaviour. Unfortunately, no sample material of the polypropylene used in the TP fabric could be investigated. As shown in Figure 3-2(b), the thermoplastic is already processed by Owens Corning into a fibrous form, but not yet intermingled with glass fibres.

Figure 3-3(a) shows a differential scanning calometry (DSC) curve for the polypropylene. During DSC the heat flow difference between the polymer and a reference is measured. When the heat flow difference is positive, i.e. exothermic, energy stored in the polymer is released and thus the sample needs less heat than the reference to keep a constant temperature. On the other hand, a negative, i.e. endothermic, heat flow difference occurs when more heat is needed to keep the polymer at a constant temperature.

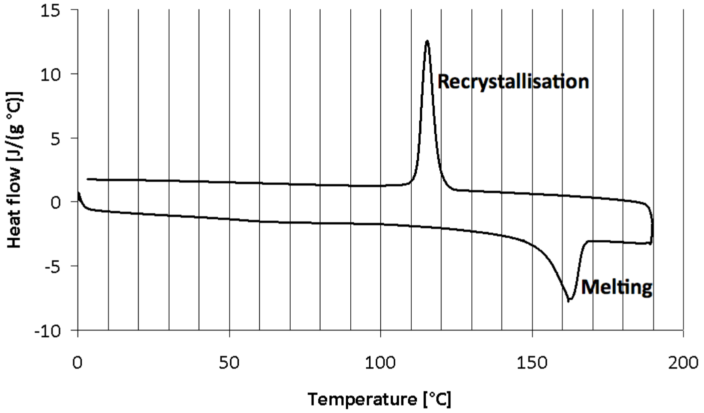

a

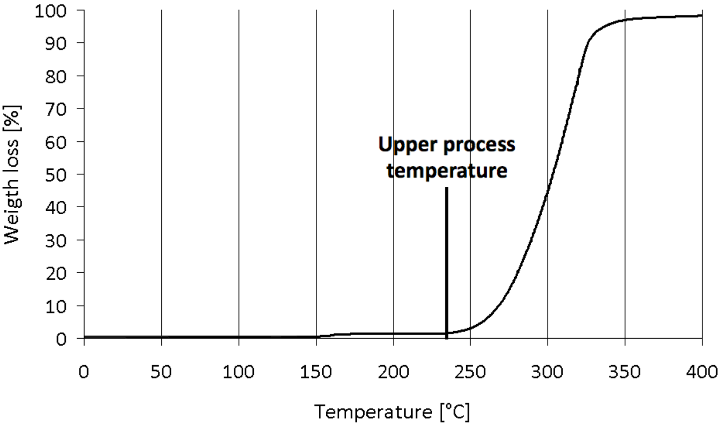

b

Figure 3-3. Thermal properties of PP_{tw} with (a) DSC-curve and (b) TGA-curve

The DSC-curve provides information on the phase transitions that occur, i.e.

the glass transition and the melt temperature of the material. At 165°C, a high amount of energy is needed to break the secondary bounds in the crystals inside the polymer, which results in melting and in an endothermic peak, this temperature refers to the melt temperature of PP_{tw}. During cooling, re-crystallization of the material is characterized by an exothermic peak at 115°C. Here the molecules orient themselves in a lower energy configuration, hence the redundant energy is dissipated. The transition to the glassy state is not noticed since for polypropylene this occurs at temperatures of -20°C [81]. Thermogravimetric analysis (TGA) is performed to determine weight change in relation to temperature change. The TGA-curve in Figure 3-3(b) shows that the polymer starts to degrade at relatively low temperatures, which limits its processing window. A temperature of 230°C is a typical upper limit for the processing of polypropylene. Above this temperature degradation becomes too severe.

Above 165°C the polypropylene behaves as a fluid, which allows for easier processing. An important material parameter for fluids is the shear viscosity, which is a measure for the resistance to shear flow. In composite materials the shear viscosity is preferably as low as possible, since this benefits the deformation and impregnation of the reinforcement. The shear viscosity is represented in flow curves as function of the shear rate. The flow curve of PP_{tw} is measured by performing a dynamic rheological test at elevated temperatures using a rotational rheometer (TA instruments ARES). During a dynamical test the sample is subjected to oscillatory shear by applying a sinusoidal deformation. A useful empirical relationship claims that the magnitude of the complex dynamic viscosity, $\eta^*(\omega)$, is comparable to shear viscosity, $\eta(\dot{\gamma})$, at equal values of angular frequency and shear rate (Cox-Merz rule):

$$\eta^*(\omega) = \eta(\dot{\gamma}) \qquad \textbf{Eq. 3-1}$$

$$\eta^*(\omega) = \frac{G^*}{\omega} \qquad \textbf{Eq. 3-2}$$

$$\omega = 2 \cdot \pi \cdot f \qquad \textbf{Eq. 3-3}$$

Where, f is the frequency in Hz, ω is the angular frequency in Hz and G^* is the complex modulus in Pa obtained from the dynamic measurements. Before testing, the PP-fibres are pressed at 185°C in thin round plates in order to eliminate the influence of air bubbles during testing. Tests are performed at different temperatures and under an inert (nitrogen) environment so degradation is eliminated. For measurements performed below the melting temperature, the polymer was first heated to 175°C and then cooled to the appropriate temperature.

A typical flow curve is presented in Figure 3-4. In such curves, the viscosity is plotted as function of the rate at which the fluid is sheared. Shear thinning behaviour, characterized by a decreasing viscosity with increasing shear rate, is observed. This shear thinning is the consequence of an increasing alignment between the polymer molecules, which results in fewer entanglements between the molecules and thus less resistance to flow.

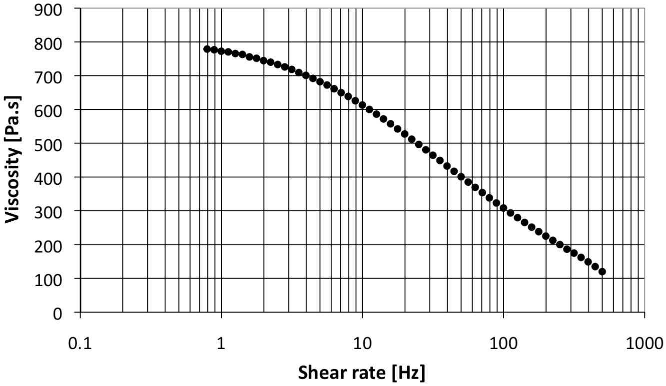

Figure 3-4. Flow curve of PP_{tw} measured at 170°C [82]

Through the flow curves an Ellis model is fitted using the least square method:

$$\eta(\dot{\gamma},T) = \frac{\eta_0(T)}{1+\left(\frac{\dot{\gamma}}{C(T)}\right)^{n-1}} \qquad \textbf{Eq. 3-4}$$

Here $\eta_0(T)$ is the zero viscosity, which is representative for the viscosity at zero shear rate, $\dot{\gamma}$ is the shear rate, *C(T)* is a fitting parameter and *n* is a power-law coefficient. To describe the temperature dependence of $\eta_0(T)$ and *C(T)*, an Arrhenius type of equation is used:

$$Ar(T) = Ar_0 \cdot \exp(Ar_1 / T) \qquad \textbf{Eq. 3-5}$$

Here *A(T)* represents the fitted parameter, Ar_0 and Ar_1 are fitting parameters and *T* is the temperature in degree Kelvin. The values of these parameters are summarized in Table 3-2.

Table 3-2. Values of the parameters for PP_{tw} in the Ellis-Arrhenius model

Ar(T)	Ar_0	Ar_1
η_0(T)	0.26	3576
C(T)	2.73 10^6	-4894
n	1.68	1.68

By combining the Arrhenius equation with the Ellis model the influence of both the temperature and shear rate on the apparent viscosity can be described. Figure 3-5 compares the experimentally obtained viscosity values and those calculated with the above-presented model. The high R^2-values are an indication for a good agreement.

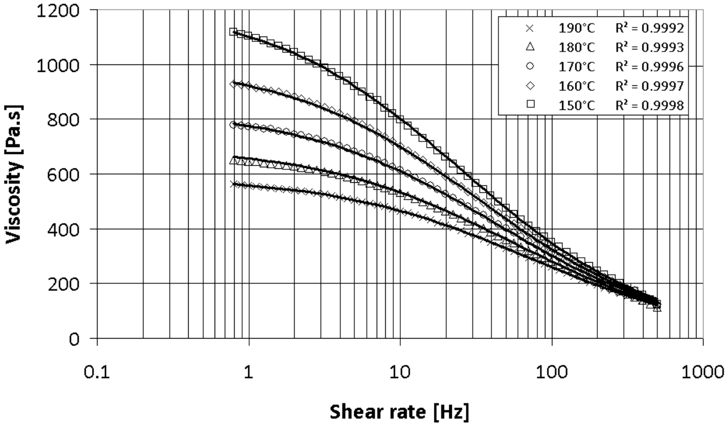

Figure 3-5. Comparison of the Ellis-Arrhenius model with the experimental flow curve data for PP_{tw} [82]

Interlayer material

Interlayer material is put between the individual plies of a multilayered laminate prior to forming.

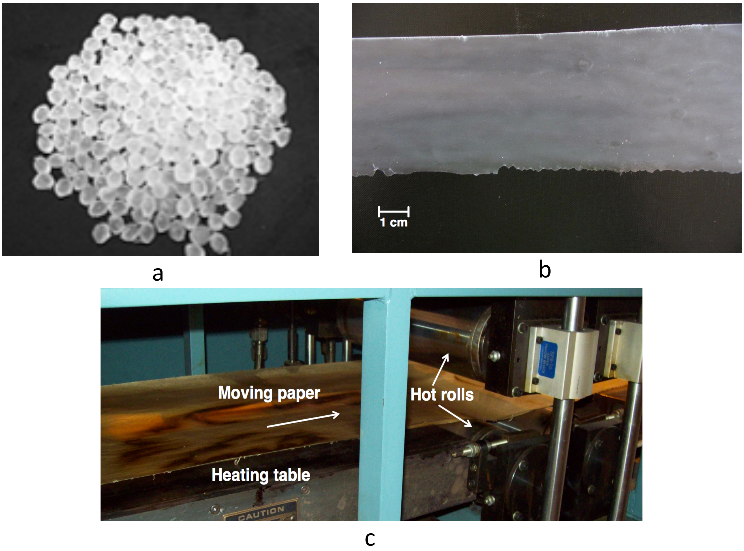

Figure 3-6. PP_{int} in (a) pelletized form and (b) as sheet material formed by using (c) the prepeg machine

This material was chosen to be a polypropylene (PP_{int}), preferably with similar flow characteristics of PP_{tw}. However, due to its low viscosity this type of PP is not available in sheet material, but rather in pelletized form as can be seen in Figure 3-6(a). Therefore, a prepreg machine (Figure 3-6(c)), which is normally used to pre-impregnate a fibrous reinforcement, is used to create flat sheets shown in Figure 3-6(b). The pellets are spread on a continuously moving paper, which passes through a heating table consisting out of two heated metal rolls. Here the polymer becomes liquid and is spread out to form a thin sheet.
The DSC and TGA-curve for PP_{int} in Figure 3-7 show a similar trend to that of PP_{tw}, with that difference that the re-crystallization temperature lies at about 125°C.

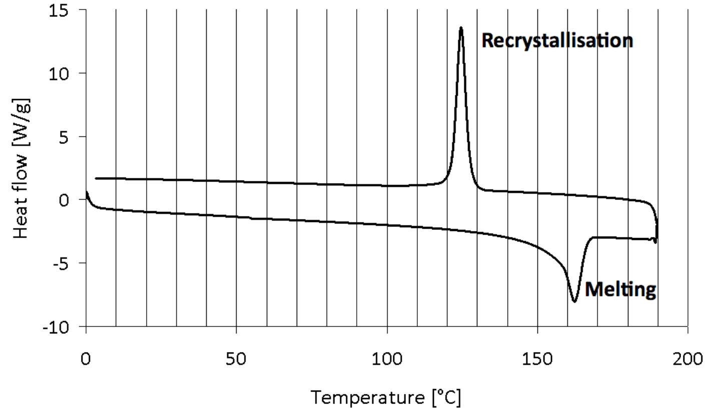

a

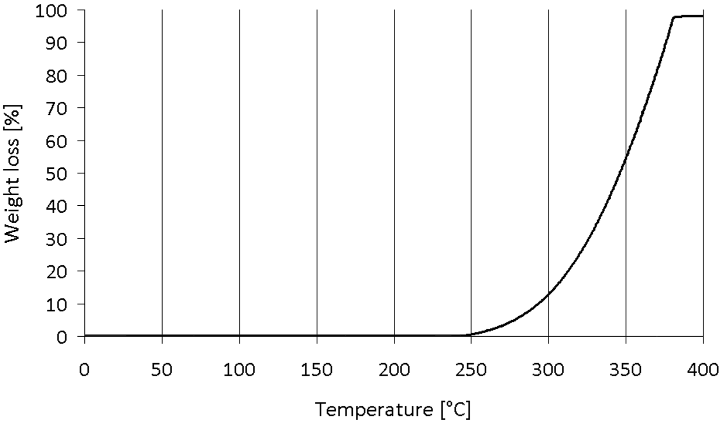

b

Figure 3-7. Thermal properties of PP_{int} with (a) DSC-curve and (b) TGA-curve

Similar to the characterization of PP_{tw}, the Cox-Merz rule is used to obtain the flow characteristics of PP_{int}. Figure 3-8 shows this material also behaves as a shear thinning fluid and that the Ellis-Arrhenius model describes the flow behaviour relatively well.

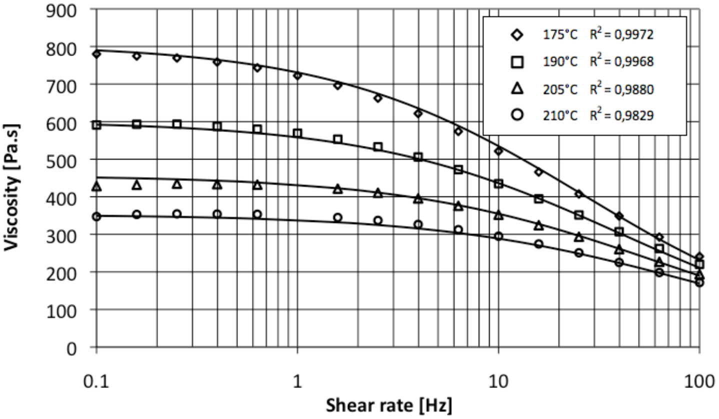

Figure 3-8. Comparison of the Ellis-Arrhenius model with the experimental flow curve data for PP_{int} [82]

Table 3-3 summarizes the parameters for the Ellis-Arrhenius model for PP_{int}.

Table 3-3. Values of the parameters for PP_{int} in the Ellis-Arrhenius model

Ar(T)	Ar_0	Ar_1
$\eta_0(T)$	0.093	4062
C(T)	$1.44\ 10^7$	-5914
n	1.74	1.74

When comparing, the viscosity for PP_{tw} and PP_{int} at different shear rates and temperatures, it is noticed that both materials have a relatively low, but similar viscosity. This is probably due to a low molecular weight. The low viscosity values are needed to assure a good impregnation and consolidation degree of the final composite product.

3.4. Shear field measurement

During draping of fabric-reinforced composites, the yarns rotated due to the inter-ply shear mechanism. This reorientation will change the enclosed angle between the two fibre directions, as illustrated in Figure 1-12(a). When comparing between simulations and experiments, this angle is taken as indication for the fibre reorientation. The angular change is expressed by the shear angle, which is defined as the complement of the enclosed angle between the fibres. The shear angle is the parameter that is often used to validate drape models. Measuring these angles along the formed composite was first attempted by using a coordinate measuring machine with a probe

[83]. However, touching the surface of the laminate gives rise to erroneous results and in addition the technique is very time consuming. Therefore, a faster non-contact technique has been developed.

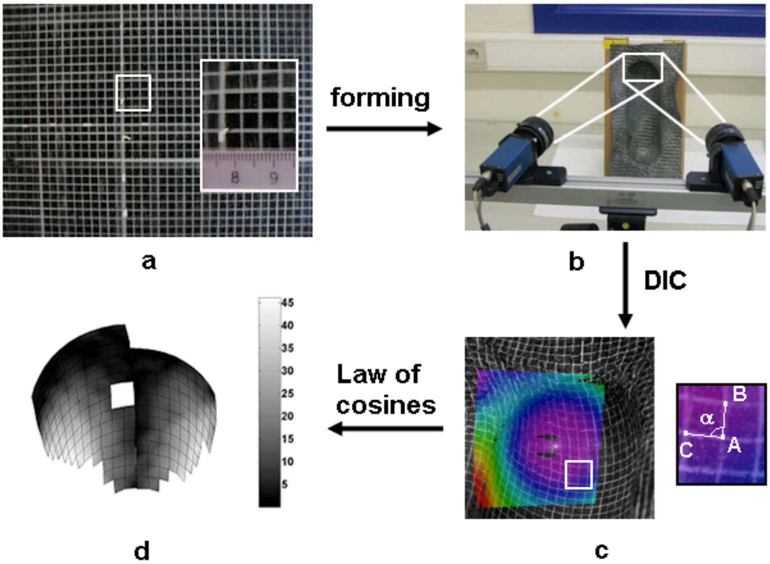

Figure 3-9. Overview of the method used to determine the distribution of shear angles on a formed composite structure: (a) reference pattern sprayed onto a pre-consolidated woven fabric, (b) set-up of the DIC measurement system, (c) a correlated surface that depicts the z-coordinate of the surface overlaid on a picture of a deformed sheet and (d) shear angle distribution on a deformed sheet

Figure 3-9 illustrates the steps needed to obtain a local shear profile of the formed composite. In order to measure the amount of shearing, it is necessary to track fibre positions and orientations within the deformed fabric. A reference pattern, indicated in Figure 3-9(a), is sprayed with white paint onto the black preconsolidated sheets with the help of a stencil that has parallel grooves. The pattern consists of a grid, with a grid size of 5 by 5 mm^2 and a line width of 0.89 ± 0.16 mm. This reference pattern follows the yarns during shearing. In a latter stage, it also serves as pattern needed for Digital Image Correlation (DIC).

After forming, the surface of the composite is measured by using a 3D DIC technique. Figure 3-9(b) depicts the setup that uses a camera system, which consists of two cameras with 16 mm lenses (1392 by 1040 pixel image size and 12 bit gray scale CCD). To obtain a 3D image, an angle of about 30° between the two cameras is preferred. First stereo-correlation and calibration of the camera set-up is performed from which the relative camera position and lens distortions are identified by the system. Afterwards, both cameras capture an image of the same region. In Figure 3-9(c), these two images are combined to obtain the three-dimensional coordinates of the surface by using the software of correlated solutions, namely VIC 3D [84]. The coordinates of the grid intersection points ABC are extracted and the angles between the grid lines are calculated using the law of cosines:

$$\alpha = \angle(AB, AC) = a\cos\left(\frac{|AB|^2 + |AC|^2 - |BC|^2}{2 \cdot |AB| \cdot |AC|}\right) \quad \textbf{Eq. 3-6}$$

A shear angle at the point A is calculated as average of four angles, complimentary to the four enclosed angles *α* for the grid lines joining at A. Figure 3-9(d) presents a measured shear angle distribution of a deformed sheet for a 0° ply-orientation. The gap in this figure is due to light reflection zones where the DIC algorithm fails.

The main benefit of this technique lies in the fact that the surface is measured via a contactless method. A drawback lies in the difficulty of tracking the fibre direction. When applying the reference pattern on the pre-consolidated sheets, it is assumed that the gridlines are parallel with the fibre directions. In practice it has been observed that the yarns inside the sheet are not straight, making it impossible to track them perfectly. At the edges of a preconsolidated plate the yarns tend to be curved. The difference between the fibre direction and grid orientation lies in the order of 2° over the length of the mould. Another problem is the destruction of the reference pattern because of frictional forces between the mould and the deformed fabric, especially pronounced in high shear zones.

This method has been successfully used to validate the material model developed by Willems [64].

3.5. Thermoforming

Thermoplastic composites are often deformed using a thermoforming operation. An overview of different thermoforming processing techniques is given in Chapter 1. In this section the thermoforming equipment used to investigate the draping of thermoplastic composites, shown in Figure 3-10, is introduced. First the material is clamped in the transport unit and is subsequently heated until the desired temperature is reached, for PP this temperature lies within the melting and degradation point (165-230°C). After heating the molten composite is automatically transported to the forming station, where the flat sheet is formed into the desired shape and subsequently cooled.

3.5.1. Transportation unit

The transportation unit has two major tasks. First, ensuring a fast and accurate movement of the flat sheet to the different stations of the thermoforming process. Second, compensating the sagging of the composite sheet when it is heated. Therefore, the transportation unit consists out of one rigid and one moveable arm. When a certain amount of bending is detected the moveable arm stretches the material and so the amount of sagging is minimized.

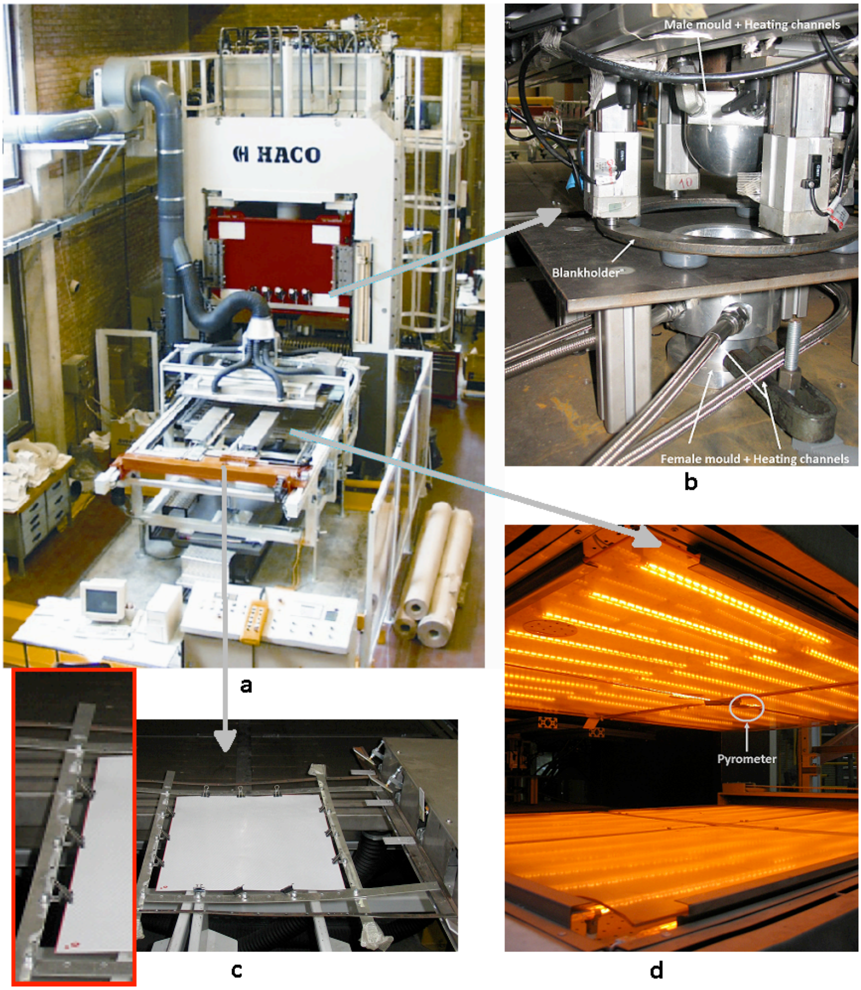

Figure 3-10. Thermoforming process with (a) an overview of the processing unit, (b) the forming unit, (c) the transport unit with a detail on the discrete gripping points and (d) the heating unit

A big drawback of this system, however, is the occurrence of cold zones at the edges of the flat sheet after heating. These cold zones should be avoided since they might reduce the formability of the material [85, 86]. Therefore, the transportation unit was adjusted by using discrete grips. These consist of small springs that gently clamp the edge of material. This allows for heating the edges of the material as can be seen in Figure 3-10(c). Sagging is not compensated by this system. However, due to the small dimensions of the laminates sagging was found to be minimal and formed no problem.

3.5.2. Heating unit

Prior to forming, the material is heated by using infrared (IR) radiation. Figure 3-10(d) shows the IR heating station. It consists of two horizontal cassettes, each having 27 IR-lights (wavelength 1.5-2.2 μm), with a total capacity of 100kW. The temperature is monitored using a pyrometer, indicated in Figure 3-10(d), which is a contactless temperature sensor that is capable of measuring the surface temperature of a sheet by determining the amount of heat it emits. In a previous study [85] it is shown that the temperature of a heated sheet is more homogenously distributed when working at a fraction, i.e. 15%, of the maximum capacity and limiting the heating rate to 1°C/s. Therefore, a typical heating cycle is made up of two steps, first the heating rate is put at 1°C/seuntil the temperature is 20° less than the desired temperature. Then, to ensure a good temperature homogeneity, i.e. a standard deviation of 2°C, the heating rate is reduced to 0.5°C/s until the desired temperature is reached. Afterwards, the sheet is transported to the forming station where the draping takes place.

3.5.3. Forming/Cooling unit

Figure 3-10(b) illustrates the forming unit, which consists out of a hydraulic press with a capacity of 1000 kN. The forming procedure is schematically explained in Figure 3-11. After heating, the material is automatically transported to the pressure unit where the tooling has been placed in the so-called “parking position”. This is the position in which the male mould and the blankholder are placed during the heating of the material. A good parking position ensures less cooling of the sheet prior to contact with the mould, but still allows for the heated sheet to be transported in between the punch and the die. During draping, first the blankholder is moved down and the pneumatic cylinders, controlling the blankholder pressure, are activated to clamp the material, indicated in Figure 3-11(b). Afterwards, moving the male mould down, at a constant speed or acceleration, deforms the sheet until a certain force level is reached that triggers the hydraulic press to go into force control. During force control the male mould is moved down until a preset force is reached. This step involves impregnation and consolidation of the sheet.

This thermoforming process is a non-isothermal operation, meaning the temperature of the sheet during forming is not constant. Figure 1-7 in Chapter 1 indicates a typical thermal cycle during non-isothermal forming. During thermoforming of reinforced polypropylene composites it has been shown that a good control of the temperature of the moulds is needed to ensure a good quality of the shaped product [87]. Therefore, a mould heating machine is used to heat the mould to the desired mould temperature. This temperature control unit, of the brand HB-Therm, uses water to heat up the mould to a maximum temperature of 160°C.

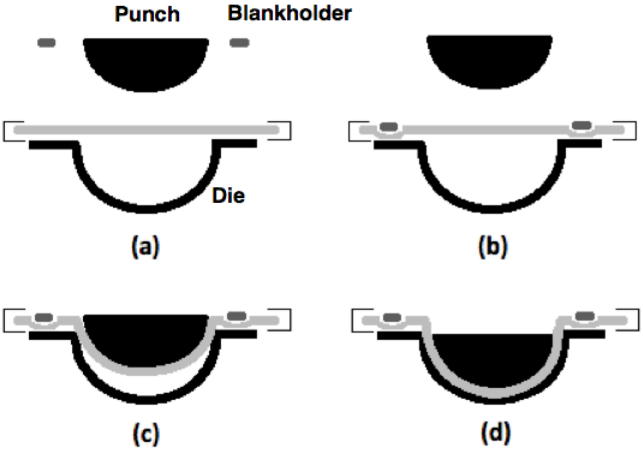

Figure 3-11. Forming procedure during the thermoforming process: (a) after pre-heating the sheet is transported to the forming station, (b) the sheet is clamped by the blankholder, (c) the male mould moves down and deforms the sheet and (d) the formed sheet is pressed and cooled down.

3.6. Conclusion

The different materials and experimental methods used in this investigation are introduced. The textile parameters of the reinforcements and the thermal and flow behaviour of the matrix material have been characterized. Two course fabric and one fine fabric composite will be used in this research to investigate the forming of thermoplastic composites. The matrix of TW_1 and TW_2 has a relatively low viscosity for a thermoplastic polymer, which is needed to assure a good impregnation and consolidation of the final composite product. A technique to measure the local amount of in-plane shear on formed fabric composites is introduced and will be used to compare experimental data with predicted shear angles in Chapter 4. The last paragraph deals with the thermoforming equipment used in the experimental part of this research. The transportation unit of this machine has been adapted so that the edges of the thermoplastic material also melt.

Chapter 4

Drape simulations for single layered woven composites

4.1. Introduction

In this chapter two modelling approaches, introduced in Chapter 1, will be applied to predict the draping of single layered woven composites. One modelling approach uses pure kinematic constraints, i.e. only intra-ply shear is allowed, and is therefore called kinematic draping. It is a very fast and easy to apply method, and has shown its benefits regarding the manual lay-up process to shape composites [60]. A second approach incorporates both the mechanical draping behaviour of the material and the boundary conditions used during draping [65]. Both the kinematic and mechanical approaches have been benchmarked previously [88-90], but only for shapes where either the distribution in shear angles is quite regular (hemisphere) or the shape is complex (double dome) and the precision of the measurements of the shear angle are not very precise. The orientation of the blank in these studies is often chosen so that the distribution in shear is symmetric, which is favourable for a kinematic method since the initial conditions are easily recognized. The aim of this chapter is to demonstrate the difference between the two approaches and compare both methods with experimentally obtained data.

The structure of this chapter is as follows. First, in section 4.2 the experimental setup is described, whereby the mould dimensions and the processing conditions are quantified. In section 4.3, the fibre reorientation is predicted by using the kinematic approach, which is applied to the mould using different initial conditions. The influence of the initial constraints is identified and a comparison is made with experimentally measured data. Afterwards, the same simulations are performed using the mechanical approach and are also compared with experimental drape results.
This chapter forms a prelude to the draping simulation of multilayered woven composites presented in Chapter 7.

4.2. Experimental method

The preconsolidated material was deformed using a non-isothermal forming process. After heating the material at 185°C, it is formed and pressed in a rigid mould, consisting of a cylindrical centre part with two half-hemispheres at the ends. Figure 4-1(a) depicts a scheme of the forming stage and Figure 4-1(b) shows a formed sample. The punch consists of two half hemispheres with a radius of 38.8 mm that are connected by a half cylinder with a length of 170 mm. The die is rounded at the edge to a radius of 10 mm. The gap between male and female mould is 1.2 mm. The steel blankholder has an offset of 30 mm from the female mould and is operated by 4 pneumatic cylinders.

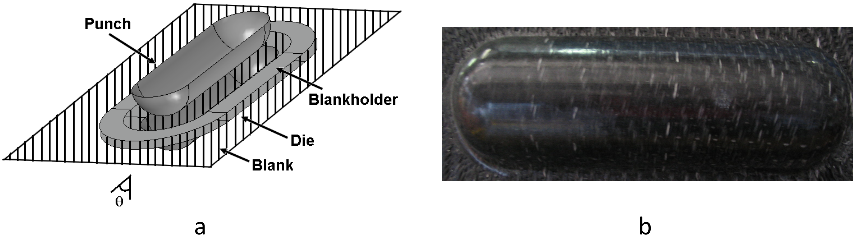

Figure 4-1. Representation of (a) the set-up of the tooling at forming unit and (b) a formed specimen

Three different ply orientations θ, specified as the angle between warp yarns and the long symmetry axis of the mould, are considered: 0, 30 and 45°. The results of forming are analyzed using the process detailed in Chapter 3. The forming velocity for all ply-orientations is 80 mm/s and the consolidation force equals 100 kN. In addition, the die is heated at a temperature of about 85°C.

4.3. Kinematic draping

4.3.1. Method

The kinematic draping model is based on the assumption that the deformation is restricted to inter-ply shear. A commercial program that uses the kinematic approach to simulate the draping of woven clothes is PAM-QUIKFORM. It uses a numerical iteration to drape the fabric onto the mould. For doing so, a discrete model of the mould surface is needed. This is obtained by meshing the mould surface using triangular and quadrilateral membranes, shown in Figure 4-2.

The problem of draping a fabric to this mould surface consists of “gluing” the fabric onto the surface in such a way that the length between the intersecting yarns of the fabric remains constant when draped. Therefore, the fabric is represented by a “fishnet”, illustrated in Figure 4-3(a), where intersection nodes are connected with straight beams of constant length, $\Delta\varepsilon$ and $\Delta\upsilon$. The problem of draping this fishnet sheet is that it has an infinite number of solutions [61], which depend on the first node of the fabric that makes contact with the surface, i.e. initial contact point, and the yarn directions in this point. Therefore, in order to assure a unique solution, it is supposed that both the impact point and the fibre directions in this point are known. These two initial constraints make the kinematic draping solution very sensitive to the experience of the operator, which will be shown in a subsequent paragraph.

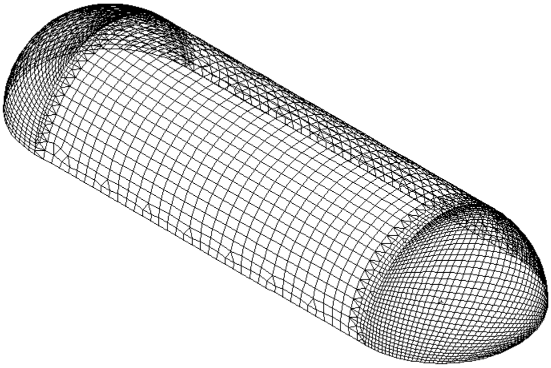

Figure 4-2. Discrete representation of the male mould

The draping procedure follows the scheme indicated in Figure 4-3(b-f):

1. In step 1 a node x_0 on the tool surface Σ is specified as the initial contact point of the fabric on the mould and has the coordinates $(\varepsilon_0,\upsilon_0)$. In this point the warp and weft direction are specified.
2. The coordinates of the nodes of the fabric following the indicated fibre directions (along the light grey lines in Figure 4-3(c)), i.e. warp and weft yarns, are calculated starting from the initial contact point along geodesic lines, i.e. the shortest route between two points, in step 2.

The nodes of the fabric calculated in step 2, illustrated in Figure 4-3(c), are placed on geodesics on the mould surface following the given fibre orientation and remain fixed during the rest of the draping procedure. The remaining nodes of the fabric in steps 3-5, Figure 4-3(e-f) are determined by completing the fabric structure using the advancing front approach (AFA). Their coordinates on the surface are calculated by solving an optimization problem that corresponds to determine a corner point of an equilateral quad on the surface of the mould from the data of the three other known corner points [91]. The AFA determines the sequence of calculating the remaining nodes: the unknown nodes closest to the impact point are calculated first and the "calculation front" moves away from the initial contact point in a circular action.

To summarize, the information provided to PAM-QUIKFORM to predict the draping of a mould with a woven fabric consists out of three parts. First, a discrete formulation of the mould is provided (Σ), then the initial contact point is defined as a node of the meshed surface (x_0) and the yarn directions in this point are indicated.

In order to assess the influence of these initial constraints, the drape simulation has been applied using different initial contact points (P1 to P3), indicated in Figure 4-4, and different fabric orientations.

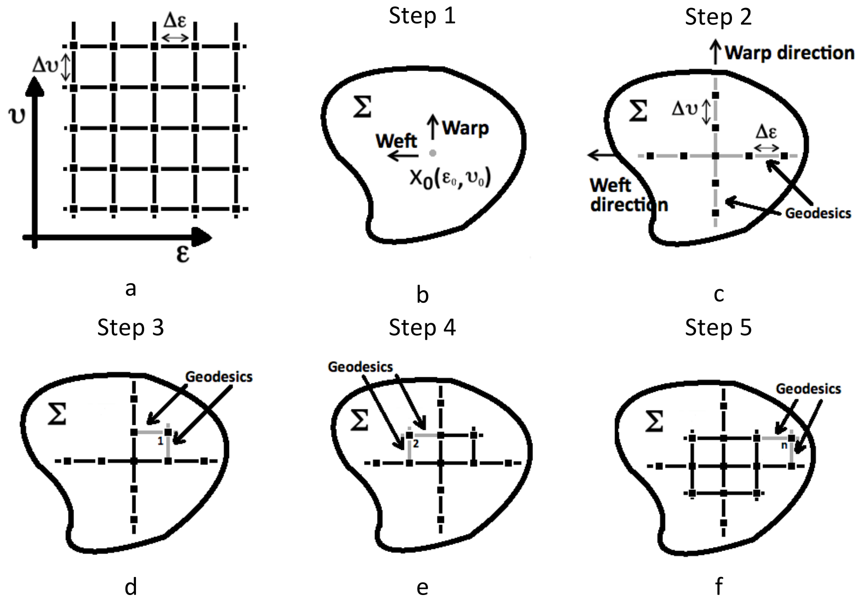

Figure 4-3. Kinematic draping approach used in PAM-QUIKFORM consists out of (a) a fishnet representation of the fabric, (b) determination of the impact point on the mould surface Σ, (c) Calculating the nodes of the constrained fibre directions on the mould surface Σ by geodesic lines, (d), (e) and (f) applying the advancing front approach to calculate the coordinates of the remaining nodes of the fabric

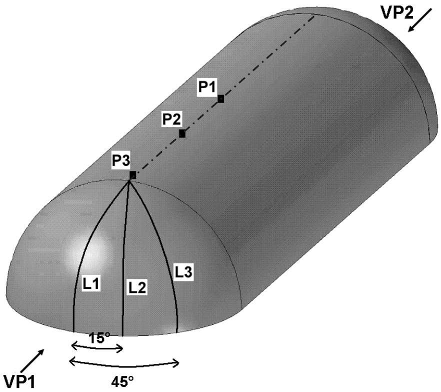

Figure 4-4. Male mould, with an overview of the initial contact points (P1, P2 and P3) used for the kinematic draping method and an indication of the cross section lines (L1, L2 and L3) and viewpoints (VP1 and VP2)

All the impact points lie on the long symmetry plane of the punch, since it forms the line of first contact between the punch and the fabric during forming. Point P1 is the symmetry point of the punch, P3 is the apex of the half hemisphere and P2 lies in the middle of the line P1-P3.

4.3.2. Results and discussion

Kinematic draping predicts the local yarn orientation after draping. Figure 4-5 shows that the shear angle level and distribution strongly depend on the ply orientation. For the same initial contact point the maximum shear angle in case of 30 and 45° orientation is much higher and the shear is concentrated in a smaller area then for a 0° orientation.

In Figure 4-6, the ply orientation is kept constant (30°), but now the initial contact point is changed. Taking impact point P1, which is the centre point of the mould, the shear profile is symmetrical along the main axis of the mould for all ply-orientations. Meaning the profile from viewpoint VP1 and VP2 is the same. The different viewpoints VP1 and VP2 are indicated in Figure 4-4. The combinations of 30 or 45° ply-orientation and initial impact points P2 or P3 resulted in an unsymmetrical prediction of the shear over the mould. The semi-hemisphere where the shear angles are smallest lies closer to the starting point and is viewed from viewpoint VP1.

P1 and VP1

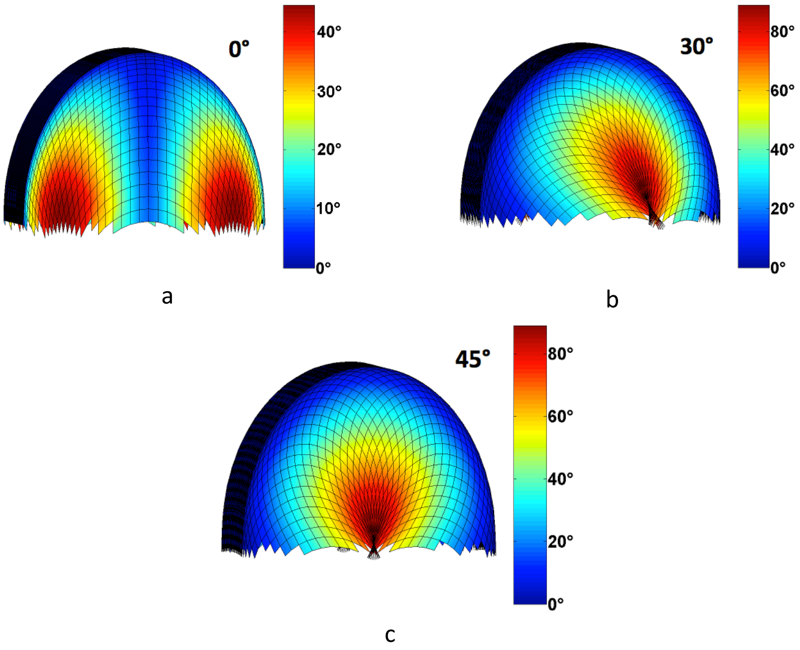

Figure 4-5. Kinematic draping solution with contact point P1 and viewpoint VP1 for (a) 0° ply-orientation, (b) 30° ply-orientation and (c) 45° ply-orientation

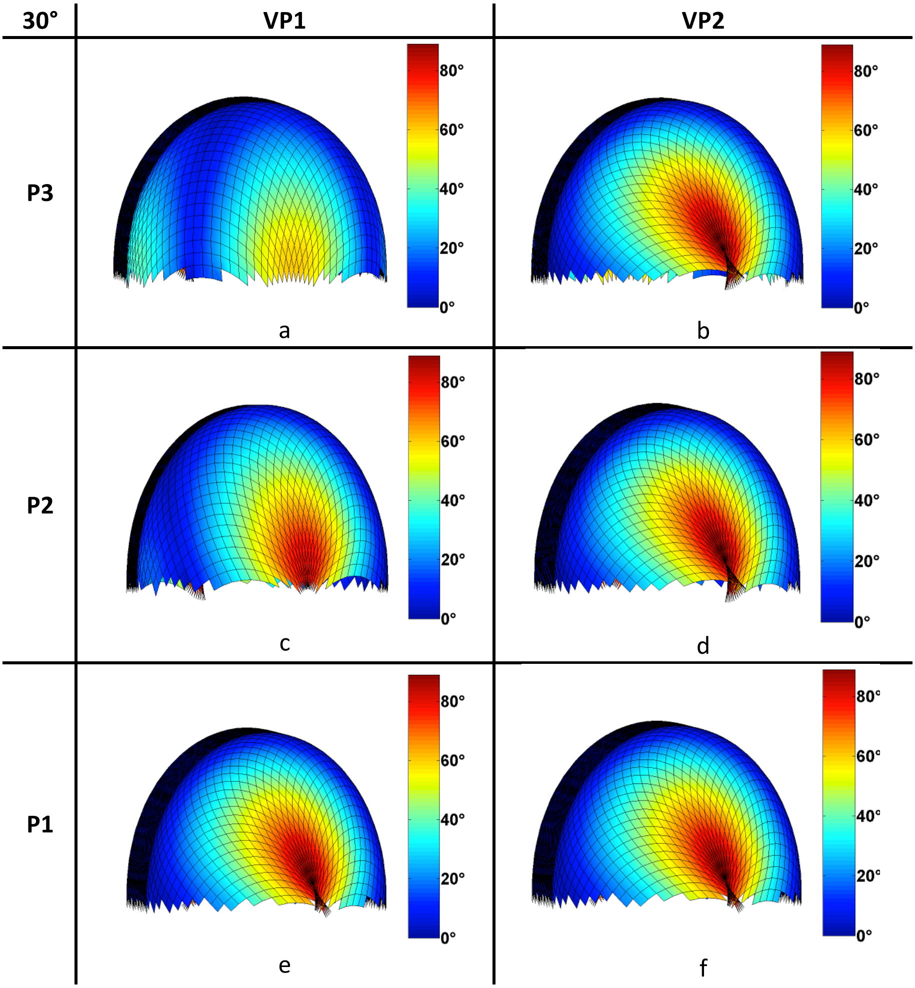

Figure 4-6. Kinematic draping solution for 30° ply-orientation with (a) impact point P3 and viewpoint VP1, (b) impact point P3 and viewpoint VP2, (c) impact point P2 and viewpoint VP1, (d) impact point P2 and viewpoint VP2 and for 45° ply-orientation with (e) impact point P3 and viewpoint VP1 and (f) impact point P3 and viewpoint VP2

To compare the experimentally obtained shear data with the kinematically predicted ones, cross sections where most shearing occurs are examined. The amount of shear along the edge of these cross sections is used to compare with the draping approach. Figure 4-4 gives an overview of the different cross sections for different ply-orientations. The line L3 corresponds to the examined cross section for a 0° preform orientation, line L1 is chosen to compare the data for a 45° preform orientation. For a 30° ply-orientation the cross section, indicated by L2, forms an angle of 15° with the long symmetry axis of the mould. A third order polynomial is fitted through the experimental data and the 90% confidence and prediction intervals are determined.

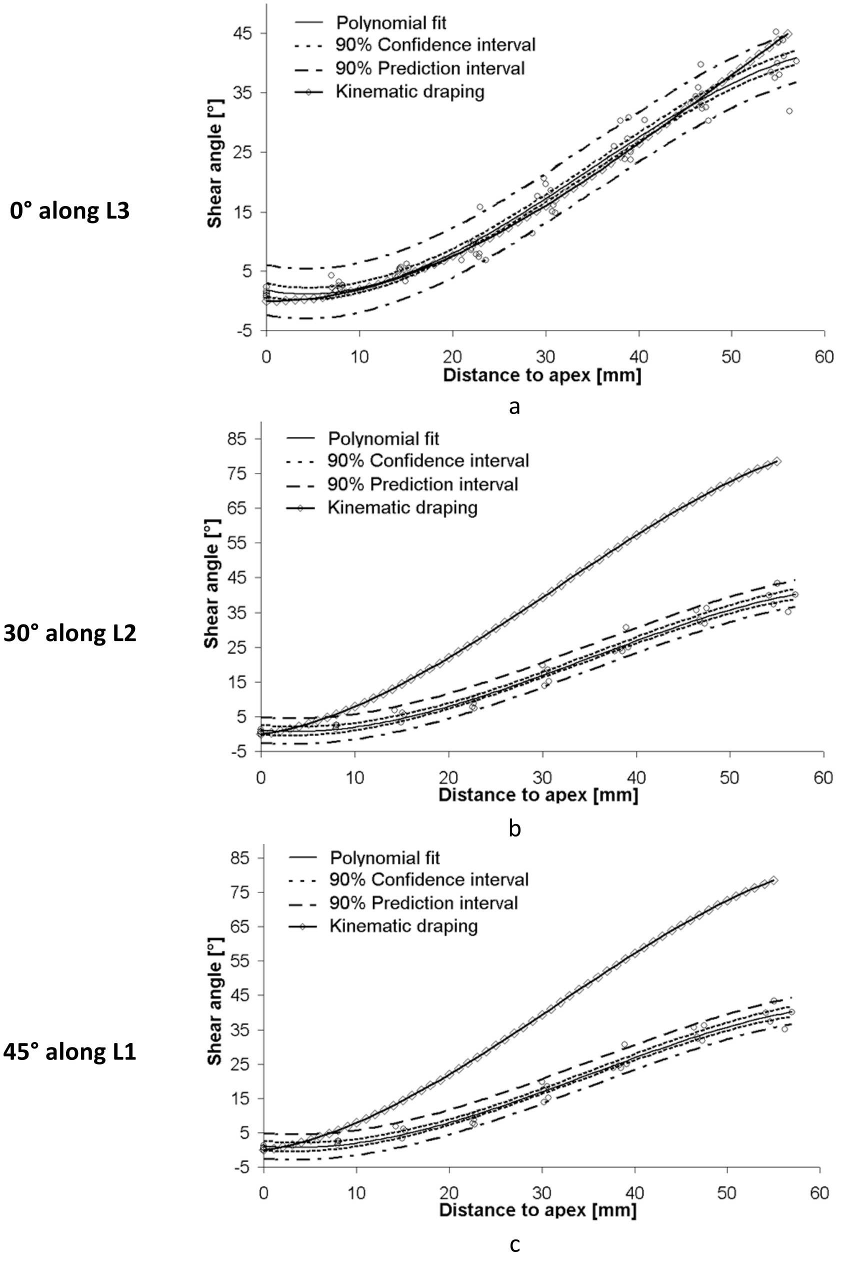

Figure 4-7. Comparison between kinematic draping (with contact point P1) and experimental results (individual data points and polynomial least-square fit) for (a) 0° ply-orientation, (b) 30° ply-orientation and (c) 45° ply-orientation

The prediction interval is an estimate of an interval in which future observations will fall, while the confidence interval provides an indication of the variability of the measured data. From Figure 4-7(a) it can be concluded that for the 0° orientation the agreement between the experimental and the kinematic draping results is good. However, at higher shear angles there seem to be small discrepancies between the model and practice: the experimental shear angle is smaller than the predicted angle. The draping model assumes a negligible shear resistance and doesn’t account for increasing shear resistance when the shear angle increases.

For drape orientations other than 0°, the results from the kinematic model do not agree at all with the experimental results. The oversimplification of the draping front in this model gives shear angles up to 88° in case of the 30° preform orientation. Most often the kinematic model is used with a cut-off shear angle based either on an experimentally determined locking angle, or the maximum misorientation that the designer is prepared to tolerate. When defining a cut-off angle of 37.5°, which equals the experimentally determined locking angle, wrinkling would be predicted for a 30° and 45° preform orientation. However, no wrinkling occurred during the stamp forming experiments. Figure 4-7(b) and (c) visualize the large difference between the kinematic model and the measured shear angles for a 30 and 45° orientation.

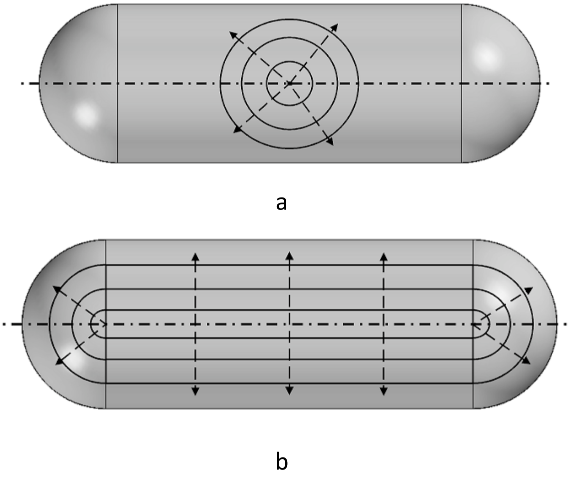

Figure 4-8. Comparison between (a) advancing front approach used in kinematic draping for impact point P1 and (b) real draping front

The unsymmetrical shear pattern makes the kinematic draping results questionable. Moreover, it does not compare well with the experimental results, since all forming experiments resulted in a symmetrical shear pattern. The origin for these unsymmetrical predictions and the high difference in shear angles between the experimental and predicted draping results lies in the advancing flow approach used by the draping algorithm. Figure 4-8 clarifies the difference between this approach and the real draping behaviour during stamp forming. The arrows in both figures indicate the direction of draping. The advancing front approach has 1 initial contact point. Though, in reality draping initiates from a line of first contact formed by the long symmetry axis of the half cylinder.

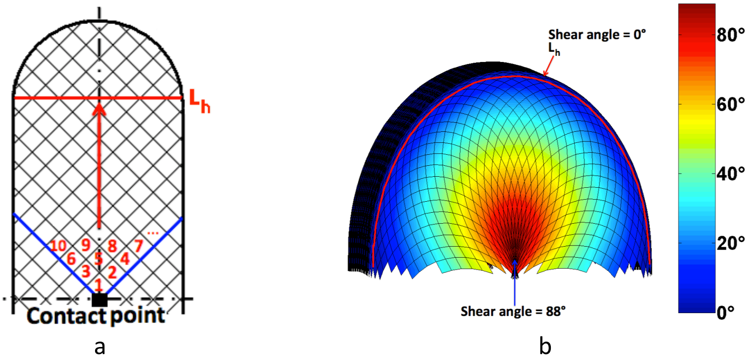

Figure 4-9. AFA for a 45° fabric orientation, impact point P1 and length of the cylinder of 170 mm: (a) scheme showing the order of calculating the unknown node points and (b) resulting shear profile obtained via PAM-QUIKFORM

Figure 4-9(a) illustrates the sequence of calculating the unknown node points for an initial contact point P1 and a yarn orientation of 45°. The unknown node points along the line, L$_h$, at the top of the semi-hemisphere are already calculated before the draping of the hemisphere is initiated.

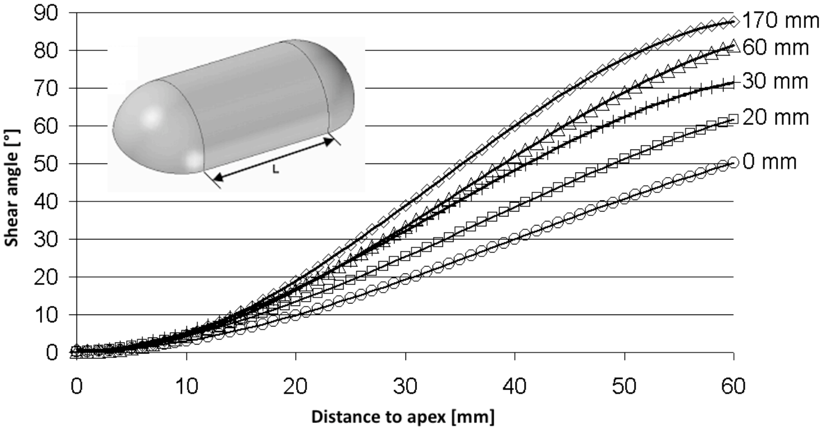

Figure 4-10. Influence of the length of the punch on the shear profile along line L1 for a 45° ply-orientation calculated via kinematic draping

In these nodes the shear angle will be zero, since no shear needs to occur to drape the central cylinder. This implies that this line forms a constraint at the start of draping the semi-hemisphere, which in reality is not present. Along this line no shearing can any more occur, thus the intra-ply shear needed to adapt to the mould surface is concentrated in those areas that are not yet fully constrained, indicated in Figure 4-9(b).

Proof to support this assumption can be obtained by performing an extra set of numerical tests, namely by changing the length of the central cylinder. Figure 4-10 depicts the influence of different lengths on the shear profile for a 45° ply-orientation. The length L of the central hemi-cylinder is gradually increased from 0 (hemisphere) to 170 mm. The contact point of draping was chosen to be the symmetry point of the mould and the shear profile is a cross section taken along line L1, which is shown in Figure 4-4. It is obvious from the results that the shear level is highly sensitive to the length of the hemi-cylinder. This result is quite remarkable as the hemi-cylinder is a single curved shape and thus the fabric does not need to undergo more intra-ply shear if its length increases. Figure 4-11 indicates that a decrease in length of the central cylinder decreases the length of the line L_h. The length of L_h corresponds to the length between the outermost fixed nodes of the fabric along L_h before the semi-hemisphere is draped. The shear in the semi-hemispheres is more evenly spread out over the surface and lower values of shear angles are obtained at low values of L_h. For a hemisphere the length of the cylinder equals zero. The impact point then coincides with the apex of the hemisphere. For a length of the central cylinder larger than 127 mm, the length of L_h corresponds to half the perimeter of the cylinder.

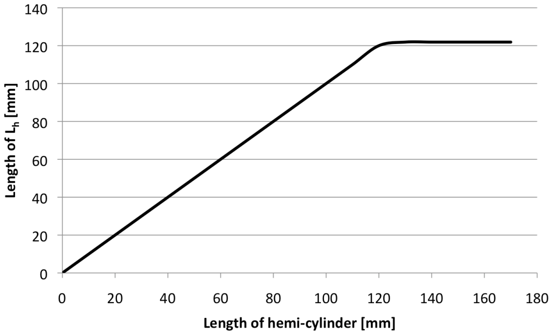

Figure 4-11. Length of the line L_h as function of the length of the cylinder connecting the semi-hemispheres

From the above-discussed results, it can be concluded that the kinematical draping method is not appropriate for predicting the yarn directions of a fabric after automated forming, unless the mould has an axisymmetrical shape with draping initialized at the top point. The error in the shear angle can be as high as 30° and the solution is strongly depending on the initial conditions, which are provided by the operator of the software. The main reason for these erroneous results lies in the advancing front approach, which simulates an unnatural draping front.

4.4. Mechanical approach using FE-software

4.4.1. Method

An alternative to the kinematic approach is an approach where the drape deformation mechanisms of the fabric and the boundary conditions are incorporated. As discussed in Chapter 1, three mechanical approaches can be identified, namely a discrete, a continuous and a semi-discrete approach. In this chapter the PAM-FORM FE-program, which is a visco-elastic continuous mechanical approach is used. This implies that the forming tools and fabric sheets are represented by a discrete structure [92]. Figure 4-12 gives an example of a 2D discrete structure. It is made up of elements, whereby each element possesses a set of distinguishing points called nodal points or nodes for short. In Figure 4-12 an element e is indicated in grey, it possesses three nodes, i,j and m. These nodes serve a dual purpose: definition of the element geometry, and home for degrees of freedom (DOF), in Figure 4-12 these DOF are the displacements in x and y direction. Nodes are usually only located at the corners or end points of elements.

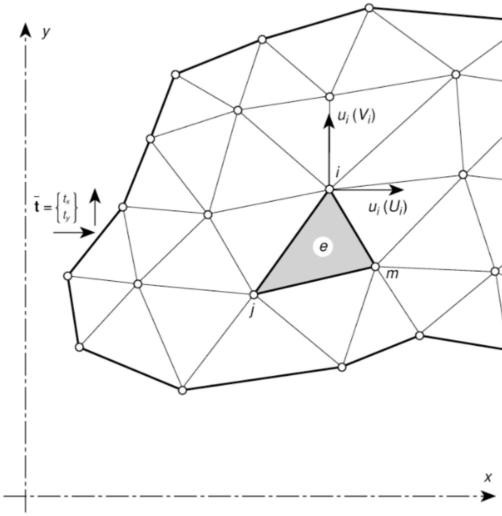

Figure 4-12. A region divided into finite elements [93]

The dynamic equations of motion, which describes the behaviour of the discrete body as a function of time, has the form:

$$\mathbf{M}\ddot{\mathbf{u}}_\mathbf{n} + \mathbf{C}\dot{\mathbf{u}}_\mathbf{n} + \mathbf{K}\mathbf{u}_\mathbf{n} - \mathbf{p}_\mathbf{n} = \mathbf{0} \qquad \textbf{Eq. 4-1}$$

Where $\mathbf{u}_\mathbf{n}$, $\dot{\mathbf{u}}_\mathbf{n}$ and $\ddot{\mathbf{u}}_\mathbf{n}$ are the vectors of nodal displacement, velocity and acceleration, *n* is the increment number at time t_n after nΔt time steps, **M**, **C** and **K** are the mass, damping and stiffness matrices and $\mathbf{p_n}$ is the total load vector. Generally material damping effects are neglected, which simplifies Eq. 4-1 to:

$$\mathbf{M\ddot{u}_n} + \mathbf{Ku_n} - \mathbf{p_n} = \mathbf{0} \qquad \text{Eq. 4-2}$$

The mass and stiffness matrix are given by:

$$\mathbf{M} = \sum_e \left[\int_{V^e} \rho \mathbf{N}^{\mathbf{T}} \mathbf{N} dV \right] \qquad \text{Eq. 4-3}$$

$$\mathbf{K} = \sum_e \left[\int_{V^e} \mathbf{B}^{\mathbf{T}} \mathbf{D} \mathbf{B} dV \right] \qquad \text{Eq. 4-4}$$

Where **N** is the matrix of shape functions, **B** is the strain-displacement matrix, **D** is the elasticity matrix, ρ is the density of the material while V^e is the volume of element *e*.

The matrix of shape functions **N** is used to approximate the displacement in every material point of the discrete structure. The strain-displacement matrix **B** is found by derivation of the shape functions with respect to the global coordinate system. The total force vector is given by the sum of the body and surface forces and the external forces in the nodes.

$$\mathbf{p_n} = \sum_e \left(\int_{V^e} \mathbf{N}^{\mathbf{T}} \mathbf{b} dV + \int_{S^e} \mathbf{N}^{\mathbf{T}} \bar{\mathbf{t}} dS + \mathbf{q}^{\mathbf{e}} \right) \qquad \text{Eq. 4-5}$$

Where **b** is the vector of the body forces, $\bar{\mathbf{t}}$ is the vector of the surface forces acting of the element surface S^e and $\mathbf{q}^{\mathbf{e}}$ is the vector of external forces that are applied to the nodes of element *e*. The equations of motion for the discrete body, Eq. 4-2, are integrated using the explicit central difference integration rule. It has been proven to be suited to non-linear geometric and material problems, especially where a large number of contacts between the parts occur [94] as is the case with forming simulations.

The implementation of an explicit integration rule is used together with the assumption of a diagonal or “lumped” element mass matrix, i.e. the mass is concentrated in the nodes. The nodal accelerations can be easily calculated:

$$\mathbf{\ddot{u}_n} = \mathbf{M}^{-1} \left(\mathbf{p_n} - \mathbf{Ku_n} \right) \qquad \text{Eq. 4-6}$$

The nodal velocities and displacements are then obtained by an explicit integration in time, using the central finite difference operators:

$$\dot{\mathbf{u}}_{\mathbf{n}+\frac{1}{2}} = \dot{\mathbf{u}}_{\mathbf{n}-\frac{1}{2}} + \ddot{\mathbf{u}}_{\mathbf{n}} \Delta t_n \qquad \text{Eq. 4-7}$$

$$\mathbf{u}_{\mathbf{n}+1} = \mathbf{u}_{\mathbf{n}} + \dot{\mathbf{u}}_{\mathbf{n}+\frac{1}{2}} \Delta t_{n+\frac{1}{2}} \qquad \text{Eq. 4-8}$$

The subscript *n* refers to the increment number and *n-1/2* and *n+1/2* refer to mid-increment values. These equations provide a stable solution, only if the time step Δt_n is lower than a critical time step, which depends on the material properties and element size.

$$\Delta t_n = \min\left(\frac{L_e}{c_d}\right) \qquad \text{Eq. 4-9}$$

here L_e is the characteristic element dimension and c_d is the current effective dilatational wave speed of the material, which is inversely proportional to the density of the material.

The calculation of the stiffness matrix requires a material law that represents the fabric. In PAM-FORM a “bi-phase” material law with visco-elastic matrix and elastic fibres is implemented. Both the non-linear inter-ply shear and tensile behaviour of the fabric can be taken into account, though no coupling between the two deformation mechanisms is considered. The material model is divided into three components. The total stress is given by the sum of the three component stresses. The first component is called the parent sheet, its elastic properties are based on the inter-ply shear behaviour of the fabric. The second component describes the visco-elastic behaviour of the matrix material using a Maxwell model. The third component describes the behaviour of the reinforcement in the fibre directions. All these components are uncoupled from each other. Figure 4-13 gives a schematic overview of the material model. The material model requires the input of an in-plane shear modulus G with corresponding Poisson ratio ν, the tensile elastic moduli E_{11} and E_{22} and the shear viscosity η.
Picture frame tests were performed to characterize the intra-ply shear behaviour in [64]. Studies have shown that this intra-ply shear characterization is prone to low repeatability [17, 22, 95, 96], which forms an important obstacle in submitting the right material input data in the material model. In order to show the importance of accurate input data, four in-plane shear curves are used during this modelling exercise.

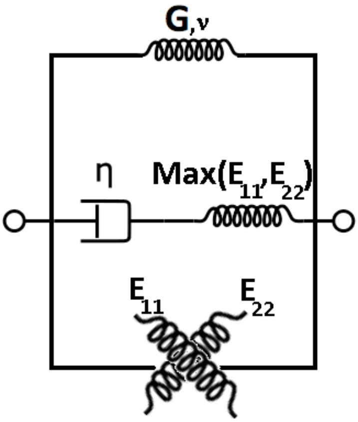

Figure 4-13. Schematic overview of the material law used for fabric composites in PAM-FORM

Three of these curves were determined during a benchmarking exercise on the characterization of the mechanical behaviour of woven fabrics in [96] and shown in Figure 4-14(a). They are measured using the picture frame experiment and reported as KUL_74b3_Dic, KUL_74b2_Dic and KUL_74b1. The Poisson coefficient is assumed to be 0.3. The non-linear behaviour of the material is a consequence of the woven structure of the fabric and explained in Chapter 1.

The fourth curve LH is a fictitious curve, the initial stiffness is negligible (=0.001 MPa) and the stiffness after locking is taken very high (=1000 MPa). The initial stiffness is chosen extremely low, in an attempt to create a similar assumption on the fabric draping behaviour as with the kinematic draping approach, i.e. only in-plane shear occurs. However, in contrast with kinematic draping after the locking angle, the deformation of the fabric in in-plane shear is restricted by defining a very large shear stiffness.

The yarns are assumed to be non-linear elastic and the tensile elastic properties (E_{11} and E_{22}) of the fibre sheet are based on the tensile properties of the fabric in warp and weft direction. Although, the tensile response depends on the strain-ratio between warp and weft, this biaxial coupling is not yet considered within the material model. Therefore, the input data used for PAM-FORM is based on uniaxial tensile test on dry TW_1 material as mentioned in [92]. The difference between dry and preconsolidated material lies in the higher crimp in the dry material (see Table 3-1). Figure 4-14(b) shows the uniaxial tensile data, which are presented in [96].

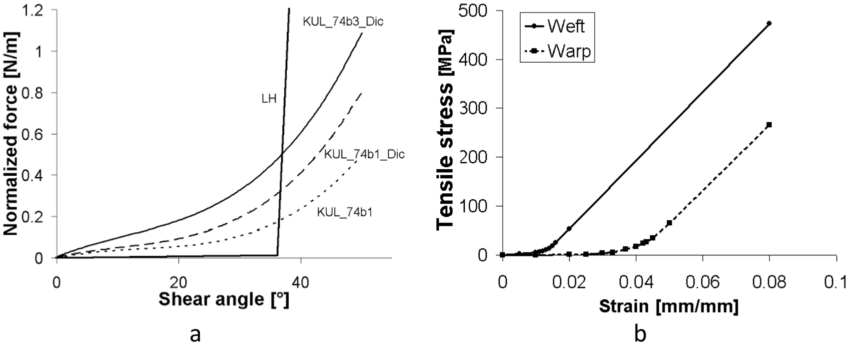

Figure 4-14. Mechanical behaviour of the fabric for (a) in-plane shear and (b) uni-axial tension

The low stiffness at the beginning of the tensile curve is due to the initial undulation of the yarns in the tensile direction. Gradual de-crimping causes the yarns to straighten and thus deformation becomes more difficult. An explanation for the different behaviour in warp and weft direction lies in the unbalanced nature of the fabric. The weft yarns of the dry fabric are not crimped (crimp is 0.1%) and stresses are built up already at small strains. On the contrary, the warp yarns are heavily crimped (crimp is 10.3%) and thus a longer de-crimping region is found in the stress-strain curve.

Due to the fibrous nature of the yarns, fabrics have small resistance to bending [97]. This results in an overestimation of the bending stiffness when applying the Euler-Bernouilli beam theory based on the tensile diagram and assuming that the shell is “solid”. A too high bending stiffness results in an overestimation of the force required to shape the composite. Therefore, a knock down factor of 0.001 is specified, which diminishes the bending stiffness of the fabric to a small value. The bending stiffness of the fabric is then calculated by multiplying the knock down factor by the bending stiffness obtained using the Euler-Bernouilli beam theory. In [98] it was shown that this knock down factor does not have a great effect on the local deformation during forming, however it does have an influence on the punch force. A higher knock down factor results in a higher force needed to drape the fabric composite.

The visco-elastic behaviour due to the polymeric matrix is described in a Maxwell model. However, in a previous study [98] it has been shown that for the material under consideration the visco-elasticity does not have a significant influence on the forming behaviour. Thus, during the simulations performed in this study, the effects of heat transfer between the hot sheet and the cold tools, and matrix viscosity are neglected.

The contact that occurs between the blank and tools during forming is defined as Coulomb friction. The friction coefficient is 0.3 [37]. Though, while evaluating preliminary simulations it was noticed that the preform and the punch didn’t remain in contact during forming as illustrated in Figure 4-15. The detachment of the preform does not occur in reality and therefore the contact definition is extended by defining a separation stress. The separation stress is applied perpendicular to the element surface from the moment it touches the punch. This option allows to model sticking contact, i.e. when a blank element touches the punch surface, a normal force on the element is exerted to prevent the element from detaching from the punch surface. The determination of an adequate separation stress is discussed in the next section.

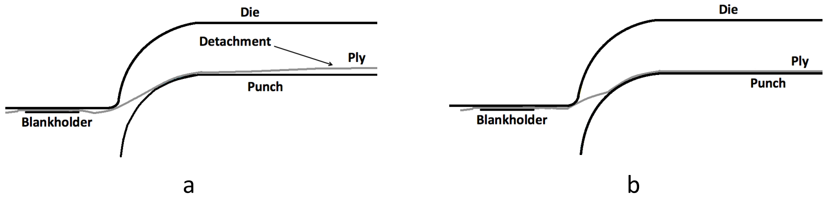

Figure 4-15. Forming simulation in PAM-FORM with (a) no separation stress and (b) a separation stress defined

The input data for the model is given in Table 4-1. The friction coefficient between the tooling and the blank is set at 0.3, the viscosity value is set to zero and any rate depended effects are neglected.

4.4.2. Discussion

Generally forming of materials is regarded as a quasi-static process, since the force and displacement is considered to vary slowly. Therefore, when performing explicit forming simulations, special care is taken since the solution needs to be quasi-static. In order to check whether or not this condition is met, the kinetic energy is compared with the internal energy. The kinetic energy of the blank should not be greater than a few percent of its internal energy. The forming velocity was taken to be 120 mm/s, which is more than the 80 mm/s forming velocity in the experimental part, but since no rate dependency is considered this will not affect the outcome.

Figure 4-16(a) shows that the ratio of kinetic to internal energy of the blank is acceptably low after a certain time, which confirms that the analysis was quasi-static. Taking a closer look at the kinetic energy curves in Figure 4-16(b) sudden energy peaks are observed. This unnatural effect is a consequence of the separation stress defined in the contact option. Neighbouring nodes of elements that are in contact with the punch are pushed towards the punch and thus get a certain acceleration, which is translated into a sudden kinetic energy increase.

Table 4-1. Input date for the material model in PAM-FORM

Shear angle [°]	Shear modulus G [MPa]	Strain [mm/mm]	Tensile modulus [MPa]
KUL_4b1		**WEFT**	**E_{22}**
0	0.058	0.00	0.0
1	0.058	0.01	24.5
5	0.056	0.02	65.2
10	0.063	0.025	159.1
15	0.067	0.03	412.5
20	0.074	0.033	710.8
25	0.073	0.037	1383.0
30	0.082	0.04	2173.0
40	0.202	0.042	2875.9
45	0.371	0.043	3288.9
50	0.584	0.045	4254.1
55	0.584	0.05	6094.0
KUL_4b1_Dic		0.055	6670.0
0	0.117	0.08	6670.0
1	0.117	1.00	6670.0
5	0.112		
10	0.126	**WARP**	**E_{11}**
15	0.133	0.00	0.0
20	0.148	0.005	461.9
25	0.147	0.01	671.0
30	0.164	0.011	942.2
40	0.304	0.012	1437.1
45	0.557	0.013	2199.7
50	0.876	0.014	3338.6
55	0.876	0.015	4925.7
KUL_4b3_Dic		0.016	7001.0
0	0.234	0.018	7001.0
1	0.234	0.02	7001.0
5	0.224	0.08	7001.0
10	0.252	1.00	7001.0
15	0.267		
20	0.297		
25	0.292		
30	0.246		
40	0.455		
45	0.835		
50	1.314		

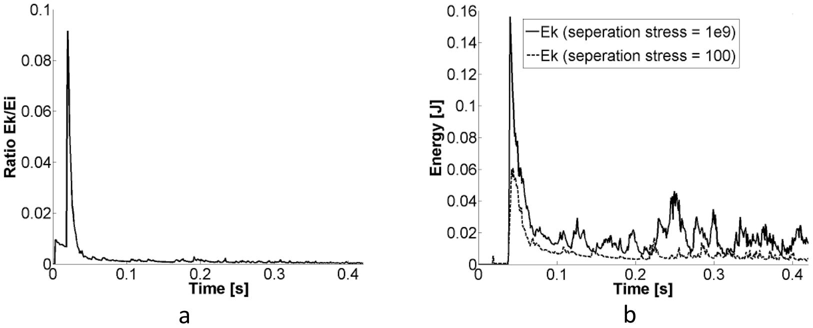

Figure 4-16. Energies of the blank during a forming simulation: (a) ratio of the kinetic (E_k) to internal energy (E_i) and (b) the kinetic energy

The higher the separation stress, the more force applied thus the higher the kinetic energy peaks will be. The separation stress was increased from 100 to 1e+9 Pa using 100000 Pa as an intermediate level. In further simulations 100000 Pa is used as separation stress value, since this value insured stick between the blank and the punch.

To compare the experimentally obtained shear data with the predictions, again the cross sections, shown in Figure 4-4, are analyzed in order to validate the forming simulation. From Figure 4-17(a), (b) and (c) it can be concluded that for all ply-orientations the agreement between the experimental and the simulated draping results, using KUL_74b1_Dic as shear resistance input, is good. Figure 4-18 shows the effect of the different in-plane shear resistance curves on the FEM-predicted shear angles. The shear angle variance along the cross-section that coincide are predictions using the different in-plane shear curves determined by the picture frame experiment in [96]. This result indicates that the influence of the variation of shear input for the studied material, caused by experimental difficulties, on the fibre reorientation can be disregarded. The fictitious in-plane shear curve gives rise to an incorrect prediction, which suggests there is a need for realistic material input data. Although the picture frame test is not yet completely reliable, resulting in a high variability in material data input for the constitutive behaviour of the material model used in the FEM-simulations, this does not significantly affect the predicted fibre orientations. This observation has recently also been stated by Lee et al. [99].

0° along L3

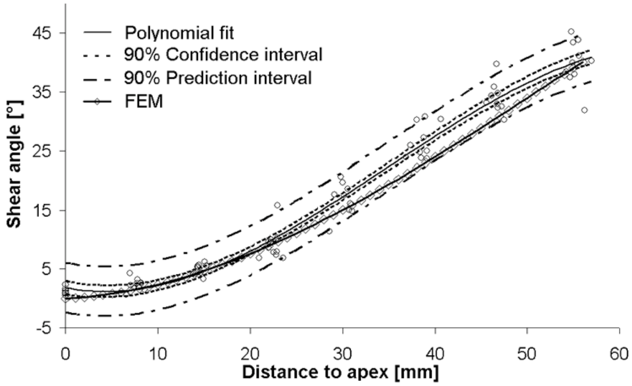

a

30° along L2

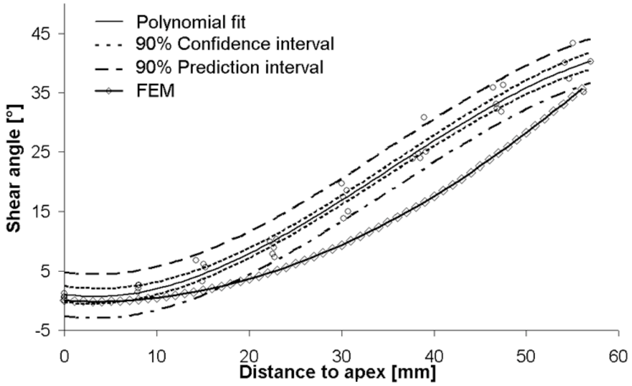

b

45° along L1

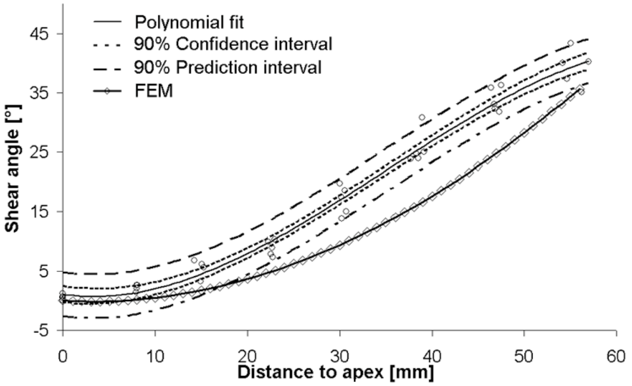

c

Figure 4-17. Comparison between experimental results obtained from PAM-FORM and experimental results for (d) 0° ply-orientation, (e) 30° ply-orientation and (f) 45° ply-orientation

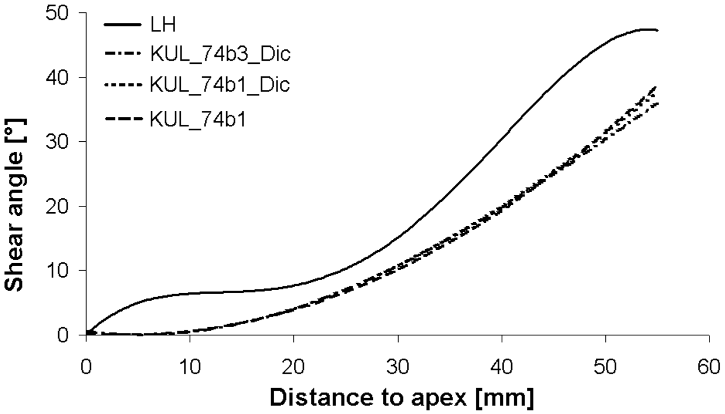

Figure 4-18. Influence of the in-plane shear data on the shear profile for a FEM-simulation of a 45° ply-orientation along line L1

The difference between the experiments and the draping results can be due to misalignment between the mesh and the fibre directions in PAM-FORM. It was shown by Yu [100] that interply shear locking may occur when the principal yarn orientations are not aligned with the element mesh as was the case for the performed simulations. The phenomenon of interply shear locking is not considered during this study and can thus affect the results. Figure 4-19 clarifies the difference between mesh orientation of the discretised blank and the yarn orientations used in the PAM-FORM simulations.

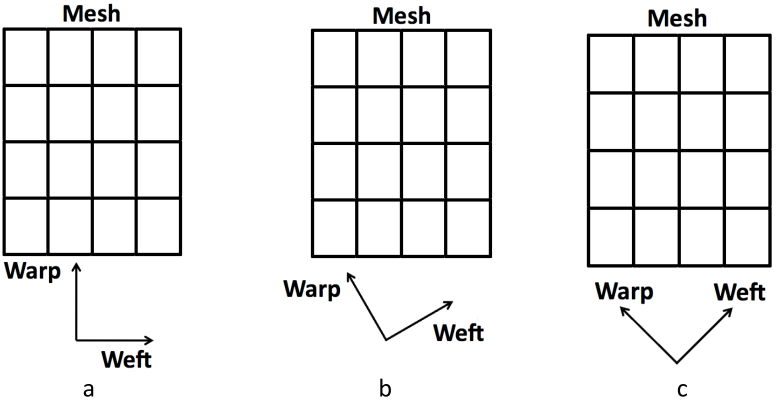

Figure 4-19. Warp and weft yarn orientations compared to the element mesh for (a) 0°, (b) 30° and (c) 45° ply-orientation

For 0° orientation no difference between the mesh orientation and yarn orientations is present, for 30 and 45° ply-orientation however there is a discrepancy of respectively 30 and 45° between the yarn and the mesh direction. The underestimation in Figure 4-17 for 30 and 45° ply-orientation of the shear angles can be due to the overestimation of the shear modulus due to this misalignment between the mesh and the warp and weft yarn orientations [100]. Another possible explanation for the deviations between experiments and predictions is attributed to the “oversimplified material model” that does not yet consider the complex interaction between warp and weft yarns of the fabric and disregards the coupling between tensile and shear properties. The material model used in PAM-FORM is based on uniaxial tensile data. However, the initial non-linear zone in Figure 4-14(b) depends on the strain-ratio between warp and weft [19]. The higher the strain in one yarn direction, the more difficult it becomes to stretch the perpendicular yarn direction. This biaxial effect is not taken into account in this material model. Also the influence of the shear on the tensile properties of the fabric and vice versa is not considered in this material model. How these interactions would influence the shear angle distribution is difficult to consider. Including the biaxial effect would probably result in a prediction of higher shear angles since the higher the resistance to extension of the fabric the more in-plane shear would occur. A third possible cause for the deviations is the complex contact behaviour between the blank and the mould. The contact definition in PAM-FORM does not take into account the dependency of the friction on the process parameters [37], this problem will be tackled in Chapter 7 for multilayered materials.

In conclusion of this section, it can be stated that FEM-simulation seems very promising for predicting the fibre re-orientation during forming, the error in local shear angle does not exceed 10°. Though, the constitutive model used in PAM-FORM is still too simplified to exactly describe the forming behaviour of woven reinforcements.

4.5. Conclusions

This chapter presents a comparison between two different modeling approaches commonly used in the simulation of draping woven composite fabric. The kinematic approach only considers unresisted in-plane shear as deformation mechanism. This method is fast and requires only a minimal data input and the geometric description of the shape to be formed. A second, more realistic, approach is a mechanical model, which considers the non-linear shear resistance and non-linear elastic tensile behaviour of the fabric and the boundary conditions during forming. Both modelling approaches are compared with experiments.

From the results it can be concluded that the kinematic approach severely fails in predicting the fibre reorientation that occurs during sheet forming when unsymmetrical blank/mould configurations are used. The main sources of these faulty predictions are (a) the strategy of the kinematic approach used in PAM-QUIKFORM, which considers that the actual forming sequence to start from an initial contact point and to a lesser degree (b) neglecting the real draping behaviour of a woven fabric. An advancing flow front technique will give reasonably good results for axisymmetric shapes with one initial contact point (e.g. hemisphere), but it fails when the mould shape deviates from this kind of symmetry. The reason is that complex shapes usually have more than one impact point, which can form an impact “line” or even an impact “surface”. Currently no automated kinematic approach exists that can tackle the problem of multiple contact points.

On the contrary, a more refined mechanical simulation approach gives a reasonably good prediction of the fibre reorientation, albeit with a higher computational cost. The influence of the scattered in-plane shear resistance curves due to experimental inaccuracy in the shear testing can be disregarded for the studied material. Though there is still need for realistic material data. The deviations noticed between experiments and predictions can be explained by a bad alignment between the mesh and the yarn orientation and the “oversimplified material model” that neglects both the biaxial interaction between the yarns that occurs inside the fabric and the lack of a coupling between the tensile and shear behaviour.

In Chapter 6, the kinematic draping software will be used to investigate the local difference in deformation between multiple layers for a hemispheric mould and in Chapter 7, a finite element approach will be used to predict the draping and wrinkling of multilayered fabric composites.

Chapter 5

Experimental studies of forming of multilayered woven composites

5.1. Introduction

This chapter deals with the experimental investigation of the forming of multilayered fabric composites. Formability studies of this type of material are usually confined to relatively easy drapeable laminate configurations, like single layers or laminates where the relative orientation between the plies is small [49, 101, 102]. In the recent past, however, some researchers [52, 103] have shown that the forming of multilayered fabric composites is often accompanied by unwanted shape distortions, especially when the laminate configuration becomes more complex. Therefore, the main goal of this chapter is to investigate the cause of these shape distortions and try to eliminate their occurrence. In order to do this in a logical manner, this chapter is divided into two key sections. The first section deals with the influence of the fabric layup on the formability. In the second section the influence of the process parameters on the occurrence of shape distortions is screened.

5.2. Influence of fabric layup

In this section multilayered woven fabric composites are formed by deepdrawing. The process parameters are kept constant, but the layup configuration is altered. First, the forming method will be briefly introduced and afterwards, the results will be discussed and explained by means of the kinematic draping prediction.

5.2.1. Experimental method

5.2.1.1. Preconsolidation

Prior to forming, a two-layered stacking of textile composite is preconsolidated using a hot press. The materials used in this study are the fine fabric reinforced TP and the coarse fabric reinforced TW_1. The layers in these laminates all have different relative orientation, defined by the angle between the warp directions of the fabric plies and illustrated in Figure 5-1(a). The relative orientations are 0, 15, 30 and 45°. Finally the stacking is preconsolidated with a pressure of 0.5 bar at temperature of 180°C.

5.2.1.2. Forming

The preconsolidated laminate is deformed using a non-isothermal deepdrawing process. During this process the wrinkles that occur inside the formed hemisphere during draping stay clearly visible for inspection, since the female die is an open ring. After heating the material to the desired temperature, it is formed using a rigid hemispherical shaped male mould with a diameter of 95.1 mm. Figure 5-1(b) shows a scheme of the forming stage. The die consists of an open ring with a diameter of 100 mm and is rounded at the edge to a radius of 12.5 mm. A mould heating machine heats the male punch to 85°C, the die and blankholder are not heated.

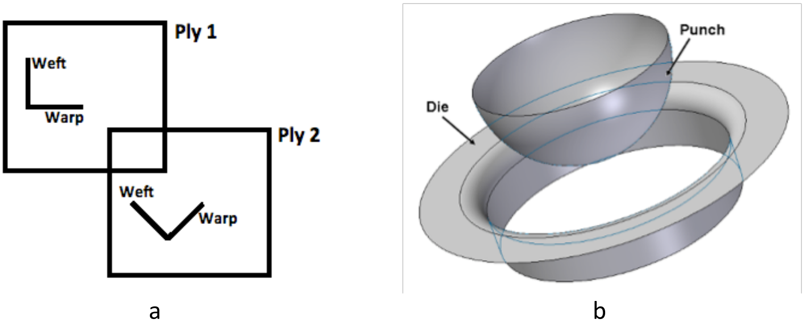

Figure 5-1. Deepdrawing of multilayered composites showing (a) the lay-up of two plies that form the multilayered laminate and (b) the set-up of forming stage

5.2.2. Results and discussion

Figure 5-2(a) and (c) show that forming a laminate with a 0° relative orientation occurs without any wrinkling. Increasing the relative orientation gives rise to severe wrinkling. This can be observed in Figure 5-2(b) and (d) where heavy wrinkling in the formed hemispherical laminate with a 45° relative orientation of the plies is noticed. These observations are in accordance with the studies performed by Lamers [103] and Promodou [52].

From these observations it can be stated that the formability of multilayered woven composites heavily depends on the orientation of the plies inside the laminate.

5.2.3. Kinematic draping

In order to gain a better understanding of the origin of this severe wrinkling in 2-layered fabric composites, the difference in local deformation between two neighbouring plies is investigated. In Chapter 4 it has been shown that kinematic draping provides a good prediction of the yarn orientations after draping for a hemispherical shaped mould.

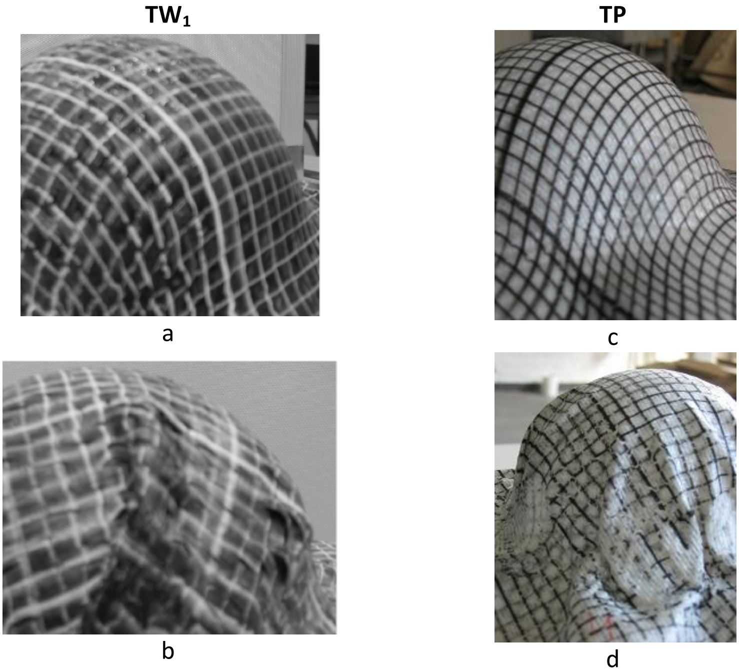

Figure 5-2. Formed two-layered stacking of (a) TW$_1$ with a relative orientation of 0°, (b) TW$_1$ with a relative orientation of 45°, (c) TP with a relative orientation of 0° and (d) TP with a relative orientation of 45°

5.2.3.1. Method

Kinematic draping is limited to single layers since no boundary conditions are taken into account. Therefore, only one layer is draped on the hemispherical surface using the apex as the impact point. Different initial fibre directions are taken, the fabric is rotated 15, 30 and 45°, corresponding to the different orientations used in the experimental forming. Figure 5-3 shows the kinematic draping solutions for a 0 and 45° initial fibre direction. The areas with a high amount of intra-ply shear are indicated with a red colour.

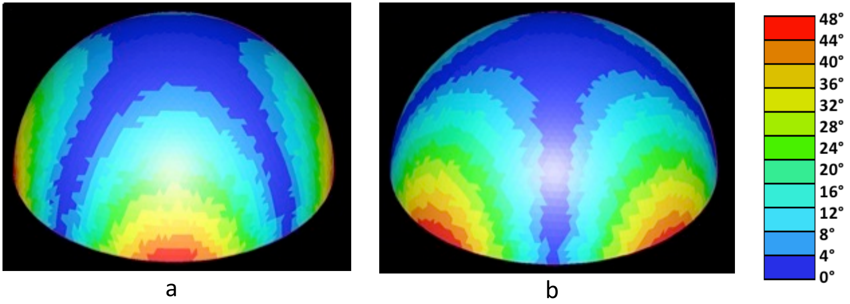

Figure 5-3. Kinematic draping solution for a hemispherical mould with a fabric orientation of (a) 0° and (b) 45°

From the kinematic draping solution the geodetic coordinates, which agree with the material frame of each node of the fabric are determined. Figure 5-4 illustrates the used procedure.

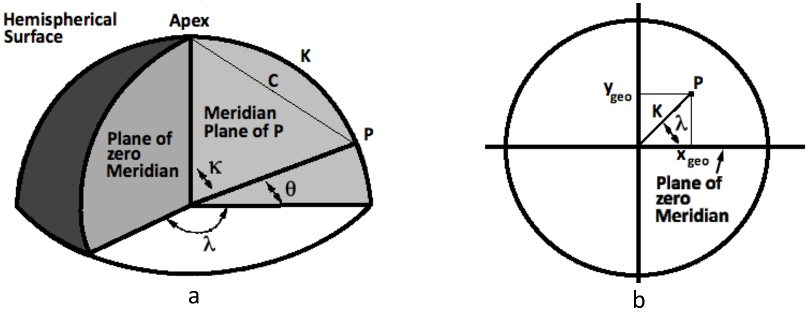

Figure 5-4. The geodetic coordinate system on a hemisphere with (a) a cross-section and (b) a top view

Point P(x_p,y_p,z_p) is a known node point calculated via the kinematic draping algorithm. In the geodetic coordinate system the apex is taken as the origin. First the latitude θ of p is calculated. The latitude allows calculation of the distance K along the hemispherical surface from the apex, with coordinates x_{Apex}, y_{Apex} and z_{Apex}, to point P by knowing the radius R of the hemisphere:

$$C = \sqrt{\left(x_p - x_{Apex}\right)^2 + \left(y_p - y_{Apex}\right)^2 + \left(z_p - z_{Apex}\right)^2} \qquad \textbf{Eq. 5-1}$$

$$\kappa = 90° - \theta = a\cos\left(\frac{C^2 - 2\cdot R^2}{-2\cdot R^2}\right) \qquad \textbf{Eq. 5-2}$$

$$K = \kappa \cdot R \qquad \textbf{Eq. 5-3}$$

Afterwards, the longitude λ and the coordinates of P, x_{geo} and y_{geo}, (see Figure 5-4(b)) in the geodetic system are calculated using following equations:

$$\lambda = a\tan\left(\frac{x_p - x_{Apex}}{y_p - y_{Apex}}\right) \qquad \textbf{Eq. 5-4}$$

$$x_{geo} = K \cdot \cos(\lambda) \qquad \textbf{Eq. 5-5}$$

$$y_{geo} = K \cdot \sin(\lambda) \qquad \textbf{Eq. 5-6}$$

The amount of displacement each node undergoes is easily calculated since the fabric initially consists of a square grid with constant grid size, where the apex point coincides with the origin of the fabric fishnet. The displacement is associated with the local amount of inter-ply shear the fabric experiences.

$$D_{f,i} = \sqrt{\left(x_{geo,i} - x_{f,i}\right)^2 + \left(y_{geo,i} - y_{f,i}\right)^2} \qquad \textbf{Eq. 5-7}$$

Where, $D_{f,i}$ is the displacement of node i that has the coordinates $x_{f,i}$ and $y_{f,i}$ in the discrete model of the flat non-draped fabric. Figure 5-5 shows the values of D_f for a fabric with 0° and 45° orientation. Since kinematic draping only accounts for intra-ply shear, high values of D_f indicate those zones where a lot of intra-ply shear occurs.

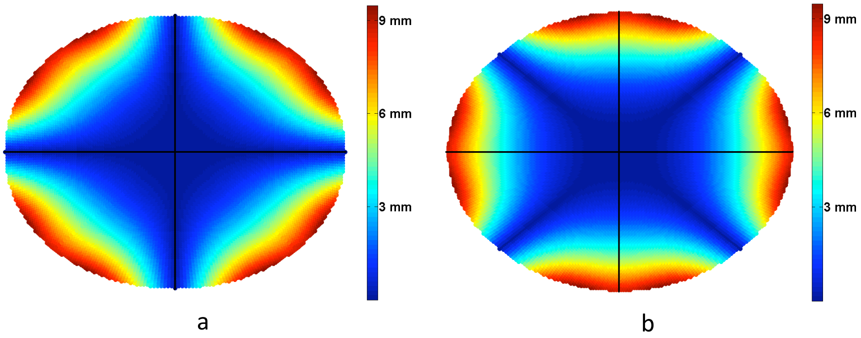

Figure 5-5. Local displacement profile for a fabric draped onto a hemispherical mould with (a) a 0° and (b) a 45° orientation with the apex as initial contact point.

5.2.4. Results and discussion

The difference in local displacement between the nodes of two layers, $\Delta D_{f,i}$,is calculated for a 0, 15, 30 and 45° relative orientation and normalized by dividing it by the radius, R, of the punch (47.55 mm):

$$D_{N,i} = \frac{\Delta D_{f,i}}{R} \qquad \textbf{Eq. 5-8}$$

The difference in local displacement is a measure for the amount of local inter-ply slip that needs to occur during forming. Figure 5-6 compares the profile of the normalized local difference in displacement with the formed laminate. In Figure 5-6(a), it is noticed that for a 0° relative orientation, the local deformation difference between the neighbouring plies is almost zero. This is due to the fact that the zones where the major deformation, i.e. intra-ply shear, occurs lie exactly on top of each other. The small values at the edge of the hemisphere are due to numerical errors in the calculations. For this relative orientation, no wrinkling occurs. For a 15° relative orientation, in Figure 5-6(b), the difference in local displacement is much more pronounced and goes up to 0.09, which in case of a punch with a radius of 47.55 mm, means that the maximum difference in local displacement is 4.28 mm.

Increasing the relative orientation difference increases the difference in local displacement. From Figure 5-6(c) and (d) it can be seen that for a 30° difference in orientation the maximum value is 0.13 and for a 45° relative orientation it goes up to 0.15. This increase is associated with more severe wrinkling during forming. It is noticed that wrinkling happens at those places where most intra- and inter-ply shear need to take place. This shows that both draping mechanisms are necessary to form a wrinkle free product.

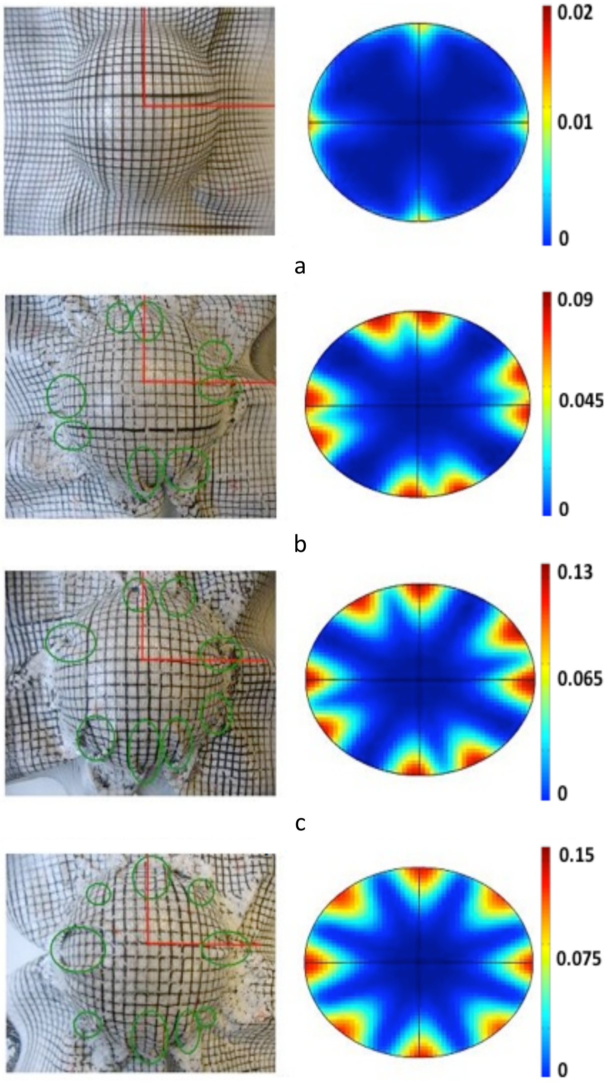

a

b

c

d

Figure 5-6. Comparison between the normalized local difference in displacement, $D_{N,i}$, and the formed laminate for (a) 0°, (b) 15°, (c) 30° and (d) 45° relative orientation.

5.3. Forming limit diagram for two-layered woven thermoplastic composites

Prior to forming a grid is painted on the top and bottom ply of the laminate in order to determine the amount of shear. The maximum amount of local shear is determined by using the method described in section 3.2 and by taking the maximum value obtained from these measurements.
The shear is only determined in those areas where no wrinkling is found. In all cases, the highest shear angles are found close to the start point of a wrinkle as can be seen in Figure 5-2(b) and (d). It seems intra-ply shear is prevented, consequently the flat fabric laminate will adapt to the mould by wrinkling. The reason wrinkling is so pronounced lies in the high friction coefficient and the low resistance of the fabric to buckling. Figure 5-7 shows for a 45° relative orientation that intra-ply shear invokes compressive forces in the stiff, undeformable yarn directions of the adjacent ply due to friction between the plies. If these compressive stresses exceed a critical limit, which is typically very low for fabrics, they induce wrinkling of the laminate.

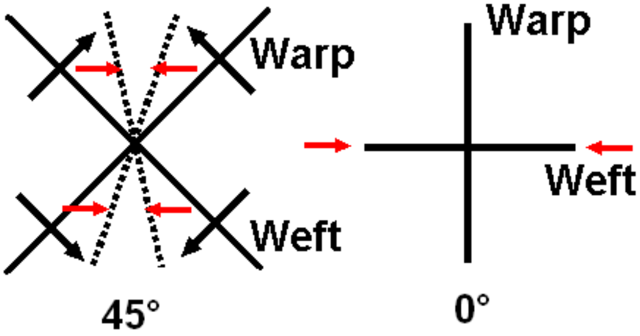

Figure 5-7. For two neighbouring plies with a relative orientation of 45° intra-ply shear in one ply invokes compressive stress in the neighbouring ply due to traction.

For the draping of a hemisphere, increasing the relative orientation between the plies from 0 to 45° increases the distances between the highly deformable zones, i.e. those regions where intra-ply shear occurs, of each ply. Thus each ply needs to deform in different regions to adapt to the hemisphere; hence locally inter-ply slip is needed to allow this relative displacement of the neighbouring plies in order to avoid wrinkling. The inter-ply slip contact between the plies will be investigated in Chapter 6.

Figure 5-8(a) visualizes the maximum shear angle measured on a formed hemisphere for different relative orientations. It is noticed that the maximum shear angle rapidly decreases as the orientation between the neighbouring plies increases. This can be interpreted as a forming limit diagram for a two-layered stacking. Figure 5-8(b) shows the relation between the maximum amount of intra-ply shear, which represents the “complexity” of the mould, and the difference in relative orientation, which represents the “complexity” of the material, of the laminate at the onset of wrinkling. The dotted line forms the forming limit curve, whenever this curve is exceeded the amount of intra-ply shear needed to form the laminate to the desired shape is too high and wrinkling will occur. For a 0° relative orientation no wrinkles are observed, therefore the highest measured shear angle is used in Figure 5-8, though for this orientation the forming limit curve may lie higher.

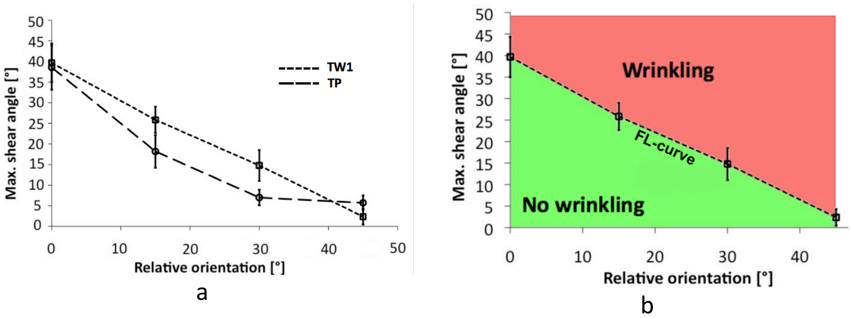

a

b

Figure 5-8. (a) Plot of the maximum shear angle vs. the relative orientation between the plies of the laminate and (b) corresponding Forming Limit Diagram for TW_1.

Whenever a laminate, consisting of neighbouring layers that have a high relative orientation, needs to adapt to a shape that requires a lot of intra-ply shear, the risk for wrinkling is high. For example, if a laminate consisting of two layers of TP-material with a relative orientation of 30°, needs to undergo more than 18° of shear to adapt to the mould, wrinkling will occur. This shows that the forming of woven thermoplastic composites is limited to, either a simple laminate configuration, i.e. the relative orientation between the plies is small and the amount of inter-ply shear is modest, or simple product shapes, i.e. shapes that can be draped with a limited amount of intra-ply shear. These considerations drastically limit the application of this type of material.

5.4. Forming of multilayered woven thermoplastic composites

To check whether the observation made in the previous section also occur with thicker laminates, the forming of a hemisphere is repeated for the two different stackings of TP indicated in Table 5-1.

Table 5-1. Stacking sequence of the multilayered composites

Stacking ID	Stacking sequence
QI	$[0,+45,-45,90]_s$
OT	$[0_2]_s$

Both stacking are symmetrical, the difference lies within the relative orientation between the neighbouring plies. For a quasi-isotropic, QI, 8-layered stacking the maximum relative orientation between adjacent plies is 45°. In the orthotropic laminate all 4 plies are oriented in the same direction and thus the maximum relative orientation is 0°.

Figure 5-9 shows the deepdrawn hemispheres. It is clear from this figure that the QI-composite is subjected to heavy wrinkling, while the OT-composite only shows some minor wrinkles at the edge of the hemisphere. This result is in accordance with the observations made in the previous section. A high relative orientation between the plies results in more severe wrinkling.

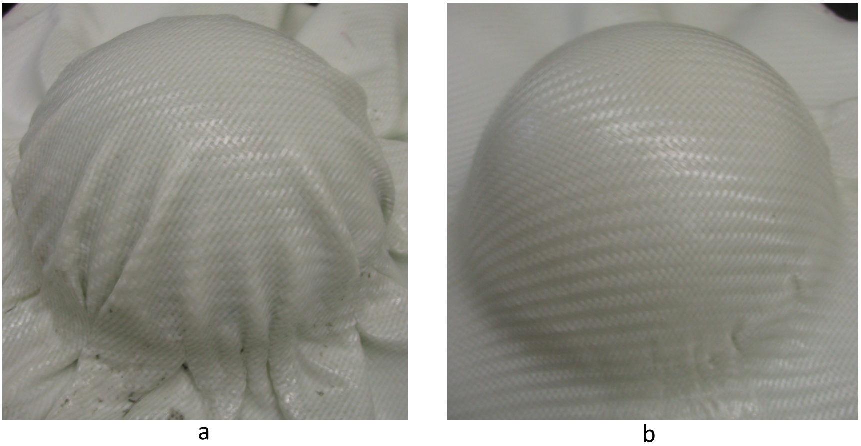

Figure 5-9. Multilayered deepdrawn fabric composite with (a) a quasi-isotropic stacking sequence and (b) an orthotropic stacking sequence

5.5. Intermediate conclusions

The formability of two-layered thermoplastic reinforced fabric laminates with different fibre orientations has been investigated. A forming limit diagram visualizes the formability of multilayered fabric laminates. A decrease in formability is characterized by a decrease in local shear and an increase in wrinkling of the laminates. It is found that the amount of wrinkling strongly depends on the fabric lay-up inside the laminate. Increasing the orientation between the yarns of the different plies decreases the formability. The shear motion develops local compressive stresses in the neighbouring ply. Due to low deformability of the neighbouring ply in the area where the compressive stresses are invoked, wrinkling occurs. When the relative orientation increases, the region of the neighbouring ply where compression takes place becomes less deformable and thus wrinkling is more severe.

5.6. Screening of the influence of the process conditions on the formability of multilayered fabric composites

Since, QI-stackings are commonly of use in the industry. An important question that now can be raised is: “How can the formability of multilayered woven composites be increased, despite a more complex lay-up sequence?” Therefore, this section deals with investigating the influence of the process conditions on the shape distortions. In addition, the influence of the interlayer thickness between the plies is also assessed.

This section is divided into 2 main parts. First the experimental methodology used to assess the influence of the process parameters on the formability will be introduced and afterwards the results will be discussed.

5.7. Experimental methods

5.7.1. Preconsolidation

Prior to forming, a two-layered stacking of the fabric TW_2 is preconsolidated using a hot press. The layers in this laminate have a relative orientation difference, defined by the angle between the warp directions of the fabric plies, of 45°, making it a quasi-isotropic, but not symmetric laminate. Extra interlayer material, introduced in section 3.1.3, is pressed between the layers when needed for the experimental design. Finally the stacking is preconsolidated with a pressure of 0.5 bar at temperature of 180°C. The forming takes place with the same set-up as discussed above, but a continuous steel blankholder is added.

5.7.2. Temperature measurements

As discussed in section 3.6, forming the hemispherical shape takes place under non-isothermal conditions. Different studies have shown that the temperature of the laminate during forming is a critical parameter in order to obtain fully formed and defect-free products [49, 101].

To obtain better knowledge of the temperature of the laminate during forming, the temperature is measured on three different locations. Three thermocouples are placed in between a double layered stacking with a 0° relative orientation, so wrinkling would not influence the measurements, prior to preconsolidation in the hot press. Thermocouple A is placed at the apex of the hemisphere, where the first contact between the punch and the laminate occurs. Thermocouple B lies between the apex and the edge of the deepdrawn shape. Thermocouple C is positioned at the edge of the hemisphere. The layers in this laminate have no relative orientation difference in order to avoid severe shape distortions during forming.

Table 5-2. Different process conditions used during the measurement of the temperature of the laminate with the temperature interval and cooling rate during forming

Measurement ID	1	2	3	4
Preheat temperature [°]	220	170	220	170
Velocity [mm/s]	100	10	100	100
Punch temperature [°]	20	20	120	20
Forming temperature interval [°C]	214-191	148-100	214-199	165-152
Cooling rate [°C/s]	28.75	8.73	15.5	17.33

Table 5-2 summarizes the different process conditions for which the temperature course of the laminate during forming is investigated.

The forming temperature interval during forming is determined by the initial and final temperature at A and is, together with the cooling rate at point A, discussed in detail in a subsequent paragraph. The influences of the blankholder pressure and interlayer thickness are not considered. Figure 5-10 shows a typical temperature profile during deepdrawing.

After the desired pre-heating temperature is reached, the laminate is transported towards the forming station. During this transport cooling takes place due to convection. During the heating cycle, the male mould is placed at a position that is 50 mm higher then the die, which explains the time lag between the start of the punch movement and the beginning of the forming. Before the punch comes into contact with the laminate the temperature has dropped between 5 to 10°C for all experiments. When the punch comes into contact with the laminate the temperature drop is more severe due to conduction of heat towards the colder punch. Obviously the region where contact between the punch and the laminate first occurs, near point A, is cooled down the fastest. The temperatures of point A at the beginning and at the end of the forming step indicate the temperature interval over which the forming takes place. The steep drop in temperature at point C at the beginning of the forming step is due to contact with the cold female die. When forming takes place this zone is drawn-in and loses contact with the die. The temperature keeps decreasing after the forming step has finished since it stays in contact with the punch until the formed laminate is dimensionally stable and can be demoulded.

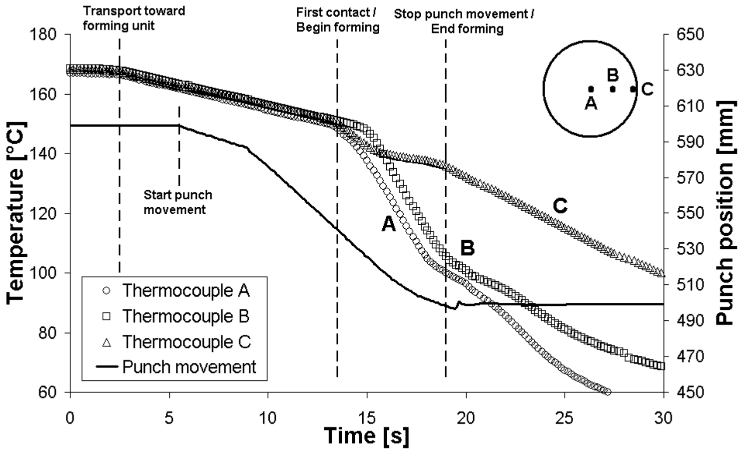

Figure 5-10. Temperature profile of the heated laminate during forming

In Table 5-2 the forming temperature interval during forming, which is determined by the initial and final temperature in A, and the cooling rate in point A are presented. The following trends are seen:

- *Influence of the preheat temperature (measurement 1 vs. 4):* a high preheat temperature leads to an increase in forming temperature, which is beneficial for forming of the laminate. Though, the cooling rate during forming is higher due to a higher driving force for heat transfer. A drawback of a higher preheat temperature is an increase in the total cycle time.
- *Influence of the punch temperature (measurement 1 vs. 3):* at a high punch temperature, slower cooling of the laminate is observed due to a lower difference in temperature between the punch and the laminate.
- *Influence of the punch velocity (measurement 2 vs. 4):* It takes longer to form the laminate, thus the total cooling is higher for a slower forming velocity, resulting in lower laminate temperatures. The cooling rate for a slower forming velocity is lower. More time is needed for the punch to make contact with the laminate when the punch velocity is lower. This causes the laminate to be cooled down more due to convection before the forming starts. Thus the driving force for heat conduction is lower, resulting in a lower cooling rate.

Overall it can be stated that the preheat temperature combined with the deepdrawing velocity determines the forming interval. The higher this temperature or velocity, the higher the temperature is during forming. The cooling rate is the largest when there is a big difference in temperature between the hot laminate and the mould

5.7.3. Process variables and design of experiments

The influence of preheat temperature, deepdrawing velocity, blankholder pressure, mould temperature and thickness of the interlayer on the shape distortions are investigated using the method of Design Of Experiments (DOF) [104]. A fractional factorial $2^{(5\text{-}1)}$ screening design with a central point and a resolution of V is developed. This means the main and second order effects are not confounded with other main effects nor with a second order effect. Second order effects form aliases with third order effects, though these interactions are neglected. A linear model describes the screening experiments:

$$y = \sum_{i=A}^{E} \beta_i \cdot \frac{x_i - \langle x_i \rangle}{\Delta x_i} + \sum_{\substack{i,j=A \\ i \neq j}}^{E} \beta_{ij} \cdot \frac{x_i - \langle x_i \rangle}{\Delta x_i} \cdot \frac{x_j - \langle x_j \rangle}{\Delta x_j} + I \qquad \textbf{Eq. 5-9}$$

Where y is the response value, x_N equals the level of factor n, $\langle x_N \rangle$ is the average value and Δx_N is the range of effect N used in the experimental design, β_i, β_{ij} and I are unknown coefficients fitted to the model. The unknown β-coefficients are estimated using the method of linear least squares. To determine the accuracy of the fitted model both the coefficient of determination (R^2) and the adjusted coefficient of determination (R^2_{adjusted}) are calculated. The R^2-coefficient indicates the proportion of variability in a data set that is accounted for by the statistical model and provides a measure for how well the model fits the experimental data. However, adding extra terms to the model will always increase the R^2-coefficient. Therefore also the R^2_{adjusted} is calculated, this coefficient takes into account the number of significant terms. Adding an extra term will only increase R^2_{adjusted}, if this term improves the model more than could be due to coincidence.

Table 5-3. High, low and intermediate levels of the process conditions used in DOE

Description	ID	Low level	Mid level	High level
Preheat temperature [°C]	A	170	195	220
Deepdrawing velocity [mm/s]	B	10	55	100
Blankholder pressure [bar]	C	0	2.5	5
Punch temperature [°C]	D	20	70	120
Thickness of PP-film [mm]	E	0	0.75	1.5

The Fisher test is used to determine whether a factor has a significant influence on the response, by comparing the variance of a factor to the variance in experimental error. The larger this ratio the more significant the influence of the factor on the response is. This value is then tested against the hypothesis that this ratio occurs due to experimental error. A probability value of one means the variance of the factor is completely due to experimental error. A probability limit of 0.05 is taken as the boundary between significant or not. This implies that a probability value below 0.05 indicates the response of the factor is not only due to experimental error, thus being significant. Since for each test only one repetition is made, the experimental error is determined by repeating the central point 4 times, i.e. test number 1,2, 18 and 20.

Table 5-4. Overview of the experimental design

ID Test #	A	B	C	D	E	ID Test #	A	B	C	D	E
1	195	55	2.5	70	0.75	**11**	220	100	0	20	1.5
2	195	55	2.5	70	0.75	**12**	220	100	5	120	1.5
3	220	10	0	120	1.5	**13**	220	10	5	120	0
4	170	10	0	20	1.5	**14**	220	100	5	20	0
5	220	10	5	20	1.5	**15**	170	100	0	120	1.5
6	170	10	5	120	1.5	**16**	170	100	5	120	0
7	170	100	0	20	0	**17**	220	100	0	120	0
8	170	10	0	120	0	**18**	195	55	2.5	70	0.75
9	170	100	5	20	1.5	**19**	220	10	0	20	0
10	170	10	5	20	0	**20**	195	55	2.5	70	0.75

The process values and the identifiers chosen for the different parameters are summarized in Table 5-3 and an overview of the experimental design is given in Table 5-4.

5.7.4. Determination of shape distortions

Ideally, when no shape distortions are present, the formed laminate can be described by a semi-spheroid. Wrinkling and springback however give rise to deviations from this spherical shape. To quantify the amount of distortion a 3D optical technique is used. It requires a random speckle pattern in order to determine the shape of an object. In this study an optical technique is used to obtain a detailed description of the formed laminate surface. Therefore, after forming a speckle pattern is sprayed upon the laminate and the surface is measured by using a 3D optical technique.

5.7.4.1. Springback

The effect of springback on the shape of the composite structure is flattening of the hemisphere, shown in Figure 5-11. This results in both a decreasing curvature as well as a diminishing height of the formed composite when more springback occurs. In this study, the height of the hemisphere is taken as the relevant parameter to determine the amount of springback. In order to accurately determine the height the contactless optical technique is used. First the data points of the inner surface that lay in the XZ and YZ-plane, measured via the 3D optical technique, are approximated by 1D-spline functions $\delta_x(x)$ and $\delta_y(y)$.

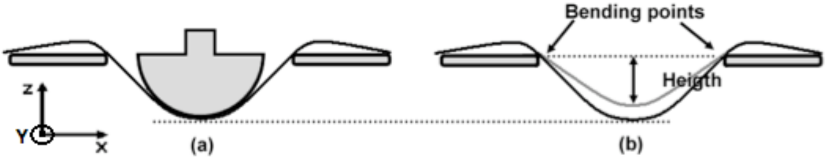

Figure 5-11. Change of the height of the formed shape due to springback: (a) Cross-section of the formed laminate at the end of the forming step and (b) Cross-section of the formed laminate after demoulding

The apex of the hemisphere forms a local minimum of both the spline functions. It is determined by calculating the coordinates for which the first derivative of the spline functions become zero. Through the apex, cross-sections for x = 0 and y = 0 are taken. The two bending points in these cross-sections, BP1 and BP2, are local extremities of the first derivative in x and y. The height h is calculated as the shortest distance between the apex and the line through the two bending points as shown in Figure 5-12. The average height taken from the two cross-sections forms the parameter that needs to be maximized.

When all samples are processed, the sample with the least amount of springback, thus with a maximal height (l_{max}), is taken as reference. The reason why the springback is not calculated with reference to the shape of the mould is due to the shape of the female mould used during forming. The open ring allows the laminate to behave more freely and thus the hemispherical shape of the punch is not fully obtained as can be seen in Figure 5-11(b). The percentage of springback in the other samples is calculated by using the following equation:

$$SB = \frac{l_{\max} - l}{l_{\max}} \qquad \textbf{Eq. 5-10}$$

Where *l* is the height of the formed cup. When SB = 0 this corresponds to the least measured springback ($l = l_{max}$) and SB = 100 equals full springback ($l = 0$ mm).

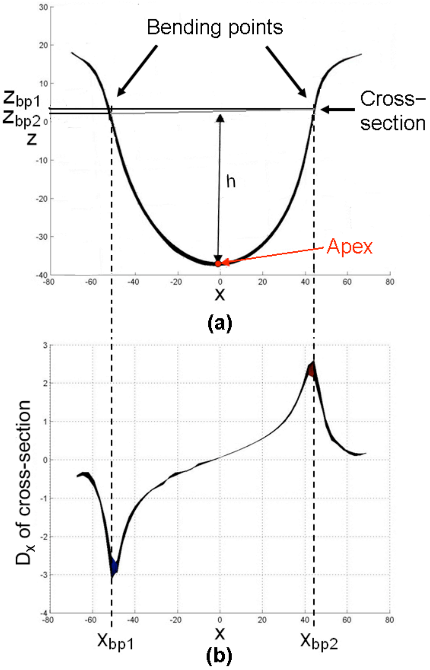

Figure 5-12. Measured cross-section of a formed laminate for (a) y=0 and (b) the derivative of this cross-section with respect to the x-coordinate

5.7.4.2. Wrinkling

Wrinkling occurs due to lateral compressive stresses that arise in the laminate. The effect of wrinkling on the shape of the composite structure is a local deviation of the ideal surface. For a hemisphere the absolute distance between the points on the surface and the ideal shape will be larger when more wrinkling occurs. Wrinkling is especially pronounced at the outer surface of the formed hemisphere. This is the surface that does not come in contact with the punch.

When measuring the wrinkling, it is not possible to capture this outer surface in one image. The formed shape is divided into 4 equal slices and each of these slices are individually processed. The edges of a slice are prone to small errors, therefore, the hemisphere is divided in quadrants using two different methods 1 and 2 as indicated in Figure 5-13(a).

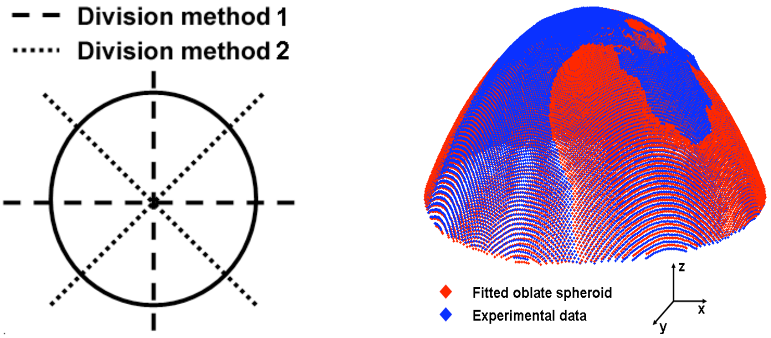

a b

Figure 5-13. (a) Division method of the hemisphere to determine the amount of wrinkling and (b) comparison between a fitted oblate spheroid and experimentally measured data

This method of dividing into different slices leads to minimal loss of information since the central region of one slice forms the borders of another slice. Wrinkling that occurs outside the formed shape, is not taken into account as this part of the form is usually trimmed off in postproduction. After each slice is measured using the 3D optical technique, the points that lie within the height determined in the springback calculation are selected. Through these points an oblate spheroid, of which the main axis equals the main axis of the mould, is fitted. An oblate spheroid has the shape of an ellipse rotated about its minor axis (see Eq. 5-11). This kind of form takes into account the flattening effect due to springback.

$$\frac{(x-x_c)^2}{R_1^{\,2}}+\frac{(y-y_c)^2}{R_1^{\,2}}+\frac{(z-z_c)^2}{R_2^{\,2}}=1$$ **Eq. 5-11**

Where R_1 is the radius along x and y axes, R_2 is the radius along the z-axis and x_c, y_c and z_c are the coordinates of the centre of the spheroid. The radii and the coordinates of the centre are determined using the method of least squares. Figure 5-13(b) compares the date from fitted oblate spheroid (red dots) with experimentally obtained data (bleu dots). For each point on the surface of the hemisphere, the distance between the fitted spheroid and the hemisphere is determined. The average distance for each slice is then obtained by dividing the sum of the distances by the number of points n:

$$d_{avg,j}=\frac{1}{n}\cdot\sum_{i=1}^{n}\sqrt{\left(x_i-x_{e,i}\right)^2+\left(y_i-y_{e,i}\right)^2+\left(z_i-z_{e,i}\right)^2}$$ **Eq. 5-12**

Here, x_i, y_i and z_i are the coordinates for the experimentally measured point i.

$X_{e,i}$, $y_{e,i}$ and $z_{e,i}$ are the coordinates of the intersection point between the fitted oblate spheroid and the line going through the centre of the spheroid and point *i*. $D_{avg,j}$ is the average distance between the fitted spheroid and the hemisphere for slice *j*. The average distance for the complete shape is calculated by taking the average of the distances of the slices, the total number of slices being 8 as seen in Figure 5-13(a).

$$d_{avg} = \frac{1}{8} \cdot \sum_{j=1}^{8} d_{avg,j} \qquad \textbf{Eq. 5-13}$$

For the same amount of wrinkling the value of d_{avg} will lower, when springback is more pronounced. Normalizing the average distance with the height measured by springback eliminates this effect, thus the response of springback and wrinkling are considered independent of each other.

$$p_h = d_{avg} \cdot \frac{l_{\max}}{l} \qquad \textbf{Eq. 5-14}$$

Where p_h is the normalized distance, d_{avg} is the average measured distance, l_{max} is the maximal measured height and l is the measured height of the considered hemisphere. The normalized distance forms the response parameter for wrinkling.

5.8. Result and discussion

5.8.1. Springback

Table 5-5 summarizes the amount of springback for all experiments, 0% indicates the minimal measured springback and 100% equals full recovery.

Table 5-5. Measured amount of springback of the different experiments

Experiment ID	Springback [%]	Experiment ID	Springback [%]
1	11.18	**11**	4.93
2	7.15	**12**	4.71
3	7.78	**13**	15.82
4	8.34	**14**	14.47
5	9.37	**15**	7.26
6	15.94	**16**	0
7	14.22	**17**	11.00
8	12.09	**18**	9.69
9	7.15	**19**	7.52
10	32.75	**20**	10.32

A linear model, given by Eq. 5-9, is fitted through the data, after which the influence of the process parameters is assessed using statistical analysis. The fitting parameters of the model are summarized in Table 5-6. The fitted model has an R^2-value of 0.9828 and an $R^2_{adjusted}$ of 0.9184, which indicates it is capable of accurately describing the variations of the response.

Table 5-6. Fitting parameters for the linear model of the screening experiment for springback

Fitting parameter	Value	Fitting parameter	Value
β_A	-1.3844	$\beta_{B \cdot E}$	0.6944
$\beta_{A \cdot B}$	2.1944	β_C	1.6919
$\beta_{A \cdot C}$	-0.0494	$\beta_{C \cdot D}$	-1.8994
$\beta_{A \cdot D}$	1.8869	$\beta_{C \cdot E}$	-0.5844
$\beta_{A \cdot E}$	-0.1031	β_D	-1.5094
β_B	-2.8669	$\beta_{D \cdot E}$	2.2469
$\beta_{B \cdot C}$	-3.0769	β_E	-2.6494
$\beta_{B \cdot D}$	-0.7156	**I**	10.5845

The effects that have a significant influence on the springback are determined by using the Fisher test. The results are summarized in Table 5-7, the significant values [$P(>F_{effect}) < 0.05$] are underlined. All main effects and some interaction effects have a significant influence on the amount of springback.

Table 5-7. Probability values of the hypothesis test for springback

Effect	$P(>F_{effect})$ springback	Effect	$P(>F_{effect})$ springback
A	<u>0.0416</u>	**B · E**	0.2121
A · B	<u>0.0094</u>	**C**	<u>0.0225</u>
A · C	0.9211	**C · D**	<u>0.0154</u>
A · D	<u>0.0157</u>	**C · E**	0.2799
A · E	0.8364	**D**	<u>0.0321</u>
B	<u>0.0036</u>	**D · E**	<u>0.0086</u>
B · C	<u>0.0028</u>	**E**	<u>0.0048</u>
B · D	0.2010		

Figure 5-14 allows discussing the main and interaction effects of the different parameters on the springback. The plots can be interpreted as follows: the closer the two lines of each individual plot, the less influence the main effect has. If the lines are parallel to each other, no interaction between the depicted effects occurs. However, when one line has a positive slope and the other has a negative slope, the depicted effects interact with each other, for example the deepdrawing velocity and the blankholder pressure heavily interact.

The most significant effects are discussed below:

- *Preheat temperature:* springback is more pronounced at low preheat temperatures. When forming occurs at lower temperature, the formability is decreased since the matrix changes from a viscous fluid at high temperatures to more elastic solid at lower temperatures. The effect of preheat temperature is influenced by the deepdrawing velocity and the punch temperature. The higher the deepdrawing velocity and punch temperature, the less influence the preheat temperature has on the springback. Both a higher deepdrawing velocity and higher punch temperature have been shown to increase the forming temperature in the temperature measurements.
- *Deepdrawing velocity:* at lower deepdrawing velocities, the forming temperature is lower and thus the amount of springback increases. However, from Figure 5-14 it can be seen that the amount of springback as function of the deepdrawing velocity has a negligible slope at 220°C preheat temperature and 0 bar blankholder pressure. This implies that the effect of a high deepdrawing velocity on the amount of springback is reduced at high preheat temperatures and low blankholder pressures.

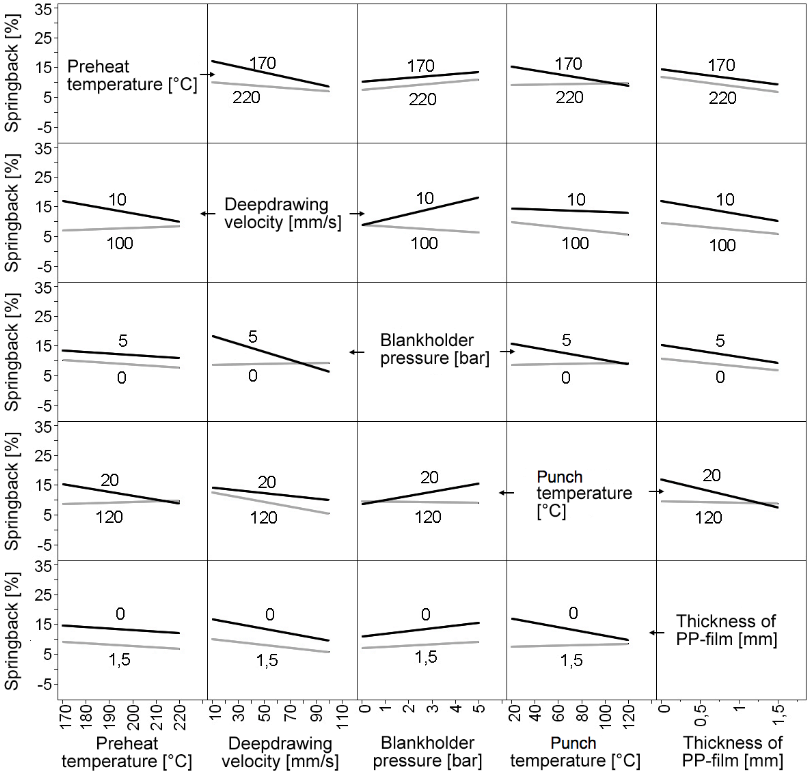

Figure 5-14. Influence of the main and second order effects on the springback of the formed laminate [82]

- *Blankholder pressure:* springback is more pronounced at higher blankholder pressures. The blankholder restrains the laminate during forming, which induces more elastic recovery after forming. This effect is especially pronounced at low deepdrawing velocities and lower mould temperatures and characterised by a steep slope.
- *Punch temperature:* a low punch temperature leads to a higher cooling velocity of the laminate and thus produces more springback. However, this effect is very small at high preheat temperatures, zero blankholder pressure and a thick interlayer.
- *Thickness of the PP-film:* increasing the interlayer thickness has a beneficial effect on the amount of springback. The influence of the interlayer thickness was not investigated during the temperature measurements. It is assumed that a thicker interlayer slows down the cooling, which is beneficial for the formability. Only at high mould temperatures this effect was less pronounced.

To end this section a ranking is shown in Table 5-8 to indicate the importance of each significant effect. This ranking is based on the probability values in Table 5-7. Especially the deepdrawing velocity is highly ranked, a high deepdrawing velocity results in less springback.

Table 5-8. Ranking of the significant effects that affect the amount of springback

Rank	Effect
1	Deepdrawing velocity – Blankholder pressure
2	Deepdrawing velocity
3	Thickness of PP-film
4	Punch temperature – Thickness of PP-film
5	Preheat temperature – Deepdrawing velocity
6	Blankholder pressure – Punch temperature
7	Preheat temperature – Punch temperature
8	Blankholder pressure
9	Punch temperature
10	Preheat temperature

5.8.2. Wrinkling

Table 5-9 summarizes the measured p_h-values. These values represent the average deviation of the measured shape and the oblate spheroid fitted through this shape, thus giving an indication on the amount of wrinkling.

Table 5-9. Measured amount of p_h of the different experiments

Experiment ID	p_h [mm]	Experiment ID	p_h [mm]
1	0.19	**11**	0.14
2	0.16	**12**	0.20
3	0.26	**13**	0.29
4	0.31	**14**	0.10
5	0.16	**15**	0.20
6	0.22	**16**	0.15
7	0.39	**17**	0.39
8	0.46	**18**	0.18
9	0.18	**19**	0.40
10	0.46	**20**	0.18

A linear model, given by Eq. 5-9, is fitted through the data, after which the influence of the process parameters is assessed using statistical analysis. The fitting parameters of the model are summarized in Table 5-10. The fitted model has an R^2-value of 0.8615 and an $R^2_{adjusted}$ of 0.3423. The relatively low R^2-value indicates the linear model is not capable of accurately describing the variations of the response. The large difference between R^2 and $R^2_{adjusted}$ suggests the model contains a lot of redundant terms.

Table 5-10. Fitting parameters for the linear model of the screening experiment for wrinkling

Fitting parameter	Value	Fitting parameter	Value
β_{A}	-0.0348	$\beta_{B \cdot E}$	0.0139
$\beta_{A \cdot B}$	0.0085	β_{C}	-0.0420
$\beta_{A \cdot C}$	-0.0127	$\beta_{C \cdot D}$	0.0015
$\beta_{A \cdot D}$	0.0335	$\beta_{C \cdot E}$	0.0233
$\beta_{A \cdot E}$	0.0160	β_{D}	0.0087
β_{B}	-0.0423	$\beta_{D \cdot E}$	0.0025
$\beta_{B \cdot C}$	-0.0047	β_{E}	-0.0687
$\beta_{B \cdot D}$	0.0231	**I**	0.2569

The effects that have a significant influence on the amount of wrinkling are determined by using the Fisher test. The results are summarized in Table 5-11, which shows that the only significant effect is the thickness of the interlayer, which explains the large difference between R^2 and $R^2_{adjusted}$. The $R^2_{adjusted}$ takes into account the number of significant terms. Adding an extra term will only increase $R^2_{adjusted}$, if this term improves the model more than could be due to coincidence. However, also the deepdrawing velocity and blankholder pressure have relatively low probability values compared to the other values.

Table 5-11. Probability values of the hypothesis test for wrinkling.

Effect	P(>Feffect) wrinkling	Effect	P(>Feffect) wrinkling
A	0.1948	**B · E**	0.5681
A · B	0.7241	**C**	0.1342
A · C	0.6006	**C · D**	0.9497
A · D	0.2092	**C · E**	0.3560
A · E	0.5150	**D**	0.7177
B	0.1318	**D · E**	0.9158
B · C	0.8428	**E**	<u>0.0373</u>
B · D	0.3599		

In Figure 5-15(a) a formed hemisphere with a small amount of wrinkling is shown, while Figure 5-15(b) shows heavy wrinkling for experiment number 8. The process conditions for these experiments are indicated in Table 5-4. The reason is the influence of the interlayer thickness on the friction coefficient between neighbouring layers. The friction between the plies during forming will be the subject of Chapter 6, it will be shown that an increase in interlayer thickness results in a lower friction coefficient. This assures a decrease in load transfer between the individual plies, they deform more independently of each other and thus wrinkling is reduced.

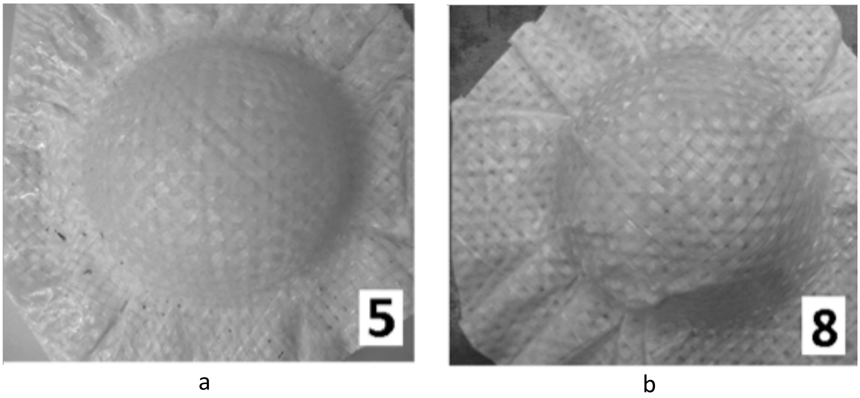

a b

Figure 5-15. Formed hemisphere from (a) experiment number 5 where wrinkling is low and (b) experiment number 8 where wrinkling is more pronounced

Although only the interlayer thickness has the most significant effect on the amount of wrinkling, the influences of the other effects are mentioned below and indicated in Figure 5-16. Especially, the deepdrawing velocity and the blankholder pressure still have a relatively low P-value.

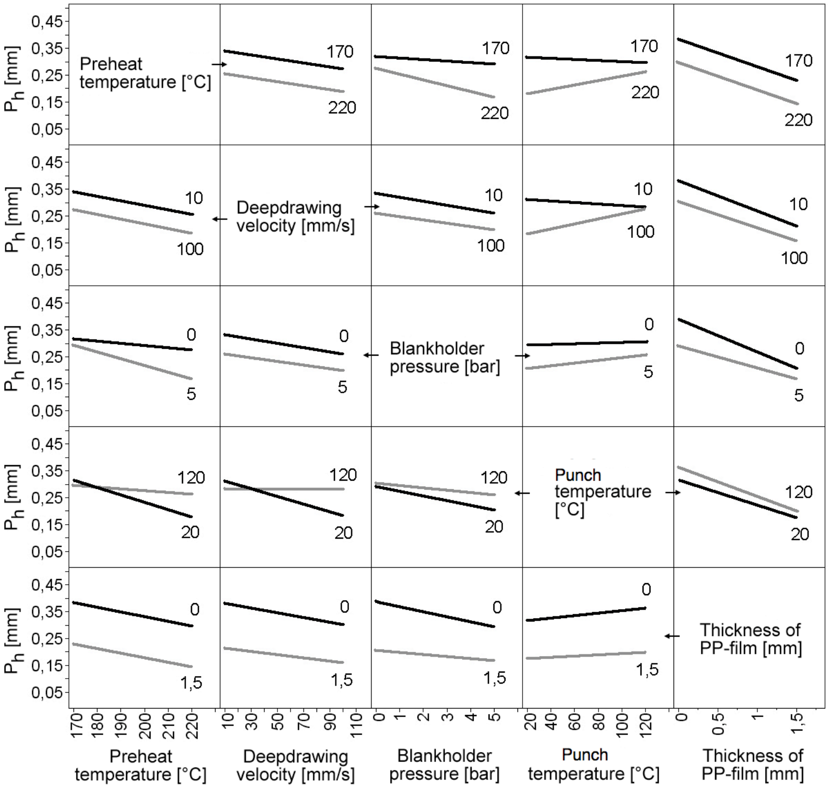

Figure 5-16. Influence of the main and second order effects on the amount of wrinkling in the formed laminate [82]

- *Preheat temperature:* wrinkling is more pronounced at low preheat temperatures. When forming occurs at lower temperature, the friction coefficient between the neighbouring plies increases. Compressive stresses are transferred more easily between the neighbouring plies and thus wrinkling occurs more easily. Increasing the mould temperature increases the forming temperature and thus reduces the effect of the preheat temperature.
- *Deepdrawing velocity:* at lower deepdrawing velocities, the forming temperature is lower and thus the amount of wrinkling increases. However, at high mould temperatures the influence of the deepdrawing velocity is less pronounced due to a decrease in cooling velocity of the laminate.
- *Blankholder pressure:* less wrinkling occurs at high blankholder pressures. The blankholder invokes tensile stresses in the laminate during forming. These tensile stresses compensate the compressive stresses that occur during forming and thus wrinkling is reduced.
- *Punch temperature:* although the friction coefficient is lower at higher

temperatures, a high mould temperature generally leads to more wrinkling. However, the wrinkling difference between a high and low punch temperature is not so pronounced.

5.9. Intermediate conclusions

The part quality of multilayered fabric composites is determined during the forming step. The laminate may wrinkle, which introduces defects in the part, and after forming springback may occur, whereby the part tends to return to its original shape.

The deepdrawing process is non-isothermal, thus forming does not take place exactly at the preheat temperature. It was found that the preheat temperature and the forming velocity determine the forming interval. The lowest forming temperature occurs at a low deepdrawing velocity, a low preheat temperature and a low mould temperature. While, a high preheat temperature, a low mould temperature and a low deepdrawing velocity give rise to the highest cooling rate.

An experimental screening design is developed to determine the influence of different process parameters on the amount of wrinkling and springback in a laminate of which the woven layers have a 45° difference in orientation. A method is proposed for the evaluation of the amount of wrinkling and springback in deepdrawn composites. Both wrinkling and springback are measured using a 3D optical technique, allowing for an objective analysis of the formed products.

Springback is found to be influenced by all process parameters. A minimum amount of springback is obtained by choosing a high preheating temperature, a high deepdrawing velocity, a low blankholder pressure, a high mould temperature and a thick interlayer. At these process conditions the temperature of the laminate during forming will be the highest and the elastic behaviour of the laminate will be low.

For wrinkling only one significant parameter is found, the thickness of the interlayer. The thicker the interlayer the less wrinkling occurs. This is due to the fact the friction coefficient between neighbouring plies diminishes, which shows the importance of the contact behaviour between fabric plies during forming. Each ply can deform more independently, the intra-ply slip does not restrict the inter-ply shear of neighbouring plies and thus wrinkling is reduced.

5.10. Influence of the interlayer thickness on the forming limit diagram – an alternative method to create complex products

In the previous section it is shown that an increase of the interlayer thickness decreases the amount of wrinkling. In Figure 5-17(a) and (b) the effect of an increase in interlayer thickness on formed specimens of TP-material with a relative orientation of 45° are depicted. The amount of wrinkling visually decreases when the interlayer between the plies of the laminate is increased from almost 0 mm to 0.6 mm. It can be seen from Figure 5-18 that for the same relative orientation more inter-ply shear occurs prior to wrinkling. The forming limit line moves to higher shear angles for the same relative orientation. This confirms the previous statement that the plies behave more independently with increasing interlayer thickness.

Figure 5-17. Deepdrawed specimens of laminates with a 45° relative orientation with (a) no extra interlayer and (b) an extra interlayer of 0.6 mm

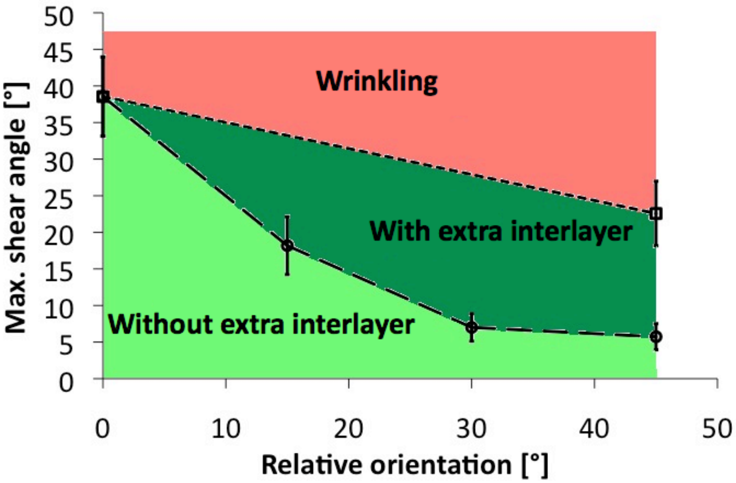

Figure 5-18. The increase of the maximum shear angle when using an extra interlayer visualised in a FLD.

From these observations, it is clear that the formability and thus the applicability of woven reinforced thermoplastic materials can be highly increased by adding extra matrix material between the plies. However, increasing the formability by adding extra matrix decreases the fibre volume fraction, and thus also the mechanical properties, of the composite. For the material used in the experimental screening the theoretical fibre volume fraction falls from 35% for 0 mm interlayer thickness, to 14% for a 1.5 mm interlayer.

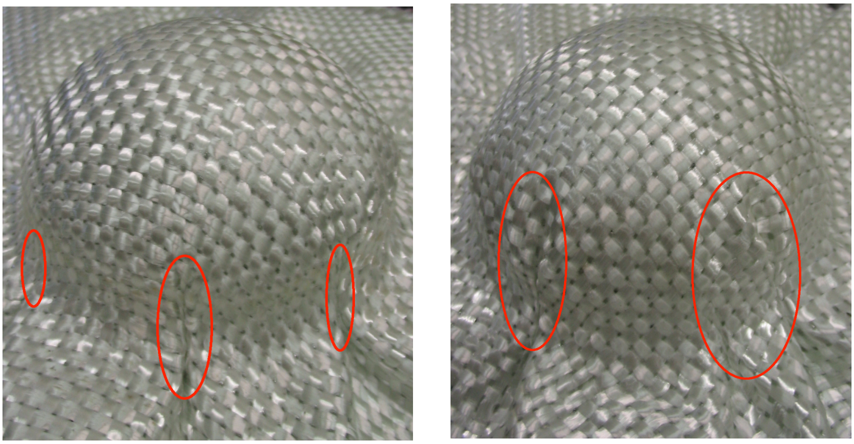

Figure 5-19. Formed hemispheres with the same fibre volume fraction using (a) a thick interlayer between the plies and (b) pre-impregnated plies.

To overcome this problem an alternative method to create complex products is tested. Instead of using pre-impregnated materials, like the ones in this study, a stacking of two layers of dry plain weave glass fibre fabric, with an areal weight of 850 g/m^2 is combined with a PP$_{int}$ sheet of 0,6 mm thickness, which results in a fibre volume fraction of 30%. This sheet is pressed at a low pressure of 0.5 bar between the fabric layers so it does not impregnate. After forming only a limited amount of wrinkling is noticed as indicated in Figure 5-19(a). This experiment is repeated, but now the fabric layers are pre-impregnated with the PP$_{int}$ before the stacking is made. Figure 5-19(b) shows that wrinkling is found to be more pronounced. This shows that using low-pressure film stacking and concentrating the matrix before forming between adjacent plies increases the formability. A drawback, however, is linked to the impregnation/consolidation quality of the final product. During the final phase of product forming, the matrix flows within the reinforcement to ensure the fibres are surrounded with polymer and the air bubbles are removed. In the material with a thick interlayer, the distance over which the matrix needs to flow is fairly large, this needs to be compensated by or a higher pressure during forming or a longer holding time in the mould. Moreover, it is difficult to have a high pressure at all locations of the mould. Both solutions are translated in a higher production cost. Nevertheless, the applicability of multilayered woven thermoplastic composites is increased.

5.11. Conclusions

This chapter discussed the formability of multilayered woven thermoplastic composites. The first section indicates that the lay-up configuration is found to be an important factor that influences the forming of the flat laminate. An increase in orientation between the layers increases the occurrence of wrinkling. This forms an important constraint in the application of woven thermoplastic composites. In general, a high quality of complex products of this type of material can only be achieved if the neighbouring reinforcements across the thickness of the laminate are oriented in the same direction, i.e. a low relative orientation, or if there is only one layer to be formed. Increasing the interlayer thickness between the layers of the laminate increases the formability and thus the quality of the final product. Moreover, it allows more flexibility when choosing the orientations of the reinforcements in the laminate and thus more freedom in designing the product.

Chapter 6

Inter-ply and tool-ply slip characterization

6.1. Introduction

From the previous chapter the importance of the inter-ply slip deformation mechanism is obvious. If inter-ply slip does not occur and thereby prevents intra-ply shear, unwanted deformation mechanisms such as wrinkling occur. The aim of this chapter is to gain a better understanding of the influence of the process parameters on the contact behaviour between thermoplastic composite layers and between the tooling and the composite during draping. Therefore, an experimental method to capture the resistance to slip has been developed. This method will also be used to characterize the tool-ply and ply-ply slip behaviour. Afterwards, different descriptive models, presented in section 6.7, are compared and an alternative model will be introduced.

6.2. Experimental method

Friction characterization between the different layers of a composite laminate and between the laminate and the tooling has been introduced in section 1.5. From the literature review it is clear that mostly the pull-out method is used to characterize the contact properties at processing conditions. An alternative forms the pull-through method, though for this the whole test setup needs to be placed inside an oven. Therefore, the experimental method that is developed during this research is also based on the pull-out method.

In this section the pull-out apparatus will be introduced and the different machine parameters will be verified. Afterwards, the experimental procedure for measuring the inter-ply and tool-ply slip behaviour is explained.

6.3. Pull-out apparatus

Figure 6-1 presents the set-up of the pull-out machine. It consists out of two vertically placed steel plates of 200 by 200mm, which are mounted on a frame. The dimensions of this frame are chosen so that it can be fitted onto an Instron tensile testing machine. One of the steel plates is rigidly attached, while the second steel plate is attached to a pneumatic cylinder of the type UNIVER RS 400. This cylinder allows translating the plate in the horizontal direction and allows for applying pressure on the samples during testing.

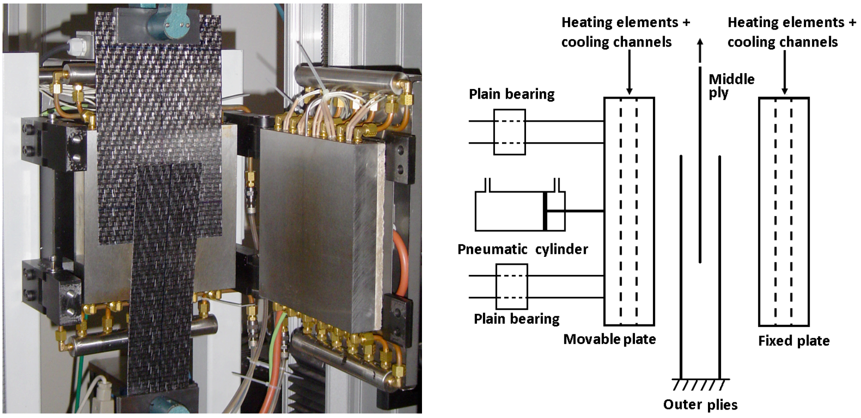

a b

Figure 6-1. The pull-out apparatus (a) mounted on a tensile testing machine and (b) a schematic overview

Each plate is also equipped with three 500W-heating elements and water cooling channels, which are operated by a PID (proportional-integral-derivative) controller. The homogeneity and the magnitude of the pressure and the temperature field are verified in the next sections.

6.3.1. Pressure distribution and magnitude

Prior to testing, a certain amount of pressure is placed on the cylinder that controls the movement of the steel plate. Such a cylinder consists of a piston that can stroke in- and outwards. By knowing the area, A_p, on which the pressure P_p takes place, it is possible to calculate the force F_p that the piston exerts on the steel plate.

$$F_p = P_p \cdot A_P \qquad \textbf{Eq. 6-1}$$

However, this theoretical value does not take into account the internal losses due to sliding of the steel plate over the gliding elements.

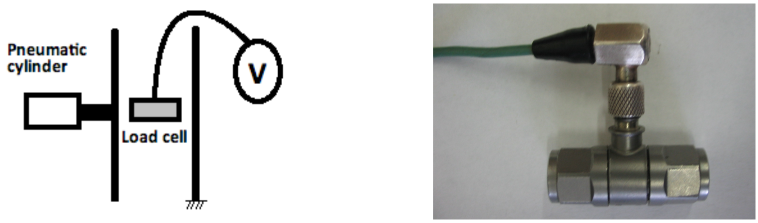

a b

Figure 6-2. The method for determining the force exerted by the pneumatic cylinder is (a) schematically represented and uses (b) a small 3 kN load cell that measures the force.

Therefore, a small load cell is used to measure the force-pressure relationship. Figure 6-2 indicates the used procedure together with the small load cell that is used. This load cell is placed between the two steel plates prior to applying pressure on the cylinder. The voltage output of the load cell is proportional to the applied load. Figure 6-3 shows the obtained force-pressure relationship.

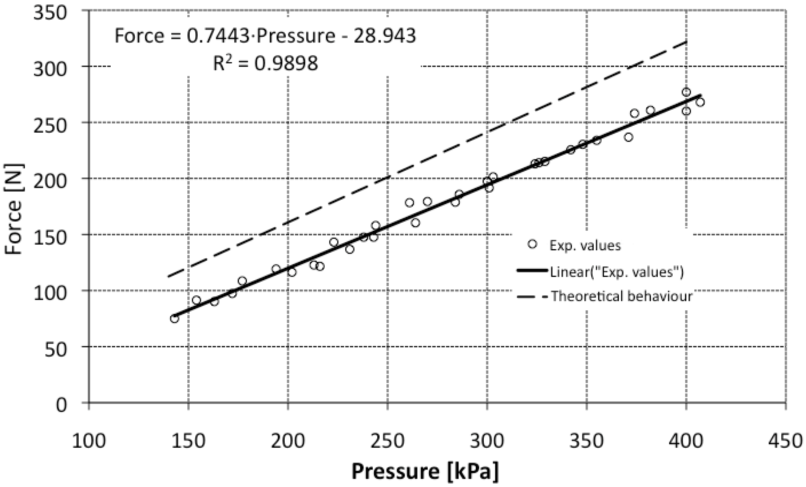

Figure 6-3. Force-pressure relationship of the pneumatic cylinder

The measured force values are lower than the theoretically predicted ones, calculated using Eq. 6-1, which can be explained by the friction that occurs during the sliding movement of the steel plate. Due to these frictional losses, it is noticed that the force only becomes positive at a pressure of about 38 kPa. The force-pressure relationship given in the following equation is used to calculate the normal force applied on the specimen during a pull-out test.

$$F_N = 0.744 \cdot P_p - 28.943 \qquad \textbf{Eq. 6-2}$$

Whereby the normal force F_N is calculated in N and the pressure P_p exerted on the pneumatic cylinder has units of kPa.

An second important parameter is the pressure homogeneity. It was shown by ten Thije et al. [38] that an inhomogeneous distribution of the pressure can lead to erroneous results, especially when determining the tool-ply contact behaviour. Therefore, in order to check whether the pressure field exerted by the steel plates is uniform, a Pressurex® pressure indicating film is used. Pressurex® is a mylar based film that contains a layer of tiny microcapsules. The application of force upon the film causes the microcapsules to rupture, which turns the colour of the film locally from white to black and thus producing an instantaneous and permanent "topographical" image of pressure variation across the contact area. Figure 6-4(a) indicates the obtained result by putting the indicating film between the two steel plates and applying pressure on the cylinder. The film is scanned in grey scale to obtain a picture of 400x400 pixels with a resolution of 200dpi, shown in Figure 6-4(a). The gray value of each pixel is associated with a certain pressure level. Unfortunately, the Pressurex® pressure film does not allow to determine exact pressure values. Therefore, the homogeneity of the gray values is calculated in MATLAB by using the binary representations of the pixel. A colour ratio is calculated whereby a pixel value 255 (=white) and is taken as 0, while a pixel value of 0 (=black) is taken as 1. This is linked to a pressure distribution where a colour ratio of 0 means no pressure is determined and a value of 1 is associated with a pressure higher than can be determined by the pressure film. The result is depicted in Figure 6-4(b). From Figure 6-4(b) the distribution of the colour ratio values is determined and shown in Figure 6-4(c). It can be seen that the homogeneity is rather poor, the colour ratio has a standard deviation of 0.03. However, in the centre part of the indicating film the pressure distribution is found to be fairly consistent with a standard deviation of 0.02. This will have its influence on the experimental procedure, which is clarified in section 6.3.3.

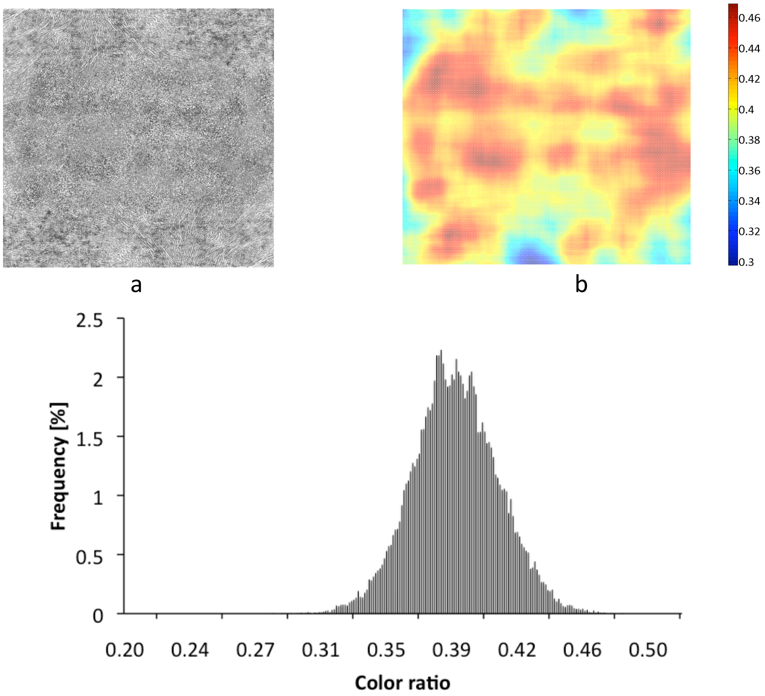

a

b

c

Figure 6-4. Pressure distribution of the pull-out apparatus with (a) the profile on the PressureEx film, (b) the distribution of the pressure and (c) the histogram of this distribution

An important issue regarding the pressure distribution is discussed in [105]. It is shown that during the pull-out test the pressure distribution changes. Since the Pressurex® pressure film cannot be used for a changing pressure distribution, this effect is not investigated for the developed pull-out apparatus.

6.3.2. Temperature homogeneity

Another machine parameter that needs to be justified is the temperature level and distribution. The temperatures serving as an input for the PID-controller are measured by two K-type thermocouples, which are placed in the center of each plate at a depth of 5 mm from the surface. The output of the controller gives a signal to the heating elements in the plates or to water-cooling valves if cooling is needed. In order to check whether the temperature between the steel plates equals the desired temperature and provides a homogeneous temperature distribution, a laminate consisting of two layers of TW_1-material is equipped with nine thermocouples between the layers.

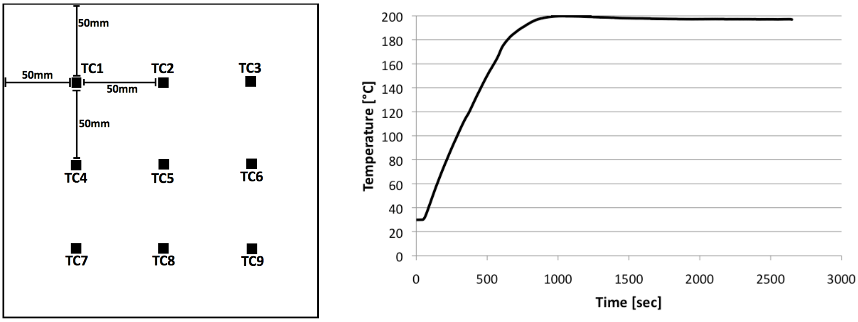

a b

Figure 6-5. Measurement of the temperature field with (a) schematic representation of the positions of the thermocouples and (b) heating profile for the pull-out set-up at 195°C at TC5

Figure 6-5(a) indicates the position of the nine thermocouples inside the laminate. The thermocouples are placed in a square configuration with a distance of 5 cm between two neighbouring thermocouples and with a 5 cm offset from the edge of the laminate. The position of the thermocouples in the steel plates that give the temperature feedback to the PID controller agrees with position TC5. Prior to activating the heating, the laminate is pressed between the steel plates with a normal force of 100N.

A typical temperature profile is shown in Figure 6-5(b). A small overshoot is noticed at about 15 minutes of heating. Afterwards, it takes about an extra 15 minutes before the desired temperature is reached.

Table 6-1 indicates the temperatures measured with three different set points, namely 180°C, 195°C and 210°C, after a heating time of 30 minutes. This discrete temperature field measurement indicates that the temperature field is relatively uniform, with an average standard deviation for the three different temperatures of 1.8°C. At the edges the temperature is consistently lower, which is probably due to convection that occurs at the edges of the steel plates.

Table 6-1. Temperatures obtained after 30 minutes of heating at the set point

Set point [°C]	TC1 [°C]	TC2 [°C]	TC3 [°C]	TC4 [°C]	TC5 [°C]	TC6 [°C]	TC7 [°C]	TC8 [°C]	TC9 [°C]
180	177,5	177,0	176,5	179,5	181,2	179,0	176,3	176,5	176,3
195	193,7	193,8	192,5	194,0	196,1	193,6	192,2	192,9	192,3
210	206,8	206,9	206,0	209,7	211,3	208,3	207,3	207,2	206,8

6.3.3. Experimental pull-out procedure

The basic idea of a pull-out test is to measure the resistance to pull material out from between two contacting materials. Prior to testing the pull-out machine is placed on an instron tensile machine, as shown in Figure 6-1(a). To determine the contact behaviour between two materials, 3 layers of material are needed. Two outer layers that are made from the same material are restricted from moving by clamping them in the bottom clamps of the Instron machine. The inner layer is made from the same material as the outer layers in case of inter-ply slip characterization (section 6.4). A different material, namely aluminium, is used in case of tool-ply slip testing (section 6.5).

The inner layer is pulled out from between the two outer plies. The force needed to invoke slippage is directly linked to the friction coefficient between the inner and outer plies and is given by following equation:

$$\mu = \frac{F_f}{2 \cdot F_N} \qquad \textbf{Eq. 6-3}$$

Where μ is the friction coefficient, F is the measured force and F_N is the applied normal force. The 2 in the denominator of Eq. 6-3 is related to the 2 contacting surfaces, namely two outer plies with the middle ply.

Alternatively also the traction can be calculated according to:

$$\tau = \frac{F_f}{A_c} \qquad \textbf{Eq. 6-4}$$

Where, τ is the traction in Pa, F_f is the frictional force in N and A_c is the total area of contact in m^2. Note that the total area of contact takes into account the contact area of the two outer plies with the inner ply.

In previous sections it has been shown that both the pressure and the temperature distribution are most uniform in the central zone between the steel plates. Therefore, the test zone is limited to a square region of 80 by 80 mm in the centre of the pull-out set-up. Figure 6-6(a) depicts a scheme of the test specimen.

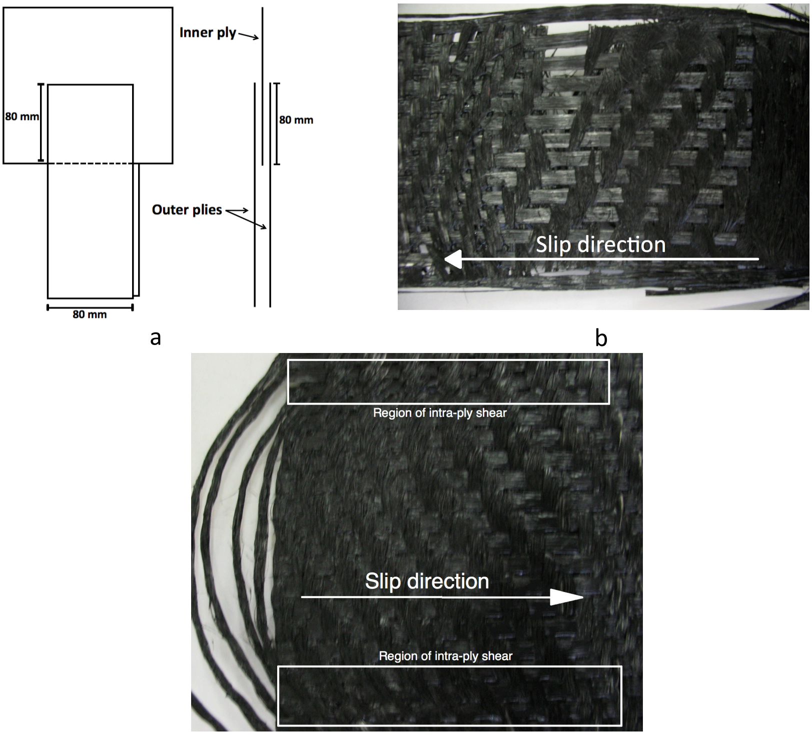

a

b

c

Figure 6-6. Pull-out test procedure with (a) a typical test specimen of a test specimen of TW$_1$ with (b) a small middle ply and with pulled out yarns and (c) a large middle ply with a small area of intra-ply shear

The outer plies have a width of 80 mm and are fixed in the bottom clamps of the instron tensile testing machine. The middle ply is 160 mm in width and is fastened in the top clamp, which can translate in an upward direction. The reason the middle ply is chosen to be wider than the outer plies is depicted in Figure 6-6(b). During pullout of a specimen with a small middle ply, the transverse bottom yarns of the middle ply are withdrawn from the sample. This conflicts with the inter-ply slip mechanism, since the yarns stay within the reinforcement during this deformation mechanism. Increasing the sample width helps to contain the yarns within the sample as indicated in Figure 6-6 (c) and thus to invoke inter-ply slip in the experiment. However, a region of intra-ply shear occurs at the edges of the middle ply, though this region is relatively

small compared to the overall size of the inter-ply slip zone. Therefore, the contribution of this intra-ply shear zones to the overall force is neglected.
The relative orientation between the plies is always 0° and moreover, the yarns are always oriented in the slip direction. The reason being the introduction of intra-ply slip when off-axis orientations are used. This study is only focused on inter-ply and tool-ply slip. A combination of multiple deformation mechanism is for the moment being not considered. After the specimen is prepared, it is pressed between the pre-heated steel plates. Then circa 3 minutes are waited before the test is started and the middle ply is pulled out from between the two outer plies and the force-displacement curve is obtained.
The results of these experiments are further elaborated in sections 6.4 and 6.5.

6.4. Inter-ply slip characterization

This section deals with the characterization of the slip behaviour between the neighbouring plies of a composite laminate. The materials TW_1, TW_2 and TP introduced in Chapter 3 will be subjected to a thorough investigation of their inter-ply slip behaviour. First, a typical force-displacement curve, obtained via the pull-out experiment, will be examined and the different mechanisms that occur during or prior to slip are explained. In the subsequent paragraphs the influence of the pull-out velocity, temperature, normal pressure and interlayer thickness will be assessed.

6.4.1. Mechanism

Figure 6-7 shows a typical force and traction-displacement curve for the pull-out experiment.

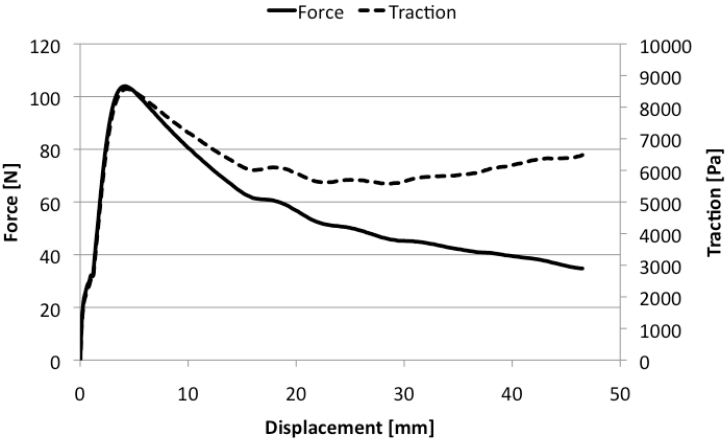

Figure 6-7. Typical force and traction displacement curve obtained for TW_1 at 195°C and 100 mm/s

An initial steep increase is noticed, where the force reaches a maximal value and then smoothly decreases. This behaviour has been reported by most researchers that have investigated the interply slip phenomenon [35, 36, 106]. It is related to both the structure of the fabric and the rheological behaviour of the matrix. Figure 6-8 shows in detail the initial section of the force-displacement where a non-linear zone is noticed. First, the sample is straightened, since it is impossible to perfectly align it with the direction of pulling. Then, pulling the middle ply from between the two outer plies, first straightens the yarns of the middle ply prior to slip. The reason being the low initial stiffness of the reinforcement (see Figure 4-14(b)), which are initially undulated because of the yarn crimp in the fabric (see Figure 6-8). When the force needed to further straighten the yarns in the fabric is higher than the force needed to initiate slippage, the middle ply will be pulled out. The peak force that is reached, is a consequence of the time-dependent rheological behaviour of the matrix.

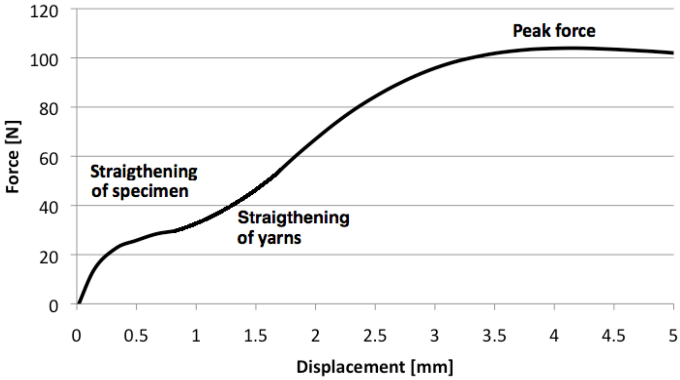

Figure 6-8. A typical force-displacement curve at low displacements

Figure 6-9 shows a cross-section of a pull-out specimen. Hereby, it is noticed that a thin interlayer of matrix material (between red lines) exists between the different plies, which agrees with previous studies [35, 37, 39]. The thickness of this interlayer varies greatly and is at some locations hardly noticeable.

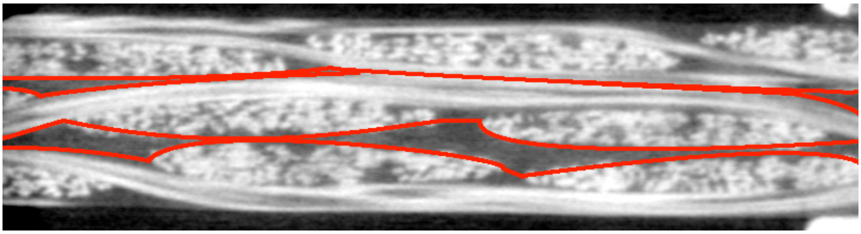

Figure 6-9. The matrix rich zones seen in a cross-section of a specimen taken via μCT-imaging

When one layer slips over the adjacent one, it will be shown in subsequent sections that this interlayer plays an important part in explaining the contact properties. At elevated temperatures the matrix becomes a viscous fluid, as is explained in section 1.2.3, which acts as a lubricant. When one layer is pulled out, the lubricant will undergo shear flow as indicated in Figure 6-10(a). Therefore, the resistance to shear flow, i.e. the shear viscosity, is an important factor that determines the force needed to pull-out the middle ply.

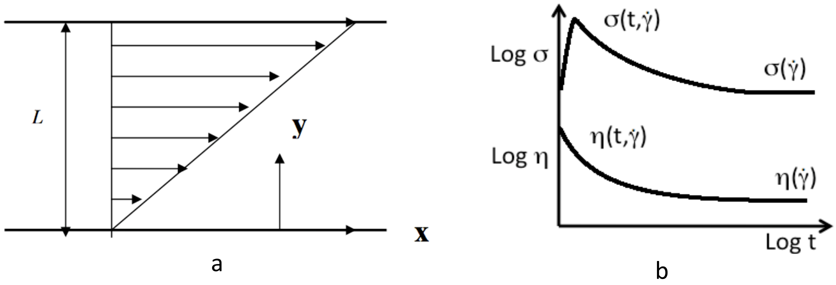

Figure 6-10. Flow behaviour of the matrix with (a) an indication of shear flow and (b) the transient shear stress and shear viscosity behaviour during start-up of shear flow (adapted from [107])

The initial peak and the following steep drop that are noticed can be explained by the transient behaviour of the shear viscosity [107, 108], schematically shown in Figure 6-10(b). Due to the visco-elastic nature of polymers, the stress growth during start-up of simple shear flow exhibits an overshoot, $\sigma(t, \dot{\gamma})$, before a steady-state value, $\sigma(\dot{\gamma})$, which only depends on the shear rate, is reached. It is this steady-state value that is used to calculate the shear viscosity, $\eta(\dot{\gamma})$, reported in Chapter 3. The transient viscosity, $\eta(t, \dot{\gamma})$, is a well-known property, but is less studied and modelled mainly due to the short-period effects in polymers and instrumentation limitations during measurements.

During the remainder of the experiment when the middle ply is moving out of the two adjacent plies, the slip area keeps decreasing and the pressure on the specimen increases as illustrated in Figure 6-11. As the steady-state viscosity is reached, the traction remains constant and the force decreases according to Eq. 6-4. Though at large displacement the traction increases, which is a consequence of the high pressure that occurs at this large displacement as indicated in Figure 6-11.

In the following paragraphs, which introduce the effect of the process parameters on the resistance to inter-ply slip, the initial peak traction will be taken as a reference. The influence of the velocity, the temperature, the normal pressure and the interlayer thickness will be investigated.

6.4.2. Influence of pull-out velocity

Prior to investigating the influence of the velocity, the range of the speed at which the inter-ply slip during forming occurs needs to be determined. In Chapter 5, the difference in local displacement was determined for a hemispherical punch with different relative orientations. In the parametric study presented in Chapter 5, the punch velocities ranged from 10 to 100 mm/s, which gives an interval of 5 to 0.5 s for the draping of the hemisphere, which has a depth of 50 mm. In other studies [109] the velocity of forming goes up to 500 mm/s, which would mean the draping of the hemisphere in Chapter 5 takes place in 0.1s. It is possible to calculate the average local inter-ply slip velocity, by dividing the displacement difference by the time of draping. Taking the draping time at 1 sec, Figure 6-12 shows the local inter-ply slip velocity for different relative orientations.

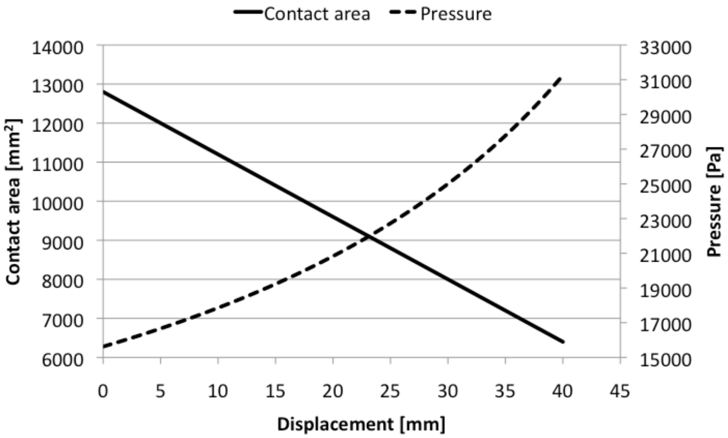

Figure 6-11. The total contact area and pressure during the pull-out test for a normal force of 100N.

The higher the relative orientation between the plies, the more inter-ply slip needs to occur to accommodate to the punch and thus the higher the local slip velocity becomes. For a 45° relative orientation a large range of inter-ply slip velocities exists, between 0 and 7.13 mm/s. It needs to be noticed that this approach assumes the hemisphere is draped without any shape distortions. As a result of these approximate calculations, the range of velocities for the pull-out experiments is chosen very broad, namely from 20 to 500 mm/min, which is the maximum obtainable speed with the instron tensile tester.

Figure 6-13 shows the typical traction-displacement curves obtained for different pull-out velocities for the three materials TW_1, TW_2 and TP. From these curves it is clear that an increase in velocity increases the traction and force needed to initiate inter-ply slip. This trend is also observed by Murtagh et al. [35] and Lebrun et al. [36].

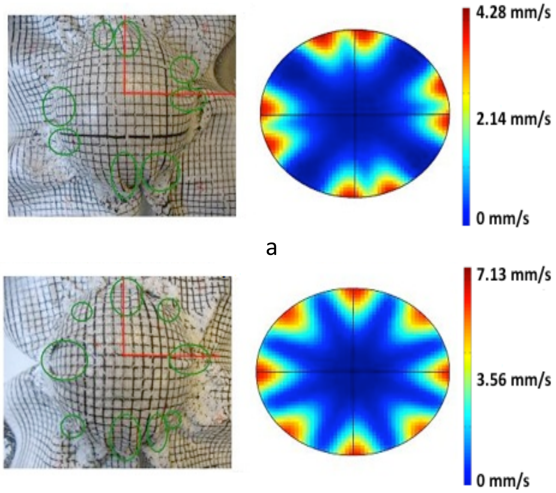

a

b

Figure 6-12. Local inter-ply slip velocity during draping of a 2-layered stacking for (a) a 15° relative orientation and (b) a 45° relative orientation

At high slip velocities the peak traction is more pronounced, while at low values the peak traction is hardly noticed. This effect is explained by the dependence of the initial stress overshoot during start-up of shear flow on the shear rate [107]. The higher the velocity, and thus the shear rate, the more pronounced the initial stress overshoot will be. When examining the change in peak traction in Figure 6-14, it is noticed that the peak traction can be described by a power-law as function of the pull-out velocity for all materials.

The reason can be found in the flow behaviour of the matrix material (see Chapter 3), which forms a small interlayer between the different plies as visualized in Figure 6-9. The viscosity of the matrix behaves as a shear-thinning fluid, meaning that the resistance to flow decreases at increasing shear rate. When the velocity of slip increases and the interlayer thickness remains constant, the shear rate of the interlayer, $\dot{\gamma}$, increases proportionally as indicated in Eq. 6-5. According to Newton's law of viscosity (Eq. 6-6), the non-linear decrease in viscosity as a function of the shear rate explains the non-linear increase of the traction τ as function of the velocity. Figure 6-15 shows this non-linear increase of traction by assuming a constant interlayer thickness of 0.05 mm and using the Ellis-Arrhenius law (Eq. 6-7 and Eq. 6-8) to calculate the viscosity of PP_{tw}.

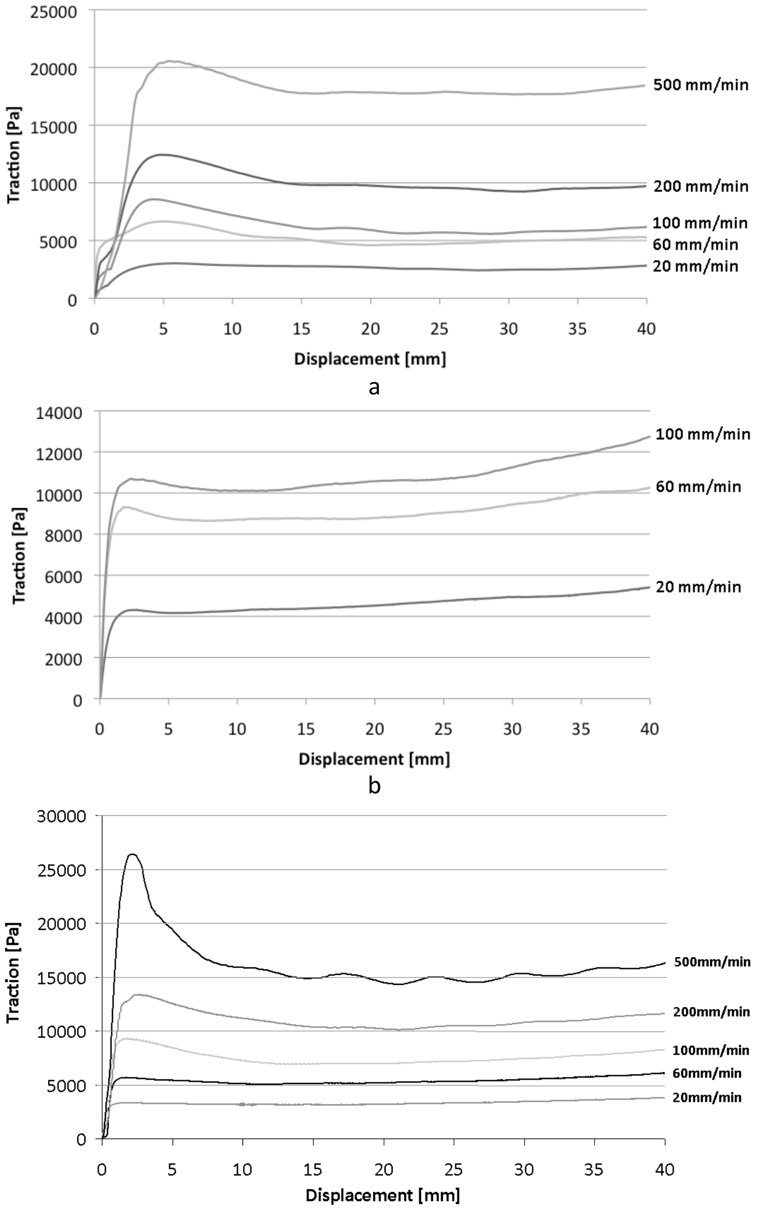

a

b

c

Figure 6-13. Influence of the pull-out velocity on the traction measured for inter-ply slip for (a) TW_1, (b) TW_2 and (b) TP

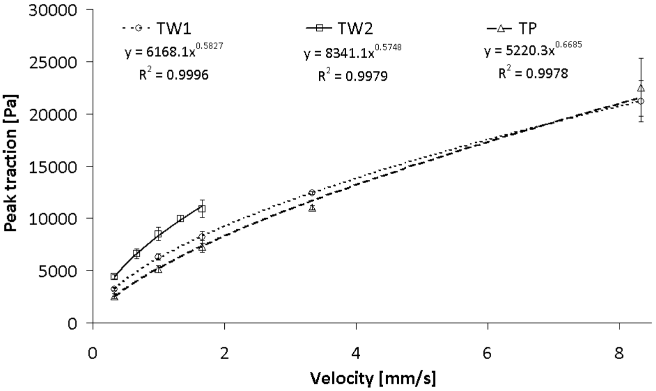

Figure 6-14. Influence of the pull-out velocity on the peak traction for inter-ply slip measurements

$$\dot{\gamma} = \frac{v}{h} \qquad \text{Eq. 6-5}$$

$$\tau = \dot{\gamma} \cdot \eta(\dot{\gamma}, T) \qquad \text{Eq. 6-6}$$

$$\eta(\dot{\gamma}, T) = \frac{\eta_0(T)}{1 + \left(\frac{\dot{\gamma}}{C(T)}\right)^{n-1}} \qquad \text{Eq. 6-7}$$

$$Ar(T) = Ar_0 \cdot \exp\left(\frac{Ar_1}{T}\right) \qquad \text{Eq. 6-8}$$

Here *v* is the velocity in m/s, *h* is the interlayer thickness in m and η is the viscosity of the matrix, which is a function of the shear rate and the temperature. The fitting parameters of the Ellis-Arrhenius equations have been introduced in Table 3-2. In section 6.7.1, Eq.6-6 will be used in an adapted form to determine the interlayer thickness.

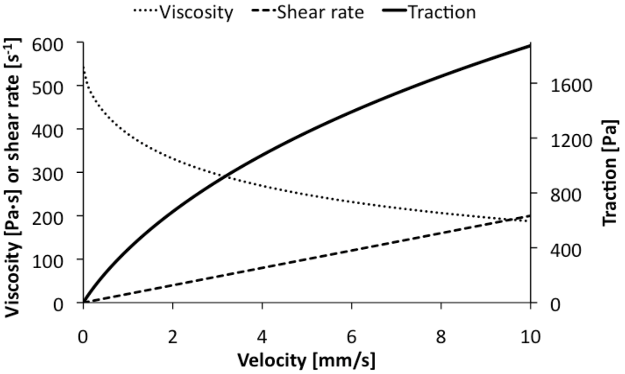

Figure 6-15. Non-linear increase of traction as function of the velocity and assuming a constant interlayer thickness of 0.05 mm at 195°C.

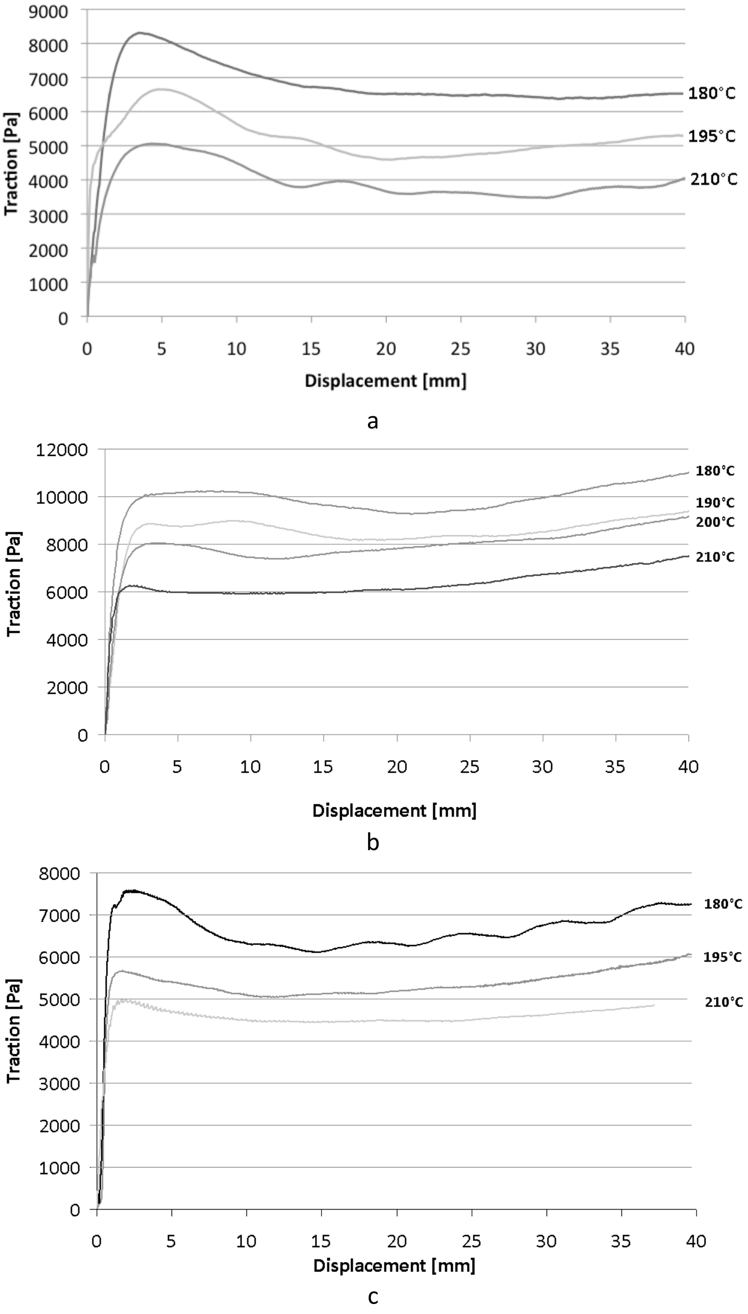

Figure 6-16. Influence of the temperature on the traction measured for inter-ply slip for (a) TW_1, (b) TW_2 and (b) TP

6.4.3. Influence of temperature

During forming, the temperature of the composite plate will be non-isothermal. Contact with the tooling will cool down the material during forming (see Figure 5-9). The temperature range for the pull-out experiments ranges from 180 to 210°C. Figure 6-16 shows the typical traction-displacement curves. For TW_2 the effects of colder temperatures is also investigated by cooling the specimen from 175°C to a temperature below the melting temperature (Figure 6-17) prior to performing a pull-out experiment.

It is obvious that increasing the temperature decreases the traction. Again this behaviour can be identified as a consequence of the viscous nature of the matrix. An increasing temperature leads to a decrease in viscosity (see Figure 3-5). This decrease can be described by an Arrhenius law, Eq. 6-8, which explains the exponential increase in peak traction when the temperature decreases.

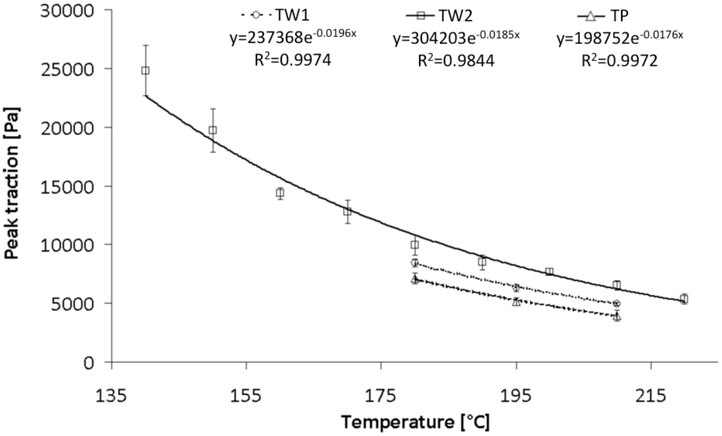

Figure 6-17. Influence of the temperature on the peak traction for inter-ply slip measurements (line = Arrhenius law)

6.4.4. Influence of normal pressure

No experimental indication of the pressure range during the draping step of forming is found in the literature. Most literature [11, 18] deals with the influence of the pressure during the impregnation and consolidation step of forming. During draping, however, the normal pressure on the composite is usually very low, since for the most part it is a consequence of the bending resistance, which is very low. The load cell of the thermoforming installation used in this research has a high range of 1000 kN, and thus the accuracy is too low to measure the load during draping of the small hemisphere.

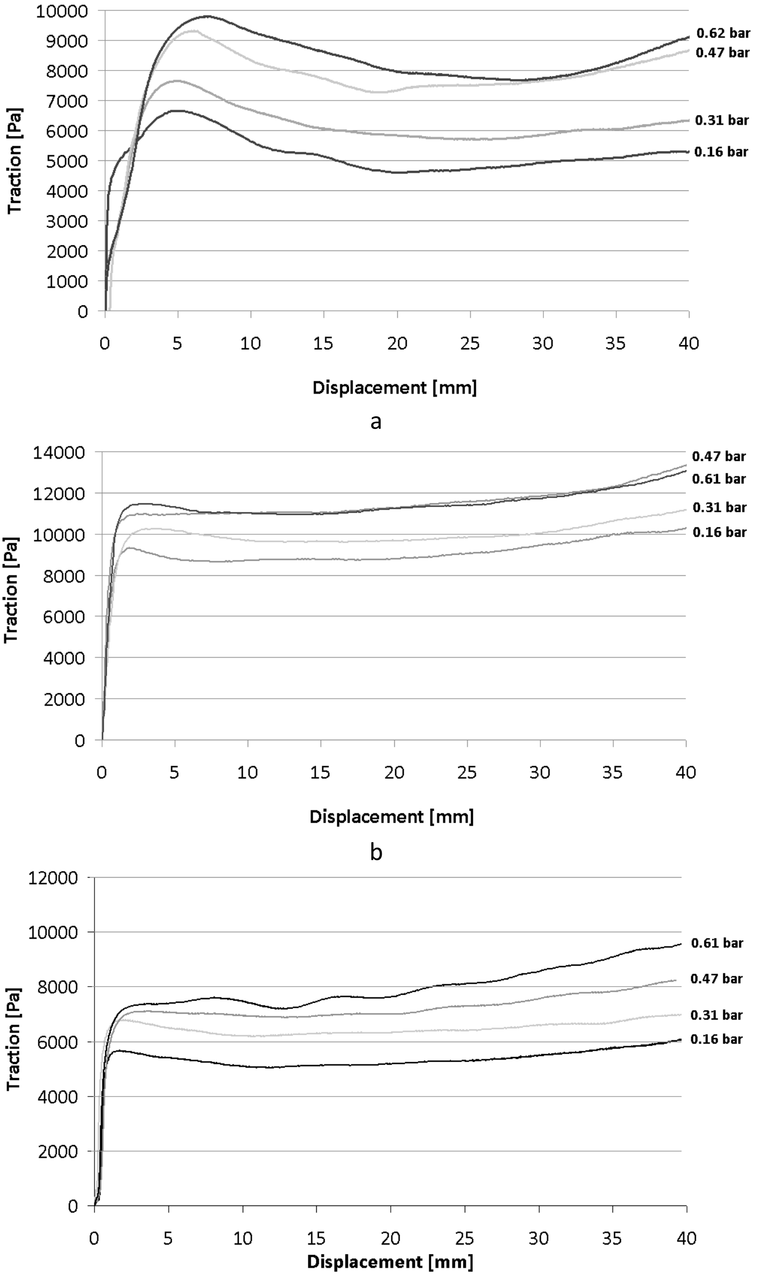

a

b

c

Figure 6-18. Influence of the normal pressure on the traction measured for inter-ply slip for (a) TW_1, (b) TW_2 and (c) TP

Willems performed draping simulations in [64], which are based on a mechanical approach for a single woven reinforced composite. During forming she noticed that the pressure can locally increase to about 1.5 bar in the zone that undergoes heavy bending, which is focused at the fillet of the die. However, a large range of pressures exists since it is dependent on the force that the blankholder applies on the blank. In this study, the influence of the normal pressure on the inter-ply slip behaviour is assessed by changing the pressure from 0.16 to 0.62 bar (see Figure 6-18).

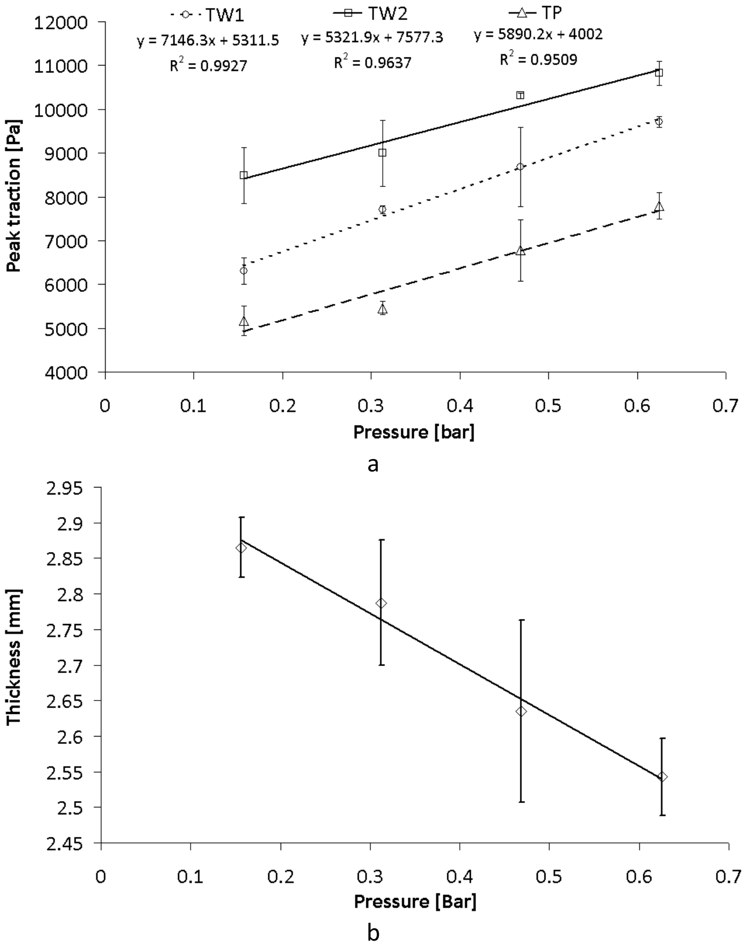

Figure 6-19. Influence of the pressure on (a) the peak traction and (b) the thickness of the specimen for inter-ply slip measurements

For all materials an increase in normal pressure, slightly increases the resistance to slip as can be noticed in Figure 6-19(a). Since the viscosity is to a first approximation independent on the normal pressure, the source of this increase needs to be found elsewhere. When examining the dependence of the thickness of the specimen as a function of the normal pressure a decrease is noticed, shown in Figure 6-19(b). To measure this thickness, 4 pull-out samples are heated at 195°C with different normal pressure. They are cooled to room temperature after a holding time of 3 minutes without performing a pull-out test. The thickness of the complete specimen is then measured using a calliper. Although a large degree of scatter is found on the thickness of the material, there is a thickness difference of 10% between the sample pressed at 0.16 bar and the sample pressed at 0.61 bar.

The matrix material, which forms the interlayer, will be squeezed from between the adjacent plies in the specimen more easily at higher pressures and thus the interlayer thickness decreases. Proof to endorse this explanation is given in section 6.7.1. A smaller interlayer will increase the shear rate and thus according to the viscosity law of Newton (Eq. 6-6), the traction will increase.

At zero pressure the traction between the plies is still relatively high. During melting the polypropylene of the adjacent plies will entangle causing a cohesive force or pressure between the plies, which makes that the plies attract each other. At zero pressure the peak traction is associated with this cohesive force.

6.4.5. Influence of interlayer thickness

One of the conclusions from Chapter 5 was that the interlayer thickness is the only parameter that significantly influences the formability in terms of wrinkling of complex shapes and lay-ups. A high interlayer thickness decreases the tendency to wrinkling. The influence of the interlayer thickness on the interply slip behaviour is shown in Figure 6-20 for the material TW_1 measured at 0.16 bar and 180°C.

To increase the thickness a small foil of PP_{int} with known thickness is pressed between the middle and the outer plies prior to pull-out. An increase in matrix material at the interface decreases the traction during slip. In terms of friction this means that an increase in interlayer thickness decreases the friction coefficient. This effect is due to a decreasing shear rate when the interlayer becomes thicker. When calculating the traction using the Ellis-Arrhenius model (Eq. 6-7 and 6-8) of PP_{int}, of which the fitting parameters are given in Table 3-3, it is noticed that the traction decreases in a non-linear manner as function of the shear rate. This is due to the shear thinning of the matrix whereby the viscosity decreases at higher shear rates (also see Figure 6-15). Comparing the predicted traction and the experimental measured peak traction the same trend is found, though the experimental peak traction lies higher than the calculated one. A possible explanation is the initial overshoot of traction due to the start-up of flow, which is not taken into account in the Ellis-Arrhenius model, though the start-up effect is noticed to be negligible.

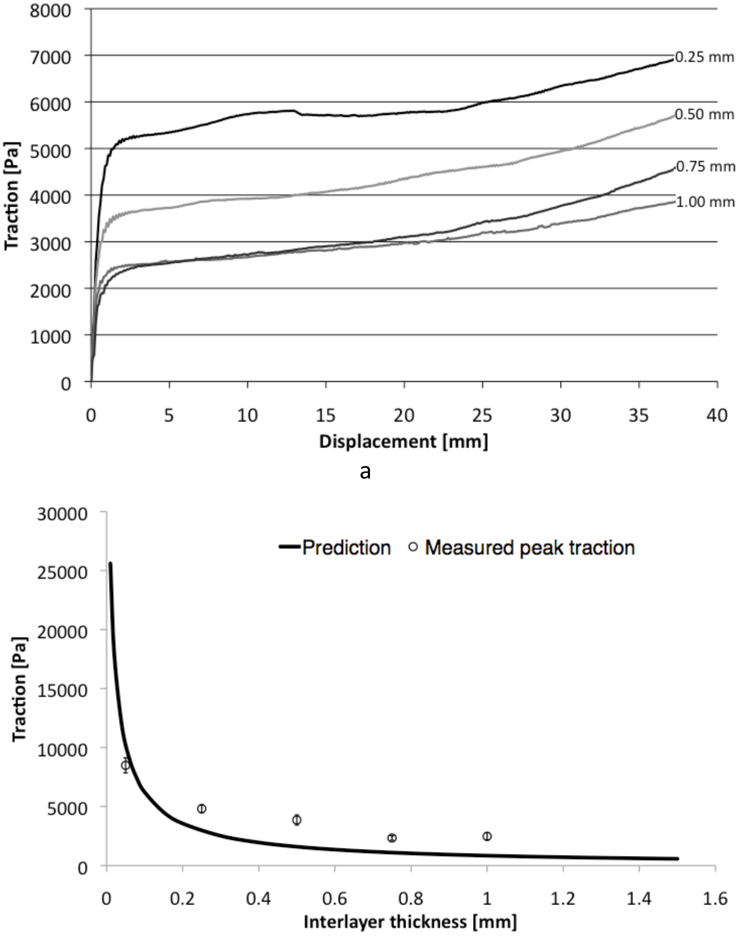

a

b

Figure 6-20. Influence of the interlayer thickness on (a) on the traction-displacement curve and (b) the peak traction for inter-ply slip measurements comparing experiments with predictions

A second effect is illustrated in Figure 6-21, where a cross section is taken for a 0.5 mm foil thickness. From this figure it is obvious that the height of the matrix rich zone between the inner and outer plies, after applying pressure on the specimen, is less than 0.5 mm. Applying pressure makes the polypropylene flow away from the region where the pressure is high and thus makes the interlayer in this region thinner than its theoretical thickness.

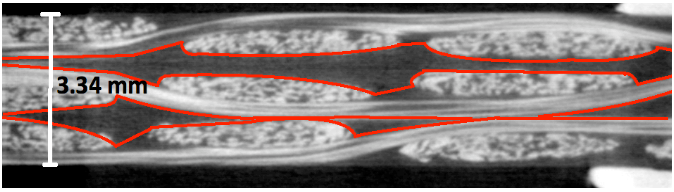

Figure 6-21. cross-section of an inter-ply slip specimen after pressing a PP_{int} foil of 0.5 mm thickness between the plies at a normal force of 100N

6.5. Tool-ply slip characterization

This section deals with the characterization of the slip behaviour between the plies of a composite laminate and the tooling materials. The material TW_1 will be subjected to a thorough investigation of its tool-ply slip behaviour. The material used to represent the tooling is aluminium

First, a typical force-displacement curve, obtained via the pull-out experiment, will be introduced and explained by the different mechanisms that occur during or prior to slip. In the subsequent paragraphs the influence of the pull-out velocity, temperature and normal pressure will be assessed.

6.5.1. Mechanism

Figure 6-22 shows a typical force and traction-displacement curve for a pull-out test in case of tool-ply contact. The same deformation mechanisms are found as for ply-ply contact (see section 6.4.1). An initial steep increase is noticed, where the force reaches a maximal value and then smoothly decreases. The peak traction associated with this maximal force value will be used to assess the influence of the velocity, temperature and pressure on the slip behaviour.

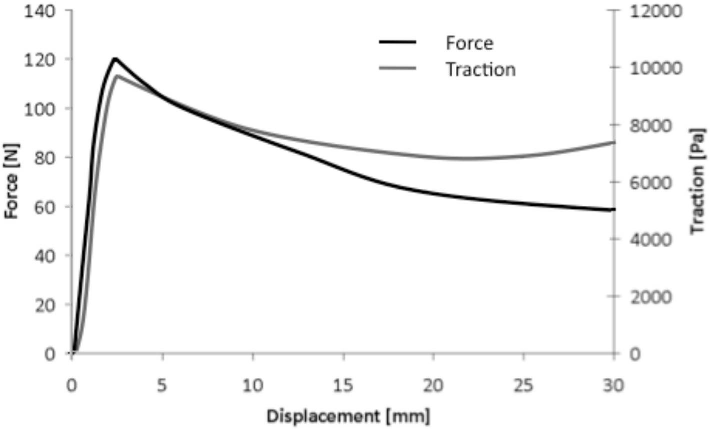

Figure 6-22. Typical force and traction-displacement curve obtained for tool-ply slip

6.5.2. Influence of velocity

Figure 6-23 shows the influence of the slip velocity on the traction response. An increase in velocity increases the traction between the tool and the ply.

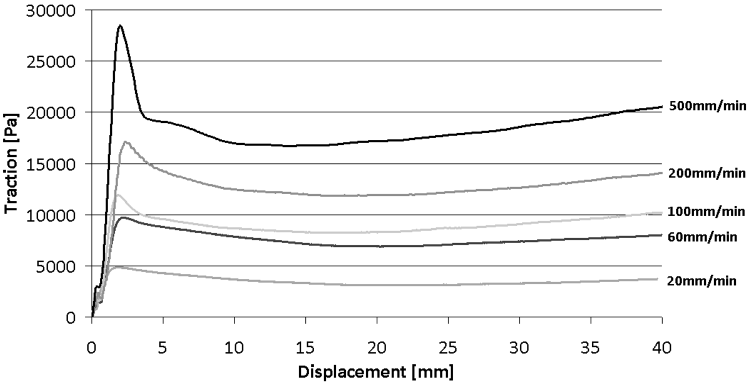

Figure 6-23. Influence of the pull-out velocity on the traction measured for tool-ply slip for TW_1

The peak traction can be described as a power-law function of the slip velocity as illustrated in Figure 6-24. The same reasoning can be used as with ply-ply slip. The viscosity of the matrix behaves as a shear-thinning fluid, which means that the resistance to flow decreases at increasing shear rates.

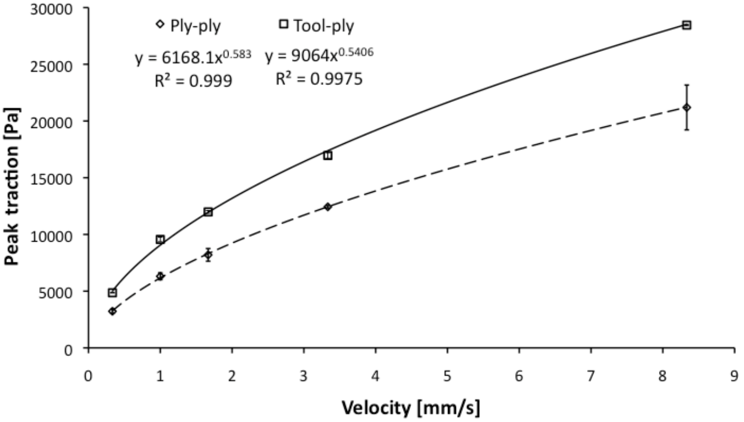

Figure 6-24. Influence of the pull-out velocity on the peak traction for tool-ply slip measurements

A smaller interlayer, and thus a higher shear rate, between the tool and the ply explains the higher traction values for tool-ply contact in comparison with ply-ply contact. Only the middle ply will contribute to the interlayer thickness, while in case of ply-ply contact two layers of thermoplastic composite will give rise to a thicker interlayer. The peak traction at the same process conditions is on an average about 30% higher for tool-ply contact than for ply-ply contact. The higher shear rate also explains the more pronounced peak traction in comparison with the ply-ply peak traction, due to the dependence of the initial stress overshoot during start-up of matrix shear flow on the shear rate.

6.5.3. Influence of temperature

Figure 6-25 shows the influence of the temperature on the traction response. An increase in temperature decreases the traction between the tool and the ply.

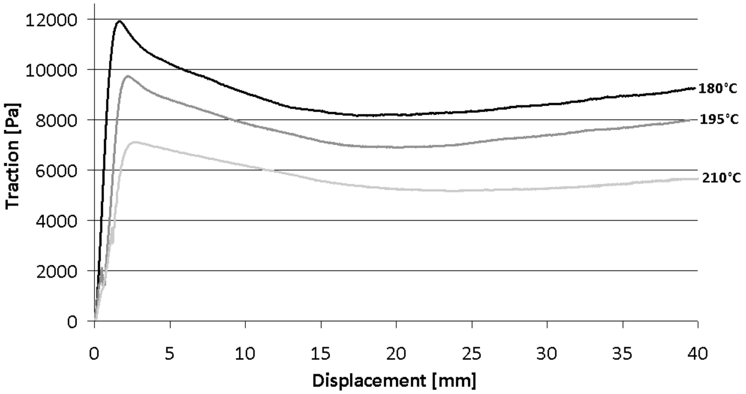

Figure 6-25. Influence of the temperature on the traction measured for tool-ply slip for TW_1

As indicated in Figure 6-26, this behaviour is similar to the ply-ply contact and can be identified as a consequence of the viscous nature of the matrix. An increasing temperature leads to a decrease in viscosity.

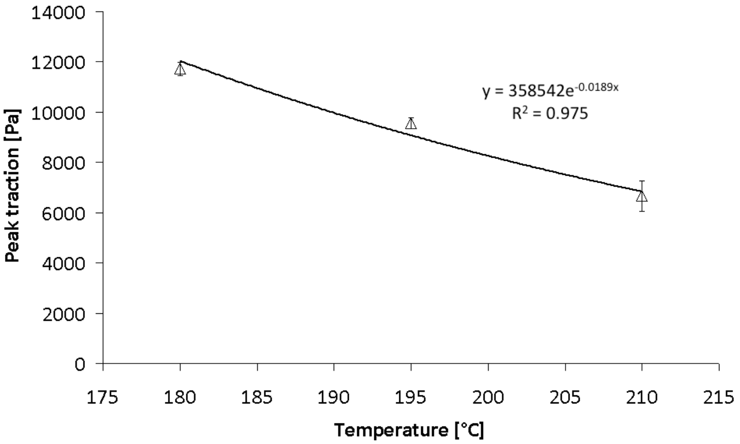

Figure 6-26. Influence of the temperature on the peak traction for tool-ply slip measurements (line = Arrhenius law)

6.5.4. Influence of normal pressure

Figure 6-27 shows the influence of the normal pressure on the traction response. An increase in pressure increases the force needed to pull the ply from between the tooling material.

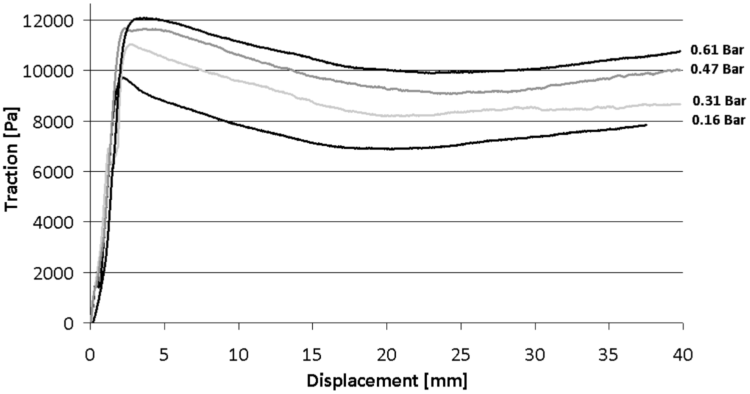

Figure 6-27. Influence of the normal pressure on the traction measured for tool-ply slip for TW_1

Figure 6-28(a) illustrates the influence of the pressure on the peak traction. When examining the dependence of the thickness of the specimen as function of the normal pressure a decrease is noticed, shown in Figure 6-28(b). The increase in traction can be explained by a decrease in interlayer thickness, since the matrix is pressed from between the tool and ply towards the edges of the sample.

6.6. Intermediate conclusions

An experimental apparatus has been introduced that by pulling one ply of material out from between two adjacent ones, is capable of measuring the tribological behaviour between different materials. The thermal and pressure homogeneity of the apparatus have been assessed. Furthermore, it is used to investigate the influence of the process conditions on the contact properties of two thermoplastic woven composites and of a thermoplastic woven composite and tooling material.

It is noticed that the transient rheological behaviour of the matrix is an important factor in determining the non-linear contact properties of thermoplastic composites. A small matrix-rich interlayer exists between the contacting surfaces. This acts as a lubricant and explains the influence of the slip velocity, temperature, pressure and interlayer thickness on the contact properties of thermoplastic woven reinforced composites.

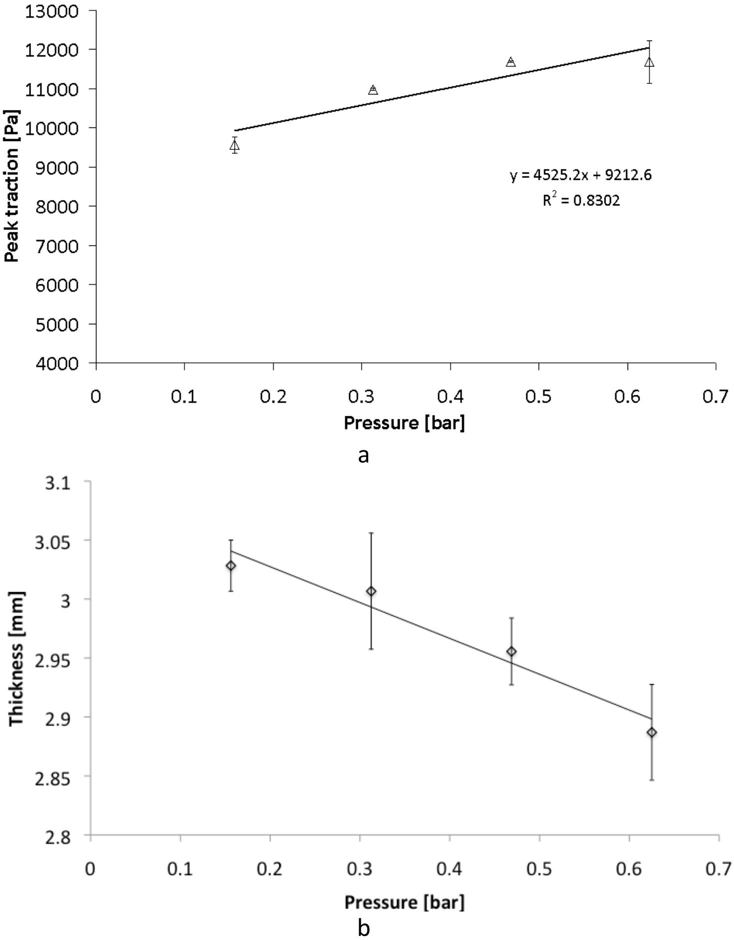

Figure 6-28. Influence of the pressure on (a) the peak traction and (b) the thickness of the specimen for tool-ply slip measurements

6.7. Models of tool-ply and ply-ply friction

In order to simulate the forming of multilayered thermoplastic composites, the complex contact behaviour of these materials needs to be implemented in predictive software. An overview of different models is given in Chapter 1. The aim of these models is to predict the relation between the traction or friction coefficient measured in the pull-out experiments and the parameters that influence them.

Two of these models, namely the model of Lamers and the Stribeck approach, are used to describe the influence of the process conditions on the contact behaviour and a third traction model is developed. To end this section the Stribeck and traction model will be compared with each other.

6.7.1. Descriptive model of Lamers

Lamers [44] developed a descriptive model based on the viscous nature of the interlaminar behaviour. He assumes a friction law that depends linearly on the velocity difference *v* between the plies and defines the interface traction τ as:

$$\tau = \frac{v}{\beta} \qquad \textbf{Eq. 6-9}$$

Where β is the constant friction factor per interface, which is defined as:

$$\beta = \frac{h}{\eta} \qquad \textbf{Eq. 6-10}$$

This approach assumes that the interlayer thickness *h* between the tool or the ply with the adjacent ply is known or can be predicted and that the viscosity η of the matrix material is available. Moreover, Lamers made the assumption to replace the variable interlayer thickness (see Figure 6-9) by a constant interlayer thickness. To determine the interlayer thickness, first, Eq. 6-9 and 6-10 are combined and Newton's law of viscosity appears, which has already been introduced in Eq. 6-6.

$$\tau = v \cdot \frac{\eta}{h} = \dot{\gamma} \cdot \eta \qquad \textbf{Eq. 6-11}$$

In the above stated equation the flow behaviour of PP_{tw} is implemented as an Ellis-Arrhenius model (Eq. 6-8). The factors for the Ellis-Arrhenius model for PP_{tw} are given in Table 3-2. An equation is found whereby, after performing pull-out experiments and determining the traction, the only unknown the interlayer thickness h.

$$\tau = \frac{v}{h} \cdot \frac{\eta_0(T)}{\left(1 + \left(\frac{v}{h \cdot C(T)}\right)^{n-1}\right)} \qquad \textbf{Eq. 6-12}$$

To determine the value of h, this equation is implemented in a MATLAB routine, where it is calculated using an iterative approach. In [17] this thickness is called the average thickness of the interlayer, though it will be shown that the obtained thickness does not necessarily equal the real average interlayer thickness. The peak traction measured in the pull-out experiments forms the input for the left-hand side of Eq. 6-12, together with the pull-out velocity and temperature used during the experiments. Figure 6-29 shows a typical convergence curve where a stable solution is reached after approximately 10 iterations.

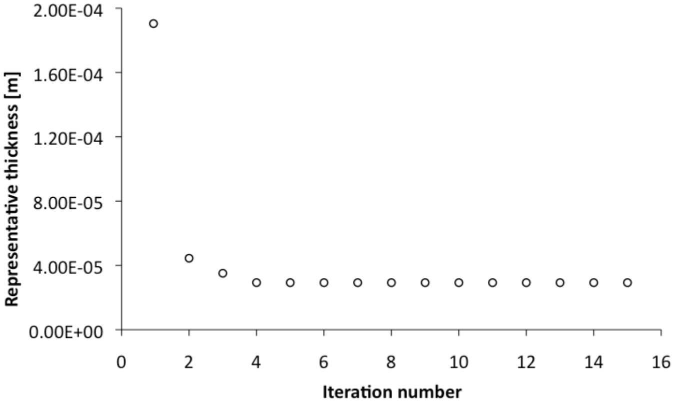

Figure 6-29. Convergence curve for the calculation of the interlayer thickness

A comparison between the tool-ply and ply-ply contact type is depicted in Figure 6-30. In this figure, the values of h are compared for the same process conditions. The overall average value of h for tool-ply and ply-ply contact is indicated in Table 6-2.

It is noticed that the average calculated thickness for ply-ply contact is found to be approximately two times higher than the representative thickness for tool-ply. This can be explained by the fact that only one layer of TW_1 comes into contact for tool-ply contact, while for ply-ply contact two layers of TW_1 are present, thus the calculated interlayer thickness doubles in thickness.

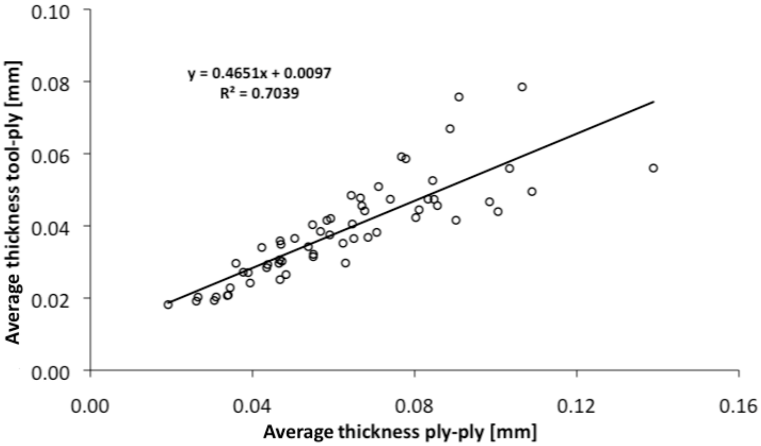

Figure 6-30. Comparison of the average interlayer thickness obtained via Eq. 6-12 for tool-ply and ply-ply slip

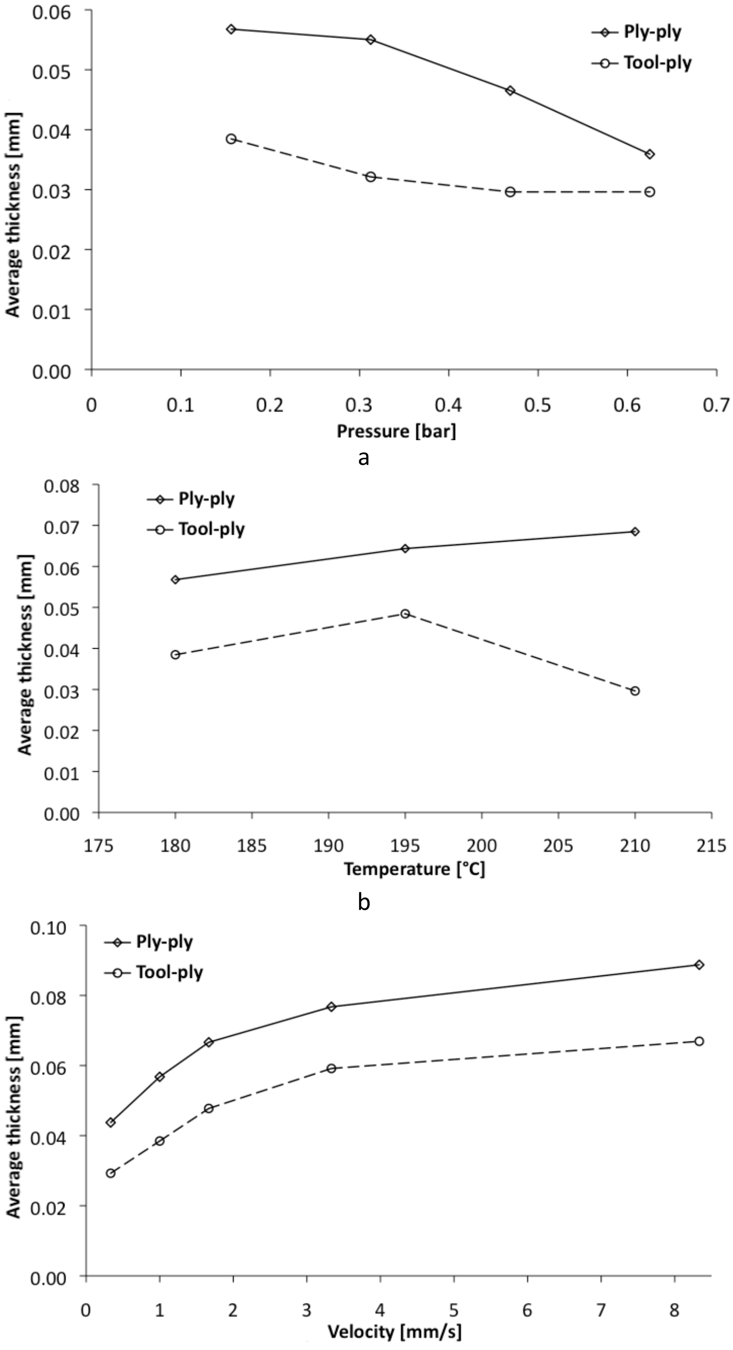

c

Figure 6-31. Average interlayer thickness as function of (a) pressure, (b) temperature and (c) the pull-out velocity

Table 6-2. Average interlayer thickness for ply-ply and tool-ply contact

Contact type	Average h [mm]
Ply-ply TW_1	0.0622 ± 0.0242
Tool-ply TW_1	0.0387 ± 0.0134

In Figure 6-31 the influence of the different process conditions on the calculated interlayer thickness are examined for both tool-ply and ply-ply contact.

An increase in normal pressure, decreases the calculated thickness of the interlayer. This agrees with the trend found in Figure 6-19 and Figure 6-28 and where a decreasing overall thickness of the specimen as the pressure increases is found. Applying pressure makes the matrix material flow away from the region where the pressure is high towards the edges of the specimen and thus makes the interlayer thinner. A rising temperature hardly affects the interlayer thickness. The slip velocity, however, has a great influence on the interlayer thickness. It increases by about 100% when the velocity increases from 0.33 to 8.33 mm/s. This effect is unexpected and can be explained by the assumption of a constant thickness. Therefore, a simple calculation is performed whereby two different cases of tool-ply contact are considered. In the first case the pulled-out ply has a smooth surface and the interlayer thickness is considered constant. In the second case the pulled-out ply has a rippled surface and the interlayer thickness varies with the standard deviation for tool-ply contact given in Table 6-2. This results in the thickness profiles schematically illustrated in Figure 6-32.

For both profiles the magnitude of the contact area between ply and tool is the same and the average thickness equals 0.0387 mm, which is the average representative thickness obtained for tool-ply contact. The peak traction τ_p for the profile depicted in Figure 6-32(b) is calculated according to the following equation:

$$\tau_p = \tau_1 \cdot \frac{A_1}{A_c} + \tau_2 \cdot \frac{A_2}{A_c} \qquad \textbf{Eq. 6-13}$$

Here τ_1 is the traction and A_1 the contact surface according to the first section and τ_2 the traction and A_2 the contact surface according to the second section from Figure 6-32(b) and A_c represents the total contact surface. The total area A_c is the sum of A_1 and A_2 and assuming that A_1 and A_2 are equal, Eq. 6-13 can be simplified to:

$$\tau_p = \frac{\tau_1 + \tau_2}{2} \qquad \textbf{Eq. 6-14}$$

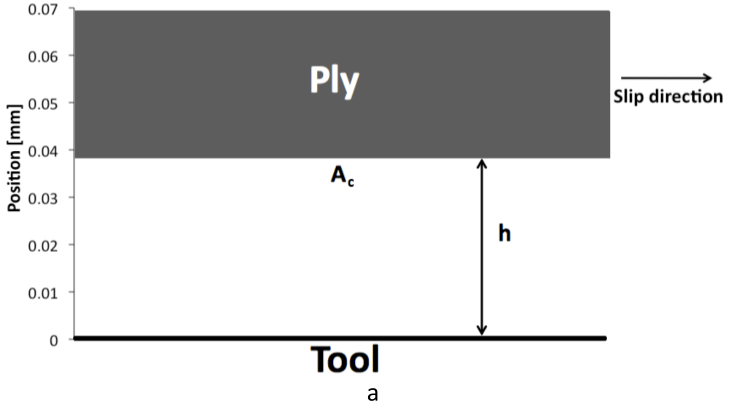

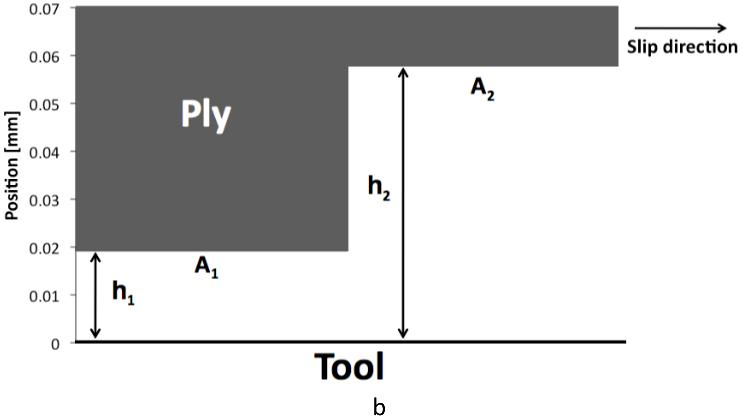

Figure 6-32. The examined profiles used to investigate the influence of the interlayer thickness with (a) a constant thickness and (b) a variable thickness

For the case where the interlayer thickness is considered constant τ_p is calculated directly from Eq. 6-12. For the second case, where the ply is rippled, Eq. 6-12 is used to calculated τ_1 and τ_2 using the local interlayer thickness h_1 and h_2. These values are then combined in Eq. 6-14 to calculated the traction on the total contact surface. Figure 6-33 depicts the traction-velocity behaviour for both profiles. It is noticed that the traction for a changing interlayer thickness is always higher than the one where the thickness stays constant.

Now, assuming that the peak traction values depicted in Figure 6-33 are obtained using pull-out experiments and the average interlayer thickness needs to be determined. These traction values are given as an input to calculate the average interlayer thickness using Eq. 6-12.

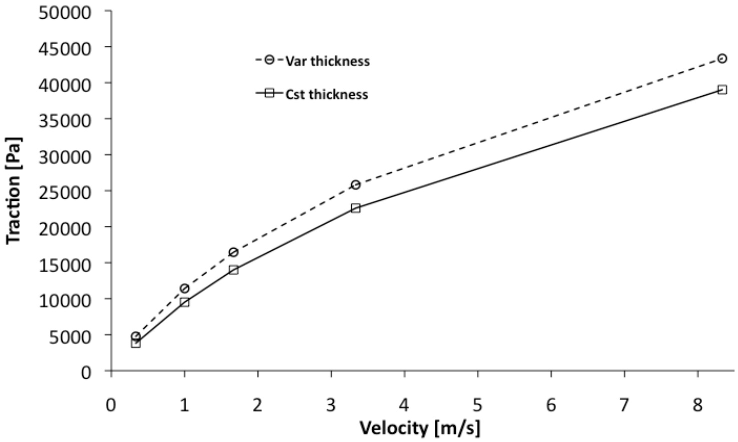

Figure 6-33. The traction response as function of the velocity for different interlayer thickness profiles

Figure 6-34 shows that for a profile where the interlayer thickness is constant, the average thickness obtained via Eq. 6-12 is also constant as a function of the velocity and equals the real average thickness of 0.0387 mm. A profile where the interlayer thickness is not constant results in a changing average thickness as function of the slip velocity. Moreover it does not equal the real average interlayer thickness of 0.0387 mm. Notice that Figure 6-34 has the same typical curve as Figure 6-31(c).

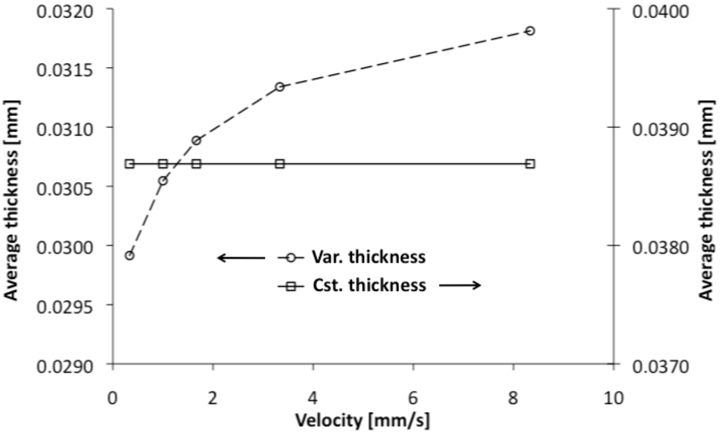

Figure 6-34. Representative interlayer thickness as function of the velocity

The reason for this increase in traction lies with the non-linear decrease of the traction as function of the interlayer thickness as shown in Figure 6-35. The interlayer thickness h calculated from the average traction value, τ, from τ_1 and τ_2, does not agree with the average interlayer thickness h' calculated from the two different thicknesses (h_1= 0.02 mm and h_2= 0.1 mm) corresponding to τ_1 and τ_2.

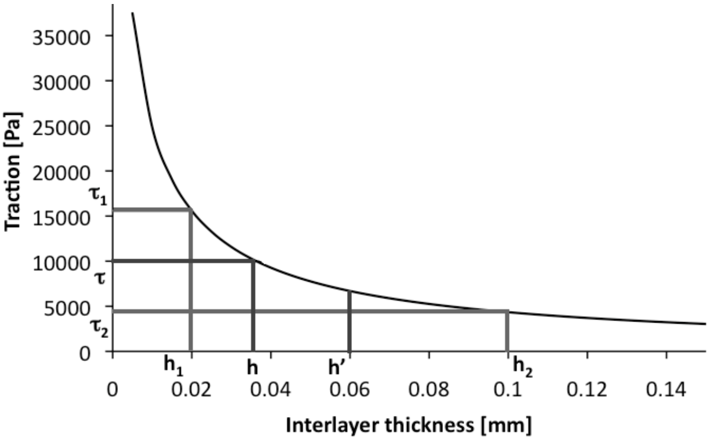

Figure 6-35. Non-linear increase of the traction as function of the interlayer thickness

From the μCt-image presented in Figure 6-8 and Figure 6-21, it is obvious that the interlayer for tool-ply and ply-ply contact has a width spectrum of heights. Therefore, the assumption made by Lamers to consider a constant interlayer results in a too difficult approach to derive a descriptive model.

6.7.2. Stribeck curve

Gorczyca et al. [37] introduced a second descriptive modelling approach for tool-ply friction based on the lubrication theory of Stribeck [46]. From the above-discussed results, it is clear that the matrix plays an important role in the tribological behaviour between the composite laminates. It seems to act as a lubricant between the sliding layers. A useful concept for understanding lubrication is the Stribeck curve as shown in Figure 6-36, which was developed by Richard Stribeck by investigating the basic properties of sliding and roller bearings [46].
The ordinate is the coefficient of friction and the abscissa plots the Hersey number, which is defined as:

$$He = \frac{\eta \cdot v}{F_N} \quad \left[m^{-1}\right]$$ **Eq. 6-15**

Where η equals the viscosity in Pa·s, *v* is the speed of sliding in m/s and F_N is the applied normal force in N. Stribeck developed his theory using lubrication fluids which did not possess shear thinning behaviour. Combining Eq. 6-15 with Newton's viscosity law the following equation appears.

$$He = \frac{\tau}{\dot{\gamma}} \cdot \frac{v}{F_N} = \frac{\tau \cdot h}{v} \cdot \frac{v}{F_N} = \frac{\tau \cdot h}{F_N}$$ **Eq. 6-16**

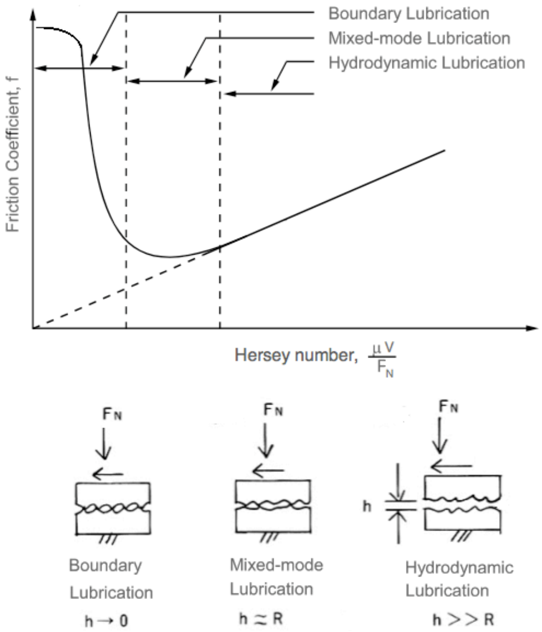

Figure 6-36. Stribeck curve and corresponding lubrication regimes [110]

The Hersey number is proportional to the interlayer thickness, thus a high Hersey number means a relatively thick lubricant film, whereas a small number results in a very thin film.

The different regimes of lubrication have been indicated on Figure 6-36 and they can be linked to the specific contact behaviour that occurs during that regime. In this figure R represents the height of the asperities and forms a measure for the roughness of the surface.

At low Hersey numbers, no real lubricant film can develop and there is significant asperity contact. The thickness of lubrication film, h, is significantly smaller than the roughness of the surface, which results in high friction. These high friction values rapidly decrease with increasing Hersey number, which represents the dominance of boundary lubrication in determining load transfer and friction between surfaces. With a further increase in Hersey number, friction reaches a lower plateau value. The thickness of the lubricant has the same value as the surface roughness, which results in a shared load support between the surface asperities and the pressurized liquid lubricant and is therefore called the mixed-mode lubrication regime. Increasing the thickness even more results in the onset of hydrodynamic lubrication. At this point, the liquid lubricant effectively separates the surfaces, and asperity contact has negligible effect on load support and friction. Figure 6-36 shows an increase in friction with respect to Hersey number in the hydrodynamic regime. Increased friction can be attributed to increased drag of the fluid, i.e. friction produced by the fluid, on the moving surface. The drag force on a moving surface is proportional to the square of the velocity as can be seen in the following equation:

$$F_D = \frac{1}{2} \cdot \rho \cdot v^2 \cdot A_c \cdot C_D \qquad \textbf{Eq. 6-17}$$

Where F_D is the drag force, ρ is the density of the fluid, v is the velocity of the object relative to the fluid, A_c is the contact area and C_D is a dimensionless parameter called the drag coefficient. This equation is attributed to Lord Rayleigh. At low velocities, when no turbulence is present the drag force is proportional to the velocity.

$$F_D = b \cdot v \qquad \textbf{Eq. 6-18}$$

Here v is the velocity of the object relative to the fluid and b is a constant that depends on the properties of the fluid and the dimensions of the object.

The Stribeck curves, shown in Figure 6-37, are constructed for TW_1 for both ply-ply and tool-ply contact. In order to calculate the Hersey number, the thickness of the interlayer needs to be known, since the viscosity needs to be calculated. Gorczyca et al. [37] also assumed a constant interlayer thickness. Although it is not correct, the same assumption is now made. Since the real average interlayer thickness in unknown, the value of the interlayer thickness is taken to be 0.0622 mm for ply-ply friction and 0.0387 mm for tool-ply friction. These values agree with the overall average interlayer thicknesses calculated in the section 6.7.1.

It is clear from the above Stribeck curves, that with increasing Hersey number, the friction coefficient increases monotonically. This agrees with the hydrodynamic regime of lubrication and endorses the fact that the matrix dominates the contact between the plies. As proposed by Gorczyca a linear relationship is found between the Hersey number and the friction coefficient μ:

$$\mu = c_1 \cdot He + c_0 \qquad \textbf{Eq. 6-19}$$

The fitting parameters c_1 and c_0 are indicated in Figure 6-37 and summarized in Table 6-3.

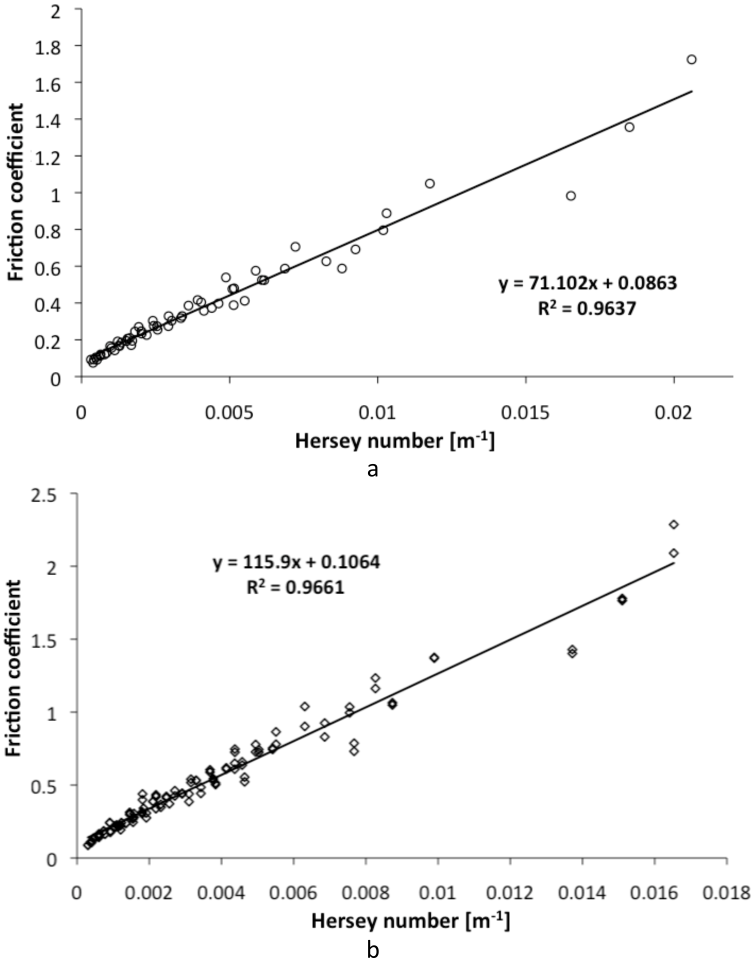

Figure 6-37. Stribeck curves for (a) ply-ply and (b) tool-ply contact for TW_1

Table 6-3. Fitting parameters for the Stribeck curves

Contact type	c_1	c_0
Ply-ply TW_1	71.102	0.0863
Tool-ply TW_1	115.900	0.1064

An important parameter for the Stribeck model is the interlayer thickness. Therefore, the sensitivity of the Stribeck model on the interlayer thickness value will be regarded now for ply-ply contact. The interlayer thickness for ply-ply contact is changed by the standard deviation (0.0622 ± 0.0242 mm) indicated in Table 6-2, the effect on the fitting parameters is shown in Table 6-4. The influence of the interlayer thickness on the friction coefficient as function of the pressure is depicted in Figure 6-38. At low pressures the influence of the interlayer thickness give rise to a difference of 10% in friction coefficient at 0.16 bar. In the high-pressure range, a difference of 26% in friction coefficient is found. This shows the sensitivity of the Stribeck model on the interlayer thickness and limits its applicability.

Table 6-4. Influence of the interlayer thickness on the fitting parameters of the Stribeck curve

Interlayer thickness [mm]	c_1	c_0
0.0380	87.884	0.0727
0.0864	62.574	0.0948

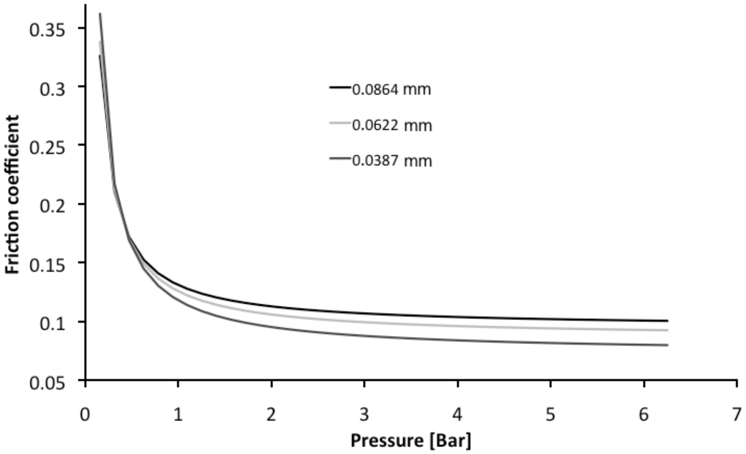

Figure 6-38. Influence of the interlayer thickness on the friction coefficient calculated from the Stribeck curve as function of the pressure

The main benefit of the approach presented by Gorczyca is that it can be used by measuring only a limited amount of data points, through which a linear trendline, according to Eq. 6-19 can be fitted. The main drawbacks are similar as those for the model of Lamers and are associated with the need of knowing the flow behaviour, i.e. the viscosity, of the matrix material, which is not usually provided by the manufacturers of the thermoplastic composites and with the need to predict or measure the interlayer thickness used to calculate the viscosity. To overcome these issues, an alternative model, which does not require the viscosity of the matrix material nor the interlayer thickness, is developed.

6.7.3. Traction model

In this section a model will be developed for both tool-ply and ply-ply contact. It is assumed that the flow behaviour of the matrix material and the height of the interlayer are not known. The traction will be directly represented as an empirical function of the velocity (power law) with the parameters of the law depending on the temperature and pressure. From sections 6.4.2 and 6.5.2 it is known that the influence of the slip velocity on the peak tractions can be described by a power law:

$$\tau_p = \tau_0 \cdot (k \cdot v)^{n_0} \qquad \textbf{Eq. 6-20}$$

Where τ_p is the peak traction in Pa, v is the velocity in mm/s, k equals 1 s/mm and τ_0 and n_0 are fitting parameters. Figure 6-39 presents the peak traction response as function of the slip velocity for different temperatures and normal pressures in case of ply-ply contact for TW_1. The same observations can be noted as presented in section 6.4. The peak traction increases with increasing slip velocity, decreasing temperature and increasing normal pressure.

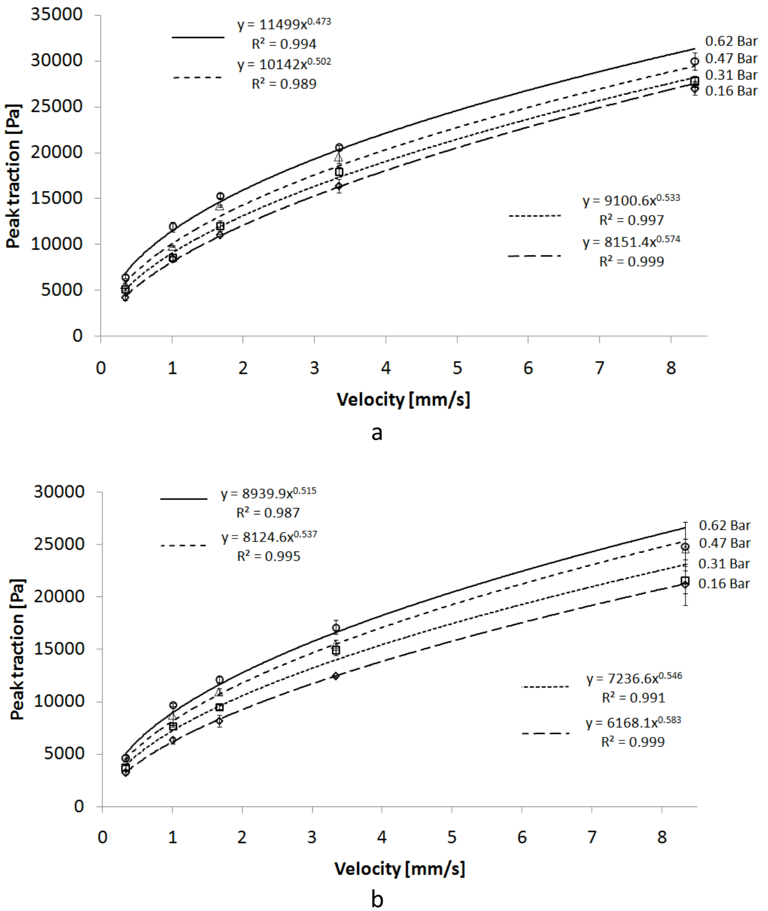

a

b

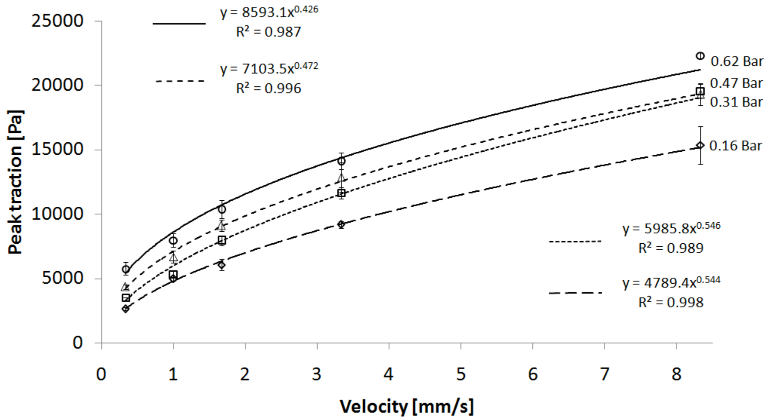

c

Figure 6-39. Influence of the slip velocity on the peak traction in case of ply-ply contact for TW_1 at (a) 180°C, (b) 195°C and (c) 210°C

The power law model parameters, indicated in Eq. 6-20, are summarized in Table 6-5 for ply-ply friction of TW_1 and TP and also for tool-ply friction using TW_1.

Table 6-5. Power-law fitting parameters for different contact types and process conditions

Ply-ply TW_1

Pressure [bar]	0.16		0.31		0.47		0.62	
T[°C]	τ_0 [Pa]	n_0	τ_0 [Pa]	n_0	τ_0 [Pa]	n_0	τ_0 [Pa]	n_0
180	8151.4	0.574	9100.6	0.533	10142	0.502	11499	0.473
195	6168.1	0.583	7236.6	0.546	8124.6	0.537	8939.9	0.515
210	4789.4	0.544	5985.8	0.546	7103.5	0.472	8593.1	0.426

Ply-ply TP

Pressure [bar]	0.16		0.31		0.47		0.62	
T[°C]	τ_0 [Pa]	n_0	τ_0 [Pa]	n_0	τ_0 [Pa]	n_0	τ_0 [Pa]	n_0
180	7753.8	0.621	8016.1	0.618	8573.5	0.626	8526.8	0.632
195	6214.4	0.674	6936.8	0.661	7166.4	0.660	7576.0	0.632
210	4952.5	0.710	5196.0	0.726	6060.7	0.634	6874.8	0.604

Tool-ply TW_1

Pressure [bar]	0.16		0.31		0.47		0.62	
T[°C]	τ_0 [Pa]	n_0	τ_0 [Pa]	n_0	τ_0 [Pa]	n_0	τ_0 [Pa]	n_0
180	11814	0.514	13472	0.493	14264	0.495	14800	0.477
195	9064.4	0.540	10826	0.526	11641	0.520	11913	0.504
210	6410.2	0.585	8584.7	0.556	9885.3	0.539	10455	0.522

Comparing the values of n_0, no real trend of these values is clear. Therefore, it is assumed that in the developed model the power law index is independent of the temperature and normal pressure and is given by the average of the power law indices n_0 measured at different process conditions. The values of the average power law index $\overline{n}_0$ are indicated in Table 6-6.

The assumption of a constant $\overline{n}_0$ is validated by calculating the peak traction at different process conditions and comparing the results with the experimental data. Figure 6-40 shows that for all contact conditions and different contact types, the slope of the linear trend line is approximately 1 and the R^2-value is close to 1. This endorses that the use of an average power law index to incorporate the velocity dependence of the frictional behaviour is a valid assumption.

Table 6-6. Average power-law index for different contact types

Contact	$\overline{n}_0$
Ply-ply TW_1	0.521 ± 0.05
Ply-ply TP	0.650 ± 0.04
Tool-ply TW_1	0.523 ± 0.03

As noticed in sections 6.4.3 and 6.5.3, the influence of the temperature on the peak traction can be described by an Arrhenius equation (Eq. 6-8). Using the same type of equation to describe the thermal influence on τ_0 for different normal pressures results in Figure 6-41.

The equation fitted through the different traction parameters of the power-law model has the form:

$$\ln(\tau_0) = Ar_0 \cdot T^{-1} + Ar_1 \qquad \textbf{Eq. 6-21}$$

The high R^2-values indicate that the Arrhenius model is adequate to describe the thermal influence on τ_0. The factors arising from the Arrhenius model are summarized in Table 6-7.

Table 6-7. Fitting parameters for the Arrhenius model that describes τ_0

Pressure [bar]	0.16		0.31		0.47		0.62	
Contact type	Ar_0	Ar_1	Ar_0	Ar_1	Ar_0	Ar_1	Ar_0	Ar_1
Ply-ply TW_1	3879.1	0.441	3057.6	2.362	2603.1	3.466	2140.3	4.593
Ply-ply TP	3268.0	1.745	3149.8	2.061	2529.7	3.471	1909.5	4.872
Tool-ply TW_1	3894.1	0.784	3283.8	2.262	2677.2	3.653	2540.0	3.982

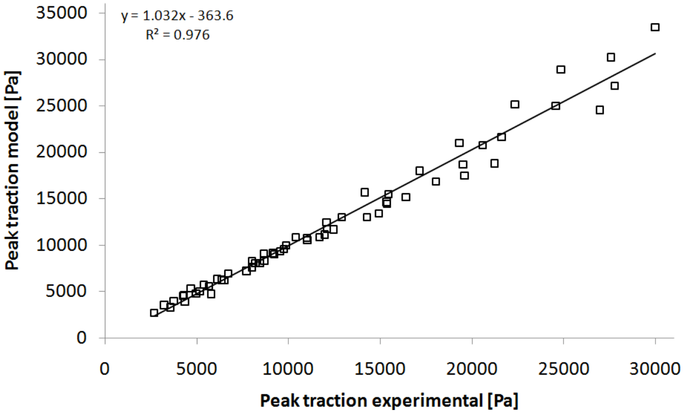

a

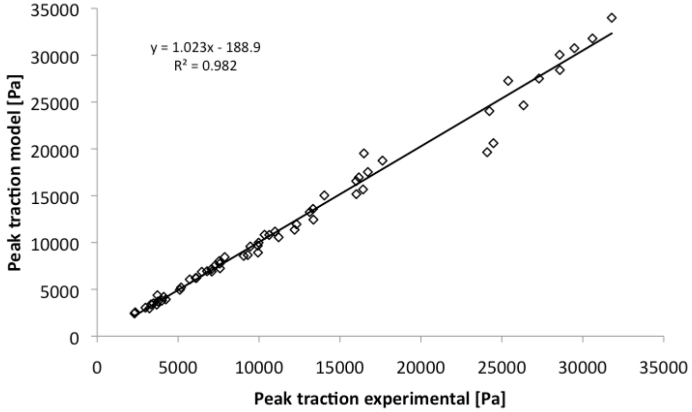

b

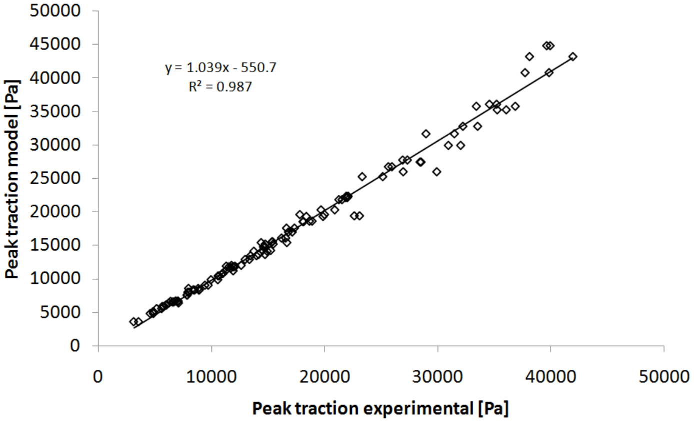

c

Figure 6-40. Predicted peak traction by assuming a constant power-law index compared with the experimentally measured peak traction for (a) ply-ply contact TW$_1$, (b) ply-ply contact TP and (c) tool-ply contact TW$_1$

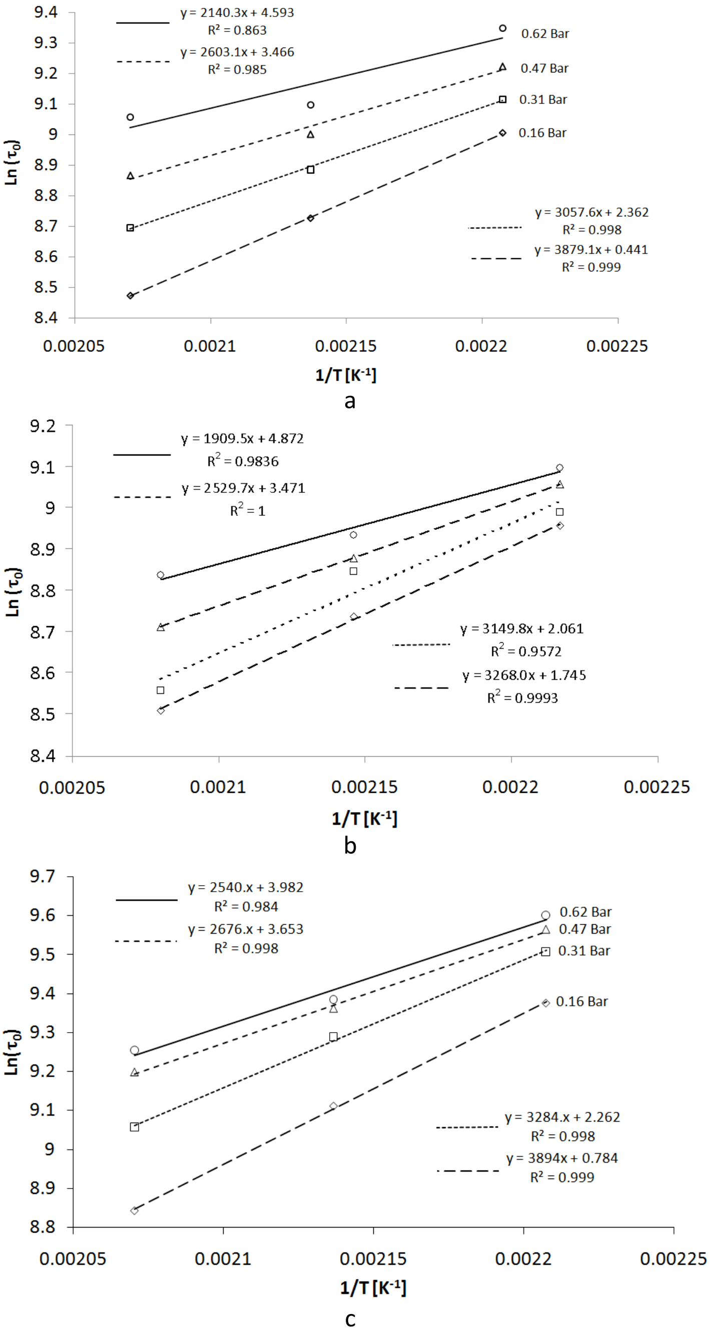

Figure 6-41. The natural logarithm of τ_0 as function of the reciprocal of the temperature for (a) ply-ply contact TW_1, (b) ply-ply contact TP and (c) tool-ply contact TP.

The influence of the normal pressure on the factors of the Arrhenius model are now investigated by plotting the A and B-factors versus the normal pressure. In Figure 6-42 a linear trend with a relatively high R^2-factor is found for both the A and B factor as function of the normal pressure.

$$Ar_0 = A_0 \cdot P + A_1 \quad \textbf{Eq. 6-22}$$

$$Ar_1 = B_0 \cdot P + B_1 \quad \textbf{Eq. 6-23}$$

Using the data presented above, the following model that describes the peak traction as function of the velocity, temperature and normal pressure is proposed.

$$\tau_p = \tau_0 \cdot (k \cdot v)^{\bar{n}_0} \quad \textbf{Eq. 6-24}$$

Where by *v* is the velocity in mm/s, *k* equals 1 s/mm and $\bar{n}_0$ is a power law coefficient, which is independent on the velocity, temperature and normal pressure.

The fitting parameter τ_0 is dependent on the temperature according to an Arrhenius law given by Eq. 6-21. The fitting parameters in Eq. 6-21 are, in their turn, dependent on the normal pressure according to Eq. 6-22 and Eq. 6-23. Combining these equations results in:

$$\tau_0 = \exp\left(B_0 \cdot P + B_1 + \left(\frac{A_0 \cdot P + A_1}{T}\right)\right) \quad \textbf{Eq. 6-25}$$

This equation can be simplified to:

$$\tau_0 = B_1' \cdot \exp(B_0 \cdot P) \cdot \exp\left(\frac{A_0 \cdot P + A_1}{T}\right) \quad \textbf{Eq. 6-26}$$

$$B_1' = \exp(B_1) \quad \textbf{Eq. 6-27}$$

Where τ_0 is the peak traction in Pa, *v* is the slip velocity in mm/s, *P* is the pressure in bar and *T* is the temperature in K. The values of the fitting parameters for the different contact types are given in Table 6-8.

Table 6-8. Fitting parameters for the traction model

Contact type	A_0 [K/bar]	A_1 [K]	B_0 [bar $^{-1}$]	B'_1 [Pa]	$\bar{n}_0$
Ply-ply TW_1	-3629.4	4338	8.678	0.510	0.521
Ply-ply TP	-3005.2	3888	6.906	1.405	0.650
Tool-ply TW_1	-3035.1	4283	7.139	0.893	0.523

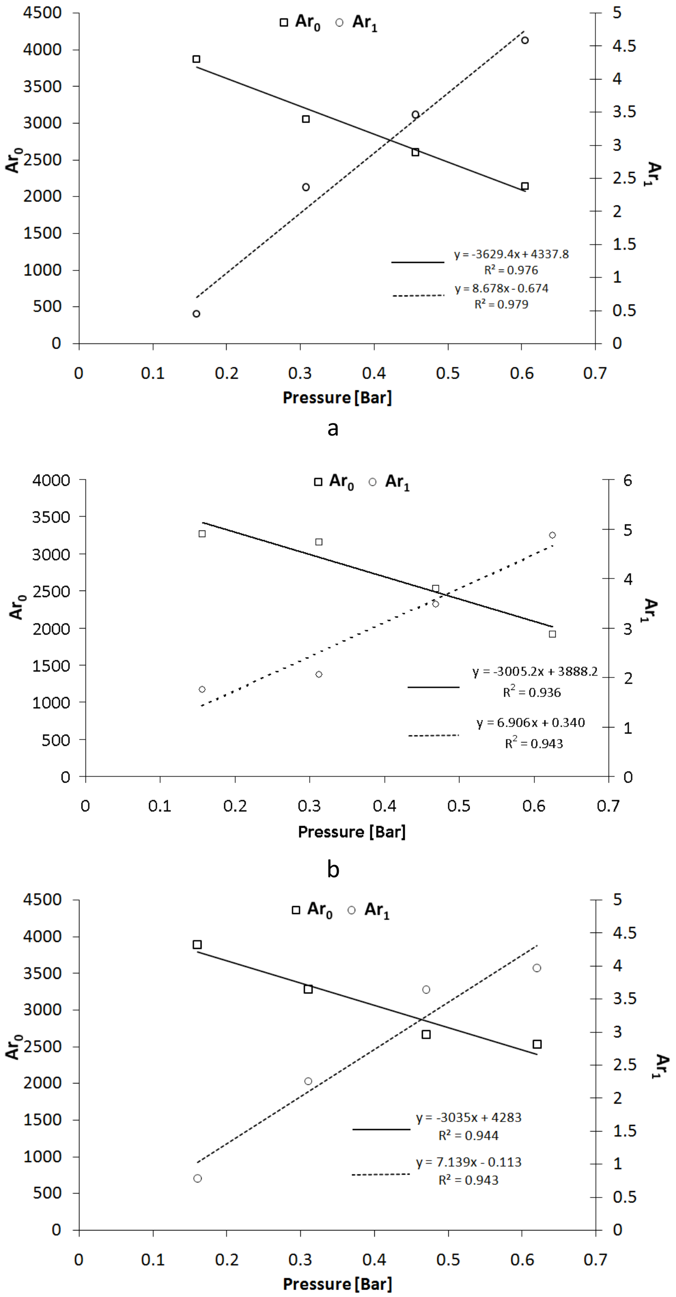

a

b

c

Figure 6-42. Fitting parameters Ar_0 and Ar_1 from the Arrhenius model as function of the pressure for (a) ply-ply contact TW_1, (b) ply-ply contact TP and (c) tool-ply contact TW_1

In Figure 6-43, the peak tractions calculated from this model are compared to the experimentally measured peak tractions. The slope of the linear trendline is close to one and the R^2-values for all contact types are very high, which indicates the traction model forms a good description of the peak traction for the different contact types.

Eq. 6-26 is also implemented in MATLAB and the method of least squares is used to find the parameters A_0, A_1, B_0, B'_1 and $\bar{n}_0$ of the model. The unknown fitting parameters are determined by minimizing the sum of the squares of the deviations of the data from the model. The input to find the fitting parameters consists of the peak traction values determined using the pull-out method and the process conditions used during the experiment, i.e. velocity, temperature and normal pressure. The results of this analysis are shown in Table 6-9.

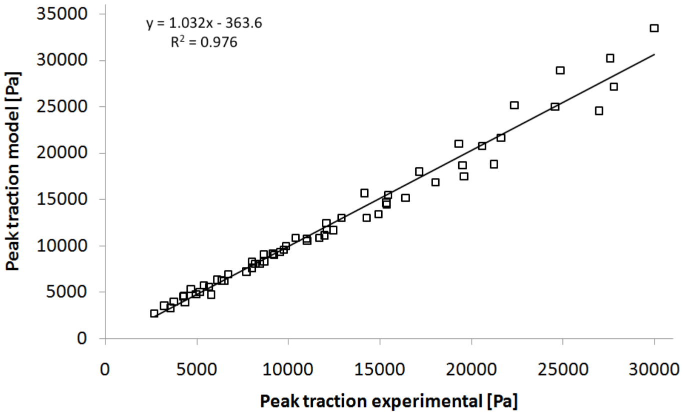

a

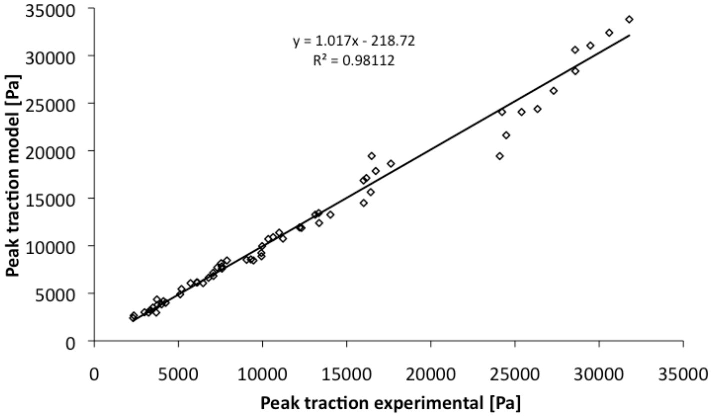

b

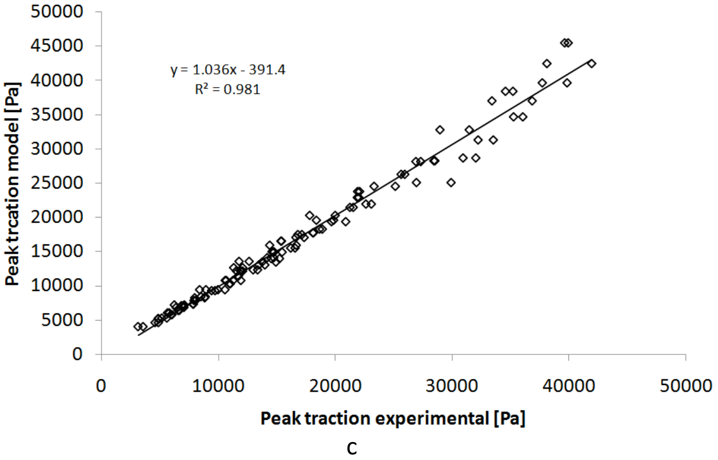

Figure 6-43. Predicted peak traction by the traction model compared with the experimentally measured peak traction for (a) ply-ply contact TW_1, (b) ply-ply contact TP and (c) tool-ply contact TW_1

Table 6-9. Fitting parameters of the traction model using method of least squares

Contact type	A_0 [K/bar]	A_1 [K]	B_0 [bar $^{-1}$]	B'_1 [Pa]	$\bar{n}_0$	R^2
Ply-ply TW_1	-3400.4	4338.5	8.073	0.532	0.521	0.9811
Ply-ply TP	-3259.1	3552.3	7.398	2.953	0.649	0.9870
Tool-ply TW_1	-3816.1	4506.9	8.799	0.550	0.523	0.9855

The percentile difference between Table 6-8 and Table 6-9 is given in Table 6-10. For most fitting parameters the difference is relatively small, except for B'_1 for which a difference of 62% is found in case of tool-ply contact.

Table 6-10. Difference between the fitting parameters

Contact type	ΔA_0 [%]	ΔA_1 [%]	ΔB_0 [%]	$\Delta B'_1$ [%]	$\Delta \bar{n}_0$ [%]
Ply-ply TW_1	6.73	0.01	7.49	4.14	0.00
Ply-ply TP	7.79	9.45	6.65	52.42	0.15
Tool-ply TW_1	20.47	4.97	18.87	62.36	0.00

The deviation between the parameters when all experiments are regarded at once and the parameters shown in Table 6-8 is probably due to the fact that in the derivation of the model parameters in Table 6-8 round off errors might have occurred.

The robustness of this model is tested by gradually decreasing the number of experiments and then determining the unknown fitting coefficients. Afterwards, the R^2-value of the model is calculated with respect to the total number of experiments. The robustness is tested for ply-ply and tool-ply contact for TW_1. First, the number of experiments that is considered is decreased by randomly choosing 25, 50 and 75% of all the peak traction values that have been measured using the pull-out apparatus. This procedure is repeated 20 times, each time randomly choosing a certain percentage, i.e. 25, 50 or 75%, of the total peak traction values. Afterwards an average R^2-coefficient is calculated.

Table 6-11 summarizes the results where the percentage of considered tests is indicated in brackets and where R^2_{avg} is the average and R^2_{min} is the minimum R^2-value found within the 20 repeats.

Table 6-11. The average and minimum R^2-value obtained for the traction model using a different number of experimental data in combination with the multiple regression analysis

Contact type	R^2_{avg}	R^2_{min}
Ply-ply TW_1 (25%)	0.9661 ± 0.0217	0.8997
Ply-ply TW_1 (50%)	0.9762 ± 0.0046	0.9687
Ply-ply TW_1 (75%)	0.9774 ± 0.0038	0.9672
Ply-ply TW_1 (ref)	0.9811	
Tool-ply TW_1 (25%)	0.9781 ± 0.0105	0.9548
Tool-ply TW_1 (50%)	0.9823 ± 0.0036	0.9757
Tool-ply TW_1 (75%)	0.9832 ± 0.0020	0.9800
Tool-ply TW_1 (ref)	0.9855	

Increasing the percentage of experimental points that are taken into account to determine the fitting coefficient increases the R^2-value of the model, which means the model describes the contact behaviour better. However, at only 50% of the performed experiments the R^2-value is relatively high and has a low standard deviation. Thus reducing the number of performed experiments with 50%, which in case of this study means a decrease from 180 to 90 experiments per contact type, still gives a good evaluation of the model. Even when considering only 25%, i.e. 45 experiments, of the total peak traction values, the model still possesses relatively high R^2-values.

However, a concern is raised when investigating the traction model outside the tested range. It is noticed that the influence of the pressure on the response of the traction model behaves unnaturally. Figure 6-44 depicts the friction coefficient and traction as function of the normal pressure for the traction model.

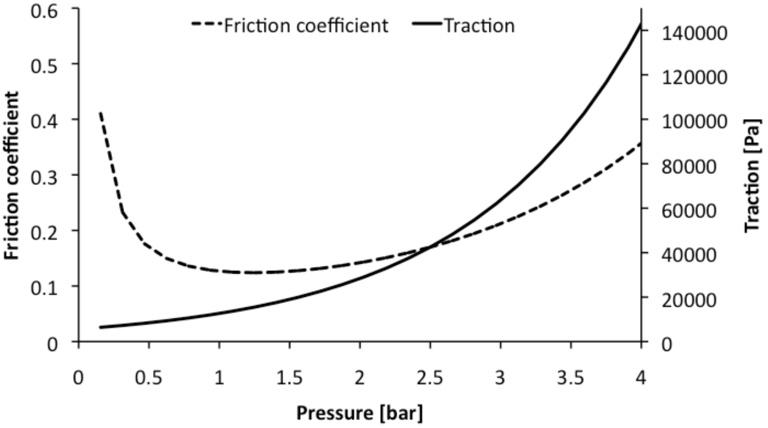

a

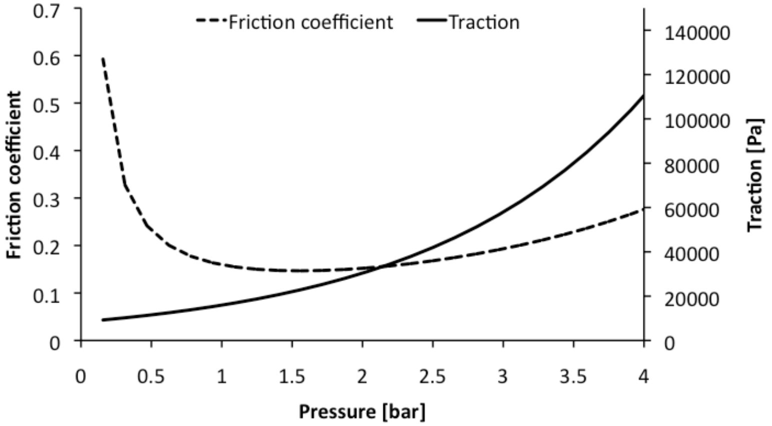

b

Figure 6-44. Peak traction and peak friction coefficient as function of the pressure calculated from the traction model for (a) ply-ply contact TW$_1$ and (b) tool-ply contact TW$_1$

It is noticed that at high pressures the friction coefficient increases dramatically. This increase is due to the fact that the factors determining the influence of the pressure on the traction lie within an exponential function. Previous studies mention that the friction coefficient decreases at higher pressure values [35, 36]. Therefore, it is not appropriate to use the model outside the range tested in the experiments. To compensate for this increase a boundary condition is added to the traction model:

$$P > P_{cr} : \mu = \mu_{cr} \qquad \textbf{Eq. 6-28}$$

When a critical pressure, P_{cr}, is reached, the influence of the pressure on the friction coefficient is neglected. This critical pressure is defined as the pressure whereby the minimum friction coefficient is reached as indicated in Figure 6-45.

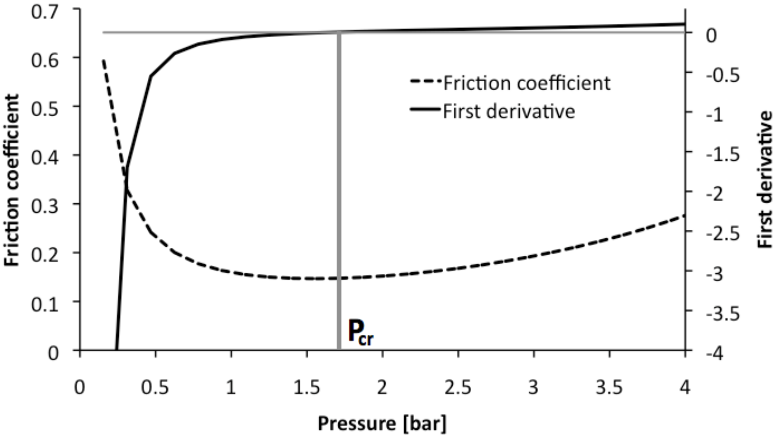

Figure 6-45. Determination of P_{cr} for tool-ply contact TW_1 at 195°C

After this pressure is reached, the friction coefficient is considered independent of the pressure. The results are indicated in Table 6-12.

Table 6-12. P_{cr} and μ_{cr} for different temperatures and contact types

Contact type	180°C	195°C	210°C
Ply-ply TW_1 (P_{cr})	1.846 bar	1.323 bar	1.054 bar
Ply-ply TW_1 (μ_{cr})	0.118	0.124	0.119
Tool-ply TW_1 (P_{cr})	2.748 bar	1.634 bar	1.198 bar
Tool-ply TW_1 (μ_{cr})	0.118	0.147	0.152

The critical pressure is found independent on the slip velocity. The temperature, however, has a large influence on the value of the critical pressure. The difference in critical friction coefficient is relatively independent of the temperature. To not severely increase the complexity of the model, the value of the critical pressure for each contact type is taken as the average of the values in Table 6-12, meaning 1.41 bar for ply-ply contact and 1.86 bar for tool-ply contact. This extra boundary condition results in the figure-pressure plot shown in Figure 6-46.

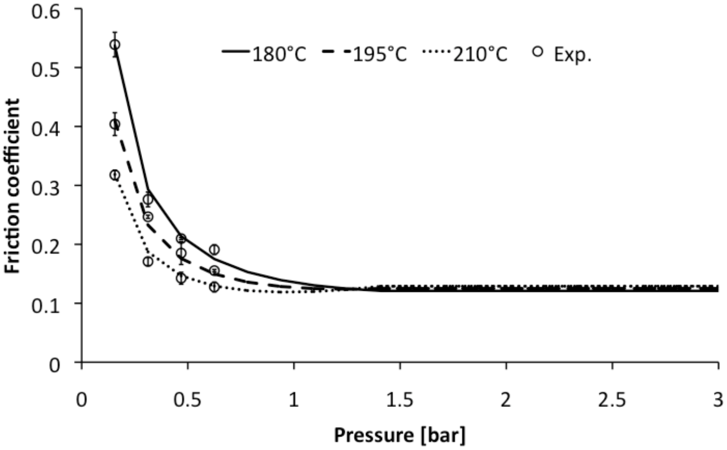

a

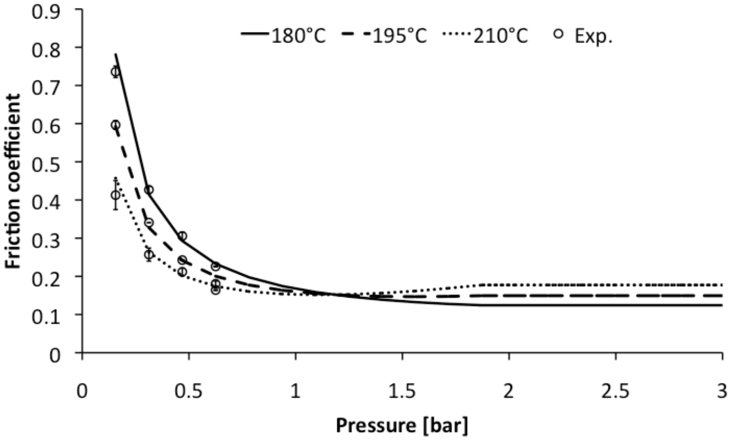

b

Figure 6-46. Peak friction coefficient as function of the pressure calculated from the traction model using the P_{cr} as a boundary condition for (a) ply-ply contact and (b) tool-ply contact.

At low-pressure values a good comparison is found between the predicted friction coefficient and the experimental values. In the high-pressure range the boundary condition counteracts the influence of the temperature on the friction, which forms a limitation of the presented model. For pressures higher than the critical pressure the traction value is calculated according to the following equation:

$$\tau = \mu_c \cdot P = \frac{F_{cr}}{2 \cdot F_{N,cr}} \cdot P = \frac{\frac{F_{cr}}{2 \cdot A_c}}{\frac{F_{N,cr}}{A_c}} \cdot P = \frac{\tau_{cr}}{P_{cr}} \cdot P \qquad \textbf{Eq. 6-29}$$

Where τ_{cr} is the critical peak traction calculated according to Eq. 6-26, using the critical pressure P_{cr} and P is the actual pressure. F_{cr} is the force associated with the critical peak traction and $F_{N,cr}$ is the force associated with the critical pressure. A_c is the area over which the pressure is acting. The 2 is related to the 2 contacting surfaces, namely the two outer plies with the middle ply.

In this section, an alternative model is developed. The model is based on the behaviour of the peak traction as function of the process parameters. The major benefit of this model is that there is no need to know the flow behaviour of the matrix or the interlayer thickness. The major drawbacks are the high number of experiments that need to be performed, though by using a random experiment design this number can be drastically decreased. At higher-pressure values, the model needs to be extended by an extra boundary condition increasing the complexity of the model.

6.8. Comparison between different models

In this section two presented descriptive models, namely the Stribeck and the traction model, will be compared to each other over a wide range of process conditions.

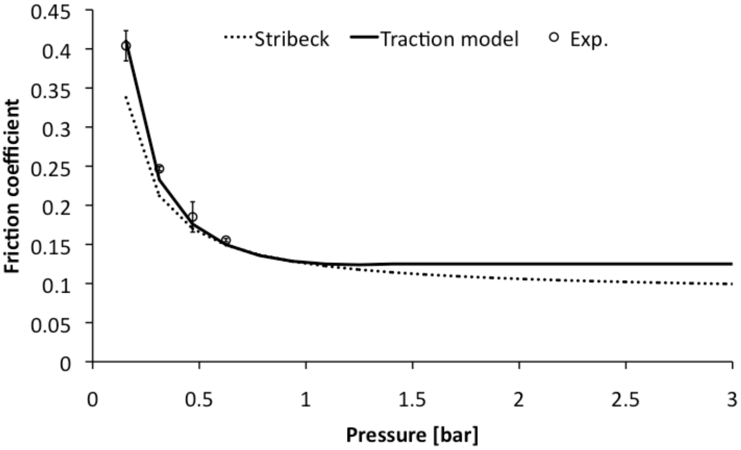

a

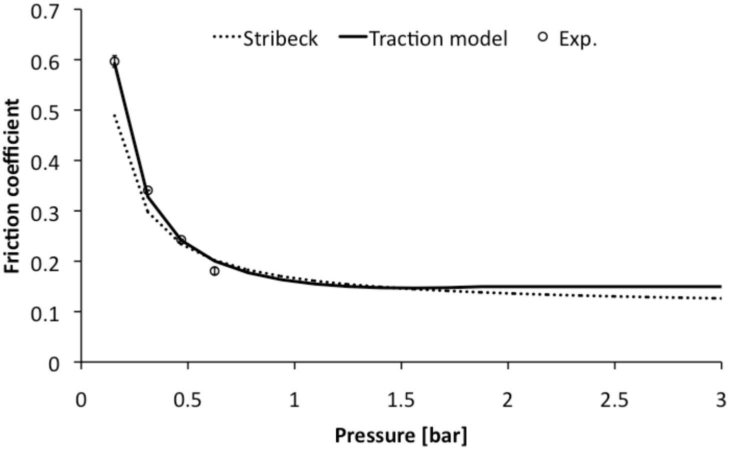

B

Figure 6-47. Comparison of the models as function of the pressure for (a) ply-ply contact TW$_1$ and (b) tool-ply contact TW$_1$ (T=195°C, v=100 mm/min)

Finite element simulation software uses the friction coefficient as an input for the calculation of the contact forces, the peak friction coefficient will be used to evaluate the different models. In Figure 6-47, 6-48 and 6-49 the traction model is compared with the Stribeck model, which is constructed using the average thicknesses from Table 6-2, and the experimental data. In Figure 6-47 the Stribeck model does not show an increasing friction coefficient with increasing pressure at high pressure values, thus no boundary condition is needed. A good agreement is found for both descriptive models. However, in the low-pressure region the adjusted traction model gives a better fit of the friction coefficient. Unfortunately, no experimental data is available in the high-pressure range.

The same comparison is made for the thermal and velocity dependence of the friction coefficient in Figure 6-48 and Figure 6-49. The Stribeck model and traction model both show the same trend, namely an increasing friction coefficient at lower temperatures and higher velocities. At low friction coefficients a good agreement is found between the Stribeck approach, the traction model and the experiments. At high friction coefficient, however, the traction model seems more capable of accurately describing the experimentally found points.

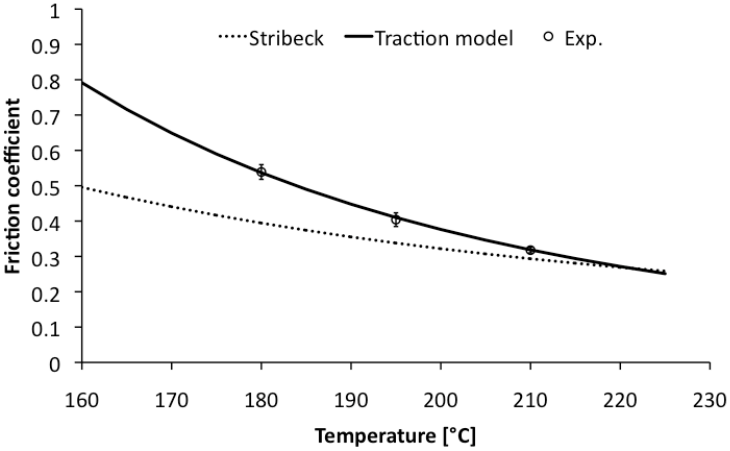

a

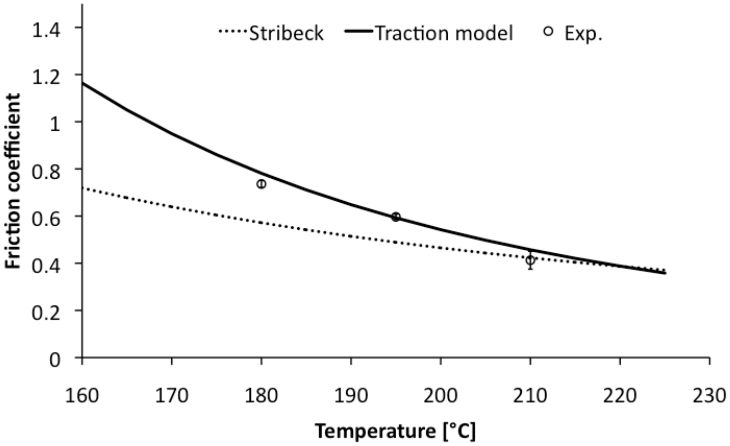

B

Figure 6-48. Comparison of the models as function of the temperature for (a) ply-ply contact TW$_1$ and (b) tool-ply contact TW$_1$ (P=0.16 bar, v=100 mm/min)

Therefore, the traction model seems the most adequate to describe the influence of the velocity, the temperature and the pressure on the contact behaviour. This model will be implemented and used to predict the friction coefficient in commercial simulation software in Chapter 7.

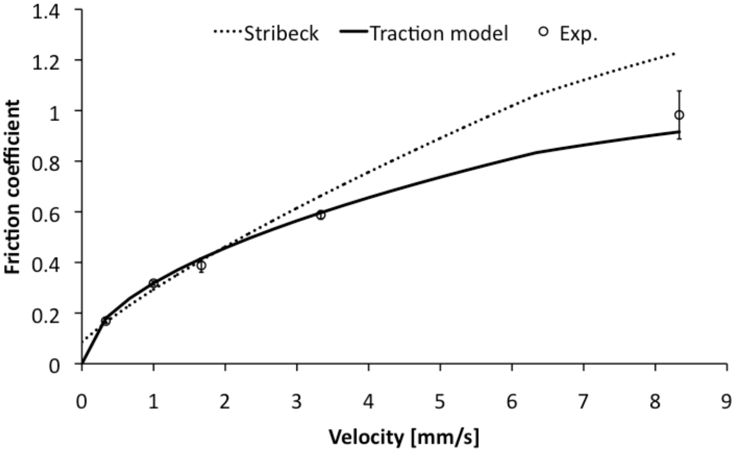

a

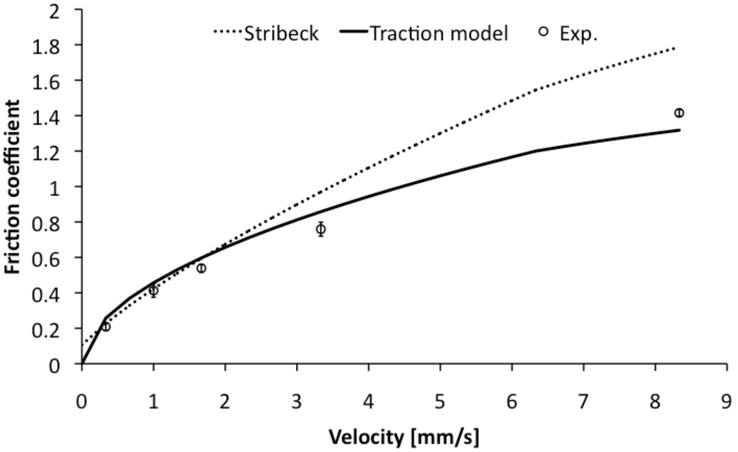

b

Figure 6-49. Comparison of the models as function as function of the velocity for (c) ply-ply contact TW$_1$ and (b) tool-ply contact TW$_1$ (P=0.16 bar, T=195°C)

6.9. Conclusions

This chapter consists of a study of the inter-ply and tool-ply slip behaviour of several glass-pp woven composites at different process conditions. The characterization of the contact behaviour is performed using an in-house developed pull-out set-up. The gathered data is used to create a descriptive model, which will be implemented in a FE software package in Chapter 7.

Inter-ply and tool-ply slip experiments showed that the contact behaviour between thermoplastic composites is influenced by the transient rheological behaviour of the matrix. An initial peak traction, which is associated to the shear stress overshoot at the start of shear flow, is used to determine the influence of slip velocity, temperature, pressure and interlayer thickness.

Three descriptive models, which are based on experimentally obtained data and try to describe how the friction coefficient or traction depends on the process conditions, were investigated and compared to each other:

- Model of Lamers
  This model is based on the viscous behaviour of the inter-ply and tool-ply slip mechanism. It starts from Newton's equation of viscosity and Lamers assumes that the variable interlayer between two contacting plies can be replaced by a constant average interlayer. It is shown that the assumption of a constant average interlayer is not correct and leads to a too cumbersome approach to derive a valid descriptive model.

- Stribeck approach
  The Stribeck curve is an empirically developed model, which is based on the lubrication theory for journal bearings. It assumes that the rheological behaviour of the matrix and the interlayer thickness are known or can be predicted. In this study an average interlayer thickness, based on inversely solving Newton's equation of viscosity, is estimated. The Stribeck curve leads to a good approximation of the contact behaviour for the pressure dependence, though at process conditions that lead to high friction coefficients some discrepancies are found.

- Traction model
  The traction model, which is developed in this PhD, is based on the observations made during pull-out experiments. Its key benefits are that it does not require the rheological behaviour of the matrix nor the height of the interlayer as an input. However, an important concern is the behaviour of the model in the high-pressure range. An unnatural increase in the traction is noticed, which is compensated by a minor increase in the complexity of the model.

In Chapter 7 the traction model will be implemented in a commercial FEM-software package. The traction model will there be used as a predictive model. The fitting coefficients determined in this chapter will be used to predict the friction coefficients that occur during forming of thermoplastic composites.

Chapter 7

Forming simulation of multilayered composite materials

7.1. Introduction

Simulation tools for fabric forming are developed to assist the design and process optimization. In Chapter 5, the forming behaviour of multilayered woven thermoplastic composites is investigated on an experimental scale. However, these kinds of studies require not only a large amount of time, but also the cost of materials and tooling. In order to reduce these costs, the quality of the product after draping is assessed using drape-forming simulations. In Chapter 1 and Chapter 4 two approaches, the kinematic and the finite element method for forming of single layered composite structures were introduced. From Chapter 4 it is obvious that the mechanical method is the most appropriate to predict the automated forming of woven textiles composites.

In this chapter, the traction model (see Chapter 6) that describes tool-ply and inter-ply contact behaviour is implemented in a commercial finite element environment (ABAQUS-explicit) and combined with a model for fabric drape developed by Willems [64] to assess the draping of multilayered woven composites. The goal of this chapter is to be able to predict whether wrinkling would occur during forming.
First, the Affine Elastic Model (AEM) developed by Willems is introduced in section 7.2. This model predicts the forming of a single woven composite. This material model requires the input of the biaxial tensile behaviour and the shear behaviour of the considered material.
In the second part of this chapter, the traction model is implemented in ABAQUS by using a user subroutine. In Chapter 6 it has been observed that the contact behaviour between two plies and the tooling and ply is dependent on the velocity, temperature, pressure and interlayer thickness. The calculation of each of these process conditions within the user subroutine is discussed in section 7.3. Afterwards the pull-out test introduced in Chapter 6 will be modelled in ABAQUS-explicit and the simulated results are compared to experimentally measured pull-out tests.
Wrinkling of membrane structures is not straightforward, since they do not possess any bending stiffness. Therefore, the third part of this chapter will

introduce the tension field theory that is commonly used to visualize wrinkling of membrane elements (Section 7.4).

To finish this chapter the deepdrawing experiments performed in Chapter 5 are repeated in ABAQUS. The minimum principal stress, i.e. the maximum compressive stress, will be used as a criterion for wrinkling. A comparison will be made between the obtained FLD in Chapter 5 and the predictions made using the finite element method.

7.2. Affine elastic model (AEM)

In order to predict the forming of single layered fabric-reinforced structures. Willems [64] has developed a macroscopic homogeneous elastic model for the draping of textile prepregs based on the previous work of Hagege [111]. She incorporated the in-plane textile drape behaviour, i.e. intra-ply shear and biaxial tension, within a plane stress element. One of the major challenges she tackled was the tracking of the fibre orientations, defined as the principal material directions (PMD's) by Willems, within the element during draping. Therefore, she makes use of a curvilinear material frame, which is shown in Figure 7-1. The constitutive axes of the material frames are aligned with the principal material directions in the reference state. This implies that for the woven structures that are examined in this PhD, the laminate is meshed by elements that are rectangles or right-angled triangles. Only these types of elements can be used since the AEM assumes that in the initial undeformed configuration the edges of the elements are parallel to the PMD's (warp and weft).

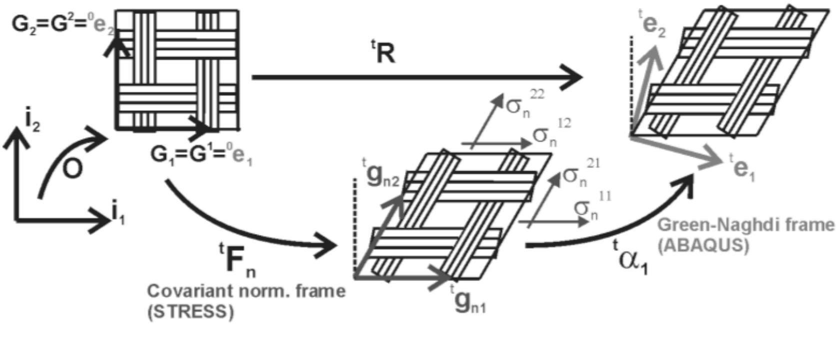

Figure 7-1. Transport of the covariant material frame and Green-Naghdi frame from the initial state to the actual state. (Adapted from [64])

Since ABAQUS uses the co-rotational Green-Naghdi frame to express the stress and strain tensors, a rotation from the curvilinear material frame to the Green-Naghdi frame is needed. The individual PMD's are tracked by the normalized covariant base vectors $\mathbf{g}_{ni}$. The stretch λ_i in each PMD equals the norm of the covariant base vector $\mathbf{g}_i$ and the stress components are calculated using:

$$\sigma_n^{11} = \frac{F_{t1}}{c\lambda_3\lambda_2\cos(\gamma)} \qquad \textbf{Eq. 7-1}$$

$$\sigma_n^{22} = \frac{F_{t2}}{c\lambda_3\lambda_2\cos(\gamma)} \qquad \textbf{Eq. 7-2}$$

$$\sigma_n^{12} = \sigma_n^{21} = \frac{f_{shear}}{c\lambda_3\cos(\gamma)} \qquad \textbf{Eq. 7-3}$$

Where σ_n^{11}, σ_n^{22} and σ_n^{12} are the Cauchy stress components in the covariant normalized frame, λ_i is the stretch along the strong direction of anisotropy i (i=1,2).

The shear angle, angle between $\mathbf{g}_{n1}$ and $\mathbf{g}_{n2}$, is given as γ, while F_{ti} is the tensile force per initial unit width along the PMD's. The original thickness of the textile is given as c and f_{shear} is defined as the shear force per deformed width. Both the tensile and shear resistance (see section 7.2.1 and 7.2.2) are determined as the force per unit width, the thickness change is not considered. From the experiments no direct measurement for the thickness change is possible. Therefore, Willems restricted the thickness to remain constant, which implies that λ_3=1 and to consider only in-plane stresses.

In Figure 7-1, $\mathbf{F_n}$ is the normalized deformation gradient and **R** is the Green-Naghdi rotation tensor. After the stress is updated in the normalized covariant frame, the stress components are transformed back to the Green-Naghdi frame using a rotation tensor α_1, see Appendix A in [64], and then the Green-Naghdi stress matrix is updated in ABAQUS.

The constitutive model requires the tensile and shear resistance for the material, which can be obtained using virtual or experimental testing. Willems determined the tensile and shear resistance for TW_1 and TW_2 using respectively a biaxial tensile machine and picture frame apparatus.

The AEM can be implemented for both membranes as shell structural elements on the condition that they have a square or right-angled triangle shape. These types of elements are suitable to represent very thin structures with a high length over thickness ratio, e.g. fabric constructions. The major difference between membrane and shell elements lies in their bending response. Membrane elements have no flexural stiffness, while shell elements possess resistance to bending. A consequence of this difference is the extra 3 rotational degrees of freedom for shell elements with respect to only 3 translational degrees of freedom per node for a membrane structure. This results in a higher computational time for simulations that use shell elements to represent composite structures. In [64] the AEM is applied in combination with membrane elements to predict the fibre reorientation of woven reinforced composites during forming. A major drawback of using membrane structural elements is formed by there are unable to predict and visualize wrinkling, which is discussed in one of the following sections.

7.2.1. Tensile resistance

The tensile diagram of the fabric in warp and weft directions are considered uncoupled. This implies that within the subroutine it is assumed that the strain in the warp direction does not influence the stiffness in the weft direction and vice versa. A typical curve is depicted in Figure 7-2. The non-linear behaviour is due to the undulation of the yarns in the fabric at small strains.

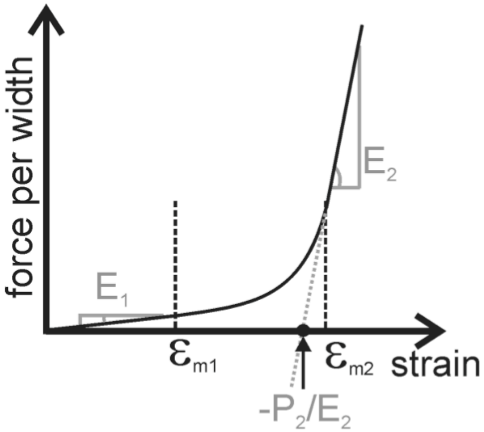

Figure 7-2. Format that is used to describe the tensile curves in the material model [64]

If both directions are strained at the same moment, both yarn directions are subjected to decrease in undulation. It is clear that in reality the phenomenon is biaxial and that warp and weft yarns interact with each other during forming. Thus in reality the force per unit width is depending on both the warp and weft strain. The influence of considering this biaxial behaviour during forming is not yet reported.

The tensile curves in warp and weft direction are subdivided into three regions, each of which is approximated by a polynomial function.

- Linear low stiffness region: when the strain falls within 0 and ε_{m1} the tensile force per unit width, F_{ti}, is linearly dependent on the strain ε, whereby the regression coefficient E_1 has the units of N/mm

$$F_{ti} = E_1\varepsilon \qquad \textbf{Eq. 7-4}$$

- Third order transition zone: when the strain ranges between ε_{m1} and ε_{m2} a third order polynomial function describes the force-strain relationship

$$F_{ti} = c_3\varepsilon^3 + c_2\varepsilon^2 + c_1\varepsilon + c_0 \qquad \textbf{Eq. 7-5}$$

- Linear high stiffness region: when the strain is larger or equals ε_{m2} a linear relationship between the force per initial width and strain

$$F_{ti} = E_2\varepsilon + P \qquad \textbf{Eq. 7-6}$$

Willems determined the fitting parameters for TW_1 and TW_2 in case of dry, i.e. not preconsolidated fabrics using a biaxial tensile tester.

7.2.2. Intra-ply shear resistance

The intra-ply shear resistance is measured using the picture frame depicted in Figure 7-3. This frame is mounted on an Instron tensile testing machine and introduces a homogeneous deformation within the sample. A typical force per deformed width versus shear angle is depicted in Figure 1-12(b).

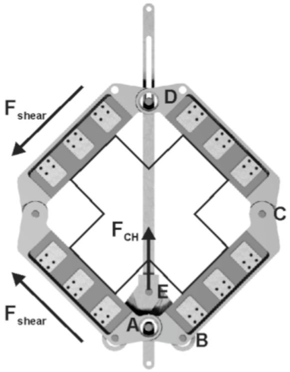

Figure 7-3. Schematic representation of the picture frame used to measure the in-plane shear resistance [64]

The intra-ply shear resistance is provided to the material subroutine in ABAQUS by approximating the shear curves by a polynomial function of order ≤ 11.

$$f_{shear} = \sum_i c_i \cdot \gamma^i \ (i \le 11) \qquad \textbf{Eq. 7-7}$$

7.2.3. AEM model parameters

This section gives an overview of the material parameters used to describe the tensile and shear behaviour introduced in 7.2.1 and 7.2.2.
The fitting parameters for Eq. 7-4, 7-5 and 7-6 are summarized in Table 7-1.
Figure 7-4 visualizes the uncoupled tensile curves using the fitting parameters. The low stiffness at the beginning of the tensile curve is due to the initial

undulation of the yarns in the tensile direction. Gradual de-crimping causes the yarns to straighten and thus deformation becomes more difficult.

Table 7-1. The fitting parameters that identify the uncoupled tensile curves. Units for tensile force per initial unit width F_{ti} is in N/mm [64]

	ε_{m1}	ε_{m2}	E_1	E_2	P_2
TW_1 warp	1.00E-2	1.70E-2	9.38E+1	2.45E+3	-3.44E+2
TW_1 weft	6.00E-3	1.15E-2	2.82E+2	1.04E+4	-9.54E+1
TW_2	2.20E-2	3.20E-2	5.98E+1	4.83E+3	-1.39E+2

	C_3	C_2	C_1	C_0
TW_1 warp	1.55+7	-4.60E+5	4.64E+3	-1.50E+1
TW_1 weft	8.65E+7	-1.35E+6	7.19E+3	-1.14E+1
TW_2	2.07E+7	-1.44E+6	3.32E+4	-2.55E+2

The large difference between the warp and weft direction for TW_1 finds its origin in the difference in crimp between these directions. In Table 3-1 it is mentioned that the crimp in the warp direction is 10.3%, while there is a negligible amount of crimp in the weft direction.

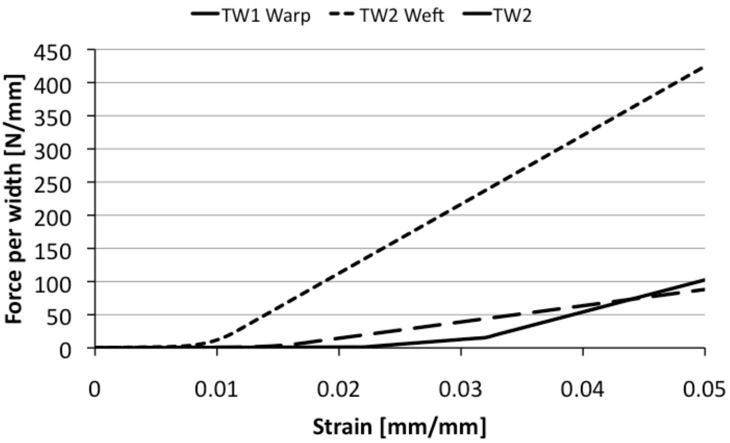

Figure 7-4. Tensile diagram for fabrics TW_1 and TW_2

The fitting coefficients for intra-ply shear resistance (Eq. 7-7) were determined by Willems for dry fabric of TW_1 and TW_2 and are summarized in Table 7-2. Figure 7-5 visualizes the shear curves using the fitting parameters, whereby it is noticed that TW_2 has a higher shear resistance than TW_1.

Table 7-2. The fitting parameters that identify the (uncoupled) shear resistance curves. Units for shear force per initial width f_{shear} is in N/mm [64]

Polynomial fitting coefficients	TW_1	TW_2
C_0	9.04E-5	6.46E-4
C_1	1.18E-3	1.27E-3
C_2	-9.05E-5	-1.73E-4
C_3	3.41E-6	1.11E-5
C_4	-7.18E-8	-3.65E-7
C_5	8.18E-10	6.45E-9
C_6	-3.75E-12	-5.71E-11
C_7	0	1.98E-13

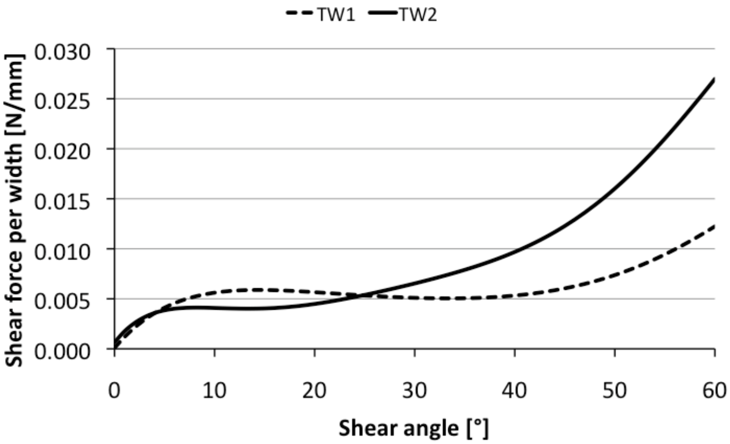

Figure 7-5. Shear diagram for fabrics TW_1 and TW_2

7.3. Implementation of the traction model in ABAQUS

This section deals with the implementation of the traction model developed in Chapter 6 within ABAQUS. ABAQUS provides a user subroutine called VFRIC, for the implementation of user-defined contact behaviour. The VFRIC can be combined with a material user subroutine VUMAT developed, e.g. the AEM model developed by Willems [64].

7.3.1. Kinematic contact

ABAQUS offers two types of contact algorithms, namely the kinematic and penalty algorithm. The major difference between them is that no penetrations between two contacting surfaces are allowed using the kinematic enforcement, while the penalty algorithm allows for penetrations. The penalty algorithm introduces additional stiffness behaviour into a model, which can decrease the stable time increment. Therefore, for the remainder of this chapter the kinematic contact option is applied.

In the contact algorithm of ABAQUS, a master and slave surface need to be defined. These surfaces are represented by a discrete number of surface nodes and elements, which are automatically created by ABAQUS when defining a surface. When using structural elements, e.g. membrane or shell elements, which is commonly the case for fabric forming simulations, 2 surfaces are defined per set of elements. To do so one must ensure that all of the structural elements have their normals oriented consistently. If they are oriented as shown in Figure 7-6, the surface normals will reverse the direction of the surface and improper results may occur.

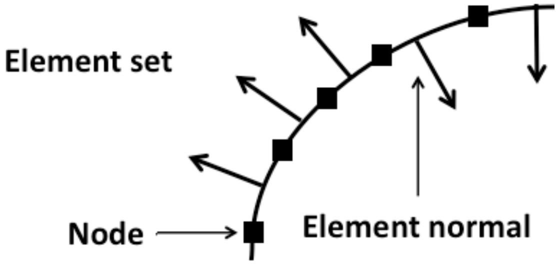

Figure 7-6. Inconsistent orientation of structural element normals

The 2 surfaces that need to be created are both single sided surfaces. A single-sided surface is defined on the positive or negative face of structural elements. The positive face is defined as the one in the direction of the positive element normal, and the negative face is defined as the one in the direction opposite to the element normal. The surface thickness equals the distance between the positive and negative face. On its turn, this surface thickness equals the thickness that is assigned to the element set.

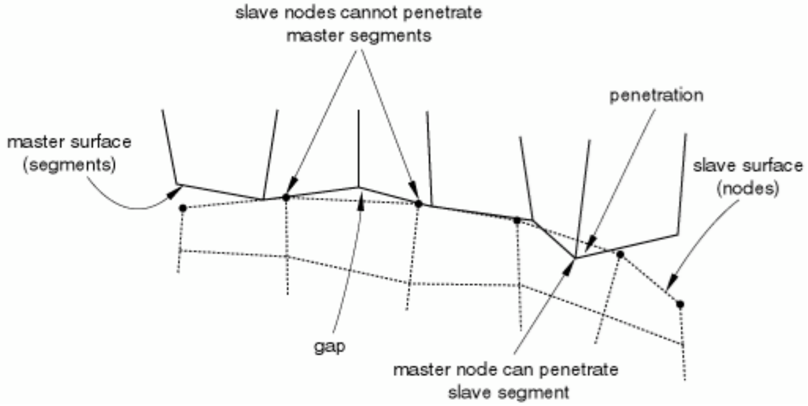

Figure 7-7. Pure master-slave behaviour for kinematic contact in ABAQUS Explicit

During each time step the predicted penetration of the master surface by a slave node is corrected by placing the slave node back on the master surface, which is referred to as hard contact. The depth of each slave node's penetration, the mass associated with it and the time increment are used to calculate the resisting force required to oppose penetration. The kinematic restriction indicates that a slave node is not allowed to penetrate the master surface, however, a master node can penetrate the slave surface as indicated in Figure 7-7. However, when using a sufficiently refined slave mesh such penetrations are minimized.

When examining the influence of the process conditions on the contact behaviour of thermoplastic woven composites in Chapter 6, it was noticed that the velocity, temperature, pressure and interlayer thickness play an important role. Therefore, the following four parts of this section will each be devoted to the implementation of a different process parameter. The subroutine is extended with a slip displacement dependence to incorporate the start-up effect during pull-out. Afterwards, the pull-out tests performed in Chapter 6 are simulated in ABAQUS in order to validate the VFRIC subroutine.

7.3.2. Velocity dependence

The influence of the velocity on the traction is represented by a power-law behaviour. The power-law coefficient $\overline{n}_0$ defined in Table 6-9 is provided as an input parameter for the VFRIC subroutine. The relative slip velocity between two contacting surfaces is not directly provided by the ABAQUS subroutine. Instead the relative amount of slip in the current local coordinate system for each time increment and for each contacting node is provided. Using Eq. 7-8 the amount of slip between the contacting surfaces can be calculated:

$$Dslip_n^2 = Dslip(x)_n^2 + Dslip(y)_n^2 + Dslip(z)_n^2 \qquad \textbf{Eq. 7-8}$$

Here *n* is the node number, *x,y* and *z* denote the direction of slip in the local coordinate system and *Dslip$_n$* is the slip increment during the current time increment for each contacting node in the local coordinate system. The local coordinate system is defined such that the predicted incremental slip vector, which is tangential to the master surface, is taken to coincide with the x-direction and the local z-direction is taken to coincide with the master surface normal direction. If the slip direction changes between increments, Dslip$_n$ may have a nonzero component in the local y-direction and, if the surface is faceted and the contact point moves from one facet to another, a nonzero component can also arise in the local z-direction. The velocity can be calculated according to Eq. 7-9:

$$v_{n,t} = \frac{Dslip_n}{\Delta t} \qquad \textbf{Eq. 7-9}$$

Where Δt is the current time increment and $v_{n,t}$ is the slip velocity of node n at a global time t.

A preliminary pull-out simulation, which will be described in section 7.3.8, with a constant friction coefficient of one and a pull-out velocity of 10 mm/s has been performed. The slip velocity was found to be heavily fluctuating. The total slip as a function of the time is indicated in Figure 7-8, initially no slip occurs since the material is stretched, when the force needed to further stretch the material is higher than the force needed to initiate slip, the middle ply is pulled from between the two adjacent plies. The average velocity of slip is close to the theoretical value of 10 mm/s.

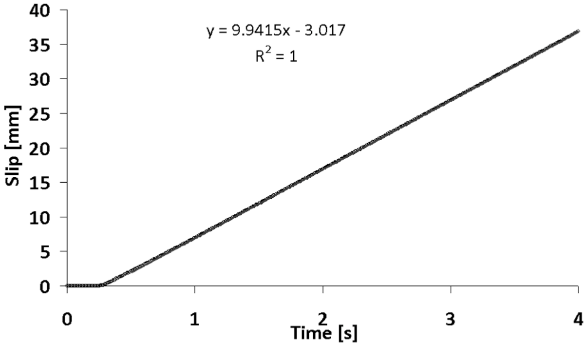

Figure 7-8. The total slip as a function of time for a surface node of the middle ply with a constant friction coefficient as contact behaviour

However, when calculating the velocity using Eq. 7-9, values between 4 and 16 mm/s are reported as shown in Figure 7-9.

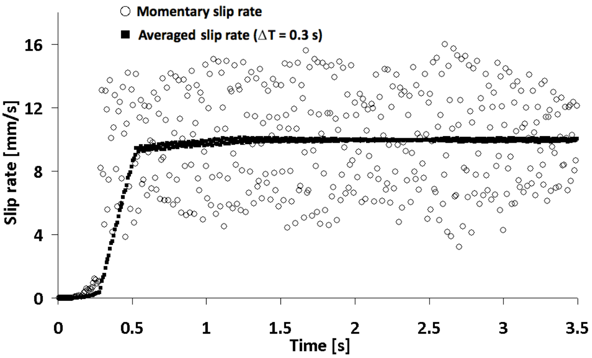

Figure 7-9. The momentary and averaged slip velocity as a function of time for a surface node of the middle ply with a constant friction coefficient as contact behaviour

A reason for this unexpected behaviour is not obvious and has not been reported yet. Probably it is related to the calculation of the relative slip increment or the local slip orientations, which is automated within ABAQUS and can thus not be altered. Using this slip velocity would result in heavily fluctuating local tractions. To minimize the fluctuation of the slip velocity in each node, the velocity is averaged over a predefined time, in this case 0.3 s, as indicated in Figure 7-9. This averaging method underestimates the velocity at the start-up of the pull-out, but provides a more stable slip velocity and thus also a more stable traction calculation. For forming simulations the predefined time interval for velocity averaging is taken as 5% of the total forming time.

7.3.3. Pressure dependence

The pressure has a big influence on the frictional properties. In the VFRIC subroutine the pressure P_n is calculated by dividing the normal force acting on a slave node with the area associated with the slave node.

$$P_n = \frac{F_{N,n}}{A_n}$$ **Eq. 7-10**

Where $F_{N,n}$ is the normal force and A_n is the area associated with the slave node. Both these parameters are provided to the subroutine by ABAQUS at each increment of time for each node that is in contact. In section 7.3.8, the homogeneity of the pressure at start and end of a modelled pull-out test is checked.

7.3.4. Temperature dependence

Thermoforming has a non-isothermal character as was indicated in Figure 5-9. To incorporate the thermal dependence of the traction, each node needs to be extended with an extra degree of freedom, the temperature. There are 2 common ways to account for temperature change during a forming simulation, a fully coupled thermal-mechanical analysis and a sequentially coupled thermal-mechanical analysis. The first adds an extra degree of freedom to the nodes of the discrete plies while the second sequentially does a forming step and a thermal analysis. Both methods increase the complexity of the model and thus the computational time. Moreover, a sequentially coupled analysis requires that the model be converted from the explicit to the implicit environment of ABAQUS and vice versa. Therefore, a third method is developed, which is based on the fact that the forming step is fast and the thermal conductivity of the composite material is low.

In this method a one dimensional explicit finite-difference formulation is used to determine the through the thickness cooling of the laminate when coming in contact with the punch, the die or the blankholder. Afterwards, the predicted temperature profile is approximated by a polynomial function with a maximum degree of 6, which is implemented in the VFRIC subroutine.

7.3.4.1. Explicit finite-difference formulation for unsteady conduction

In this section the general formulation of finite difference equations to heat conduction phenomena is briefly outlined [112]. Figure 7-10 shows the finite difference approximation for a plate. The plate is divided into a number of intervals (sub-plates) of length Δx and Δx/2 at the boundaries and a temperature is assigned to each of the grid points.

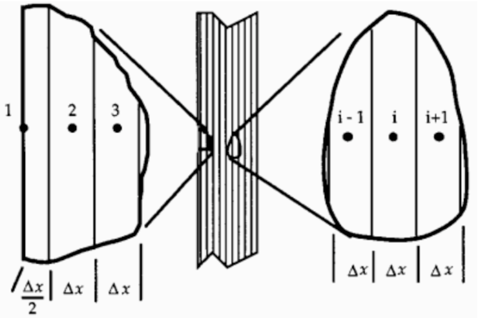

Figure 7-10. A one-dimensional finite difference model of a plate with a general interior node and one surface node detailed [113]

The thermal balance will be considered within the direct neighbourhood of each point, by assigning the first law of thermodynamics, Eq. 7-11, to each node.

$$dU = \delta Q - \delta W \qquad \textbf{Eq. 7-11}$$

Where *dU* is the change in internal energy of the system, δQ is the energy received by the system and *δW* is the work done by the system. The first law of thermodynamics says that the change in the internal energy of a system is equal to the amount of heat added to the system minus the work done by the system on its surroundings. In the case of transient thermal analysis the work done by or on the system equals zero. The change in internal energy in node i for a timestep *Δt* is given by:

$$\frac{\Delta U}{\Delta t} = \rho \cdot c_p \cdot \Delta x \cdot \frac{T_i^{n+1} - T_i^n}{\Delta t} \qquad \textbf{Eq. 7-12}$$

Where, ρ is the density of the material, c_p is the specific heat capacity of the material, T_i^{n+1} is the temperature in node *i* at the time increment *n+1* and T_i^n is the temperature in node *i* at the time increment *n*.

The heat transfer from and to each node is calculated using Fourier's law of conduction if the node does not lie at the surface and using Newton's law of convection when the node is found at a free surface of the system.

$$Q = k_t \cdot \frac{T_{i\pm 1}^n - T_i^n}{\Delta x} \quad \textbf{Eq. 7-13}$$

$$Q = h_t \cdot \left(T_i^n - T_\infty\right) \quad \textbf{Eq. 7-14}$$

Where Q is the heat flow, k_t is the thermal conductivity of the system, h_t is the heat transfer coefficient and T_∞ is the temperature of the environment.

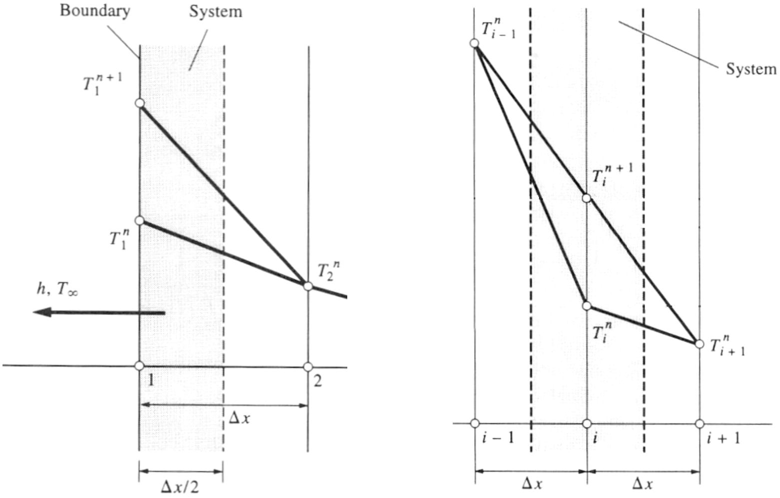

a b

Figure 7-11. The finite-difference approximation for (a) the boundary and (b) the inner thermal energy [112]

Figure 7-11 presents the balance of boundary thermal energy and internal thermal energy. Combining the above equations leads to the following formulation at the boundary of the system:

$$\rho \cdot c_p \cdot \frac{\Delta x}{2} \cdot \frac{T_1^{n+1} - T_1^n}{\Delta t} = k_t \cdot \frac{T_2^n - T_1^n}{\Delta x} - h_t \cdot \left(T_1^n - T_\infty\right) \quad \textbf{Eq. 7-15}$$

And for the internal thermal energy:

$$\rho \cdot c_p \cdot \frac{\Delta x}{2} \cdot \frac{T_i^{n+1} - T_i^n}{\Delta t} = k_t \cdot \frac{T_{i+1}^n - T_i^n}{\Delta x} - k_t \cdot \frac{T_{i-1}^n - T_i^n}{\Delta x} \quad \textbf{Eq. 7-16}$$

With known thermal and contact properties as well as the temperatures from a time step t_n, T_i^n, the temperature at location i for subsequent time *n+1* is obtained from Eq. 7-15 and 7-16. This is called an explicit time marching scheme, which allows direct calculation of the unknowns at each time step from the preceding step. The thermal properties for consolidated TW_1 and aluminium are summarized in Table 7-3.

Table 7-3. Thermal properties for TW_1 [114] and aluminium [112]

Property	TW_1	Aluminium
Density (ρ) [kg/m^3]	1448	2700
Specific heat capacity (c_p) [J/(kg K)]	1481	900
Thermal conductivity (k_t) [W/(m K)]	0.304	270

7.3.4.2. Thermal contact conductivity

In the special case of contact between two solid materials, the thermal contact resistance (TCR), or its reciprocal the thermal contact conductivity (TCC), forms an important parameter that determines the amount of heat flowing from one material to the other. The TCC between TW_1 and a metal is not known. Therefore, an inverse method is used to determine the TCR between TW_1 and the steel plates of the pull-out machine.

An experimental setup to identify the TCC is created. A double-layered laminate is equipped with a thermocouple and pressed between the pull-out machine with a pressure of 100N. This is then modelled by discretising the laminate cross section by nodes that are placed 0.2 mm.
The temperature is measured experimentally in the middle of the laminate, in between the two plies, and thus the predicted temperature profile at the middle of the laminate is taken as a comparison. Figure 7-12 shows the temperature increase as function of the time. The formulation at the boundaries of the system, Eq. 7-15, is changed as follows:

$$\rho \cdot c_p \cdot \frac{\Delta x}{2} \cdot \frac{T_1^{n+1} - T_1^n}{\Delta t} = k_t \cdot \frac{T_2^n - T_1^n}{\Delta x} - TCC \cdot \left(T_1^n - T_p\right) \quad \textbf{Eq. 7-17}$$

$$\rho \cdot c_p \cdot \frac{\Delta x}{2} \cdot \frac{T_{10}^{n+1} - T_{10}^n}{\Delta t} = k_t \cdot \frac{T_{10}^n - T_9^n}{\Delta x} - TCC \cdot \left(T_{10}^n - T_p\right) \quad \textbf{Eq. 7-18}$$

Here T_p is considered to be constant and to be the predefined temperature of the steel plates and h_t is replaced by the TCC.
Using the Eq. 7-16 and 7-17 presented above, the only unknown in the finite difference approach is the TCC. The value of the TCC is iterated until a reasonable fit is accomplished. Figure 7-12 indicates the difference in the

temperature-time as function of the TCC. It is noticed that for a value of 200 W/mK for the TCC, the predicted transient heating at the inside of the laminate agrees well with the measured temperature change. This value is also reported for non-reinforced polypropylene used in injection moulding application [115].

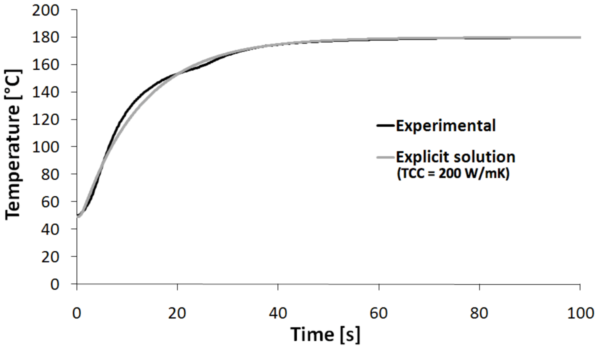

Figure 7-12. Determination of the thermal contact conductivity between TW_1 and a steel plate

The TCC is about 660 times higher than the thermal conductivity of TW_1, which validates the one-dimensional approach. Heat is transported 660 times faster to the punch than within the laminate. However, this causes a thermal gradient through the thickness of the laminate as will be shown in the next section. In further calculations the TCC between the punch, die and blankholder and TW_1 is considered to be 200 W/mK.

7.3.4.3. Laminate cooling during forming

The above-presented one-dimensional method is used to describe the cooling of a hot laminate of 2 plies of TW_1 when it comes into contact with one of the components of the forming station, e.g. the punch (see Figure 7-13(a)). The plies within the laminate are considered to form a homogeneous system. Figure 7-13(b) shows the thermal gradient through the thickness of the laminate as function of the contact time for a laminate pre-heated at 195°C and a punch temperature of 55°C. The laminate is considered to be 2 mm thick, while the punch is considered 95.1 mm thick, which equals the diameter of the hemisphere. Both are divided into 11 pieces of equal length, thus Δx for the laminate is 0.18 mm and Δx for the punch is 8.64 mm. The temperature of the laminate and the punch at the beginning of cooling is homogeneous. The outer surface of the laminate is also cooled by natural convection, which generally means that the thermal conductivity is considered to be 5 W/mK [112]. The inner surface comes into contact with the punch at a time t=0. The temperature of the node at the position 95.1 mm, which equals the radius of the hemisphere, from the surface of the punch is considered to remain constant. This forms the location where in the real hemisphere the cooling/heating channels are present. It is assumed that the temperature at the surface of these channels remains constant.

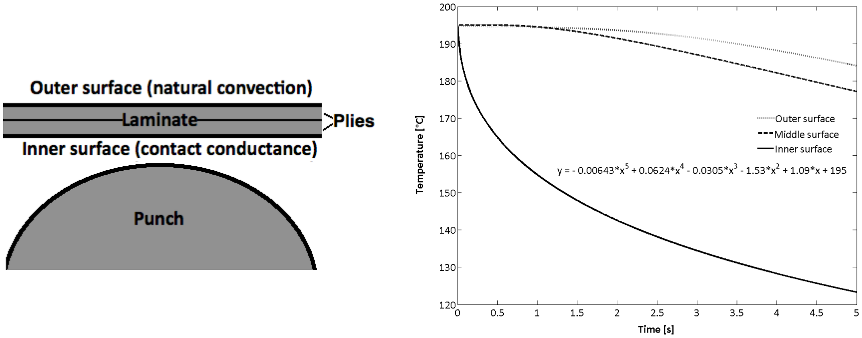

a b

Figure 7-13. Finite difference approach for contact between the punch and the laminate with (a) a schematic representation of the contact and (b) the transient solution at different locations in the laminate

The thermal profile at the inner surface is considered for punch-ply contact. The middle surface of the laminate is used to describe the cooling at the ply-ply interface for a laminate consisting of 2 plies. Both profiles are described by a polynomial function.

$$T_i = \sum_j h_j \cdot t_i^j \quad (j \leq 6)$$

Eq. 7-19

The parameters h_j of this polynomial function form an input variable for the user subroutine. The temperature T_i at the contacting node i, in the VFRIC subroutine, is then calculated using the time t_i the node has already been in contact with the opposite surface.

In case of contact the laminate is pressed between the blankholder and the die, there is no natural convection at the surfaces. Instead the TCC determines the cooling rate of the laminate at both the inner and outer surface. The temperatures of the die and blankholder are considered constant and equal to the room temperature, since these were not heated during forming experiments in Chapter 5. Afterwards the temperature variation at both surfaces is parameterized using a polynomial function, Eq. 7-19, of which the fitting coefficients are again provided to the subroutine.

For the pull-out simulations performed in section 7.3.8, the temperature is considered constant during pull-out. In section 7.5, the above described method is used to determine the cooling of the laminate during forming simulations.

7.3.5. Influence of interlayer thickness

The experiments in the two previous chapters proved that the interlayer thickness has a large influence on the formability and the contact properties between two plies. In Figure 6-20(b) the experimentally measured traction value shows the same trend as the traction value obtained from the Ellis-Arrhenius model of PP_{int} (Eq. 3-4). It has been noticed that the traction decreases with a non-linear behaviour. This is due to the shear thinning of the matrix whereby the viscosity decreases at higher shear rates.

When the user subroutine is provided with an interlayer thickness value larger than zero, the traction is calculated using Eq. 3-4. Although, an increase in pressure will decrease the interlayer thickness and thus increase the traction value, the influence of the pressure on the traction response, if the interlayer is increased is neglected.

7.3.6. Adjustment for steady-state traction

A typical force-displacement or traction-displacement curve is characterized by a peak that decreases towards a steady-state value as shown in Figure 6-7. Since the inter-ply and tool-ply slip displacement can go up to several millimetres, as indicated in Figure 5-5, this non-linear behaviour is accounted for by using the following assumptions:

$$if \quad s_T < d_{cr} : \tau = \tau_p - \frac{\tau_p - \tau^*}{d_{cr}} \cdot s_T \qquad \textbf{Eq. 7-20}$$

$$if \quad s_T \geq d_{cr} : \tau = \tau^* \qquad \textbf{Eq. 7-21}$$

Where, τ is the calculated traction, τ_p is the peak traction obtained according to Eq. 6-24 and τ^* is the steady-state traction, which is defined as a fraction of the peak traction. The total slip is denoted by s_T and d_{cr} is the critical slip displacement where the steady state traction is reached. This behaviour is schematically shown in Figure 7-14.

The values of τ^*, s_T and d_{cr} arise from evaluating the traction-displacement figures in Chapter 6. In these figures it is noticed that the ratio between peak and steady-state traction is not constant and depends on the process conditions. However, this would lead to a too complex contact model and therefore, the ratio between the peak and steady-state traction is chosen to be constant at 0.8 and the critical displacement lies at 15 mm of slip. This expansion of the traction model is only used when the interlayer thickness parameter is set to zero, since the peak traction at increasing thicknesses, Figure 6-20(a), is seen to be less pronounced.

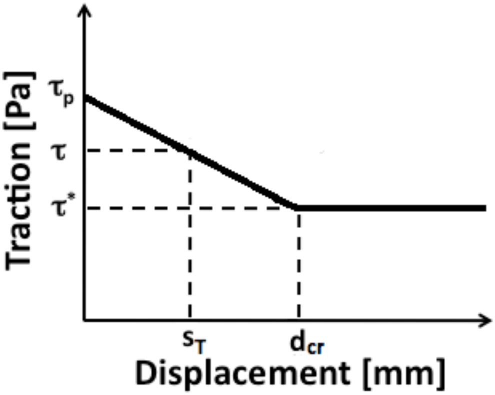

Figure 7-14. Schematic representation of the influence of the slip displacement on the traction value

At slip displacements between 0 and d the friction is dependent on the pressure, temperature, velocity and total slip. At a total slip above the value d, the traction is dependent on the pressure, temperature and velocity. If the interlayer thickness is set larger than zero, the traction is only dependent on the temperature and velocity. An interlayer thickness larger than zero means the traction is calculated using the procedure explained in 7.3.5.

Table 7-4. The input parameters required for the VFRIC subroutine for TW_1

Input parameter	Ply-ply	Tool-ply
A_0 [K/bar]	-3400.4	-3816.1
A_1 [K]	4338.5	4506.9
B_0 [bar^{-1}]	8.073	8.799
B'_1 [Pa]	0.532	0.550
$\overline{n}_0$	0.521	0.523
P_{cr} [bar]	1.41	1.86
Interlayer thickness [mm]	Only provided when needed	
d_{cr} [mm]	15	15
Ratio τ^*/τ_p	0.8	0.8
h_j [°C/s^j]	Determined using method in section 7.3.4	

7.3.7. Flow chart

Figure 7-15 presents a flow chart of the VFRIC subroutine. The input parameters are the coefficients needed to describe the contact behaviour between two adjacent surfaces. The input parameters for ply-ply and tool-ply contact of material TW_1 are given in Table 7-4.

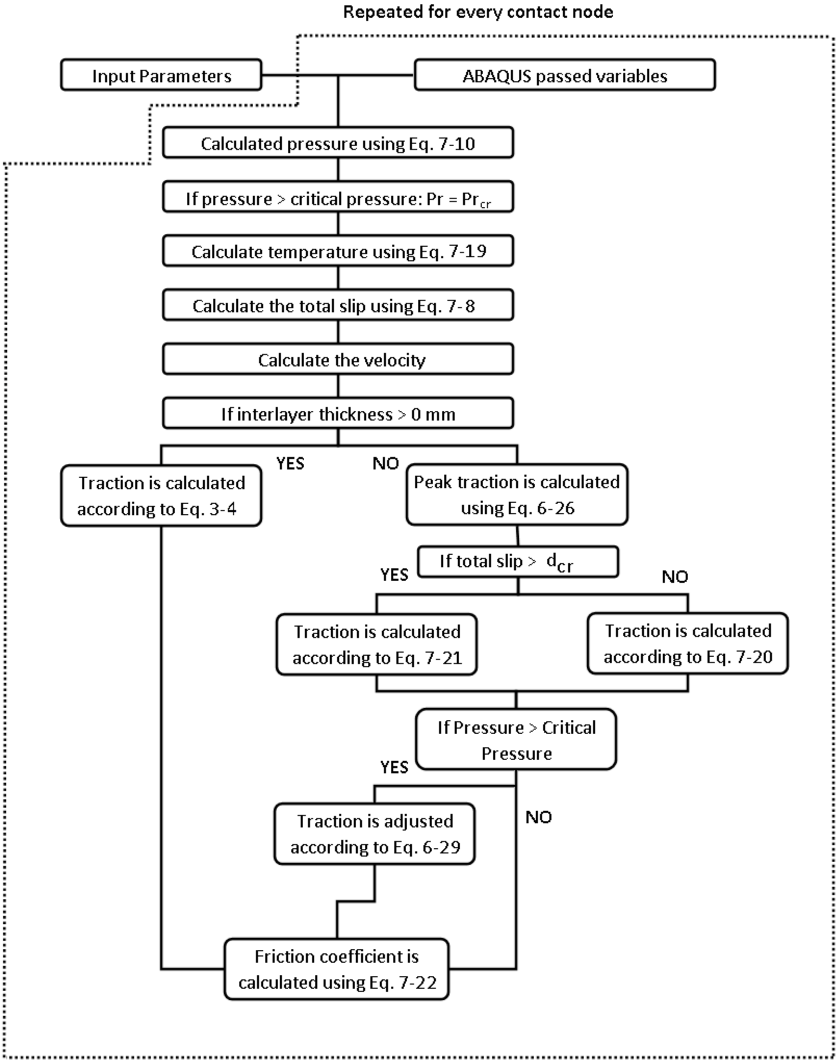

Figure 7-15. Flow chart of the VFRIC user subroutine implemented in ABAQUS explicit

Since the VFRIC subroutine requires a friction coefficient, which defines the contact of the slave node with the master surface, as an output value, the traction value obtained from Eq. 3-4, 7-20, 7-21 or 6-29 is translated to a friction coefficient according to:

$$\mu_i = \frac{\tau_i \cdot A_i}{F_{N,i}}$$ **Eq. 7-22**

Where μ_i is the friction coefficient, τ_i the traction, A_i the area and $F_{N,i}$ the normal force associated with a slave node i. The user subroutine is repeated for every node that is in contact with the opposite surface if the contact behaviour is defined using the VFRIC. Unfortunately, the output of the subroutine, the value of the friction coefficient or the temperature, cannot be visualized in ABAQUS. A possible solution for this problem might be to write each increment the values of the friction coefficient in a separate file.

7.3.8. Comparison between traction model in ABAQUS and experiments

To conclude this section, the experimental pull-out test described in Chapter 6 is modelled into ABAQUS-explicit. The above-presented VFRIC subroutine is now applied using the set-up presented in Figure 7-16 for both inter-ply and tool-ply friction of TW_1 and compared with the experimental behaviour. The steel plates that are used to heat and press the pull-out specimen are represented by 2 rigid plates. One of these plates is fixed and the other one can be translated in the vertical direction to apply pressure on the specimen. The fabric pull-out specimen is meshed using square membrane elements and a difference between the middle and the outer plies is made as illustrated in Figure 7-16(a). The outer plies are 80mm in width, while the outer ply is 160mm wide. The initial total contact area is 80x80 mm^2. The middle ply is defined as the slave surface and the two outer plies are considered to be the master surfaces. The two outer plies are on their turn defined as the slave surfaces in the contact definition between the outer plies and the rigid plates.

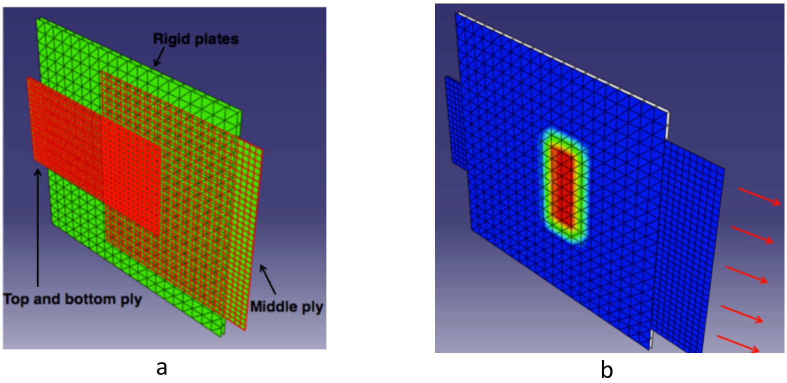

a b

Figure 7-16. The pull-out set-up in ABAQUS consists out of (a) two rigid plates and a top, middle and bottom ply and (b) showing the pulling of the middle ply

The simulation consists of two steps. First, a force is applied on one of the rigid plates so that the pull-out specimen is pressed between the rigid plates. When the pressure between the middle and outer plies reaches the prescribed value, the middle ply is pulled out with a constant velocity and at a constant temperature in the second step (Figure 7-16(b)).

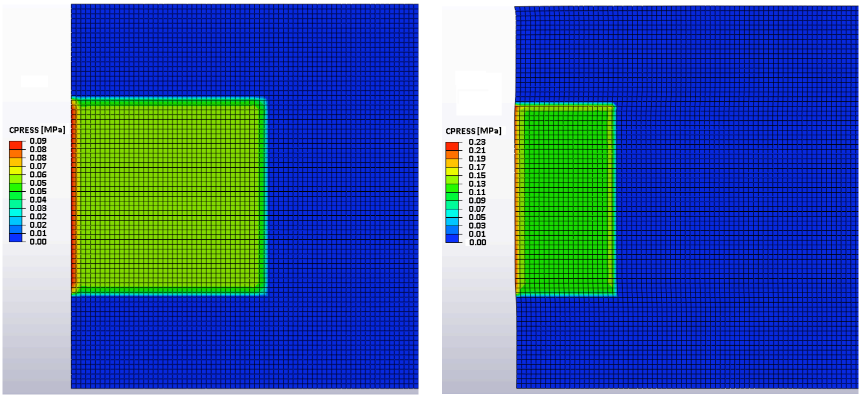

a b

Figure 7-17. Pressure profile over the middle ply for a 400N normal force at (a) 0 mm displacement and (b) 40 mm displacement

In Figure 7-17 the pressure profile over the middle ply is visualised, a good homogeneity is observed, except at the edges where the pressure is higher. However, a higher edge pressure is also noticed in reality as is reported in [105].

The user-defined contact is applied between the middle and the outer plies, while the friction between the outer plies and the steel plates is set to zero.

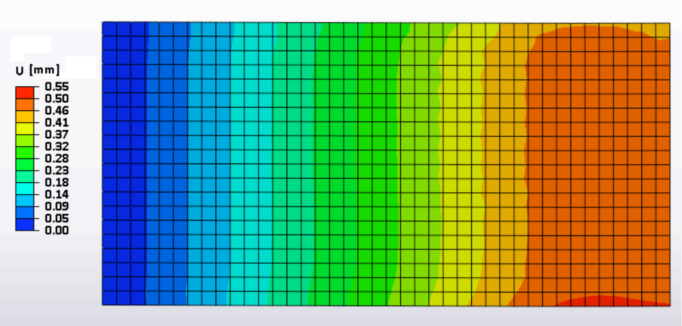

Figure 7-18. Displacement profile of one of the outer plies at the end of the pull-out simulation, i.e. after 40 mm of displacement of the middle ply

From Figure 7-18 it can be seen that the displacement of the outer plies is negligible for a zero friction coefficient. When the middle ply is pulled out 40 mm the outer plies have a maximum displacement of 0.55 mm. The friction force between the outer plies and the rigid plates will not affect the pull-out of the middle specimen and can therefore be neglected.

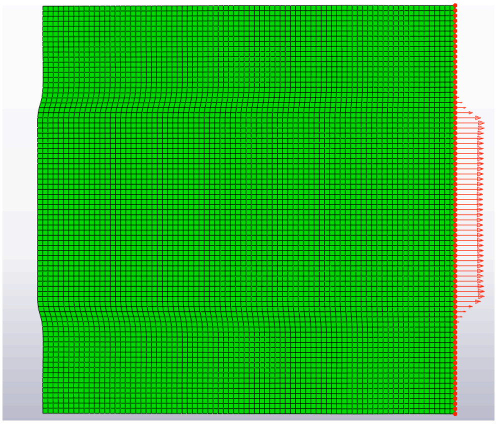

Figure 7-19. Reaction forces in the middle ply due to the pulling action

The reaction forces, indicated as red vectors in Figure 7-19, acting in the nodes of the middle ply that are pulled (highlighted as red dots) are summed up to obtain the global reaction force. The reaction force when using a constant friction coefficient of 1 and applying a constant normal load of 100 N is depicted in Figure 7-20, showing typical coulomb friction behaviour. The friction force is proportional to the normal load, opposes the direction of motion and is independent of contact area.

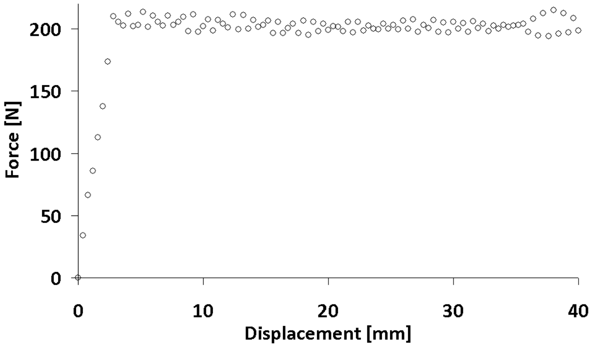

Figure 7-20. The force-displacement curve using a constant friction coefficient of 1

The pull-out force of 200 N agrees with the predefined friction coefficient of 1 (see Eq. 6-3). A small oscillation of the reaction force is noticed, the reason for this oscillation is not obvious and is not reported in the users manual of ABAQUS. Probably this is numeric noise within the explicit integration.

Figure 7-21 shows that the general trend agrees with the experimentally measured pull-out curves, some discrepancies are noticed, though overall a relatively good comparison is found. The temperatures for these pull-out simulations is set to a constant value, since this is also the case reality.

The peak traction values are all quite well predicted for ply-ply contact, with a maximum difference found for the high pull-out velocities of about 15%. Both in the experiments and in the simulation, a decrease in frictional force is noticed with increasing displacement. However, the difference between the experimental and predicted values can occasionally be fairly large, e.g. 35% for the simulation of ply-ply contact performed with process conditions of 1mm/s, 180°C, 0.16 bar and 0 mm interlayer thickness. Though, generally the difference falls within 10%.

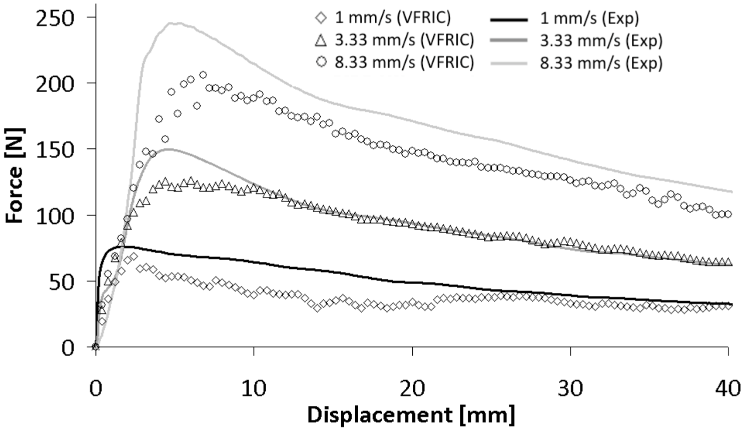

a

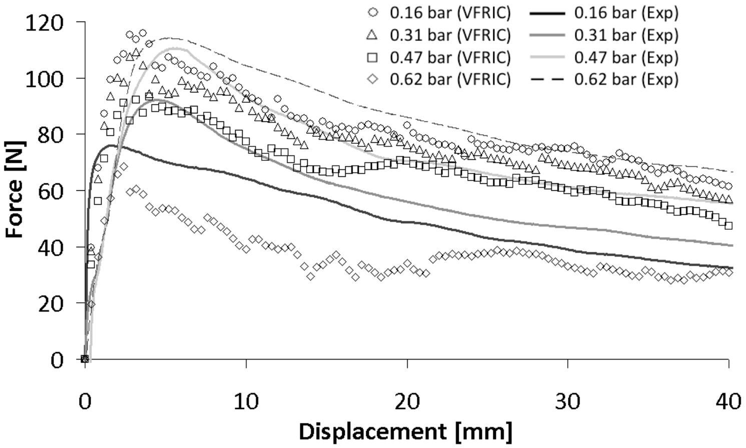

b

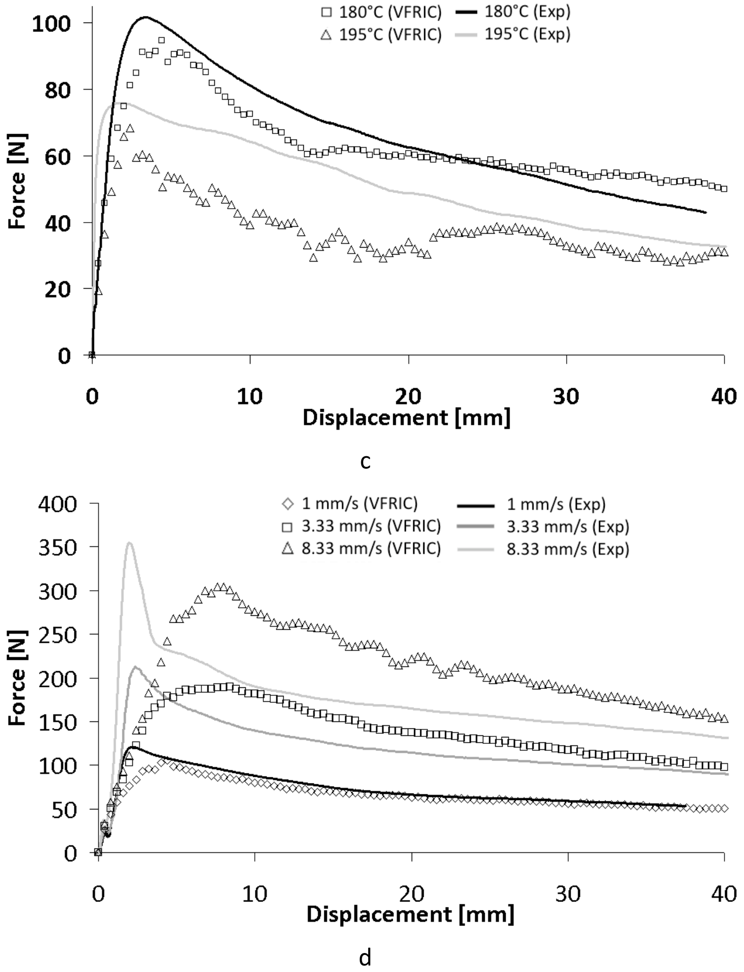

Figure 7-21. Comparison between the results obtained using the VFRIC subroutine and the experimentally measured pull-out curves for ply-ply contact for a 0 mm interlayer thickness and at different (a) pull-out velocities (T=195 °C, P=0.16 bar), (b) pressures (T=195°C, v=1mm/s) and (c) temperatures (P=0.16 bar, v=1 mm/s) and (d) for tool-ply contact at different pull-out velocities (T=195 °C, P=0.16 bar)

For tool-ply contact the initial peak value is reached at a lower slip displacement as is predicted. However, the magnitude of the measured and predicted peak tractions are fairly equal.

The oscillations in the force output of the FE-approach are similar to the oscillations noticed when applying Coulomb friction conditions (see Figure 7-20).

7.4. Wrinkling of membrane structures

Chapter 5 indicated that wrinkling is one of the main defects that occur during forming of woven reinforced composites. However, membranes cannot accurately represent wrinkling, since they do not possess any flexural stiffness. Shell elements are better suited to investigate wrinkling, though a very dense mesh, which increases the computational time of the model, is required. Since, the number of elements needed is inversely proportional to the expected size of the wrinkles [116]. Therefore, membrane elements will be used to simulate the forming of multilayered fabric composites.

Wrinkling of membranes has been investigated by many scientists [74, 75, 117]. The major assumption they all have in common, is that no or a small amount of compressive stresses may be present in a membrane, which is reasonable for a fabric. This assumption has led to the development of the tension field theory. In the tension field theory the state of stress in a membrane is evaluated using the principal stresses or strains and they are tested to a wrinkling criterion. Figure 7-22 visualizes that depending on the applied loads, a membrane can achieve the taut, slack or wrinkled state.

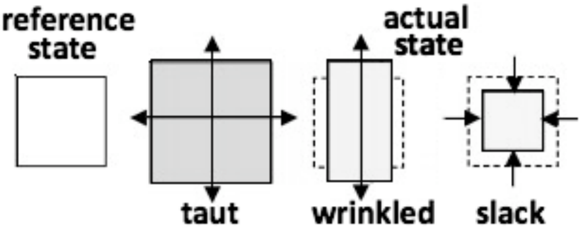

Figure 7-22. Principal status of membranes – taut, wrinkled, slack (adapted from [74])

In the reference state the membrane is free from any stresses or strains. A membrane becomes taut, which means tightly drawn, when the minimal principal stress (S_{min}) or the minor strain (ε_{min}) is larger then zero. The opposite of taut is slack, which is defined by a negative major stress or strain. Wrinkling falls within these conditions. A membrane is considered in a wrinkled state if the minimum principal stress or the minor strain is negative and the maximum principal stress (S_{max}) or the major strain (ε_{max}) is positive. Various wrinkling criteria are summarized in Table 7-5 and have been proposed in [74].

Table 7-5. Summary of different wrinkling criteria [74]

State of stress	Principal stress criterion	Principal strain criterion	Mixed criterion
Taut	$S_{min} > 0$	$\varepsilon_{min} > 0$	$S_{min} > 0$
Wrinkled	$S_{min} \leq 0$ and $S_{max} > 0$	$\varepsilon_{min} \leq 0$ and $\varepsilon_{max} > 0$	$S_{min} \leq 0$ and $\varepsilon_{max} > 0$
Slack	$S_{min} \leq 0$ and $S_{max} \leq 0$	$\varepsilon_{min} \leq 0$ and $\varepsilon_{max} \leq 0$	$\varepsilon_{max} \leq 0$

The different wrinkling criteria have been evaluated in [118, 119]. It was found that the mixed criterion of stress and strain is best for the analysis of wrinkling. When compressive stresses are about to occur in the membrane structure, a wrinkling deformation builds up in the membrane. This means that the stiffness of the membrane perpendicular to the direction of the wrinkles reduces to zero. Therefore, when a membrane reaches a wrinkled state, the stiffness of the material in the membrane is adapted so the minimum principal stress vanishes. However, in this study, the minimum principal stress (S_{min}), i.e. the maximum compressive stress, of a membrane will be taken as a factor that determines the possibility of a wrinkling to occur. Therefore, a Python subroutine is used to determine the minimal S_{min} during the forming of the woven composite laminate, based on the current ABAQUS solution.

7.5. Simulation of the forming of two-layered composites – comparison with the Forming Limit Diagram

In Chapter 5, a forming limit diagram for the drapeability of two-layered woven thermoplastic composites was presented. It was noticed that an increase in the difference in yarn orientation between the neighbouring plies invoked more severe wrinkling. The experiments that have led to the derivation of the FLD are repeated using the AEM model and the implemented traction model. The finite element representation of the forming station is depicted in Figure 7-23(a). The tooling, i.e. the punch, the die and the blankholder, are represented by rigid elements. The laminate stack consists of two plies, which are each represented by three node membrane elements. A prerequisite in the AEM model is that yarn orientations (warp and weft) are aligned to the element edges prior to forming; therefore the membrane elements are right triangles. The orientation between the plies is increased from 0 to 45° in steps of 15° and the process parameters are summarized in Table 7-6.

Table 7-6. Process parameters used in the forming simulations

Process parameter	Value
Pre-heat temperature	195°C
Punch temperature	80°C
Blankholder pressure	0.1 bar
Forming velocity	200 mm/min

First the transient cooling is predicted using the method presented in section 7.3.4 and by knowing the pre-heat and punch temperature. The parameters describing the temperature decrease serve as an input for the VFRIC subroutine. There exist four different contact interactions: contact of (a) the top ply with the blankholder and (b) with the punch, (c) the bottom ply with the die and (d) between the neighbouring plies. For the three first contacting interactions, the temperature decrease that occurs at the outer surfaces of the laminate is considered using the method developed in section 7.3.4. The contact interaction between the adjacent plies is divided in two contact zones, namely one in the region of the punch (red mesh) and one in the region of the blankholder as indicated in Figure 7-23(b). For these two contact conditions, a different transient cooling profile at the central surface is used to incorporate the non-isothermal behaviour of the thermoforming operation, which is also determined by the method described in section 7.3.4. Instead of contact with a heated punch, contact with the cold blankholder and die are considered.

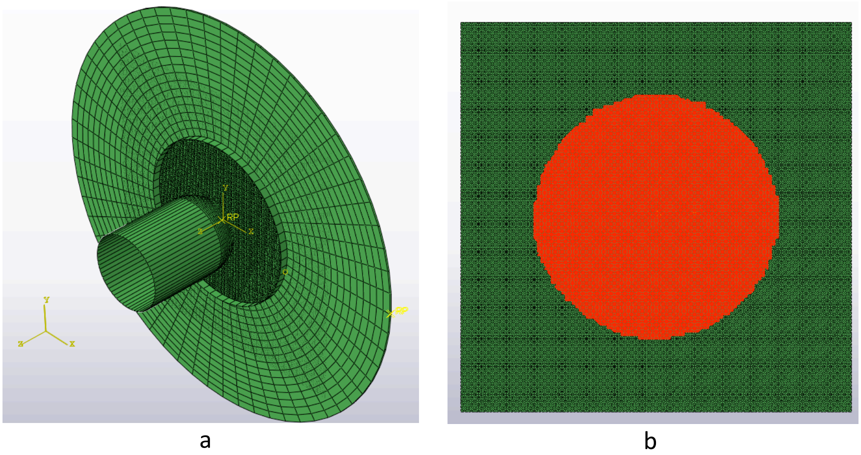

Figure 7-23. Forming simulations performed in ABAQUS require (a) a discrete representation of the deepdrawing set-up and (b) a division in 2 zones according to the different contact interactions

When the forming simulation is finished, a Python routine is used to determine the minimal “minimum principal stress”, i.e. the maximum compressive stress, within the laminate at a certain punch depth. Figure 7-24(a) shows the compressive stress vs. punch depth for different lay-up configurations.

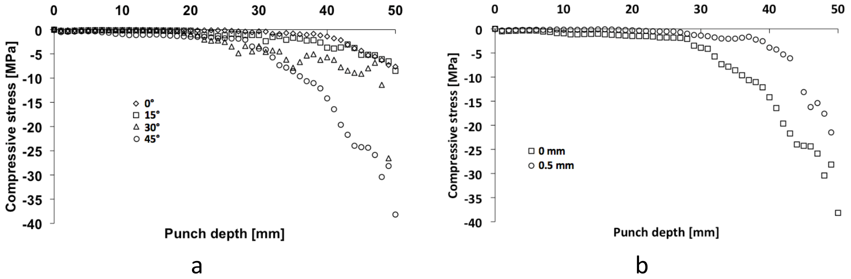

Figure 7-24. The compressive stress as function of the punch displacement for (a) different relative orientations and (b) for a 45° relative orientation and different interlayer thicknesses

An increase in relative orientation between the plies results in larger compressive stresses. According to the previous section higher compressive stresses lead to more severe wrinkling, this is in agreement with the observations made in Chapter 5. Increasing the interlayer thickness results in lower compressive stresses during forming as can be seen in Figure 7-24(b) for a 45° relative orientation between the plies, again this is in agreement with the results of the experimental screening done in Chapter 5. There it has been concluded that a higher interlayer thickness results in products with the least amount of wrinkles. The highest compressive stresses in the laminate occur there were the laminate passes the fillet of the die and they are parallel with the tangent at the fillet.

Table 7-7 indicates the punch depth at which the maximum compressive stress becomes higher than 1 MPa for different lay-up configurations. The value of 1 MPa is arbitrary chosen, since no values of a maximum allowable compressive stress prior to buckling are available.

Table 7-7. Punch depth when the maximum compressive stress reaches 1MPa

Relative orientation	0 mm interlayer thickness	0.5 mm interlayer thickness
0°	37 mm	40 mm
15°	22 mm	39 mm
30°	21 mm	39 mm
45°	11 mm	28 mm

It is obvious from the presented results that the higher the relative orientation, the faster in the forming step the compressive stresses become higher and thus the more severe wrinkling will occur. This agrees with the FLD presented in Chapter 6, since wrinkling is more pronounced at increasing relative orientations. An increase in interlayer thickness increases the punch depth at which the compressive stress becomes higher than 1 MPa. Figure 7-25 shows the contour plot of the minimum in-plane principal stress for different relative orientations at a punch depth of 50 mm and a interlayer thickness of 0 mm. Wrinkling is visible in the simulations in case of 15, 30 and 45° relative orientation, though the amount of wrinkling is less severe as is experimentally observed in Chapter 5.

7.6. Conclusions

This chapter describes the implementation of ply-ply and tool-ply friction into a finite element software package. The influence of the process conditions on the contact behaviour between the plies and between the tool and the laminate are incorporated. It has been combined with the fabric AEM-model in order to simulate the pull-out tests reported in Chapter 6. Afterwards, the draping of a double-layered composite is simulated.

The compressive stresses that arise during forming simulations are taken as an indication for the amount of wrinkling. A high compressive stress increases the chance for wrinkling. The simulations agree well with the experimental observations made in Chapter 5. An increase in compressive stresses, and thus wrinkling, is found when the interlayer thickness is low and the relative orientations between the adjacent plies of the laminate increases. This implies that in the absence of a good visualization method for wrinkling, optimization of the forming can be performed by pursuing a processing path such that the material points of the laminate will experience a minimum amount of compressive stresses.

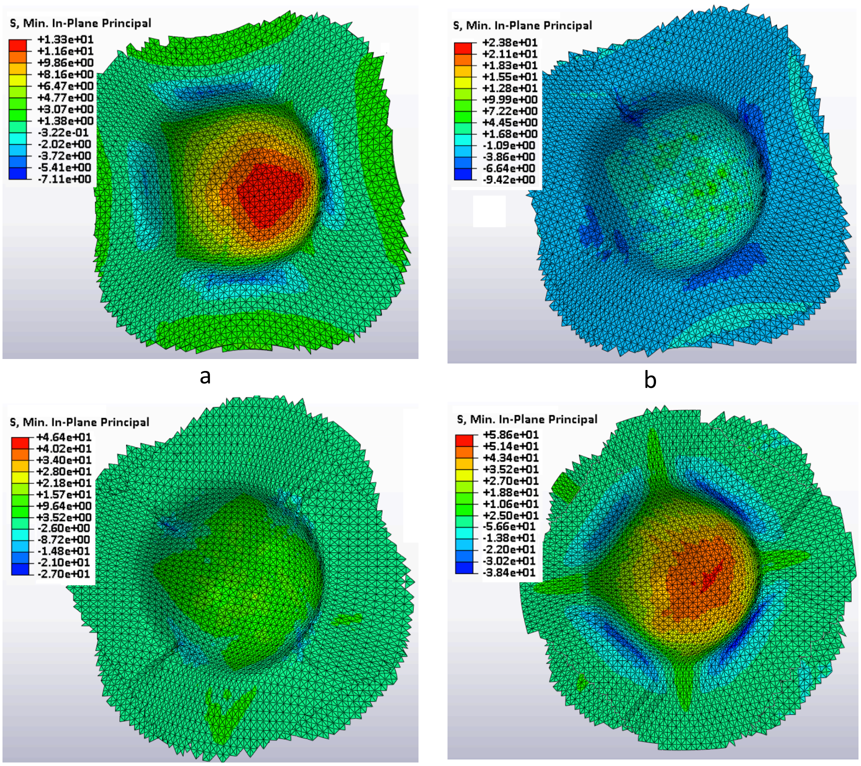

a b

c d

Figure 7-25. Contour plot of the minimum principal stress at 50 mm of punch depth for a (a) 0°, (b) 15°, (c) 30° and (d) 45° relative orientation between the plies of the laminate

Chapter 8

Conclusions

8.1. Summary of the results

Woven reinforced thermoplastic composites possess some unique mechanisms that allow them to conform to complex shapes using rapid thermoforming techniques, which is attractive in for example the automotive or sporting goods industry. However, when forming a multilayered laminate as is generally the case in the industry, the laminate lay-up and the shape complexity of the final product influence its formability. Therefore, a study of the forming of multilayered woven reinforced thermoplastic composites has been performed.

The thesis has examined the formability of several commercially available woven composites. The aim of this work was to investigate the influence of the process conditions on the formability of a layered stacking and to determine the influence of the key draping mechanisms on the occurrence of defects. This was achieved by performing an extensive experimental program, screening the influence of the process parameters used during forming and by developing an experimental apparatus to investigate the frictional properties between the different layers of the laminate under process conditions. In order to diminish such heavy experimental work in future, the contact behaviour was implemented into a commercial finite element code for shaping simulations, which allows supporting the optimization of product manufacturing.

8.1.1. Forming limit diagram and experimental screening

In a first step, the formability of a double-layered laminate was experimentally investigated by deepdrawing the laminate into a hemispherical shape. The influence of the laminate configuration is assessed by increasing the orientation between the adjacent plies from 0 to 45° in steps of 15°. A large influence on the formability is found, whereby no wrinkling is noticed if the relative orientation between the plies of the laminate is negligible. Increasing the relative orientation leads to a gradual increase in wrinkling. This increase in wrinkling is accompanied by a large decrease in intra-ply shear of each ply of the laminate, which suggests that intra-ply shear is prevented and buckling becomes the dominant mode of deformation. A forming limit diagram is identified, which visualizes the limitations associated with thermoforming of woven thermoplastic composites. It shows that the forming of woven thermoplastic composites is limited to, either a simple laminate configuration, i.e. the relative orientation between the plies is small and the amount of inter-ply shear is modest, or to simple product shapes, i.e. shapes that can be draped with a limited amount of intra-ply shear.

A second step was to investigate the influence of the process conditions on the formability of such a double-layered laminate. Therefore, a design of experiment was developed, screening the influence of the preheating and punch temperature, the velocity of forming, the blankholder pressure and additional matrix thickness between the plies. A laminate that consisted of plies with a 45° difference in orientation was chosen. The amount of wrinkling was taken as an indication of the formability. From the study it was noticed that the only significant factor, which influenced the formability is the interlayer thickness, whereby a thicker interlayer results in less wrinkling. This effect was also shown in the forming limit diagram, where for a thicker interlayer the amount of intra-ply shear for the same laminate configuration drastically increases. This makes it possible to create complex shapes with more complex laminate configurations. An alternative method, whereby a film of matrix material is pressed between a stacking of dry fabric is proposed. The resulting laminate is not preconsolidated and gives rise to material with a relatively high formability. However, the degree of impregnation and consolidation after forming is questionable. The matrix material needs flow over a large distance in order to wet the reinforcing fabrics.

8.1.2. Ply-ply and tool-ply contact behaviour

Forming multilayered materials involves that relative slip between the layers of the material needs to occur if the final product shape is to be single or doubly curved. If this inter-ply slip does not occur, the plies at the outside of the curve will undergo tension and the plies at the inside of the bend will be compressed. If the compressive forces exceed a critical load, the inner plies will buckle and wrinkling will occur. A second contact type takes place at the interface between the material that is shaped and the tooling, i.e. punch, die and blankholder, equipment. A high friction coefficient can lead to local tearing of the material, while a to low friction coefficient invites wrinkling to occur, since the blankholder would not introduce forces that counteract compressive stresses.

Therefore, an extensive study has been performed to investigate the influence of the process conditions on the two contact types described above. Both ply-ply and tool-ply contact were found to be dominated by the matrix rich interlayer that exists between the plies or the tool-ply surfaces. The transient rheological behaviour of the matrix explains the influence of the slip distance and process conditions on the contact behaviour. At the start of slip, the matrix viscosity exhibits an overshoot due to its visco-elastic behaviour. This overshoot makes the contact behaviour highly non-linear, since afterwards it decreases towards a steady-state value.

The influence of the velocity, temperature, normal pressure and interlayer thickness on the traction overshoot value was assessed. It has been shown that the velocity influence could be described by power-law behaviour and the temperature influence has the shape of an Arrhenius equation. The influence of the pressure on the overshoot value was found to be small. A large decrease was noticed when the interlayer thickness was increased, which suggest that the plies behave more independent.

Different phenomenological models (Lamers' model and the Stribeck approach) were investigated. Both these models require knowing the matrix rheological behaviour and the height of the interlayer between the contacting materials. In this thesis, an alternative model, i.e. the traction model, is developed that does not need the flow behaviour of the matrix nor the interlayer thickness.

The newly proposed model requires more experiment data than the Lamers' or Stribeck model, but is found to give a good prediction for the velocity and temperature influence at relatively low pressures (< 1bar).

8.1.3. Forming simulation

To support the optimization of the textile drape forming process, simulation software is developed to investigate the forming of woven reinforced composites. Currently two simulation approaches, a kinematical and a mechanical, are often used to predict the draping of textile reinforcements.

In this thesis, first a comparative study between the kinematical and mechanical approach for a single layered woven reinforced composite is undertaken. An extended hemispherical shaped punch was draped, and the results were compared to experimentally obtained data. The kinematic draping algorithm, PAM-QUIKFORM, failed to adequately predict the fibre reorientation after draping for certain ply configurations. The reason lies within the algorithm used to calculate the sequence of the unknown material points. This algorithm does not agree with the real draping front, forms local constraints, which are not found in reality, and gives rise to erroneous results. A mechanical finite element approach, PAM-FORM, was also used to simulate the forming. Here, the comparison with the experimental results shows good agreement.

It was felt that the mechanical approach was best suited for the forming prediction of woven reinforced composites. This approach also allows incorporating realistic inter-ply and tool-ply contact behaviour. The kinematic draping approach cannot be used to predict the forming of multilayered materials, since the interaction between the different layers is not taken into account.

Secondly, the traction model developed in Chapter 6 was implemented in a commercial finite element package, ABAQUS, in order to simulate the draping of multilayered composites. Forming simulations were performed, which corresponded to the experiments that lead to the forming limit diagram. The minimum principal stress, i.e. the maximum compressive stress, was taken as a parameter for the occurrence of wrinkling. High compressive stresses give a higher chance of unwanted wrinkling. The simulations showed the same trend as was found experimentally. An increase in relative orientation between the plies of the laminate gives rise to more wrinkling. Decreasing the friction coefficient between the plies by increasing the interlayer thickness, drastically decreased the compressive stresses and thus also the possibility that wrinkling would occur.

8.2. General conclusions and outlook

8.2.1. Conclusions for practical use

From the studies presented in this thesis text several general conclusions can be stated, all of them are linked to the research questions in Chapter 2:

- It has been shown that kinematic draping has difficulties to predict the correct fibber reorientation of textile reinforcements during forming of complex shapes. The results are heavily dependent on the experience of the software operator. Moreover, the difference in predicted and observed shear angle can go as high as 40°, which in most cases would lead to the conclusion that wrinkling occurs. Thus, it is highly possible that when kinematic draping predicts that a product cannot be formed wrinkle-free, in reality it can. The finite element method on the other hand, provides a good, but less computationally effective alternative. The shear angle difference between simulation and experiment stays within a reasonable 10°.

- The drapeability of multilayered woven reinforced composites depends on the amount of inter-ply slip necessary to adapt to the desired shape. A forming limit diagram for two-layered fabric reinforced composites is suggested. From this diagram it is noticed that when only a small amount of inter-ply slip needs to occur, the forming limit prior to wrinkling will be determined by the intra-ply shear behaviour of the composite. If a large amount of inter-ply slip needs to take place, wrinkling is difficult to eliminate. Out-of-plane buckling is triggered by the compressive stresses, which are normally dissipated by slip between the plies.

- A solution to increase the formability is proposed by adding matrix material between the plies of the laminate, which makes them deform more independently from each other. The adjacent plies can more easily slip relative to each other and thus the compressive stresses are relieved.

- A resin rich interlayer dominates the inter-ply and tool-ply slip behaviour. This layer acts as a lubricant, which is sheared when two surfaces slide relative from each other. The influence of the process conditions on the tool-ply and ply-ply contact can be attributed to the rheological properties of this lubricant.

- The finite element method can be used to investigate the influence of the process parameters on the formability. The compressive stresses that are calculated during a forming simulation can be used as a parameter to assess the possibility that wrinkling will occur. Thus, an objective function, which minimizes the compressive stresses during forming, could form the input for an optimization routine. However, an exact prediction on if wrinkling would occur is difficult since stress values at the onset of buckling are not yet available.

8.2.2. Suggestions for future research and improvements

The above stated general conclusions are based on the observations made in this study, which was focused on a double-layered stacking of plies. In reality, laminates can go up to tens of plies in thickness, depending on the application. It is a natural follow up from this work that the above-presented conclusions are checked for more complex laminates.

The descriptive models presented in Chapter 6, all have their shortcomings, and therefore, further work on the contact behaviour between adjacent plies and between tooling and ply should involve the development of a predictive model. Especially, the start-up effect of shear flow forms an important phenomenon that should be taken into account when developing such models. Incorporating the complex contact behaviour of thermoplastic composites at elevated temperatures is not a straightforward task. Also, when a realistic representation of wrinkling is desired, shell elements provide a good alternative for membrane elements. However, this implicates that the out-of-plane shear stiffness should be experimentally identified or realistically estimated and the AEM model is to be extended to include out-of-plane stiffness components. An adequate wrinkling criterion for fabric reinforcements can help to better visualize the local wrinkling zones and thus increase the potential for simulation tools to support process optimization.

Appendix A

Woven fabric parameters

This appendix introduces the most common woven fabric parameters. Most of the terms used to describe both fibbers and fabrics come from the textile industry, predating composite materials. These parameters are used to characterize the woven textile. The most important elements are ends and picks count, linear density of the yarn, weave pattern, areal density of the fabric and crimp. More information regarding textiles used in technical applications can be found in [120].

A.1. Ends and picks count

The ends and picks count are linked to the number of threads per unit length of a woven fabric. The ends count is the number of warp yarns per unit length, while the picks count denotes the number of weft yarns per unit length.
In general, a fabric with a high ends and picks count has a fine weave, while fabrics with a low number of ends and picks are called course.

A.2. Yarn linear density

The yarns linear density provides information about the mass per unit length of the yarn. There are two units of measure that are commonly used, namely denier and tex. Denier is defined as the mass of the yarn in gram per 9000m, while tex expresses the mass of the yarn in grams per 1000m. The higher the linear density, the thicker the yarn is and vice-versa.

A.3. Crimp

Crimp refers to the amount of bending that is done by thread as it interlaces with the threads that are lying in the opposite direction of the fabric. Crimp is defined as the ratio of difference of length of yarn (L_y) taken from length of fabric (L_f) to the length of fabric (L_f), indicated in Figure A-1.

$$Crimp = \frac{L_y - L_f}{L_f} \cdot 100 \qquad \textbf{Eq. A-1}$$

Crimp is related to many aspects of the fabric. It affects the smoothness, the mechanical properties, the thickness and the handleability of the fabric. The crimp balance is affected by the tensions in the fabric during, but also after weaving. If the weft is kept at low tension while the tension in warp directions is high, then there will be considerable crimp in the weft and very little in the warp.

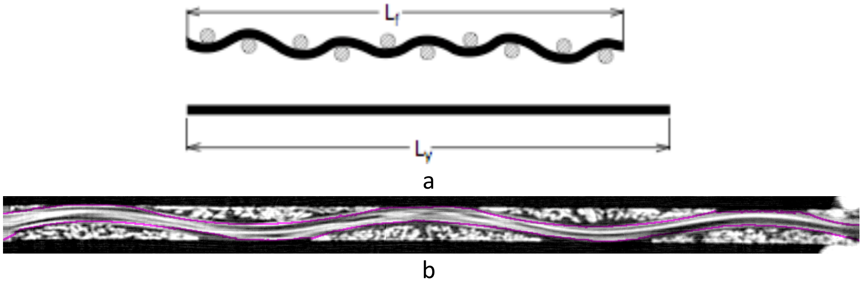

b

Figure A-1. (a) scheme of crimp, which shows the relation of length of the yarn in the fabric to the length of the fabric and (b) crimp in fabric TW$_1$

A.4. Weave or fabric pattern

The fabric pattern refers to the arrangement of warp and weft yarns in the fabric. The number of weave structures that can be produced is practically unlimited. In this section only the basic structures are discussed, since most two-dimensional woven technical fabrics are constructed from simple weaves and of these at least 90% use plain or twill weave.

A plain weave structure the simplest interlacing pattern that can be produced. Figure A-2(a) illustrates a plain weave structure, which is formed by alternatively lifting and lowering one warp yarn across one weft yarn. A twill is a weave that consists of one or more warp yarns running over and under two or more weft yarns. This results in diagonal lines that run on the face of a fabric as can be seen in Figure A-2(b). The final basic weave structure is a satin, shown in Figure A-2(c), which is a warp-dominated weaving technique that forms a minimum number of interlacing in a fabric.

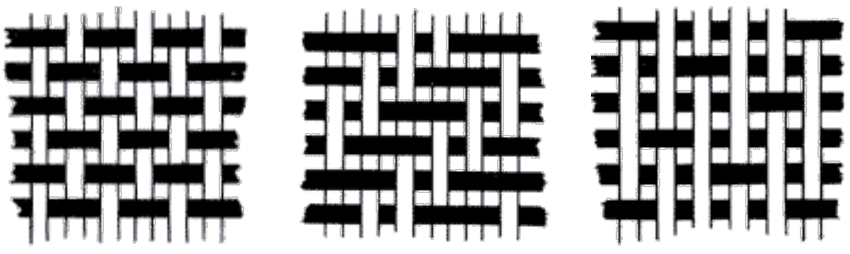

a b c

Figure A-2. Three basic weave pattern: (a) plain, (b) 2/2 twill and (c) 5 harness satin

The weave pattern has an important influence on the handleability, smoothness, drapeability and the mechanical properties of the fabric.

Due to the high interlacing degree with a plain weave it possesses supreme handleability. However, the high degree of crimp reduces the mechanical properties when compared to twill or satin weaves. Moreover, the high degree of contact points between the warp and weft yarn generally result in a less smooth and drapeable material. Satin weaves on the other hand, have very low crimp and thus high smoothness, drapeability and mechanical properties, but the reduction in the interlocking of warp and fill greatly increases the possibility of distortion during handling.

A.5. Areal density

The areal density is a fabric parameter that is often used by fabric suppliers to describe their materials. It provides the weight of the fabric per unit area. The most common unit of measure is gram per square metre.

References

1. Long, A.C., *Design and Manufacture of textile composites*. 2005: Woodhead Publishing Limited in association with the Textile Institute
2. Gommers, B., I. Verpoest, and P. Van Houtte, *Analysis of knitted fabric reinforced composites: Part II. Stiffness and strength.* Composites Part a-Applied Science and Manufacturing, 1998. **29**(12): p. 1589-1601.
3. Chu, C.C., C.L. Cummings, and N.A. Teixeira, *Mechanics of elastic performanc of textile materials. Part V: A study of the factors affecting the drape of fabrics - The development of a drape meter.* Textile research journal, 1950. **20**(8): p. 539-548.
4. Kenkare, N. and T.M. Plumlee, *Fabric drape measurement: A modified method using digital image processing.* Journal of Textile and Apparel, Technology and Management, 2005. **4**(3): p. 1-8.
5. Cusick, G.E., *Measurement of fabric drape.* Journal of the textile institute, 1968. **59**(6): p. 253-260.
6. Hu, J., *Structure and mechanics of woven fabrics*. 2004, Cambridge, England: Woodhead publishing limited. 308.
7. Chen, B.J. and M. Govindaraj, *A parametric study of fabric drape.* Textile research journal, 1996. **66**(1): p. 17-24.
8. Hu, J.L. and Y.F. Chan, *Effect of fabric mechanical properties on drape.* Textile research journal, 1998. **68**(1): p. 57-64.
9. Kawabata, S. and M. Niwa, *Fabric performance in clothing and clothing manufacture.* Journal of the textile institute, 1989. **80**(1): p. 19-50.
10. Rozant, O., P.E. Bourban, and J.A.E. Månson, *Drapability of dry textile fabrics for stampable thermoplastic preforms.* Composites Part A: Applied Science and Manufacturing, 2000. **31**(11): p. 1167-1177.
11. Wysocki, M., *Continuum modelling of composites consolidation*, in *Departement of Applied Mechanics*. 2006, Chalmers University of Technology: Göteborg, Sweden. p. 152.
12. Bernet, N., et al., *Commingled yarn composites for rapid processing of complex shapes.* Composites Part A: Applied Science and Manufacturing, 2001. **32**(11): p. 1613-1626.
13. Vaidy, U.K. and K.K. Chawla, *Processing of fibre reinforced thermoplastic composites.* International materials reviews, 2008. **53**(4): p. 185-218.
14. Gutowski, T.G., *Advanced composites manufacturing*. 1997, New York: John Wiley & Sons.
15. Breuer, U., et al., *Deep drawing of fabric-reinforced thermoplastics: Wrinkle formation and their reduction.* Polymer Composites, 1996. **17**(4): p. 643-647.

16. Bersee, H.E.N. and A. Beukers, *Diaphragm forming of continuous fibre reinforced thermoplastics: influence of temperature, pressure and forming velocity on the forming of Upilex-RÆ diaphragms.* Composites Part A: Applied Science and Manufacturing, 2002. **33**(7): p. 949-958.
17. Long, A.C., *Composites forming technologies*. Vol. 1. 2007, Cambridge: Woodhead publishing in textiles. 328.
18. Long, A.C., C.E. Wilks, and C.D. Rudd, *Experimental characterisation of the consolidation of a commingled glass/polypropylene composite.* Composites Science and Technology, 2001. **61**(11): p. 1591-1603.
19. Boisse, P., A. Gasser, and G. Hivet, *Analyses of fabric tensile behaviour: determination of the biaxial tension-strain surfaces and their use in forming simulations.* Composites Part a-Applied Science and Manufacturing, 2001. **32**(10): p. 1395-1414.
20. Willems, A., et al., *Optical strain fields in shear and tensile testing of textile reinforcements* Composites Science and Technology, 2007. **68**(3-4): p. 807-819.
21. Hivet, G., et al. *Optical analysis of woven fabric`s shear behavior*. in *ESAFORM*. 2004. Trondheim, Norway.
22. Cao, J., et al., *Characterization of mechanical behavior of woven fabrics: Experimental methods and benchmark results.* Composites Part A: Applied Science and Manufacturing, 2008. **39**(6): p. 1037-1053.
23. Harrison, P., M.J. Clifford, and A.C. Long, *Shear characterisation of viscous woven textile composites: a comparison between picture frame and bias extension experiments.* Composites Science and Technology, 2004. **64**(10-11): p. 1453-1465.
24. Harrison, P. and P. Potluri. *Shear tension coupling in biaxial bias extension tests*. in *17th International Conference on Composite Materials*. 2009. Edinburgh, Scotland.
25. Harrison, P., et al. *A Normalisation Procedure for Biaxial Bias Extension Tests*. in *11th International ESAFORM Conference on Materials Forming*. 2008. Lyon, France.
26. Zouari, B., J.-L. Daniel, and P. Boisse, *A woven reinforcement forming simulation method. Influence of the shear stiffness.* Computers & Structures, 2006. **84**(5-6): p. 351-363.
27. Harrison, P., et al., *Constitutive modelling of impregnated continuous fibre reinforced composites: a micro-mechanical approach.* Plastics, Rubber and Composites, 2002. **2**(31): p. 76-86.
28. Skelton, J. and W.D. Freeston, *Mechanics of Elastic Performance of Textile Materials .19. Shear Behavior of Fabrics Under Biaxial Loads.* Textile Research Journal, 1971. **41**(11): p. 871-880.
29. Zouari, B., J.L. Daniel, and P. Boisse, *A woven reinforcement forming simulation method. Influence of the shear stiffness.* Computers and Structures, 2006. **84**(5-6): p. 351-363.

30. Amirbayat, J. and J.W.S. Hearle, *The Anatomy of Buckling of Textile Fabrics - Drape and Conformability.* Journal of the textile institute, 1989. **80**(1): p. 51-70.
31. Clapp, T.G. and H. Peng, *Buckling of Woven Fabrics .3. Experimental Validation of Theoretical-Models.* Textile Research Journal, 1990. **60**(11): p. 641-645.
32. Wang, J., et al. *Energy analysis of reinforcement deformations during viscous textile composite forming*. in *Proceedings of ESAFORM*. 2008. Lyon, France.
33. ASTM, *D4918 Standard Test Method for Coefficient of Static Friction of Uncoated Writing and Printing Paper by Use of the Inclined Plane Method*. 2007. p. 4.
34. TAPPI, *Coefficient of static friction (slide angle) of packaging and packaging materials (including shipping sack papers, corrugated and solid fiberboard) (inclined plane method), Test Method T 815*. 2007. p. 5.
35. Murtagh, A.M., M.R. Monoghan, and P.J. Mallon. *Development of shear deformation apparatus to characterize the interply slip mechanism of advanced thermoplastic composites*. in *8th Irish Materials Forum Conference (IMF8) - Engineered Materials*. 1992. Dublin, Ireland: Trans Tech Publications.
36. Lebrun, G., M.N. Bureau, and J. Denault, *Thermoforming-stamping of continuous glass fiber/polypropylene composites: Interlaminar and tool-laminate shear properties.* Journal of thermoplastic composite materials, 2004. **17**(2): p. 137-165.
37. Gorczyca, J.L., et al., *Modeling of friction and shear in thermostamping of composites - Part I.* Journal of Composite Materials, 2004. **38**(21): p. 1911-1929.
38. ten Thije, R. and R. Akkerman. *Tool-ply friction in thermoplastic composite forming*. in *The 11th International ESAFORM conference on Materials Forming*. 2008. Lyon, France: Springer.
39. Scherer, R. and K. Friedrich, *Inter- and intra-ply-slip process during thermoforming of CF/PP laminates.* Composites manufacturing, 1991. **2**(2): p. 92-96.
40. Goshawk, J.A. and R.S. Jones, *Structure reorganization during the rheological characterization of continuous fibre-reinforced composites in plane shear.* Composite Part A-Applied Science and Manufacturing, 1996. **27**(4): p. 279-286.
41. Gorczyca-Cole, J.L., J.A. Sherwood, and J. Chen, *A friction model for use with a commingled fiberglass-polypropylene plain-weave fabric and the metal tool during thermostamping.* European Finite Element Revenue, 2004. **14**(6-7): p. 729-751.
42. Akkerman, R., et al. *Tool-ply friction in composite forming*. in *10th ESAFORM Conference on Material Forming*. 2007. Zaragoza, Spain: American Institute of Physics.

43. Wilks, C.E., *Processing technologies for woven glass/polypropylene composites*. 1999, University of Nottingham
44. Lamers, E.A.D., *Shape distortions in fabric reinforced composite products due to processing induced fibre reorientation*. 2004, Universiteit Twente: Enschede. p. 134.
45. Gorczyca-Cole, J.L., J.A. Sherwood, and J. Chen, *A friction model for thermostamping commingled glass-polypropylene woven fabrics.* Composites Part A: Applied Science and Manufacturing, 2007. **38**(2): p. 393-406.
46. Stribeck, R., *Kugellager Für Beliebige Belastungen.* Zeitschrift des Vereines Deutscher Ingenieure, 1902. **46**: p. 1341-1348.
47. Lin, H., et al. *Investigation of tool-ply friction of viscous textile composites*. in *The 8th International Conference on textile Composites (TEXCOMP-8)*. 2006. Nottingham, United Kingdom.
48. Stachowiak, G.W. and A.W. Batchelor, *Engineering Tribology*. 2005: Elsevier-Butterworth-Heineman. 832.
49. Wakeman, M.D., et al., *Compression moulding of glass and polypropylene composites for optimised macro- and micro-mechanical properties - 1 Commingled glass and polypropylene.* Composites Science and Technology, 1998. **58**(12): p. 1879-1898.
50. Gutowski, T.G., et al., *Consolidation Experiments for Laminate Composites.* Journal of Composite Materials, 1987. **21**(7): p. 650-669.
51. Nowacki, T., et al., *Deep drawing of fabric reinforced thermoplastics: Maximum drawing depth and mechanism of wrinkle formation.* Polymers & Polymer Composites, 1998. **6**(4): p. 215-222.
52. Prodromou, A.G. and J. Chen, *On the relationship between shear angle and wrinkling of textile composite preforms.* Composites Part A: Applied Science and Manufacturing, 1997. **28**(5): p. 491-503.
53. Mack, C. and H.M. Taylor, *The fitting of woven cloth to surfaces.* Journal of the textile institute, 1956. **47**: p. 477-488.
54. Mack, C. and H. Taylor, *The fitting of woven cloth to surfaces.* Journal of the Textile Institute, 1956. **47**: p. 477-487.
55. Heisey, F.L. and K.D. Haller, *Fitting Woven Fabric to Surfaces in 3 Dimensions.* Journal of the Textile Institute, 1988. **79**(2): p. 250-263.
56. Vanderweeen, F., *Algorithms for Draping Fabrics on Doubly-Curved Surfaces.* International Journal for Numerical Methods in Engineering, 1991. **31**(7): p. 1415-1426.
57. Van West, B.P. and S.C. Luby, *Fabric draping simulation in composites manufacturing part, Part I and II.* Journal of Advanced Materials, 1997. **4**: p. 29-41.
58. Long, A.C., et al., *Effects of fibre architecture on reinforcement fabric deformation.* Plastics Rubber and Composites, 2002. **31**(2): p. 87-97.
59. Long, A.C., J. Wiggers, and P. Harrison. *Modelling the effects of blankholder pressure and material variability on forming of textile*

preforms. in *9th International ESAFORM Conference on Material Forming*. 2005. Cluj-Napoca, Romania.

60. Hancock, S.G. and K.D. Potter, *The use of kinematic drape modelling to inform the hand lay-up of complex composite components using woven reinforcements.* Composites Part A: Applied Science and Manufacturing, 2006. **37**(3): p. 413-422.
61. Hancock, S.G. and K.D. Potter, *Inverse drape modelling--an investigation of the set of shapes that can be formed from continuous aligned woven fibre reinforcements.* Composites Part A: Applied Science and Manufacturing, 2005. **36**(7): p. 947-953.
62. Cook, R.D., D.S. Malkus, and M.E. Plesha, *Concepts and applications of Finite Element Analysis*. 3 ed. 1989, New York: Wiley.
63. Scherer, R., N. Zahlan, and K. Friedrich. *Modeling the interply-slip process during thermoforming of thermoplastic composites using finite-element analysis*. in *Composite materials: design and analysis*. 1990. Brussels, Belgium: Computational mechanics publications ltd, Southampton.
64. Willems, A., *Forming simulations of textile reinforced composite shell structures*. 2008, Katholieke Universiteit Leuven: Leuven. p. 299.
65. Lim, T.C. and S. Ramakrishna, *Modelling of composite sheet forming: a review.* Composites Part a-Applied Science and Manufacturing, 2002. **33**(4): p. 515-537.
66. Boisse, P., et al., *Different approaches for woven composite reinforcement forming simulation.* International Journal of Material Forming, 2008. **1**(1): p. 21-29.
67. Boisse, P., B. Zouari, and A. Gasser, *A mesoscopic approach for the simulation of woven fibre composite forming.* Composites Science and Technology, 2005. **65**(3-4): p. 429-436.
68. Hamila, N. and P. Boisse, *Simulations of textile composite reinforcement draping using a new semi-discrete three node finite element.* Composites Part B: Engineering, 2008. **39**(6): p. 999-1010.
69. de Luca, P., P. Lef\'bure, and A.K. Pickett, *Numerical and experimental investigation of some press forming parameters of two fibre reinforced thermoplastics: APC2-AS4 and PEI-CETEX.* Composites Part A: Applied Science and Manufacturing, 1998. **29**(1-2): p. 101-110.
70. Dessenberger, R.B. and C.L. Tucker, *Forming limit measurements for random-fiber mats.* Polymer Composites, 1998. **19**(4): p. 370-376.
71. Hivet, G., et al. *Analysis of woven reinforcement preforming using an experimental approach*. in *Proceedings of the 17th International Conference on Composite Materials (ICCM 17)*. 2009. Edingburgh, United Kingdom.
72. ten Thije, R.H.W., *Finite element simulations of laminated composite processes*. 2007, University of Twente

73. Skordos, A.A., C. Monroy Aceves, and M.P.F. Sutcliffe, *A simplified rate dependent model of forming and wrinkling of pre-impregnated woven composites.* Composites Part A: Applied Science and Manufacturing, 2007. **38**(5): p. 1318-1330.
74. Jarasjarungkiat, A., R. Wuechner, and K.U. Bletzinger, *A wrinkling model based on material modification for isotropic and orthotropic membranes.* Computer Methods in Applied Mechanics and Engineering, 2008. **197**(6-8): p. 773-788.
75. Stanuszek, M., *FE analysis of large deformations of membranes with wrinkling.* Finite Elements in Analysis and Design, 2003. **39**(7): p. 599-618.
76. Miyazaki, Y., *Wrinkle/slack model and finite element dynamics of membrane.* International Journal for Numerical Methods in Engineering, 2006. **66**(7): p. 1179-1209.
77. Manthey, D.W. and D. Lee, *Recent Developments in a Vision-Based Surface Strain-Measurement System.* Jom-Journal of the Minerals Metals & Materials Society, 1995. **47**(7): p. 46-49.
78. Long, A.C., et al., *Characterizing the processing and performance of aligned reinforcements during preform manufacture.* Composites Part a-Applied Science and Manufacturing, 1996. **27**(4): p. 247-253.
79. Nino, G.F. and H.E.N. Bersee. *Internal behaviour of intraply shear in thermoformed composites*. in *Proceedings of the 8th International Conference on Textile Composites (TEXCOMP-8)*. 2006. Nottingham.
80. Stoilova, T. and S.V. Lomov, *Round-robin formability study, Characterization of glass-PP fabrics CORRECTED VERSION*. 2005, Katholieke Universiteit Leuven, department of Metallurgy and Materials Engineering.
81. Chanda, M. and S.R. Roy, *Plastics technology handbook*. 1998: CRC press. 1214.
82. Van Goidsenhoven, S., *Analyse van de belangrijkste parameters bij het dieptrekken van meerlaagse weefselcomposieten*, in *Departement of Metallurgy and Materials Engineering*. 2008, Katholieke Universiteit Leuven: Leuven. p. 66.
83. http://www.metris.com.
84. http://www.correlatedsolutions.com.
85. Decoster, K., *Experimentele optimalisatie van de thermische vormgeving van textielcomposieten*, in *Departement werktuigkunde*. 2006, K.U.Leuven: Leuven. p. 154.
86. Crispeels, P., *Vormgeven van thermoplastische weefselcomposieten*, in *Departement werktuigkunde*. 2007, K.U.Leuven: Leuven. p. 94.
87. Wakeman, M.D. and J.A.E. Manson, *Composites manufacturing -- thermoplastics*, in *Design and manufacture of textile composites*. 2005, Woodhead publishing Limited and CRC Press LLC.

88. Boisse, P., et al., *Composites forming* Advances in material forming. Esaform 10 years on, 2007: p. 61-79.
89. Sharma, S.B. and M.P.F. Sutcliffe, *Draping of woven fabrics: Progressive drape model.* Plastics Rubber and Composites, 2003. **32**(2): p. 57-64.
90. Cherouat, A. and J.L. Bill\"et, *Mechanical and numerical modelling of composite manufacturing processes deep-drawing and laying-up of thin pre-impregnated woven fabrics.* Journal of Materials Processing Technology, 2001. **118**(1-3): p. 460-471.
91. Borouchaki, H. and A. Cherouat, *Geometrical draping of composite fabrics.* Comptes Rendus Mecanique, 2003. **331**(6): p. 437-442.
92. ESI-Group, *PAM-FORM 2G 2005*. 2005.
93. Zienkiewicz, O.C. and R.L. Taylor, *The Finite Element Method: Volume 1 The Basis*. 2000, Oxford, UK: Butterworth - Heineman. 708.
94. Sun, J.S., K.H. Lee, and H.P. Lee, *Comparison of implicit and explicit finite element methods for dynamic problems.* Journal of Materials Processing Technology, 2000. **105**(1-2): p. 110-118.
95. Lomov, S.V., et al., *Picture frame test of woven composite reinforcements with a full-field strain registration.* Textile Research Journal, 2006. **76**(3): p. 243-252.
96. Willems, A., et al., *Optical strain fields in shear and tensile testing of textile reinforcements.* Composites Science and Technology, 2008. **68**(3-4): p. 807-819.
97. Lomov, S.V., A.V. Truevtzev, and C. Cassidy, *A predictive model for the fabric-to-yarn bending stiffness ratio of a plain-woven set fabric.* Textile Research Journal, 2000. **70**(12): p. 1088-1096.
98. Willems, A., et al. *Double dome forming simulation of woven textile composites*. in *The 9th International Conference on Material Forming (ESAFORM 2006)*. 2006. Glasgow.
99. Lee, W. and J. Cao. *Numerical simulations on double-dome forming of woven composites using the coupled non-orthogonal constitutive model*. in *12TH ESAFORM Conference on Material Forming*. 2009. Twente, the Netherlands.
100. Yu, X., et al., *Intraply shear locking in finite element analysis of woven fabric forming processes.* Composite Part A-Applied Science and Manufacturing, 2006. **37**(5): p. 790-803.
101. Hou, M., K. Friedrich, and R. Scherer, *Optimization of Stamp Forming of Thermoplastic Composite Bends.* Composite Structures, 1994. **27**(1-2): p. 157-167.
102. Hua, L., et al., *Predictive FE Modelling of Prepreg Forming to Determine Optimum Processing Conditions.* AIP Conference Proceedings, 2007. **907**(1): p. 1092-1097.
103. Lamers, E.A.D., *Shape distortions in fabric reinforced composite products due to processing induced fibre orientation*. 2004, Universiteit Twente.

104. Montgomory, D.C., *Design and analysis of experiments*. 5th ed. 1997, New York: John Wiley and Sons. 680.
105. ten Thije, R. and R. Akkerman. *Design of an experimental setup to measure tool-ply and ply-ply friction in thermoplastic laminates*. in *The 12th International ESAFORM Conference on Material Forming*. 2009. Enschede, the Netherlands.
106. Friedrich, K. and R. Scherer, *Inter- and Intraply-slip flow processes during thermoforming of CF/PP-laminates.* Composites Manufacturing, 1991. **2**(2): p. 92-96.
107. Borg, T. and E.J. Paakkonen, *Linear viscoelastic models Part III. Start-up and transient flow effects from the molecular weight distribution.* Journal of Non-Newtonian Fluid Mechanics, 2009. **159**(1-3): p. 17-25.
108. Rubio, P. and M.H. Wagner, *LDPE melt rheology and the pom-pom model.* Journal of Non-Newtonian Fluid Mechanics, 2000. **92**(2-3): p. 245-259.
109. Bogaerts, L., M. Lossie, and D. Vandepitte. *Study of the Deepdrawing Process of Technical Textile Reinforced Thermoplastics*. in *4th International Esaform Conference on Material Forming*. 2001. Liege, Belgium.
110. Hamrock, B.J., S.R. Schmid, and B.O. Jacobson, *Fundamentals of fluid film lubrication*. 2004, New York: Marcel Dekker.
111. Hagege, B., *Simulation du comportement mécanique des milieux firbeux en grandes transformation: Application aux renforts tricotes*, in *Laboratoire de Mécanique des Systèmes et des Procédés*. 2004, Ecole nationale supérieure d'arts et métiers: Paris.
112. Arpaci, V.S., A. Selamet, and S. Kao, *Introduction to heat transfer*. 2000, Lebanon: Prentice hall. 614.
113. Kreith, F. and R.F. Boehm, *Heat and Mass Transfer*. Mechanical Engineering Handbook, ed. F. Kreith. 1999, Boca raton: CRC Press. 287.
114. Schell, J.S.U., et al., *Computational and experimental analysis of fusion bonding in thermoplastic composites: Influence of process parameters.* Journal of Materials Processing Technology, 2009. **209**(11): p. 5211-5219.
115. Massé, H., et al., *Heat transfer with mechanically driven thermal contact resistance at the polymer-mold interface in injection molding of polymers.* International Journal of Heat and Mass Transfer, 2004. **47**(8-9): p. 2015-2027.
116. Wong, Y.W. and S. Pellegrino, *Wrinkles in Square Membranes*, in *Textiles composites and inflatable structures*. 2005, Springer Netherlands. p. 109-122.
117. Raible, T., et al., *Development of a wrinkling algorithm for orthotropic membrane materials.* Computer Methods in Applied Mechanics and Engineering, 2005. **194**(21-24): p. 2550-2568.

118. Rossi, R., et al., *Simulation of light-weight membrane structures by wrinkling model.* International Journal for Numerical Methods in Engineering, 2005. **62**(15): p. 2127-2153.
119. Kang, S. and S. Im, *Finite element analysis of dynamic response of wrinkling membranes.* Computer Methods in Applied Mechanics and Engineering, 1999. **173**(1-2): p. 227-240.
120. Horrocks, A.R. and S.C. Anand, *Handbook of technical textile*. 2000, Cambridge, England: Woodhead Publishing Limited. 559.

Curriculum vitae

Name **Kristof Vanclooster**

Address Predikherenhoevestraat 81
2840 Reet (Rumst)
Belgium

Telephone +32 (0)477 22 67 09

E-mail kristof.vanclooster@pandora.be

Education

2005-Present	**Katholieke Universiteit Leuven** Leuven	**Doctoral Assistant** Dissertation: **“Forming of multilayered fabric reinforced thermoplastic composites”**
2004-2005	**Katholieke Universiteit Leuven** Leuven	**Master of materials engineering option polymers and composites** Thesis: **“Study of EVOH-barrier resins for injection moulding applications”** in corporation with EVAL Belgium (in english) **Magna Cum laude**
2000-2004	**Karel de Grote Hogeschool** Antwerp	**Master of industrial science option chemistry** Thesis: **“Water based dispersions of (meth)acrylate copolymer made via mass polymerisation”** in corporation with Dupont de Nemours (in dutch) **Magna Cum laude**

Work experience

05/2005 – 11/2005 **Laboratory assistant**	**British Plaster Board** Antwerp	Quality control of raw materials and final products

Internship

06/2004 – 05/2005 **Laboratory assistant**	**Dupont de Nemours** Mechelen	Production and evaluation of water-based resins for the car paint industry on lab scale

List of publications

1. **Vanclooster K.**, Lomov S.V., Willems A., Verpoest I. *Measurement of local deformations on thermoformed composite parts under different process conditions.* The 10th International ESAFORM Conference on Material Forming. Zaragoza, Spain; 2007. p. 1058-1063.
2. Lomov S.V., Boisse P., Deluycker E., Morestin F., **Vanclooster K.**, Vandepitte D., Verpoest I., Willems A. *Full-field strain measurements in textile deformability studies.* Composites Part a-Applied Science and Manufacturing. 2008;**39**(8):1232-1244.
3. **Vanclooster K.**, Lomov S.V., Verpoest I. *Investigation of interply shear in composite forming.* The 11th International ESAFORM Conference on Material Forming. Lyon, France; 2008.
4. **Vanclooster K.**, Lomov S.V., Verpoest I. *Simulating and validating the draping of woven fibre reinforced polymers.* ECCM 13th European Conference on Composite Materials. Stockholm, Sweden; 2008.
5. **Vanclooster K.**, Lomov S.V., Verpoest I. *Experimental validation of forming simulations of fabric reinforced polymers using an unsymmetrical mould configuration.* Composites Part A: Applied Science and Manufacturing. 2009;**40**(4):530-539.
6. **Vanclooster K.**, Van Goidsenhoven S., Lomov S.V., Verpoest I. *Optimizing the deepdrawing of multilayered woven fabric composites.* The 12th International ESAFORM Conference on Material Forming. Twente, the Netherlands; 2009. (Keynote presentation)
7. **Vanclooster K.**, Lomov S.V., Verpoest I. *On the formability of multi-layered fabric composites.* ICCM - 17th International Conference on Composite Materials. Edinburgh, United Kingdom; 2009.
8. **Vanclooster K.**, Lomov S.V., Verpoest I. *Simulation of multi-layered composites forming.* The 13th International ESAFORM Conference on Material Forming. Brescia, Italy; 2010.
9. Sargent J., Chen J., Sherwood J., Cao J., Boisse P., Willems A., **Vanclooster K.,** Lomov S.V., Khan M., Mabrouki T., Fetfatsidis K., Jaufrrès D. Benchmark *Study of Finite Element Models for Simulating the Thermostamping of Woven-Fabric Reinforced Composites.* The 13th International ESAFORM Conference on Material Forming. Brescia, Italy; 2010.